UNIVERSITÀ DEGLI STUDI
DI MILANO

DIPARTIMENTO DI CHIMICA

PhD course in Chemistry – XXXI cycle

Nanostructured Oxides as Leading Actors for Environmental Remediation, Smart Surfaces and Energy Applications

PhD candidate:
Luca Rimoldi

Tutor: Prof. Silvia Ardizzone
Coordinator: Prof. Emanuela Licandro

2018

Contents

Abstract

In the last decades, metal oxides have been widely employed in the field of nanotechnology, thanks to their physicochemical characteristics. In fact, oxidic compounds can be exploited for manifold applications due to their chemical, thermal and mechanical stability, the low-cost, the low- or non-toxicity. Moreover, the possibility to easily obtain metal oxides as nano or nanostructured powders together with their high reactivity, mainly due to the presence of polar hydroxyl groups populating the surface, have always attracted the scientific community interested in the field connected to catalysis. Among the most adopted metal oxide in materials science, titanium dioxide (TiO_2), tungsten oxide (WO_3), silicon dioxide (SiO_2) and aluminium oxide (Al_2O_3) can be mentioned.

Actually, the properties of the metal oxides strictly depend on their electronic structure. Some of them are semiconductors (*e.g.* TiO_2 and WO_3), while others are insulators (*e.g.* SiO_2 and Al_2O_3), in dependence on the width of the energy gap between the valence and the conduction bands.

Semiconductors, thanks to the relatively small band gap with respect to insulators, can be exploited for a wide number of recently developed applications in chemistry, physics and materials science. One of these applications exploited light with suitable wavelength for the promotion of electrons from the valence band to the conduction band, in order to promote reduction or oxidation reactions. This field of the physical chemistry is called photocatalysis and is the main focus of this Thesis.

Photocatalysis, especially if titanium dioxide-based, can be useful for promoting a wide range of chemical reactions, *e.g.* hydrogen and fuels production, CO_2 reduction, metal reduction/oxidation. In the last decades, photocatalysis was also proposed as an innovative and effective environmental remediation technique for the oxidative degradation of organic compounds constituting atmospheric or water pollution. In fact, photocatalysis can be able, differently from traditional remediation techniques (*e.g.* biological treatments, adsorption by activated carbon, …),

to completely degrade the pollutants and their oxidation intermediates and by-products to harmless compounds (water, CO_2, and, in case, inorganic salts).

Nonetheless, photocatalysis suffers from critical issues which, nowadays, still prevent its use on a large utility-scale. Among these, the low quantum yields and, thus, efficiency of the photocatalytic process with respect to the light irradiation adopted to activate the photocatalyst, the need of UV light to activate large band gap semiconductors, such as TiO_2, and the high costs for the removal of the photocatalyst from the polluted effluent once the remediation treatment has been performed.

This Thesis is divided into three different parts, on the grounds of the materials studied and their final application. In Part I (Chapters 1–7), TiO_2-based materials for photocatalysis, variably modified and engineered by adopting different strategies for the promotion of specific properties, are reported. In Part II (Chapters 8–11), the preparation and the characterization (also by means of electrochemical techniques) of silica and titania films with tailored porosity and surface properties are presented. Eventually, Part III (Chapters 12–13) reports the study of active materials for heterogeneous catalysis and photo-electrocatalysis in the framework of the research of new energy sources and novel materials with energy conversion applications.

More in detail, Part I of this Thesis (Chapters 1–7) was devoted to the study of TiO_2-based photocatalysts for application in the field of pollutants degradation (both in the gas and the liquid phase) and to the effort to overcome the typical issues of photocatalysis by adopting different approaches (*e.g.* doping, co-doping, coupling with smaller band gap semiconductors, development of floating device). Moreover, photocatalysis was also exploited for surface modification / lithographic purposes and for photoelectrochemical applications, which will be described in Chapters 11 and 13, respectively.

Firstly, the characterization and the photocatalytic activity tests of differently prepared TiO_2 nanostructured samples were performed. By varying the calcination temperature (from 300 to 600 °C) different phase composition and morphologies were obtained and the efficiency towards

tetracycline degradation was thus optimized for the laboratory synthesized TiO_2 samples. Tetracycline is an antibiotic compound of recent interest as a micropollutant of wastewaters and surface waters, due to its wide use for both human and animal treatments. In Chapter 1, the development of two different low-cost TiO_2 immobilized systems is also reported: alumina macroscopic supports were adopted together with a prepared titania sol and an easy deposition technique, revealing good activity, as well as resistance, towards tetracycline degradation. In order to develop accessible active devices through the photocatalyst immobilization on a support, titanium meshes were also employed (Chapter 2). However, differently from the work reported in Chapter 1, in Chapter 2, the focus of the work was addressed to the study of the photocatalytic environment, in terms of water medium composition. The photocatalytic degradation of four different organic compounds (tetracycline, paracetamol, caffeine and atenolol) belonging to the class of pharmaceutics and personal care products (PPCPs) and classified as emerging contaminants was tested both for the single pollutants and for their mixture. The role of the solution composition and especially the role of electrolytes, were also studied by performing photocatalytic tests in commercial and simulated drinking waters. This work falls within the framework of the necessity to comprehend the potential of photocatalysis even in the case of water effluent constituted by complex matrix in terms of solvent composition and presence of many different pollutants at low concentration ranges. In fact, the presence of several organic compounds to be degraded, as well as the electrolytes present in the water matrix and its composition and physicochemical properties can deeply affect the efficiency of the photocatalytic process, the adsorption and the degradation mechanisms.

Then, in the following three Chapters (3–5), the effects of doping and co-doping of titanium dioxide with metal and non-metal species, mainly in order to promote the activity of TiO_2 under visible light, but also to enhance its efficiency were explored. In-depth characterizations were performed on N,Ta/Nb titania samples from the structural, morphological, spectroscopic and electronic point of view (by XRPD, surface area and porosity, XPS, EPR and DRS analyses) to comprehend the modifications provided by the guest species on the photocatalysts and how this could reflect on the photocatalytic performance. Moreover, a combined experimental /

theoretical approach was followed for a better comprehension, by means of DFT simulations. The samples were finally tested towards the photocatalytic degradation of ethanol in the gas phase. The sole Ta doping on differently synthesized TiO_2 samples and for paracetamol degradation was also studied, with particular emphasis on the photocatalyst surface acidity (performing titrations of the photocatalyst acid sites by phenylethylamine adsorption in liquid-solid phase), its stability in suspension and the recognition of degradation intermediates (by gas chromatography – mass spectroscopy analyses) possibly responsible for the photocatalytic performance among the different samples. This permitted to evaluate parameters which are often disregarded but become pivotal when photocatalytic degradations in the aqueous phase are considered. Sn and Zn were also investigated as elements able to strongly modify the structural characteristics of TiO_2 samples, mainly in terms of phase composition and surface defectivity (recognized by HR-TEM, XPS and electrophoretic analyses). The adopted amount of metal modifiers during synthesis also allowed the possible formation of composite oxidic materials to be observed and its effects to be studied. Moreover, the concomitant use of N as a guest species able to promote the visible light absorption, allowed superior effects in the visible light harvesting to be recognized and enhanced activity under visible irradiation to be proved. The effect of the guest species on the reaction mechanism was also investigated by mass spectroscopy analyses, proving significant variations in the case of Zn promoted samples, with respect to pristine, N- and Sn-modified photocatalysts.

This work paved the way for the last two Chapters of Part I of the Thesis, regarding composite photocatalytic materials, both in the case of oxidic composites (Chapter 6) and inorganic-organic ones (Chapter 7). In the former case, WO_3 was selected as a minority photocatalyst together with TiO_2 in order to comprehend the effects provided by a sort of co-photocatalyst in the degradation of tetracycline (in the liquid phase) and ethanol (in the gas phase). Also in this case, the differences pertaining the degradation mechanisms reported for both reactions were reconnected to the specific modifications of the bulk and the surface properties of TiO_2 by WO_3 species. In the latter case, instead, a novel methyl methacrylate-based ter-polymer, with specific dual wetting properties (thanks to the use of a

fluorinated co-monomer) when reduced in foils, was adopted to assemble a floating, transparent and photocatalytically active device. For this purpose, the physicochemical characteristics of the ter-polymer were finely tailored and, successively, SiO_2 (with adhesion and protection tasks) and TiO_2 (photoactive) layers were deposited from home-made colloidal solutions by spray-coating technique. The photocatalytic activity of this organic-inorganic multilayer device was successfully tested towards the degradation of both atmosphere and water contaminants, in the context of its possible use for remediation from organic substances and their vapours from polluted large water basins. In these cases, in fact, the use of nanostructured powders, even as immobilized systems, should be avoided for issues related to photocatalyst removal, while the floatability promotes light harvesting.

Throughout Part II of the Thesis, instead, the wide range of applicability of oxide nanomaterials obtained as films is reported. In fact, oxidic compounds such as SiO_2 and TiO_2 can be easily obtained as nanometric or micrometric films deposited on supports (*e.g.* glass slide, silicon wafer, conductive glass) from colloidal solutions or powder suspensions.

In this regard, in this Thesis, SiO_2 films were exploited for understanding the effects provided by surface or morphology modifications from a fundamental point of view. For this purpose, an intense use of electrochemical characterization techniques (cyclic voltammetry and electrochemical impedance spectroscopy) and surface wettability analyses by contact angle measurements was done.

In Chapter 8 the effects provided by the deposition of an insulating layers of SiO_2 onto a conductive glass were studied in terms of mass transport and charge transfer phenomena. By varying the thickness of these devices, which actually can be described as modified electrodes, different behaviours in the voltammetric signal were recorded, despite their strong insulating character. The voltammogram shape variations were interpreted in the light of previous theoretical studies reporting simulations of cyclic voltammetry analyses for electrodes modified by deposition of electroinactive layers. For the first time, the outcomes only reported on the basis of theoretical simulations were experimentally observed.

The work presented in the Chapter 8 can be also seen as introductory to the following one. In fact, on the basis of the results obtained by electroinactive layers modified electrodes, especially regarding the variation of the diffusion and transport phenomena to the electroactive surface, porous SiO_2-based electrodes with peculiar properties were developed. These electrodes, characterized by controlled mesoporosity due to the preparation involving nanometric polystyrene latex beads as solid templating agents, were deeply characterized under the physicochemical point of view (by SEM, FE-SEM, AFM, UV-vis spectroscopy, water contact angle measurements) and exploited for sensing applications. In particular, thanks to its morphological, surface charge and wetting properties, the modified electrode proved effective in the selective detection of dopamine in the presence of mucin as interfering agent. Dopamine is a neurotransmitter whose quantification in biofluids is pivotal for the diagnosis of the Parkinson's disease, while mucin is a large dimension protein which can interfere in dopamine detection, as actually proved in the case of a bare electrode. The development of these tailored morphologies is to be seen in the context of the research devoted to the preparation of high selective and antifouling sensors. High selectivity and antifouling (*i.e.* reliable quantifications together with long electrode durability) are considered major issues nowadays in the field of electroanalysis.

In the following two Chapters, instead, the behaviour of organic-inorganic hybrids is reported. In Chapter 10, SiO_2 substrates were adopted for surface modification by alkylsilanes, molecules easily reacting with oxidic surfaces thus modifying their wettability, even for obtaining superhydrophobic surfaces. A vast number of characterizations (solid state NMR, surface free energy analyses, FTIR, electrochemical techniques) allowed the behaviour from a molecular point of view of alkylsilanes chemisorbed on a silica surface to be understood. In Chapter 11, in the framework of a hands-on activity for students and with both research and didactic purposes, the wetting modifications of TiO_2 films from suprhydrophilicity to superhydrophobicity were investigated by means of functionalization by alkylsilanes as well as of photocatalysis. In this case, the formation of organic-inorganic hybrids as films was exploited not only to obtain superhydrophobic surfaces but also for patterning applications

thanks to photocatalysis. In fact, by irradiating such a modified TiO_2 surface by UV light, the photocatalytic process can be activated for selectively degrade the functionalizing molecule and create patterned surfaces characterized by wetting contrasts. This approach is generally called photocatalytic lithography and falls in the framework of surface wettability modifications by functionalizing oxidic compounds with organic amphiphilic molecules. In the last decades, these approaches have been receiving great interest for their everyday-life impacting aspects: self-cleaning, anti-stain and anti-corrosion surfaces are just few examples of the applicability of these complex materials which can be used for new technologies such as smart glasses, pollution remediating buildings, long-lasting ship hulls.

Eventually, in the last part of the Thesis, studies regarding the preparation on composite materials for energy-related applications are presented. In Chapter 12, SiO_2/Al_2O_3 powders with different relative composition were adopted as catalytic supports for the hydrodeoxygenation reaction of guaiacol. Ni was selected as active catalyst the effects of its concentration onto the support were explored. The guaiacol hydrodeoxygenation reaction is often taken into account as a model reaction for studying the upgrading of bio-oils. Bio-oils are the product of the conversion of lignocellulosic biomass, a renewable source of energy which received great attention in the last few years, in the context of the progressive depletion of fossil fuels and the incumbent need to find new and renewable energy sources. In the last Chapter, instead, colloidal synthesis approaches were adopted to obtain oxidic heterojunctions for photoelectrochemical applications. The two components of these heterojunctions were WO_3 and copper vanadate ($Cu_2V_2O_7$), in different ratios. $Cu_2V_2O_7$ is a small band gap semiconductor which enables the heterojunction to be active under visible light and to promote charge transfer phenomena, favourable for enhancing the photocatalytic efficiency with respect to bare WO_3. A vast characterization was performed adopting HR-TEM, in-situ XRD, photoluminescence and nanosecond transient absorption spectroscopies, in order to understand the physicochemical phenomena occurring at the interface between the two oxides and to optimize the heterojunction composition for the final application.

Oxides: leading actors of nowadays challenges

Worldwide, a large number of researchers in universities, research centres and companies dedicate themselves to studies related to materials science and nanotechnology, mainly with the aim of solving problems connected to everyday life. The multidisciplinary aspects of these topics mean that not only chemists, but also physicists, engineers, physicians, material scientists, biologists and biotechnologists are involved in developing new strategies for the manifold challenges of the new century.

For the more chemistry-related aspects, physical chemists are often involved not only in developing new engineered materials and devices, increasing processes efficiency or searching innovative technologies, but also understanding the fundamental physicochemical aspects which govern the behaviour of the chemical compounds and their performance for the final application.

In this sense, one of the classes of materials standing out for their versatility and wide range of applicability is that of metal oxides. Typically, metal oxides are characterized by abundancy, low-cost, chemical and mechanical stability and non-toxicity, properties which favour their use and application, even at industrial scale. Moreover, the physical and chemical properties, such as the possibility to act as semiconductors, insulators or electronic conductors, the high reactivity of their surface and the biocompatibility act as peculiar characteristics exploitable for the development of novel devices in the fields of *e.g.* heterogeneous catalysis, solar cells, batteries, (bio)sensors, smart surfaces, nanoelectronics, drug-delivery[1–10]. Further, for all the materials, and especially in the case of oxides, the nano size is usually sought, as promoting all physicochemical properties, with respect to micro and macro sizes. The ease to modulate shape, size, texture and to obtain composites and hybrids amplify the range of application of oxidic materials.

Some of the main issues of our century are **environmental remediation**, the need of **smart surfaces development** and the **search for new energy sources**. In all these fields, in the last decades, metal oxides have received great attention for developing and implementing new techniques, procedures and devices for enhancing efficiencies, testing new strategies and/or solving analytical issues. Moreover, also fundamental researches and theoretical studies aimed at understanding the basics physicochemical phenomena occurring on the metal oxides surface and in the bulk, have been receiving particular attention[11–15].

These three main topics will be approached in this Thesis with reference to nanosized oxide systems.

Part I

Titanium dioxide-based photocatalysts for environmental remediation application

Part I – Introduction

Environmental remediation of water and of air is one of the most felt issues of our century, not only regarding the volatile organic compounds (VOCs) which pollute the atmosphere of our cities, but also, especially in the last few years, the so-called *emerging pollutants*.

Emerging pollutants are harmful organic molecules recently detected in low amounts (traces concentration) in water effluents and basins and whose dispersion in the environment is mainly due to human activities[16,17]. These compounds often represent a serious threat for human health and ecosystems, since they were found not only in wastewaters, but also in surface and groundwaters. Emerging pollutants can be divided between new chemicals recently brought to the fore by novel synthetic strategies and new technological needs and compounds whose detection have recently become possible thanks to the development of new technologies, able to detect and quantify them even when present at very low concentrations (from μg L^{-1} to ng L^{-1}). In this case, the definition of *contaminants of recent concern* has been proposed and is maybe to be preferred[18]. In this regard, traditional remediation techniques very often fail to completely remove the polluting agents from its matrix. In fact, sometimes organic molecules are recalcitrant to degradation, cannot be degraded by biological treatment plants or just give rise to even more toxic by-products. Recently, the researchers involved in studies about wastewater treatment intensively dedicate to specific classes of emerging pollutants (perfluoroalkyl compounds, dioxins, pharmaceutics and their metabolites, herbicides, pesticides, industrial additives)[19,20]. For example, among the class of *pharmaceutics and personal care products* (PPCPs), probably the most studied class of emerging contaminants in recent years[20], antibiotics can be cited as very problematic molecules for their wide use and dispersion in the environment, but most of all for their critical removal from water effluent. In fact, in the case of antibiotics, biological treatment

plants, based on the degradative action of bacteria towards organic molecules cannot be adopted[21]. In other cases, PPCPs stand out as typical recalcitrant molecules unlikely to be degraded by traditional techniques. Further, traditional techniques are often not able to mineralize organic pollutants, *i.e.* completely oxidize them to harmless compounds. In other cases, for example by means of *phase-changing technologies*, such as adsorption techniques, the polluting molecule is just removed from the water effluent but not the degraded, thus not solving completely the underlying problem[22].

For these reasons, *advanced oxidation processes* (AOPs) have attracted great attention in the last decades for wastewater and air treatments with respect to conventional techniques, since they are often able to completely degrade pollutants to harmless compounds (water, CO_2, inorganic salts)[22,23]. Among this class of new technologies for environmental remediation applications, ozonation, electrochemical, Fenton and UV/H_2O_2 processes can be cited[24], as well as combined treatments[25]. Basically, AOPs exploit the generation of radical species (especially $^{\bullet}OH$ radicals) for oxidatively destroy the organic pollutants present in water streams or in the atmosphere[26].

However, the most diffuse technique among AOPs is for sure heterogeneous photocatalysis, often proving its superior efficacy with respect to the other innovative techniques[27]. Moreover, in this specific field, titanium dioxide (TiO_2) is by the most used semiconductor adopted as a photocatalyst for its characteristics of high abundance, low-cost, non-toxicity, high efficiency and above all for its high oxidative but also good reductive potential with respect to other photocatalytic materials. In this sense, in fact, TiO_2 is exploited for many different photocatalytic purposes, not only for oxidative degradations of organic pollutants, but also for fuels production, water splitting, CO_2 reduction, bacteria inactivation (sterilization), development of antifogging surface and fabrication of patterned surfaces and devices by photocatalytic lithography.

TiO_2 and water/air pollutants are certainly the leading actors in the first part of this Thesis. In fact, I devoted much of my PhD to the synthesis, the physicochemical characterization and the activity tests of TiO_2-based nanomaterials for photocatalytic applications in the field of air and water remediation, especially regarding emerging pollutants and VOCs. The

focus was always on the development of efficient photocatalysts able to overcome the intrinsic problematics of the use of photocatalysis by TiO_2, *e.g.* promoting the visible light absorption, constructing semiconductor heterostructures for enhancing the efficiency of TiO_2, preparing immobilized photocatalytic systems for an easier removal after the water treatment. Further, I focused on the understanding of how the structural, morphological, optical and spectroscopic features of the prepared photocatalysts influence the overall photocatalytic performance, also in terms of degradation mechanisms. In this regard, I also dedicated to the study of some parameters often disregarded but certainly playing a remarkable role on the photocatalytic activity, especially in the case of water treatment, such as photocatalyst surface acidity, suspension stability and matrix composition.

I.1 Basic principles of photocatalysis

Photocatalysis is a physicochemical process which exploits a semiconductor material, the *photocatalyst* and light of suitable energy to promote oxidation and/or reduction chemical reactions.

More in detail, a semiconductor is a solid material characterized, from the electronic point of view, by the presence of a low energy band, the *valence band*, in which the large majority of the electrons stays without any particular stimulus, and a more energetic band, the *conduction band*, is which the electron can be promoted upon light absorption. These two electronic bands are separated by a gap, called *band gap*, constituted by forbidden energy levels.

Conventionally, on the grounds of the position of the energy levels, materials are divided among conductors, semiconductors and insulators. Conductors are characterized by continuity of permitted energy levels, *i.e.* superposition of the valence and the conduction bands, while the division between semiconductors and insulators is more arbitrary. In fact, it can be stated that the band gap of semiconductors is not so wide to render the promotion of electrons from the valence to the conduction band impossible with standard techniques. A band gap width of 3.5 eV can be assumed to discriminate between semiconductors and insulators.

Semiconductors have a wide range of applications and one of these is for sure photocatalysis. In this field, for semiconductor activation, light with energy equal or greater than the band gap is needed. When the semiconductor is irradiated by photons of adequate wavelength, they cause electrons promotion into the conduction band, thus leaving an *electron hole*, h^+, assumable as a positively charged carrier, in the valence band. In this way, two different charge carriers with opposite charge, generally referred as *electron-hole couple*, e^-/h^+, are formed. Both charge carriers can migrate onto the surface of the photocatalyst to promote a large number of reactions, for reducing or oxidizing molecules (*electron acceptors* and *electron donors*, respectively) adsorbed onto the photocatalyst surface either directly or by means of highly reactive (usually radical) species. In a typical photocatalytic process, hydroxyl radicals, $^{\bullet}OH$, and superoxide radical anions, $O_2^{-\bullet}$, are usually the main actors of oxidation reactions, together with h^+. However, several other oxidative species can be formed, depending on the adopted photocatalyst, by the direct action of electrons and holes on H_2O and/or O_2 molecules, which are typically the two sources of oxidizing and radical species, which finally attack the target molecule(s) (Fig. I.1).

Unfortunately, photocatalysis suffers from low quantum yield (intended as number of irradiating photons with respect to electron transfer phenomena) due to the high probability of e^-/h^+ recombination phenomena, either occurring at the semiconductor surface after migration or at bulk sites.

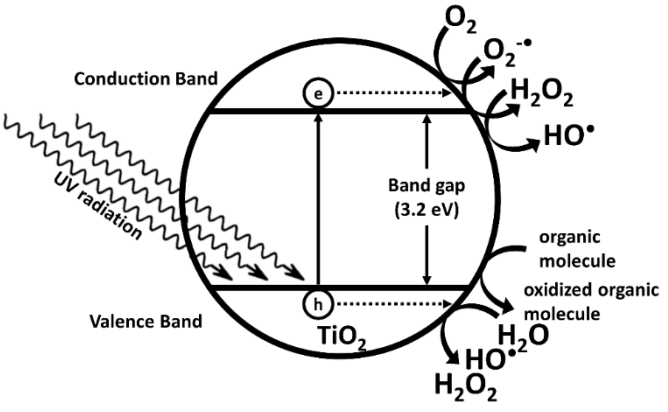

Figure I.1 – Schematics of the photocatalytic process, in the case of the most adopted photocatalyst, TiO_2.

Further, a very important parameter for the selection of an adequate semiconductor for photocatalysis in dependence of the reaction which has to be carried out is the bands energy position. In this sense, the higher is the energy level of the conduction band minimum (*i.e.* more negative potential with respect to that of water reduction, H_2/H_2O redox couple), the stronger is the reductive potential of the electrons photopromoted into the valence band. Conversely, the lower is the energy level of the valence band maximum (*i.e.* more positive potential with respect to that of water oxidation, O_2/H_2O or even $^{\bullet}OH/H_2O$ redox couples), the stronger is the oxidative potential of the electron holes located into the valence band. Thus, depending on the valence and conduction band energy levels, semiconductors can promote only reduction, only oxidation or both classes of chemical reactions, as well as the formation of different radical species. Also on the grounds of these properties, different semiconductors are more or less suitable for the different photocatalytically promoted reaction, *e.g.* water splitting, oxidation of organics, methane steam reforming. Moreover, the energy position of the bands should also go hand in hand with the possibility to activate the semiconductor by irradiation with light of suitable wavelength.

For all these reasons, since photocatalysis stands as a new innovative and green technology for environmental remediation and other applications, great efforts have been devoted by the scientific community to enhance the process efficiencies, by applying different strategies and investigating several different semiconductors. For sure, above all for water/air treatment applications, photocatalysts firstly need chemical, photochemical and thermal stability. Moreover, non-toxicity and synthetic easiness are pivotal aspects. Other aspects still deserving further attention and investigations are photocatalysts selectivity, visible light response, photocatalysts immobilization, long reusability and proper band structures[28]. For enhancing the performances, the design of engineered composite photocatalysts and devices with specific morphologies and nanoarchitectures are future prospect of principal interest[29,30].

Intense activity and novel strategies for the development of efficient photocatalytic processes may overcome the critical issues which up to now, despite the great efforts profuse in the last decades and testified by the large

number of publications on photocatalysis, still prevent the extensive use of this technique on a commercial/industrial scale[31].

I.2 Titanium dioxide (TiO_2) photocatalysis

Titanium dioxide is a metal oxide which has been widely adopted as a pigment in paints, personal care products, plastics, papers and foods, since its commercialization at the beginning of the twentieth century.

Then, in 1972, Fujishima and Honda for the first time described the capability of TiO_2 to split water into oxygen and hydrogen molecules upon UV light irradiation[32], paving the way to the tremendous research in TiO_2 photocatalysis for a wide number of reactions up to now.

Since the publication of this pioneering work, among all the available photocatalysts, TiO_2 has been the most adopted one, thanks to its abundance, stability, non-toxicity, low-cost, high activity and bands positioning[33,34]. At least from a thermodynamic point of view, TiO_2 conduction band minimum, situated above the potential of the H_2/H_2O redox couple (*ca.* –0.3 V *vs.* NHE) is suitable for promoting water reduction (although the overpotentials extent which decreases this capability should always be considered), while its valence band minimum, situated below the potential of the O_2/H_2O, but also of the $^{\bullet}OH/H_2O$ redox couples (*ca.* +2.9 V *vs.* NHE), allows oxidation reactions, such as oxidative degradation of organics, to be performed.

Moreover, it can be easily synthesized on a lab scale, by different and versatile routes (*e.g.* sol-gel, hydrothermal, solvothermal and pyrolysis procedures), with the possibility of obtaining both nano or nanostructured and micro powders, even in many different and even unusual morphologies, principally developed in the last decades[35–41].

However, beside the aspects responsible for its wide use in photocatalysis, TiO_2 has also some important drawbacks which limit its use on a commercial and industrial scale. The most negative aspects of TiO_2 are the following:

1. the possibility to promote photoexcitation just under UV light;
2. the high electron/hole recombination rate;

3. the high cost of post treatment processes for the removal of the powder photocatalyst in the case of water effluent treatments.

For these reasons, especially in the last decades, new complex TiO_2-based photocatalytic materials with tailored properties were explored. Different strategies were proposed and adopted to overcome these drawbacks.

For the first one, since the solar emission spectrum extends just for the 5% in the UV region, many efforts for promoting the light absorption to the visible range with the aim of better exploiting solar light were done. In this regard, doping with non-metal elements, metal nanoparticles surface deposition and coupling with small band-gap semiconductors proved to be efficient strategies. Non-metal doping, *i.e.* insertion of non-metal guest elements in interstitial or substitutional to oxygen positions in the crystalline cell of TiO_2, usually promotes the formation of *intra-gap* states (Fig. I.2)[42–45]. These are permitted energy levels between the valence and the conduction bands, which make the absorption of light with energy lower with respect to that of the band gap possible. In fact, in these cases, regardless of the position of the intra-gap states, the electrons can be promoted in the conduction band in a "multistep path", *i.e.* from the valence band to the intra-gap level(s) and from there to the conduction band, which can be completed with lower energetic irradiation[42,43,46]. For these reasons, the effects of non-metal doping are often referred, sometimes misleadingly, as *band gap narrowing*[47]. This is true, instead, when conduction band minimum or valence band maximum shifts occur (Fig. I.2). However, non-metal doping has a main drawback, which is the possibility, still depending on the position of the intra-gap level, to accelerate the charge carriers recombination phenomena. In order to address this issue, in the last few years codoping with a metal and a non-metal guests was investigated as a strategy able to reduce the negative bulk defectivity introduced by the sole non-metal doping and responsible for the higher recombination rates[48–50]. These effects are usually traced back to charge compensation phenomena, which support the use of pentavalent cations with higher valence with respect to Ti when N is used as non-metal guest[51–53].

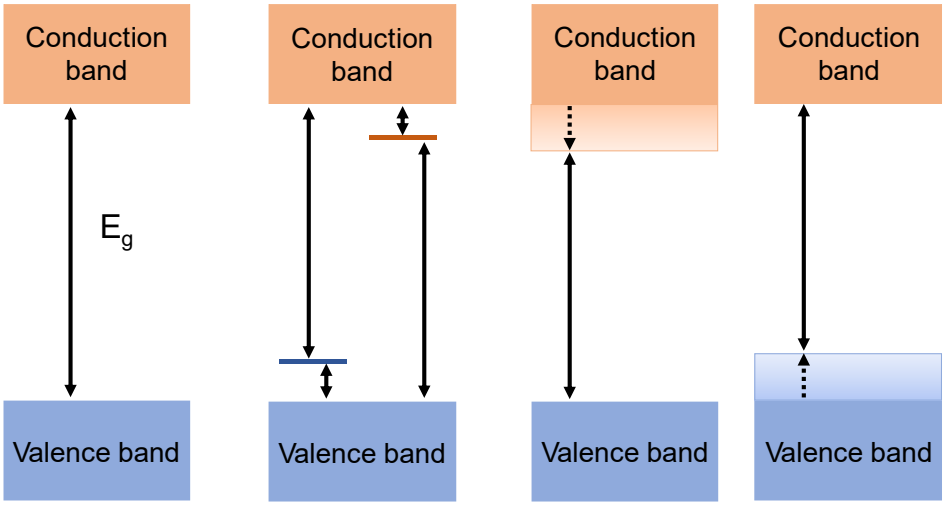

Figure I.2 – Different electronic modifications usually provided by non-metal doping (generation of intragap levels above the valence band maximum or below the conduction band minimum, conduction band minimum downshift and valence band maximum upshift), with respect to the electronic structure of pristine TiO_2.

The use of metal nanoparticles, usually Ag, Pt or Au, for TiO_2 surface decoration, is adopted for reasons related to the plasmonic absorbance of this metals in the visible region. Further, reduced metal nanoparticles act as traps for the photopromoted electrons, thus decreasing the recombination rate. The activation of the small band gap semiconductors achievable by visible light, together with occurring charge transfer phenomena are usually at the basis of small band gap – large band gap semiconductor junctions.

In fact, the high recombination rate has to be slowed down if the photocatalytic efficiency of TiO_2 has to be increased. For this purpose, semiconductor coupling aimed at creating heterojunctions is often adopted. In these binary (or even ternary) systems, in fact, the photopromoted electron and/or the electron hole can move from the first to the second semiconductor conduction or valence bands, thus possibly disfavouring recombination. Another very common strategy is metal doping, even if with alternative results on the photocatalytic performance due to the possibility to promote instead of to decrease the charge carriers recombination.

Regarding the use of expensive post treatments for photocatalyst removal after water treatments, as well as the adventitious dispersion of the photocatalyst in the environment, especially in the case of nanopowders,

the immobilization of the photocatalyst on a at least micrometric or, better, macroscopic support is a viable approach[54–56]. In more recent years, the researchers have also devoted their efforts to the preparation of magnetic or buoyant photocatalyst which allow an easier removal to be performed. The two principal positive aspects of floating photocatalysts are easiness of separation and the high light harvesting. Apart from self-floating photocatalysts, many different substrates were adopted for this purpose: perlite, polymers, cork, glass microbeads, expanded graphite[57–60]. Very recently, Xing *et al.* revised ultimate trends and development on floating photocatalyst individuating the development of new support, the catalyst adhesion on the support, visible light activity, other semiconductors with respect to TiO_2, the understanding and development of new structures, production methods and reaction mechanisms as the most important points for future advances in this field[58].

I.2.1 Structure and properties

Titanium dioxide mainly occurs in nature in three different polymorphic structures: anatase, rutile and brookite. These polymorphs differ not only from the crystallographic habit point of view, but also for other physicochemical properties (*e.g.* band-gap width, surface structure, density, refractive index), obtainability on a lab-scale and photocatalytic activity. Other crystallographic structures are obtained only *via* specific synthetic procedures and at high pressure and temperature conditions.

Anatase, from the Greek word *anatasis*, meaning "extension", due to its pyramidal crystal structure has a tetragonal crystalline habit (space group: $I4_1/amd$), a band-gap of 3.2 eV, and is easy to produce, especially by sol-gel synthetic routes. It is thermodynamically metastable stable but highly kinetically favoured at low pressures and temperatures (< 500°C). Further, it is reported as its most photocatalytically active polymorph[33].

Rutile, from the Latin word *rutilus*, meaning "red", due to its red colour appearance in some mineral specimens, is the most diffuse polymorph of TiO_2 and is usually the adopted form for its industrial applications. It has a tetragonal structure (space group: $P4_2/mnm$) and a band gap of 3.0 eV. It is the thermodynamically stable polymorph of TiO_2 and is also kinetically favoured at high temperature conditions (> 500°C).

Brookite, named in honour of the English mineralogist Henry James Brooke, is the least studied among the three natural structures of TiO_2. It is a metastable polymorph, with an orthorhombic crystallographic structure (space group: *Pbca*) and a band gap usually reported as slightly larger than that of anatase (*ca.* 3.3 eV)[61].

Very often, TiO_2 samples are obtained as a mixture of these three polymorphs, both in the case of laboratory-made samples and commercial products. The role of structural composition (*e.g.* pure anatase *vs.* biphasic samples) on the photocatalytic performance is still intensively debated in the literature. In fact, given anatase is the most active TiO_2 polymorph, multiphasic titania can benefit from the effect provided by semiconductor coupling[62,63], as discussed above. For example, the high photocatalytic activity of Evonik P25®, *i.e.* the most used commercial titanium dioxide usually adopted as reference for photocatalytic studies and composed of a mixture of anatase and rutile (*ca.* 80:20), is generally traced back to its biphasic composition[62].

Different sol-gel synthetic approaches were adopted in this Thesis obtaining nanostructured titania samples with tailored polymorphic composition. In fact, the photocatalytic performance varies depending on the different polymorphs, their physicochemical properties and their relative ratios for multiphasic samples. In the studies presented in this Thesis, the structural composition and other physicochemical features were varied and studied in order to comprehend the origin of the overall photocatalytic performance.

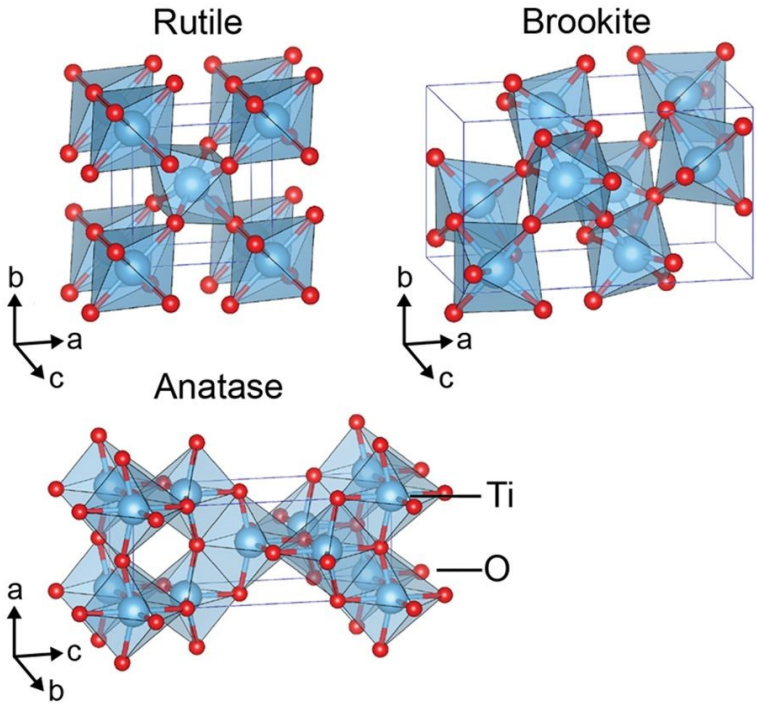

Figure I.4 – Crystalline structures of the three natural polymorphs of TiO_2. Reprinted from Sci. Rep., 7, 2017, 15232, J.E.S. Huggerty, L.T. Schelhas, D.A. Kitchaev, J.S. Mangum, L.M. Garten, W. Sun, K.H. Stone, J.D. Perkins, M.F. Toney, G. Ceder, D.S. Ginley, B.P. Gorman, J. Tate, DOI: 10.1038/s41598-017-15364-y, http://creativecommons.org/licenses/by/4.0/.

Moreover, many other physicochemical properties, mainly pertaining the morphological and the surface-related aspects, may be dependent from the structural composition and the adopted synthetic route, finally influencing the photocatalytic activity[33,64]. In this Thesis, the morphological, spectroscopic and surface aspects dependent on the preparation procedure and the structural composition of the samples were investigated.

References

1 Y. Zhang, Z. Zhang, W. Yan, B. Zhang, Y. Feng, A. M. Asiri, M. K. Nazeeruddin and P. Gao, *J. Mater. Chem. A*, 2017, **5**, 1415–1420.

2 K. Sivula, F. Le Formal and M. Grätzel, *ChemSusChem*, 2011, **4**, 432–449.

3 W. O. Yah, A. Takahara and Y. M. Lvov, *J. Am. Chem. Soc.*, 2012, **134**, 1853–1859.

4 A. Labidi, C. Lambert-Mauriat, C. Jacolin, M. Bendahan, M. Maaref and K. Aguir, *Sensors Actuators B Chem.*, 2006, **119**, 374–379.

5 A. Loiudice, J. K. Cooper, L. H. Hess, T. M. Mattox, I. D. Sharp and R. Buonsanti, *Nano Lett.*, 2015, **15**, 7347–7354.

6 C. Gadiyar, M. Strach, P. Schouwink, A. Loiudice and R. Buonsanti, *Chem. Sci.*, 2018.

7 D. Meroni, S. Ardizzone, U. S. Schubert and S. Hoeppener, *Adv. Funct. Mater.*, 2012, **22**, 4376–4382.

8 M. Grilc, G. Veryasov, B. Likozar, A. Jesih and J. Levec, *Appl. Catal. B Environ.*, 2015, **163**, 467–477.

9 C. Larabi, A. Garron, P. Rouge, K. C. Szeto, S. Norsic, A. De Mallmann, N. Merle and M. Taoufik, *ChemCatChem*, 2017, **9**, 2160–2166.

10 E. Pargoletti, G. Cappelletti, A. Minguzzi, S. Rondinini, M. Leoni, M. Marelli and A. Vertova, *J. Power Sources*, 2016, **325**, 116–128.

11 F. De Angelis, C. Di Valentin, S. Fantacci, A. Vittadini and A. Selloni, *Chem. Rev.*, 2014, **114**, 9708–9753.

12 S. Livraghi, M. C. Paganini, E. Giamello, A. Selloni, C. Di Valentin and G. Pacchioni, *J. Am. Chem. Soc.*, 2006, **128**, 15666–15671.

13 D. Menshykau and R. G. Compton, *Langmuir*, 2009, **25**, 2519–2529.

14 D. O. Scanlon, C. W. Dunnill, J. Buckeridge, S. A. Shevlin, A. J. Logsdail, S. M. Woodley, C. R. A. Catlow, M. J. Powell, R. G. Palgrave, I. P. Parkin, G. W. Watson, T. W. Keal, P. Sherwood, A. Walsh and A. A. Sokol, *Nat. Mater.*, 2013, **12**, 798–801.

15 T. J. Davies, R. R. Moore, C. E. Banks and R. G. Compton, *J. Electroanal. Chem.*, 2004, **574**, 123–152.

16 United Nations, *Transforming our world: the 2030 agenda for sustainable development A/RES/70/1*, 2015.

17 *Directive 2013/39/EU of the European Parliament and the Council*, 2013.
18 S. Sauvé and M. Desrosiers, *Chem. Cent. J.*, 2014, **8**, 15.
19 F. G. Calvo-Flores, J. Isac-Garcia and J. A. Dobado Jiménez, *Emerging Pollutants: Origin, Structure, and Properties*, WILEY-VCH Verlag, Weinheim, Germany, 2018.
20 T. Deblonde, C. Cossu-Leguille and P. Hartemann, *Int. J. Hyg. Environ. Health*, 2011, **214**, 442–448.
21 R. Daghrir and P. Drogui, *Environ. Chem. Lett.*, 2013, **11**, 209–227.
22 O. M. Rodriguez-Narvaez, J. M. Peralta-Hernandez, A. Goonetilleke and E. R. Bandala, *Chem. Eng. J.*, 2017, **323**, 361–380.
23 V. Homem and L. Santos, *J. Environ. Manage.*, 2011, **92**, 2304–2347.
24 A. R. Ribeiro, O. C. Nunes, M. F. R. Pereira and A. M. T. Silva, *Environ. Int.*, 2015, **75**, 33–51.
25 I. Oller, S. Malato and J. A. Sánchez-Pérez, *Sci. Total Environ.*, 2011, **409**, 4141–4166.
26 J. L. Wang and L. J. Xu, *Crit. Rev. Environ. Sci. Technol.*, 2012, **42**, 251–325.
27 M. R. D. Khaki, M. S. Shafeeyan, A. A. A. Raman and W. M. A. W. Daud, *J. Environ. Manage.*, 2017, **198**, 78–94.
28 Y. Boyjoo, H. Sun, J. Liu, V. K. Pareek and S. Wang, *Chem. Eng. J.*, 2017, **310**, 537–559.
29 N. Serpone and A. V. Emeline, *J. Phys. Chem. Lett.*, 2012, **3**, 673–677.
30 L. Zhong and F. Haghighat, *Build. Environ.*, 2015, **91**, 191–203.
31 Y. Paz, *Appl. Catal. B Environ.*, 2010, **99**, 448–460.
32 A. Fujishima and K. Honda, *Nature*, 1972, **238**, 37–38.
33 A. Fujishima, X. Zhang and D. Tryk, *Surf. Sci. Rep.*, 2008, **63**, 515–582.
34 K. Liu, M. Cao, A. Fujishima and L. Jiang, *Chem. Rev.*, 2014, **114**, 10044–10094.
35 T. Kasuga, M. Hiramatsu, A. Hoson, T. Sekino and K. Niihara, *Langmuir*, 1998, **14**, 3160–3163.
36 T. Kasuga, M. Hiramatsu, A. Hoson, T. Sekino and K. Niihara, *Adv. Mater.*, 1999, **11**, 1307–1311.

37 P. D. Cozzoli, A. Kornowski and H. Weller, *J. Am. Chem. Soc.*, 2003, **125**, 14539–14548.
38 Y. Liu, L. Chen, J. Hu, J. Li and R. Richards, *J. Phys. Chem. C*, 2010, **114**, 1641–1645.
39 S. Liu, J. Yu and M. Jaroniec, *J. Am. Chem. Soc.*, 2010, **132**, 11914–11916.
40 D. Li and Y. Xia, *Nano Lett.*, 2003, **3**, 555–560.
41 H. G. Yang, C. H. Sun, S. Z. Qiao, J. Zou, G. Liu, S. C. Smith, H. M. Cheng and G. Q. Lu, *Nature*, 2008, **453**, 638–641.
42 R. Asahi, T. Morikawa, H. Irie and T. Ohwaki, *Chem. Rev.*, 2014, **114**, 9824–9852.
43 L. G. Devi and R. Kavitha, *Appl. Catal. B Environ.*, 2013, **140**–**141**, 559–587.
44 M. Ceotto, L. Lo Presti, G. Cappelletti, D. Meroni, F. Spadavecchia, R. Zecca, M. Leoni, P. Scardi, C. L. Bianchi and S. Ardizzone, *J. Phys. Chem. C*, 2012, **116**, 1764–1771.
45 V. N. Kuznetsov and N. Serpone, *J. Phys. Chem. C*, 2009, **113**, 15110–15123.
46 M. Pelaez, N. T. Nolan, S. C. Pillai, M. K. Seery, P. Falaras, A. G. Kontos, P. S. M. Dunlop, J. W. J. Hamilton, J. A. Byrne, K. O'Shea, M. H. Entezari and D. D. Dionysiou, *Appl. Catal. B Environ.*, 2012, **125**, 331–349.
47 N. Serpone, *J. Phys. Chem. B*, 2006, **110**, 24287–24293.
48 J. Lim, P. Murugan, N. Lakshminarasimhan, J. Y. Kim, J. S. Lee, S. H. Lee and W. Choi, *J. Catal.*, 2014, **310**, 91–99.
49 X. Ma, Y. Wu, Y. Lu, J. Xu, Y. Wang and Y. Zhu, *J. Phys. Chem. C*, 2011, **115**, 16963–16969.
50 R. Long and N. J. English, *Chem. Phys. Lett.*, 2009, **478**, 175–179.
51 J. Huang, S. Wen, J. Liu and G. He, *J. Nat. Gas Chem.*, 2012, **21**, 302–307.
52 W. Wang, C. Lu, Y. Ni, M. Su, W. Huang and Z. Xu, *Appl. Surf. Sci.*, 2012, **258**, 8696–8703.
53 C. Marchiori, G. Di Liberto, G. Soliveri, L. Loconte, L. Lo Presti, D. Meroni, M. Ceotto, C. Oliva, S. Cappelli, G. Cappelletti, C. Aieta and S. Ardizzone, *J. Phys. Chem. C*, 2014, **118**, 24152–24164.
54 C. Lalhriatpuia, D. Tiwari, A. Tiwari and S. M. Lee, *Chem. Eng. J.*,

2015, **281**, 782–792.

55 J. Krýsa, G. Waldner, H. Měšťánková, J. Jirkovský and G. Grabner, *Appl. Catal. B Environ.*, 2006, **64**, 290–301.

56 A. Antonello, G. Soliveri, D. Meroni, G. Cappelletti and S. Ardizzone, *Catal. Today*, 2014, **230**, 35–40.

57 H. Li, L. Shen, K. Zhang, B. Sun, L. Ren, P. Qiao, K. Pan, L. Wang and W. Zhou, *Appl. Catal. B Environ.*, 2018, **220**, 111–117.

58 Z. Xing, J. Zhang, J. Cui, J. Yin, T. Zhao, J. Kuang, Z. Xiu, N. Wan and W. Zhou, *Appl. Catal. B Environ.*, 2018, **225**, 452–467.

59 X. Zhou, C. Shao, S. Yang, X. Li, X. Guo, X. Wang, X. Li and Y. Liu, *ACS Sustain. Chem. Eng.*, 2018, **6**, 2316–2323.

60 N. Pronina, D. Klauson, A. Moiseev, J. Deubener and M. Krichevskaya, *Appl. Catal. B Environ.*, 2014, **178**, 117–123.

61 A. Di Paola, M. Bellardita and L. Palmisano, *Catalysts*, 2013, **3**, 36–73.

62 D. C. Hurum, A. G. Agrios, K. A. Gray, T. Rajh and M. C. Thurnauer, *J. Phys. Chem. B*, 2003, **107**, 4545–4549.

63 X. Jiang, M. Manawan, T. Feng, R. Qian, T. Zhao, G. Zhou, F. Kong, Q. Wang, S. Dai and J. H. Pan, *Catal. Today*, 2018, **300**, 12–17.

64 K. Nakata and A. Fujishima, *J. Photochem. Photobiol. C Photochem. Rev.*, 2012, **13**, 169–189.

Chapter 1

Green and low-cost tetracycline degradation processes by nanometric and immobilized TiO_2 systems

Tetracyclines, among the most common antibiotics, are classified as emerging micro-pollutants since their accumulation in the environment can induce long-term effects such as endocrine disruption, antibiotic resistance and toxicity on living organisms[1]. Due to their extensive use over the years, traces of tetracycline and of their metabolites have been found in many different environments, like wastewaters, drinking waters and soils [2]. Moreover, these antibiotics, due to their physicochemical properties, are mostly excreted after use in the pristine un-metabolized form.

Conventional wastewater treatments for the removal of organic pollutants usually fail to achieve a complete degradation of tetracycline, favouring the production of toxic reaction intermediates. Moreover, by-products often maintain high antibacterial activity, preventing the use of biological remediation methods, even as post-treatments[3]. Consequently, the search for effective and economical processes to reduce tetracycline release into the ecosystem has become imperative.

Remediation methods based on adsorption and/or filtration, although being applied to tetracycline-polluted systems[4–6], have the only effect to move the pollutant from the liquid to the solid phase without degrading it. In the last few years, advanced oxidation processes have been proposed as efficient methods to perform tetracycline degradation. In this regard, photolysis, ozonation, inverse osmosis, electrochemical, Fenton and photo-Fenton processes have been studied[7–11]. However, photocatalysis is arguably the most promising technique, giving rise to by-products characterized by a lower toxicity[12]. Different materials have been investigated as photocatalysts for tetracycline degradation. Several

complex multi-component materials have been recently proposed to improve the photocatalytic degradation of tetracyclines, such as carbon nanotubes/Bi_2WO_3 composites[13], BiOI microspheres[14] and Ag/Fe_2O_3/C_3N_4 magnetic materials showing visible-light absorption[15]. However, starting from the pivotal studies of Reyes *et al.* and Palominos *et al.*[16,17], the chemical and photochemical stability, natural abundance and low cost have made TiO_2 one of the best choices for removing tetracyclines from the environment by photocatalytic processes[18–20]. In this respect, commercial powders were mainly adopted in literature works[21,22]. Zhu *et al.*, by using P25 TiO_2, studied the molecule degradation pathway and the changes in the tetracycline solution toxicity during the reaction[23]; the influence of interferents and the optimization of the physicochemical parameters affecting the photocatalytic efficiency were also investigated[17,24,25].

In this Chapter, the photocatalytic degradation of tetracycline by TiO_2 powders prepared by a multi-step procedure and thermally treated at four different temperatures is reported. The choice of the calcination temperature is not trivial when large organic target molecules are considered, since the pollutant/oxide interactions can be deeply affected by the physicochemical features of the photocatalyst. Higher calcination temperatures can produce diverging effects on the material, *e.g.* decreasing the surface area while increasing the crystallite size, reducing the hydrophilicity but increasing the regularity. To the authors' best knowledge, no results can be found in the literature concerning this aspect in the case of the photocatalytic degradation of tetracycline.

A second relevant point is addressed in the present work: the transfer of the knowledge acquired on powders to parent immobilized systems. The immobilization of the photocatalyst on removable or reusable substrates has become an urgent issue. Few literature works address this problem. Very recently, Pronina and coworkers used TiO_2-coated clay granules for the degradation of tetracycline, with low degradation efficiency due to the low surface area of the supports[26]. Lu *et al.* synthesized TiO_2/Fe_2O_3/carbon nanotubes composites removable with magnets[27]. Borosilicate glass was used as a support for TiO_2 by Lalhariatpuia *et al.*[25]. In this work, two different strategies are proposed as viable solutions to the longstanding problem of the removal of suspended photocatalysts from the stream after

use: titania films were deposited, starting from a sol developed in our laboratory[28], on two different kinds of supports (metal laminas or ceramic pellets). For both powders and immobilized films, the degradation process was followed by monitoring both the pollutant disappearance and the mineralization degree. The reusability of the photocatalyst and the role played by radical species in supporting the reaction were also investigated.

1.1 Results and discussion

1.1.1 Powder materials characterization

The first part of the work focuses on the role played by the calcination temperature on the physicochemical properties and on the photocatalytic activity of home-made titania powders. As the lowest calcinations temperature (200 °C) yielded samples containing significant amounts of organic contaminants (as revealed by the dark colour of the powders), the work will focus on the T300, T400, T500 and T600 samples.

Crystal Structure and Morphology. XRPD spectra of all samples show a good degree of crystallinity (Fig. 1.1a), which increases with the calcination temperature (the highest signal to noise ratio was achieved by the T600 sample). In all samples, anatase is the main polymorph (Tab. 1.1). T300 and T400 are biphasic, containing both anatase and brookite. Due to the relatively low calcination temperatures, anatase crystallites have a diameter smaller than 10 nm (Tab. 1.1). On the contrary, T500 is composed of pure anatase with larger crystallites (d_a^{101} = 14 nm), as shown by the sharper diffraction peaks. T600 is the most crystalline sample, and it is characterized by a 20% rutile content, as expected on the grounds of the calcination temperature. The anatase average crystallite dimension further increases, reaching a diameter of 50 nm. The commercial Alfa Aesar sample is mainly composed by anatase with rutile traces and shows a crystallite size of 15 nm. The N_2 adsorption-desorption isotherms in subcritical conditions of the four TiO_2 powders and of the commercial sample are shown in Figure 1.1b. T300, T400 and T500 samples reveal hysteresis loops characteristic of mesoporosity. The profile of the hysteresis loops is H2-type, characteristic of “bottle-neck”-shaped pores and the vast majority of the pores has a diameter smaller than 6 nm (Fig. 1.1c). The different position of the isotherm “knee”, which identifies the

creation of a N_2 monolayer on the solid surface, shows that the T400 specific surface area (162 m^2 g^{-1}) is about twice that of T500 (73 m^2 g^{-1}), as reported in Table 1.1. Interestingly, T300 showed a decrease in specific surface area and pore volume with respect to T400, which might be related to an uncompleted removal of organic residues at this low calcination temperature, as also supported by the sample whitish colour (see DRS results). Sintering effects and crystallite growth are responsible for the marked decrease of specific surface area of T500, as well as for a remarkable decrease of total porosity (from 0.284 to 0.103 mL g^{-1}), especially concerning the smallest pores (< 6 nm). Further increasing the calcination temperature to 600 °C leads to a tremendous decrease in the specific surface area (2 m^2 g^{-1}) and to an almost complete disappearance of the pores smaller than 6 nm. The hysteresis loop of the T600 sample, probably of H3-type, is almost unappreciable. It is noteworthy that the amount of bigger pores (> 80 nm) is not dependent on the calcination treatment. The shape of the hysteresis loop of the commercial sample is different from the low temperature home-made ones and can be labelled as H3-type, typical of slit-shaped pores. This sample shows the largest total pore volume (Fig. 1.1c and Tab. 1.1).

Sample	Phase composition (%)	d_a^{101} (nm)	S_{BET} (m^2 g^{-1})	V_{pores} (mL g^{-1})	E_g (eV)
T300	95 A – 5 B	9	134	0.205	2.97
T400	98 A – 2 B	8	162	0.284	3.15
T500	100 A	14	73	0.103	3.07
T600	80 A – 20 R	50	2	0.018	2.96
Alfa Aesar	95 A – 5 R	15	141	0.456	3.30

Table 1.1 – Specific surface area (S_{BET}), total pore volume (V_{pores}), average crystallite dimension of the anatase phase calculated by applying the Scherrer equation (d_a^{101}), phase composition (A: anatase; B: brookite; R: rutile), and apparent band gap value retrieved by Kubelka-Munk elaboration (E_g) of the powder samples.

Optical Characterization. DRS spectra of T400, T500 and T600 samples (Fig. 1.1d) show slight variations of the absorption edge among the different samples. This is testified by the apparent band gap values (Tab. 1.1): T400 has the highest band gap value (3.15 eV), possibly due to the lower crystallinity and the slight amount of brookite, whose band gap is wider with respect to anatase[29]. On the other hand, the presence of rutile in T600 results in a red shift of the absorption edge and a decrease in the sample band gap value (2.96 eV with respect to 3.07 eV for T500), as expected on the grounds of rutile smaller band gap[30]. Unlike the other samples, T300 shows a higher absorption in the visible region (400–700 nm), which may be indicative of the presence of carbonaceous contaminants, in agreement with BET results. Figure 1.1d reports also the curve relative to the commercial sample which appears slightly blue-shifted, giving rise to the slightly higher band gap value.

Photocatalytic activity. The photocatalytic activity of the different samples was tested toward the degradation of tetracycline hydrochloride in aqueous solution at natural pH. Although literature works indicate that the molecule photodegradation is favoured by alkaline pH values[17], no pH correction was introduced in the present work to simplify at best the chemistry of the process. The target molecule degradation was followed by UV-vis spectroscopy on the grounds of an established method widely proposed in the literature[8,14,16,17] and previously validated by HPLC determinations[13,16]. The mineralization degree was obtained by TOC measurements as an indication of the complete oxidation of tetracycline to CO_2, H_2O and NH_4^+.

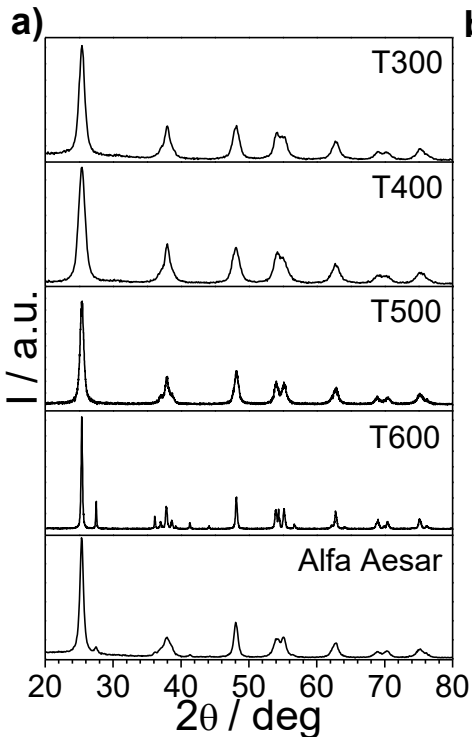

a) XRPD patterns of the different powder samples.

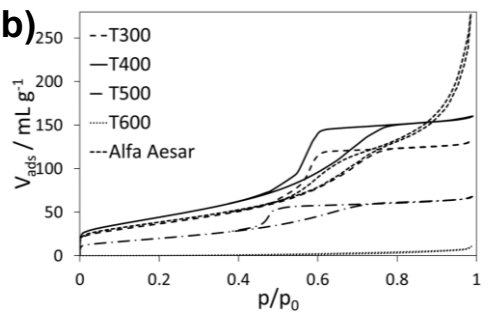

b) N_2 adsorption-desorption isotherms in subcritical conditions of the home-made powder photocatalysts and of the commercial sample.

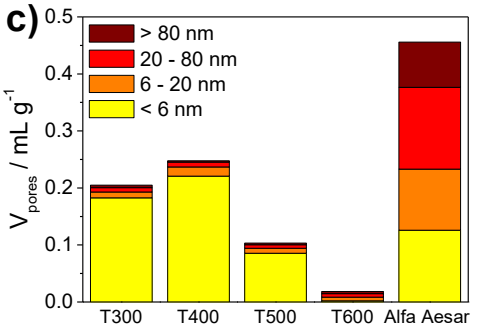

c) Pore volume distributions of the home-made and commercial powder samples.

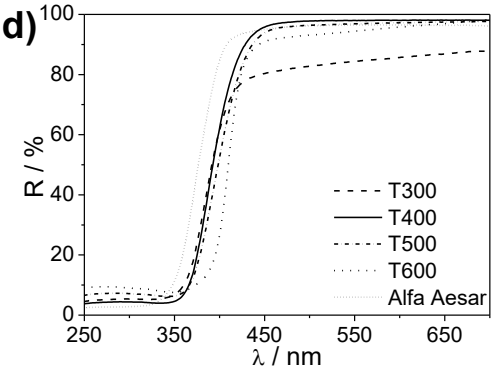

d) DRS spectra of the powder samples.

Figure 1.1 – Structural, morphological and optical properties of the synthesized samples.

All samples were submitted to a UV irradiation step (90 min) prior to the photocatalytic tests. This procedure was adopted after observing an appreciable promotion of the overall activity of the photocatalyst upon irradiation treatment, from both the molecule disappearance and the

mineralization viewpoint (Fig. 1.2a). The prolonged pre-irradiation step may favour the hydroxylation of the powder surface and promote a cleaning effect from adsorbed impurities[31–34]. The increase in the –OH population at the surface of the photocatalyst, in its turn, may allow a better water wetting and the ensuing formation of more stable suspensions. Further effects may be related to a possible surface reconstruction occurring upon prolonged UV irradiation[35]. These effects play also a relevant role in affecting the activity of reused samples. The reused T400 sample is even more active than the pristine irradiated sample. The total absence of inactivation of the sample could have been expected on the grounds of the complete mineralization of the pollutant, as proved by FTIR spectra of the used photocatalyst (Fig. 1.2b). However, the slight increase in performance can be possibly attributed to the further irradiation step received by the reused sample and to the prolonged wetting in water during the former reaction.

In order to investigate the role played by oxidant species and charge carriers on the mechanism of tetracycline degradation, photocatalytic tests were carried out in the presence of two different scavengers (isopropanol and Na-EDTA) adopting T400 as the reference photocatalyst. Isopropanol was used as $OH^{\bullet}$ scavenger, according to other literature studies[13,17,23,25], while Na-EDTA was chosen as h^+ scavenger as proposed by Zhu *et al.* and Lalhriatpuia *et al.*[23,25]. The degradation profiles are compared in Figure 1.2c. Both scavengers inhibit the degradation, implying that both $OH^{\bullet}$ and h^+ species are responsible for the oxidation of tetracycline, but the addition of Na-EDTA produces a larger inhibition with respect to isopropanol. This occurrence can be the result of two parallel effects: the competitive adsorption between EDTA and tetracycline at the surface of the photocatalyst, and the depletion of holes which directly oxidize the target molecule. A combined role played by both holes and $OH^{\bullet}$ on the photodegradation of tetracycline by TiO_2 was previously observed by Zhu *et al.* and by Palominos *et al.*[17,23], whereas Luo *et al.*[36] recently proposed a reaction mechanism not involving $OH^{\bullet}$ species. Yue *et al.*[13], on the other hand, attributed a stronger effect on $OH^{\bullet}$ species, adopting ammonium oxalate as a hole scavenger. The combined role played by $OH^{\bullet}$ and h^+ species is supported, in the present case, by reaction intermediates investigated by ESI-MS analyses (Fig. 1.3a). In the initial solution, the peak

at m/z = 445 can be attributed to the molecular ion of tetracycline $[M+H]^+$, while the other peaks are relative to ionization products of the molecular ion[37]. By comparing the ESI-MS spectra before and after 1 h irradiation, several peaks relative to degradation intermediates can be identified. The two peaks at m/z = 459 and 477 have been previously observed by several authors as intermediates in the degradation of tetracyclines[7,12]. Maroga Mboula *et al.* proposed a mechanism implying an initial attack by $OH^{\bullet}$ followed by the loss of NH_3 supported by the interaction with h^+ species[12]. The presence of a peak at m/z = 495 could be related to a further attack by $OH^{\bullet}$ to the intermediate at m/z = 477, as proposed by Zhu *et al.* [17]. The oxidation products at m/z = 229 and 287 revealed that the opening of the non-aromatic rings of tetracycline already occurred after 1 h of irradiation[38,39].

Fig. 1.2d compares the degradation curves of the different photocatalysts. All powder samples, except T600, produce a complete degradation of tetracycline in 2 h, with a fast kinetics. The initial rates were calculated as pseudo-first order constants (Tab. 1.2) in agreement with literature results[23]. T400 exhibits the best performance, reaching 90% degradation after 35 min of irradiation. The T300 sample leads to a slightly slower pollutant disappearance, degrading 83% of the molecule after 35 min. Despite the carbon contamination, T300 presents a good photocatalytic performance, possibly due to its better stability in water ensuing the lower calcinations temperature. The degradation produced by T500 is somewhat lower (66% degradation in 35 min) while T600 gives rise only to a degradation of about 30% in the same time. These results are mirrored by the mineralization degrees obtained for the three samples (Fig. 1.2d): T400 and T300 produce complete mineralization after 6 h, similarly to T500 which achieves more than 95% mineralization. Again, the activity of T600 appears to be the lowest, producing a mineralization lower than 40% after 6 h.

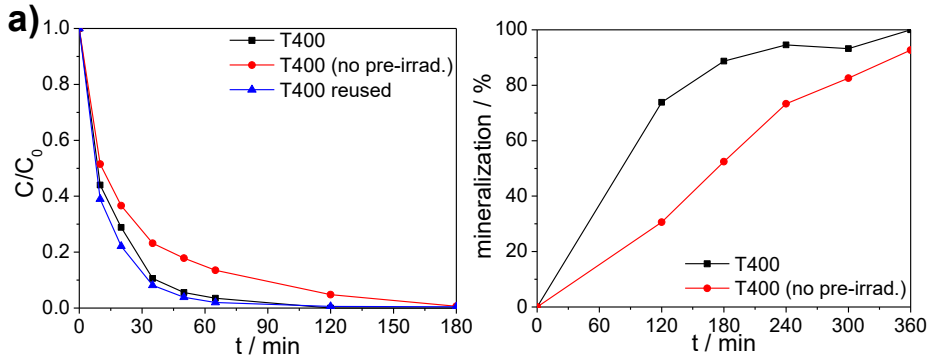

a) Effect of UV pre-irradiation and recycle on tetracycline disappearance (left) and mineralization degree (right).

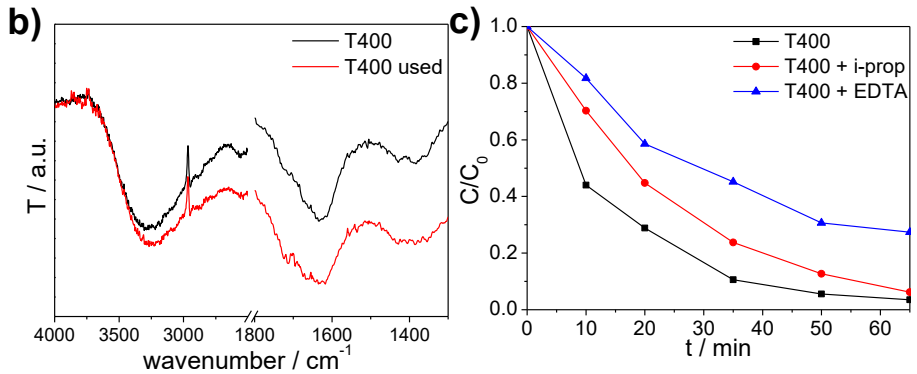

b) FTIR spectra of T400 sample before and after photocatalytic test.

c) Effect of the radical and hole scavengers on tetracycline disappearance curves

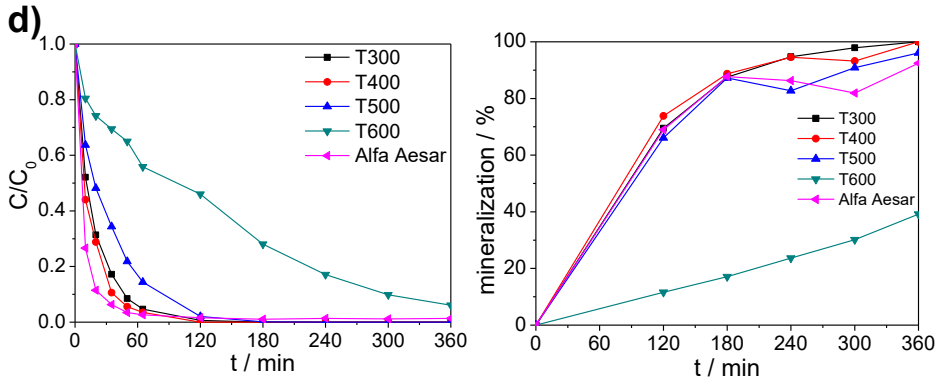

d) Tetracycline disappearance (left) and mineralization degree (right) as a function of irradiation time during photocatalytic tests for all powder samples.

Figure 1.2 – Photocatalytic tests results.

The elaboration of kinetic data of the commercial sample by a pseudo-first order law was not satisfactory. In the case of this sample, the molecule disappearance is fast (Fig. 1.2d), however tetracycline traces still remained

at the end of the test and an incomplete mineralization (92%, after 6 h) was achieved.

Our sol-gel powder samples proved very promising materials for the photocatalysis of tetracycline. T400, favoured by the large surface area, appears to be the most efficient material, especially for what concerns the molecule disappearance. However, the mineralization produced by T500, characterized by half the surface area, is quite comparable to that produced by T400. The comparison of the behaviour of the two photocatalysts may suggest that the mechanism of degradation is different in the two cases: the large surface area of T400 favours the fast disappearance of the pristine molecule, while the mineralization seems to be more direct in the case of T500. Some specific features of the latter sample, apparently, promote its photocatalytic activity, overcoming the decrease in active surface produced by the higher calcination temperature. A first aspect can be suggested on the grounds of DRS spectra showing for T500 a larger absorption of light between 350 and 450 nm, *i.e.* in the emission range of the adopted lamp, improving light harvesting. Further, the higher calcination temperature promotes crystal growth and surface regularity, as suggested by the almost double value of crystallite size. A decrease in defectivity can be expected to reduce recombination between photogenerated holes and electrons[40], improving photocatalytic efficiency. T600 shows the lowest performance due to the very poor morphological features; however, it is worth noting that its mineralization curve (Fig. 1.2d) clearly exhibits an increasing trend for all the duration of the photocatalytic test. Despite the very low porosity and photoactive available surface, this fact suggests that the active sites of T600 are not completely inactivated either by tetracycline or by its reaction intermediates.

1.1.2 Immobilized photocatalysts

A titania sol, previously developed in our laboratory, was adopted to produce mechanically robust and highly photoactive anatase layers[41,42] on supports with two different geometries. A roughened aluminium lamina (Fig. 1.3b), covered by a native alumina layer, was chosen as a stable, eco-friendly and cheap substrate for the deposition of TiO_2. Then, a second system was developed with the aim of increasing the accessible surface area of the photocatalyst, while using a support with the same chemical

composition: commercial alumina pellets (Fig. 1.3b) with a surface area of around 100 m^2 g^{-1} were chosen. The weight of the TiO_2 deposit was estimated in 30 mg per gram of pellets. Interestingly, the pellet specific surface area did not change after the deposition of the TiO_2 layers. Fig. 1.3c reports cross-sectional SEM images of cut pellets before and after the deposition of TiO_2. The surface appears rough in both cases while the deposition of the titania layer does not seem to produce appreciable heterogeneity at the surface of the pellet. The TiO_2 layer on commercial pellets was *ca.* 5 μm thick.

The TiO_2-immobilized systems were tested photocatalytically in the same experimental conditions of the TiO_2 nanostructured powders. The aluminium lamina was suspended in the reactor, while the alumina pellets were deposited at the bottom of the reactor forming a compact and stable layer. The photocatalytic degradation was slower with respect to the TiO_2 slurries commented above (Fig. 1.3d, Tab. 1.2). Both systems, however, accomplished degradation of tetracycline accompanied by a partial mineralization in the short time scale of the test (6 h). The alumina pellets showed a better performance with respect to the Al lamina. After two hours of irradiation, around 60% of tetracycline was degraded by pellets, while only 47% by the lamina. At the end of the reaction, both systems produced more than 80% degradation (93% for pellets). The mineralization trend of both supports did not give rise to a plateau, confirming the efficacy of these TiO_2-immobilized macroscopic devices. A complete oxidation of the target molecule has to be expected by prolonging the reaction time. The present results can be analyzed with respect to those reported by He *et al.*[43] concerning the photocatalytic degradation of various pharmaceuticals by titania deposited onto quartz sand. In the literature work the adopted concentration of the pollutant was much lower than in the present case (20 instead of 35 mg L^{-1}) and the degradation of the molecules was obtained by a larger amount of supported photocatalyst (25 instead of 10 g) and after much longer irradiation time (80–100 h for the best conditions). No mineralization data were reported. Although data by He *et al.* pertain to a different wavelength of irradiation with respect to the present ones (300–800 nm) the comparison of the photocatalytic activity of the two immobilized titania systems seems to strongly favour the present materials. Furthermore, the presented sol-gel-based coatings have been previously

reported to be more robust and stable to deactivation than films from commercial powders[41].

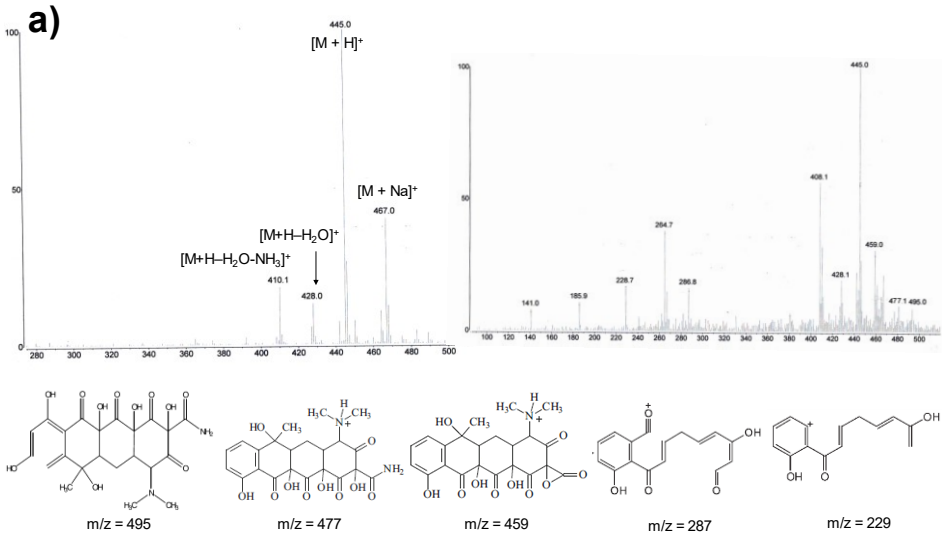

a) ESI-MS spectra of tetracycline solution before (left) and after 1 h of irradiation (right) during photocatalytic tests with T400, together with proposed structures attributed to main ESI-MS peaks.

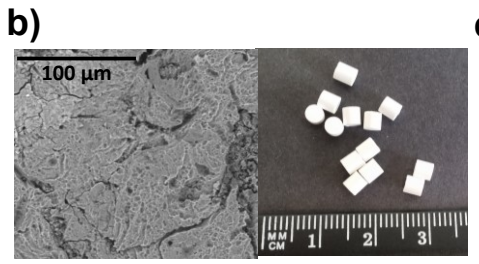

b) Substrates for TiO_2 immobilization: SEM image of the roughened aluminum lamina (left) and commercial alumina pellets (right).

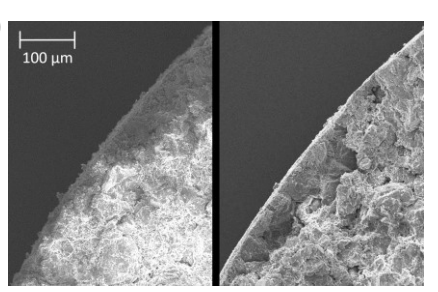

c) SEM images of bare (left) and TiO_2-coated (right) alumina pellets.

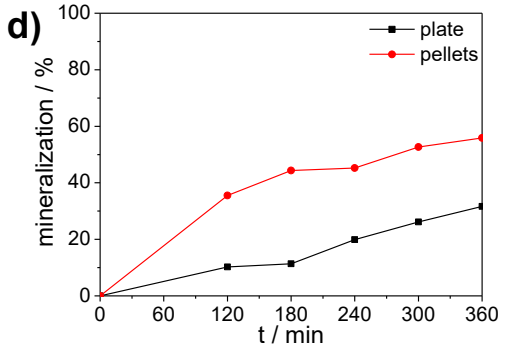

d) Mineralization degree as a function of irradiation time for the immobilized systems.

Figure 1.3 – Degradation pathway and adopted immobilized systems information.

Sample	k ($\times 10^{-3}$ min^{-1})	mineralization (%)
photolysis	3.0 ± 0.4	5 ± 1
T300	49 ± 1	88 ± 1
T400	56 ± 2	89 ± 1
T500	31 ± 3	87 ± 1
T600	9.5 ± 0.9	17 ± 1
Alfa Aesar	-	88 ± 1
lamina	6.2 ± 0.5	11 ± 1
pellets	8.5 ± 0.4	44 ± 1

Table 1.2 – Pseudo-first order constants, *k*, of tetracycline disappearance in the first 65 min of irradiation and mineralization degrees after 3 h of irradiation for powder samples and immobilized systems.

1.2 Conclusions

The photocatalytic degradation of tetracycline by TiO_2 nanostructured powders and immobilized macroscopic systems was investigated. Powder samples provided an insight into the relevant physicochemical aspects at play in the process. Home-made sol-gel powders calcined at different temperatures were studied.

Prolonged UV irradiation of the photocatalyst was found to be beneficial for the photocatalytic performance. Such an observation could be related to an increased surface hydroxylation and/or to the occurrence of surface reconstruction upon irradiation. The beneficial effect of light irradiation is profitable for the reusability of the photocatalyst, as shown by recycle tests.

The calcination temperature had a complex effect on the photocatalytic behaviour of the samples. While increasing the calcination temperature to 600 °C proved detrimental, probably as a result of the drastic drop of surface area and porosity, lower calcination temperatures showed high activity with respect to both the molecule disappearance and mineralization. In particular, the sample calcined at 400 °C showed the best performance in tetracycline disappearance, whereas mineralization curves were comparable for both the 300, 400 and 500 °C treated samples. The photocatalytic activity seems to be the result of an interplay among

morphology, crystallinity and absorption features of the oxide, which can possibly determine different reaction mechanisms. As a whole, photocatalytic results seem to point out that the rate of tetracycline disappearance increases with the photocatalyst surface area, while its mineralization is less dependent on the photocatalyst morphological features, being fully comparable for the T300, T400 and T500 samples. This latter observation is instrumental for the development of immobilized photocatalysts, since higher calcination temperatures lead to more robust photocatalyst coatings.

In this respect, the role of radical species and electron holes was investigated. The role of hydroxyl radicals in tetracycline photocatalytic degradation is in fact a debated topic in the literature. Our tests with radical scavengers showed that both $OH^{\bullet}$ and h^{+} species take part in the tetracycline degradation, with the holes playing a more relevant role. The concomitant occurrence of both $OH^{\bullet}$- and h^{+}- mediated pathways was confirmed also by ESI-MS determinations of the degradation intermediates.

Finally, a crucial aspect for the real-life application of the remediation test was considered: the immobilization of TiO_2 on macroscopic substrates. The immobilization of photocatalysts on macroscopic substrates enables their easier removal from the treated effluent; further, it allows to overcome the health concerns associated with volatile nanostructured materials. However, the lower number of active sites in immobilized systems leads to detrimental effects on the process efficiency and makes the photocatalyst more prone to poisoning phenomena. In this respect, we tested two possible geometries for the substrates: roughened laminas and macroscopic pellets. In order to keep the costs low while promoting the adhesion of the TiO_2 layer on the substrate, aluminium/alumina supports were chosen. The TiO_2 deposition was carried out starting from a stable sol in order to guarantee the formation of a mechanically robust anatase layer. Photocatalytic tests showed that both immobilized substrates present notable photoactivity. The most performing immobilized photocatalyst proved to be the TiO_2-coated alumina pellets, possibly due to their higher available surface area. Despite the high pollutant content, no plateaus were observed in the mineralization curve, confirming the efficacy of these devices.

1.3 Specific procedures

Samples preparation. Reactants were purchased from Sigma Aldrich and were used without any further purification. Solutions and suspensions were prepared by using doubly distilled water passed through a Milli-Q apparatus.

TiO_2 nanostructured powders were prepared by a modification of the procedure reported by Behnajady *et al.*[44]. In a flask kept in an ice/water bath, 3.78 g of acetic acid (AcOH) was mixed with 18.38 g of titanium(IV) isopropoxide (97%) (TTIP). Then, 220 mL of water was added dropwise in about 30 min while stirring vigorously. The TTIP:AcOH:H_2O molar ratios were 1:1:200. The reaction mixture was stirred for 1 h and then stored in the dark overnight at room temperature. The suspension was subsequently dried in an oven at 70 °C for 3 h and then at 100 °C for 24 h. The ground powder was purified by osmosis, centrifuged and dried in an oven at 80 °C. Finally, the powder was calcined at different temperatures for 6 h under an O_2 flux (9 NL h^{-1}). The powder samples calcined at 200, 300, 400, 500 and 600 °C were labelled as T200, T300, T400, T500 and T600, respectively.

Immobilized catalysts preparation. Immobilized titania samples were prepared by depositing two successive TiO_2 layers on two different commercial supports, starting from a sol whose preparation procedure can be found in Appendix A. Sandblasted Al laminas were used as cheap and recyclable supports since the native alumina film favours the adhesion of the titania layer. The second selected support consisted in alumina commercial pellets (AL60610300 Goodfellow). Al plates (5.5 × 15 cm^2) and 10 g of the millimetric rods were dipped in 40 mL of titania sol for 1 h, then drained from the sol onto a steel grid and immediately calcined at 500 °C for 5 h in O_2 flux (9 NL h^{-1}). The entire procedure was repeated twice. Before the layer deposition, laminas were cleaned by a previously reported procedure by sonication in water and isopropanol (15 min each).

Photocatalytic activity tests. Samples were tested under UV irradiation in the degradation of aqueous solutions of tetracycline hydrochloride. The effective input power density of the lamp was 30 mW cm^{-2}, while the radiation energy leaving the jacketed reactor was 5 mW cm^{-2} in the case of the TiO_2 suspension and around zero in the case of the Al lamina, respectively. A commercial TiO_2 nanopowder (Alfa Aesar) was also tested as a reference; this commercial sample was selected due to its similar phase

composition (anatase plus rutile traces) and specific surface area (141 m^2 g^{-1}) with respect to the synthesized samples. The photocatalytic tests were performed in a closed Pyrex glass jacketed reactor with a volume of 600 mL. Tests were carried out at 20 °C and natural pH (*ca.* 3), with magnetic stirring and oxygen bubbling (9 NL h^{-1}). The initial pollutant concentration was 35 ppm.

Tetracycline adsorption on TiO_2 was quantified by a test performed in the dark. The system reached its equilibrium after 20 min, with a 30% maximum amount of adsorbed molecule for T400. Direct photolysis was also evaluated by a test in the absence of photocatalyst, leading to negligible mineralization.

Tests with TiO_2 powders were performed in slurry, by suspending 300 mg of the photocatalyst (0.5 g L^{-1}). The suspensions were sampled using a syringe and filtered with a Millipore MF-membrane filter (0.45 μm-HA). In the case of immobilized supports, either one Al lamina or 10 g of pellets (deposited at the bottom of the reactor) were utilized. The amount of TiO_2-coated pellets (10 g) was specifically selected in order to provide an amount of TiO_2 equivalent to tests with powders (300 mg). Both powders and immobilized supports were irradiated with UV light for 1.5 h before the photocatalytic test.

The disappearance of the target molecule was followed by UV-vis spectroscopy, measuring the intensity of the absorption peak at 357 nm, typical of tetracycline. The mineralization degree was estimated by Total Organic Carbon (TOC) measurements according to the following equation:

$$\boldsymbol{mineralization\ degree} = \frac{\boldsymbol{TOC_0 - TOC_t}}{\boldsymbol{TOC_0}} \cdot \mathbf{100}$$

Scavengers tests. Tests with radical and hole scavengers were carried out. Isopropanol and disodium ethylenediaminetetraacetate (Na-EDTA) were selected as scavenger compounds of hydroxyl radicals ($OH^{\bullet}$) and electron holes (h^+) species, respectively. Isopropanol was added with a molar concentration 1000:1 with respect to tetracycline hydrochloride, while Na-EDTA with a molar proportion equal to 30:1.

Reusability tests. At the end of a photocatalytic test, the used photocatalyst was recovered by drying the slurry in an oven at 80 °C overnight. Reusability test were carried out on 300 mg of photocatalyst (slurry concentration: 0.5 g L^{-1}), possibly integrating the amount of

recovered photocatalyst with other used powder (from repeatability tests). The same photocatalytic procedure was then applied.

Further details about preparation and characterization methods can be found in Appendix A.

References

1 V. Homem and L. Santos, *J. Environ. Manage.*, 2011, **92**, 2304–2347.

2 Executive Agency for Health and Consumers, *Study on the environmental risks of medicinal products*, 2013.

3 R. Daghrir and P. Drogui, *Environ. Chem. Lett.*, 2013, **11**, 209–227.

4 C. Adams, Y. Wang, K. Loftin and M. Meyer, *J. Environ. Eng.*, 2002, **128**, 253–260.

5 P. E. Stackelberg, J. Gibs, E. T. Furlong, M. T. Meyer, S. D. Zaugg and R. L. Lippincott, *Sci. Total Environ.*, 2007, **377**, 255–272.

6 A. Göbel, C. S. McArdell, A. Joss, H. Siegrist and W. Giger, *Sci. Total Environ.*, 2007, **372**, 361–371.

7 I. Dalmázio, M. O. Almeida, R. Augusti and T. M. A. Alves, *J. Am. Soc. Mass Spectrom.*, 2007, **18**, 679–687.

8 C. V. Gómez-Pacheco, M. Sánchez-Polo, J. Rivera-Utrilla and J. J. López-Peñalver, *Chem. Eng. J.*, 2012, **187**, 89–95.

9 J. Zhang, P. Zhou, J. Liu and J. Yu, *Phys. Chem. Chem. Phys.*, 2014, **16**, 20382–20386.

10 Y. Liu, X. Gan, B. Zhou, B. Xiong, J. Li, C. Dong, J. Bai and W. Cai, *J. Hazard. Mater.*, 2009, **171**, 678–683.

11 S. Liu, X. Zhao, H. Sun, R. Li, Y. Fang and Y. Huang, *Chem. Eng. J.*, 2013, **231**, 441–448.

12 V. Maroga Mboula, V. Héquet, Y. Gru, R. Colin and Y. Andrès, *J. Hazard. Mater.*, 2012, **209**–**210**, 355–364.

13 L. Yue, S. Wang, G. Shan, W. Wu, L. Qiang and L. Zhu, *Appl. Catal. B Environ.*, 2015, **176**–**177**, 11–19.

14 R. Hao, X. Xiao, X. Zuo, J. Nan and W. Zhang, *J. Hazard. Mater.*, 2012, **209**–**210**, 137–145.

15 Z. Zhu, Z. Lu, D. Wang, X. Tang, Y. Yan, W. Shi, Y. Wang, N. Gao, X. Yao and H. Dong, *Appl. Catal. B Environ.*, 2016, **182**, 115–122.

16 C. Reyes, J. Fernández, J. Freer, M. A. Mondaca, C. Zaror, S. Malato and H. D. Mansilla, *J. Photochem. Photobiol. A Chem.*, 2006, **184**, 141–146.

17 R. A. Palominos, M. A. Mondaca, A. Giraldo, G. Peñuela, M. Pérez-Moya and H. D. Mansilla, *Catal. Today*, 2009, **144**, 100–105.

18 G. H. Safari, M. Hoseini, M. Seyedsalehi, H. Kamani, J. Jaafari and A. H. Mahvi, *Int. J. Environ. Sci. Technol.*, 2015, **12**, 603–616.
19 P. Wang, P.-S. Yap and T.-T. Lim, *Appl. Catal. A Gen.*, 2011, **399**, 252–261.
20 M. Brigante and P. C. Schulz, *J. Hazard. Mater.*, 2011, **192**, 1597–1608.
21 M. Addamo, V. Augugliaro, A. Di Paola, E. García-López, V. Loddo, G. Marcì and L. Palmisano, *J. Appl. Electrochem.*, 2005, **35**, 765–774.
22 A. Di Paola, M. Addamo, V. Augugliaro, E. García-López, V. Loddo, G. Marcì and L. Palmisano, *Fresenius Environ. Bull.*, 2004, **13**, 1275–1280.
23 X. D. Zhu, Y. J. Wang, R. J. Sun and D. M. Zhou, *Chemosphere*, 2013, **92**, 925–932.
24 X. Zhu, Y. Wang and D. Zhou, *J. Soils Sediments*, 2014, **14**, 1350–1358.
25 C. Lalhriatpuia, D. Tiwari, A. Tiwari and S. M. Lee, *Chem. Eng. J.*, 2015, **281**, 782–792.
26 N. Pronina, D. Klauson, A. Moiseev, J. Deubener and M. Krichevskaya, *Appl. Catal. B Environ.*, 2014, **178**, 117–123.
27 C. Lu, Y. Zhou, G. Zhang, W. Guan, X. Zhang and L. Ye, *Micro & Nano Lett.*, 2013, **8**, 749–752.
28 G. Maino, D. Meroni, V. Pifferi, L. Falciola, G. Soliveri, G. Cappelletti and S. Ardizzone, *J. Nanoparticle Res.*, 2013, **15**, 2087.
29 A. Di Paola, M. Bellardita and L. Palmisano, *Catalysts*, 2013, **3**, 36–73.
30 D. O. Scanlon, C. W. Dunnill, J. Buckeridge, S. A. Shevlin, A. J. Logsdail, S. M. Woodley, C. R. A. Catlow, M. J. Powell, R. G. Palgrave, I. P. Parkin, G. W. Watson, T. W. Keal, P. Sherwood, A. Walsh and A. A. Sokol, *Nat. Mater.*, 2013, **12**, 798–801.
31 T. L. Thompson and J. T. Yates, *Chem. Rev.*, 2006, **106**, 4428–4453.
32 A. Fujishima, X. Zhang and D. A. Tryk, *Surf. Sci. Rep.*, 2008, **63**, 515–582.
33 A. Di Paola, M. Bellardita, L. Palmisano, Z. Barbieriková and V. Brezová, *J. Photochem. Photobiol. A Chem.*, 2014, **273**, 59–67.
34 J. M. Coronado, A. J. Maira, J. C. Conesa, K. L. Yeung, V.

Augugliaro and J. Soria, *Langmuir*, 2001, **17**, 5368–5374.
35 R. Li, Y. Weng, X. Zhou, X. Wang, Y. Mi, R. Chong, H. Han and C. Li, *Energy Environ. Sci.*, 2015, **8**, 2377–2382.
36 Z. Luo, L. Li, C. Wei, H. Li and D. Chen, *J. Environ. Biol.*, 2015, **36**, 837–843.
37 A. M. Kamel, H. G. Fouda, P. R. Brown and B. Munson, *J. Am. Soc. Mass Spectrom.*, 2002, **13**, 543–557.
38 Z. Lu, P. Huo, Y. Luo, X. Liu, D. Wu, X. Gao, C. Li and Y. Yan, *J. Mol. Catal. A Chem.*, 2013, **378**, 91–98.
39 J. Niu, S. Ding, L. Zhang, J. Zhao and C. Feng, *Chemosphere*, 2013, **93**, 1–8.
40 S. Ardizzone, C. L. Bianchi, G. Cappelletti, S. Gialanella, C. Pirola and V. Ragaini, *J. Phys. Chem. C*, 2007, **111**, 13222–13231.
41 A. Antonello, G. Soliveri, D. Meroni, G. Cappelletti and S. Ardizzone, *Catal. Today*, 2014, **230**, 35–40.
42 G. Soliveri, V. Pifferi, G. Panzarasa, S. Ardizzone, G. Cappelletti, D. Meroni, K. Sparnacci and L. Falciola, *Analyst*, 2015, **140**, 1486–1494.
43 Y. He, N. B. Sutton, H. H. H. Rijnaarts and A. A. M. Langenhoff, *Appl. Catal. B Environ.*, 2016, **182**, 132–141.
44 M. A. Behnajady, H. Eskandarloo, N. Modirshahla and M. Shokri, *Photochem. Photobiol.*, 2011, **87**, 1002–1008.

This Chapter has been adapted with permission from Rimoldi *et al.*, *Catal. Today*, 2017, **281**, 38−44.

Chapter 2

Emerging pollutant mixture mineralization by TiO_2 photocatalysts. The role of the water medium

As already described in the previous Chapter in the case of tetracycline, in the last few years pharmaceuticals and personal care products (PPCPs) have attracted much attention as a new class of persistent organic pollutants (POPs)[1,2]. Among these emerging contaminants, pharmaceuticals, such as antibiotics, beta-blockers, antipyretics and stimulants, represent a notable source of concern due to their biological activity and potential health and environmental effects[3,4]. Owing to their large usage, high excretion rate, persistence and resistance to conventional wastewater treatments, they are nowadays widespread in wastewaters, water effluents, and surface waters, in concentrations ranging from ng L^{-1} to μg L^{-1} [5,6]. Being recalcitrant molecules, they tend to accumulate in the environment[7] and conventional treatments are often unable to completely remove them from wastewaters. For example, many pharmaceuticals, such as antibiotics, are not feasible to degrade by biological treatments.[8,9]

Photocatalysis has been proposed as an effective Advanced Oxidation Process (AOP) for the degradation of this class of compounds in waters[10]. This technique may permit not only to remove the contaminant from the polluted system, but also to completely degrade it without giving rise to undesired by-products, which may be even more noxious than the parent compound[11–13]. TiO_2 is still the most widely used photocatalyst for environmental remediation purposes because of its low cost, abundance, chemical and photochemical stability, and high activity[14–16].

Although a great deal of effort has been recently devoted to investigate the efficiency of TiO_2-based systems for the photocatalytic degradation of single PPCPs[17–21], much fewer studies deal with the development of effective degradation methods for systems mimicking real effluents[22]. Wastewaters usually contain complex pollutant mixtures as well as numerous other organic and inorganic species, which can affect the degradation process through interference and matrix effects. A few literature studies investigate the photocatalytic degradation of pollutant mixtures in real effluents[23,24]. Van Doorslaer *et al.* compared the photocatalytic efficiency of TiO_2 for the degradation of moxifloxacin in hospital effluents, achieving 70% of inhibition with respect to demineralized water, as a result of different combined effects, such as different adsorption, presence of scavenger species, formation of complexes[25]. Very recently, a detailed scenario on the detrimental effect of several electrolytes on TiO_2 photocatalysis was provided by Rioja *et al.*[26]. Species such as Cl^- and HCO_3^- have been reported to act as scavengers on TiO_2 photocatalysis of dyes and pharmaceuticals[27,28]. In order to develop efficient remediation treatments for emerging pollutants, it is thus imperative to get a clearer picture of the complex interactions taking place in pollutant mixtures in real life matrices during the photocatalytic process.

In this Chapter, the photodegradation reaction of four PPCPs by home-made anatase TiO_2 is presented. The target molecules were selected among the emerging pollutants found in the rivers and lakes of Northern Italy[29–31], in order to represent different classes of PPCPs. Tetracycline (TC) is a widely used antibiotic for both animals and humans. Caffeine (CF) is a stimulant in pharmaceutical formulations and is the most widely consumed psychoactive drug. Paracetamol (PC), also known as acetaminophen, is the active ingredient of many analgesic and antipyretic medicaments. Atenolol (AT) is a beta-blocker used in the treatment of cardiovascular diseases and hypertension. Each molecule was studied both independently and in mixture with the other compounds. Moreover, the effect of the water medium composition on the photocatalytic efficiency was investigated by tests performed both in a simulated drinking water, prepared according to a normed protocol and in a commercial bottled mineral water. The feasibility of photocatalytic treatments in real life set ups was further

explored by tests under simulated solar irradiation and with immobilized TiO_2 systems.

2.1 Results and discussion

2.1.1 Material characterization

The synthesized photocatalyst consisted of pure anatase with an average crystallite size of 7 nm, as calculated according to the Scherrer equation.

The morphology of the photocatalyst was studied by N_2 adsorption-desorption isotherms in subcritical conditions, revealing a specific surface area of 176 m^2 g^{-1}. The oxide appeared to be mesoporous with an H2-type hysteresis loop. The total pore volume was 0.238 mL g^{-1} with the vast majority of the pores (90%) smaller than 6 nm.

The main parameters characterizing the reference Evonik P25 sample are 50 m^2 g^{-1} as specific surface area and 80% anatase and 20% rutile as phase composition[26].

2.1.2 Photocatalytic activity

The samples were tested toward the photocatalytic degradation of four emerging organic pollutants (tetracycline, caffeine, paracetamol and atenolol) found in the water bodies of Northern Italy[29–31]. Tetracyclines have been linked to the growth of antibiotic resistant bacterial strains in the Maggiore and Geneva lakes[29,30]. Caffeine, a known marker to investigate pollution in surface waters, was detected in many rivers of Trentino region. Paracetamol is the active ingredient of the best seller over-the-counter drug in Italy. Atenolol was found in several of the main rivers of Northern Italy[31].

Dark adsorption curves of the pollutant at the pre-irradiated TiO_2 surface (Fig. 2.1a) showed that adsorption equilibrium was reached in less than 10 min for CF, PC and AT, with limited adsorption (< 10%). On the contrary, TC strongly adsorbs on TiO_2 (*ca.* 40%), possibly due to its chemical structure (the least soluble among the different tested molecules). The effect of pre-irradiation on the pollutant adsorption was studied by comparing dark adsorption tests on a pre-irradiated sample with adsorption

tests on a sample that did not receive an irradiation pretreatment. Differences in the adsorption curves were within experimental error.

Photolysis tests of the single molecules under UV light showed a molecule disappearance after 6 h lower than 20% for CF, PC and AT, while TC reached a slightly higher value (*ca.* 30%). It is noteworthy that the mineralization degree upon 6 h of UV photolysis was limited to 5-6% for all molecules. Incomplete degradation products of PPCPs have been reported to be more noxious than the parent compound[11,13].

The photocatalytic degradation curves of the single molecules under UV irradiation are reported in Fig. 2.1a. TC concentration decreases much faster than those of the other three molecules, completely disappearing after 120 min. It is worth noting that 35 min are sufficient to degrade 90% of this molecule. The other photocatalytic reactions proceed more slowly: CF and PC behaved similarly, being degraded, almost completely, at the end of the tests (> 90% for both molecules). AT appeared to be the most recalcitrant molecule, reaching an 80% degradation at the end of the reaction time. The reaction rates of pollutant disappearance were evaluated by means of pseudo-first order kinetic constants (Tab. 2.1).

Our results compare well with literature data, although obtained under different experimental conditions TC degradation by photocatalysis is reported to proceed successfully also with respect to other emerging pollutants. In the work by Di *et al.*, for example, the photodegradation of TC is much faster than that of another antibiotics (ciprofloxacin) and of an endocrine disrupting compound (BPA)[35]. The photocatalysis of PC was studied by Rivas *et al.* in experiments promoted by ozone[36]. In this case, the degradation of PC occurs faster than that of caffeine. Similar results were confirmed by Espejo *et al.*[37] AT instead is generally reported to be recalcitrant to photodegradation. Both in mixture with other beta-blockers or with other emerging pollutants including CF, AT is one of the slowest to be degraded[24].

TOC measurements showed that all pollutants gave rise to mineralization under the selected conditions (Fig. 2.1a). TC almost completed photocatalytic oxidation to CO_2, water and ammonium salts within the irradiation time (93%). PC showed a good capability to reach complete oxidation (77%), notwithstanding the much slower degradation kinetics with respect to TC (Tab. 2.1). AT showed a final mineralization

degree higher than 50%. Surprisingly, CF showed the slowest mineralization trend, although the molecule disappears faster than AT. The purinic moiety in the CF structure probably disfavoured a process of complete oxidation. Despite the slowness of the process, the mineralization was not completely inhibited, as shown by the positive trend with respect of time. These latter results are in agreement with the work by Dalmazio *et al.*[32], who suggested the generation of persistent intermediates of CF degradation after a fast initial pollutant oxidation.

As a further step, the photocatalytic degradation of mixtures of the selected pollutants was studied in different conditions, *i.e.* with and without the addition of electrolytes, under UV and simulated solar irradiation, with slurry or immobilized photocatalyst.

Molecule	k (50 min) (10^{-3} min^{-1})	Mineralization (360 min) (%)
TC	65 ± 3	94 ± 1
CF	8 ± 1	41 ± 1
PC	7.2 ± 0.1	77 ± 1
AT	6 ± 1	61 ± 1

Table 2.1 – Pseudo-first order constants, k, in the first 50 min and final mineralization degree of the different molecules, in single pollutant photocatalytic tests (C_0 = 35 mg L^{-1}; 0.5 g L^{-1} TiO_2; ultrapure water matrix).

In tests with ultrapure water and TiO_2 slurry under UV irradiation, the molecules in the mixture showed a disappearance trend fully comparable with that shown by single molecule tests. As a representative example, the disappearance of CF as a single molecule and in the mixture was tested, showing similar trends. ESI-MS spectra of the mixture as a function of irradiation time (Fig. 2.1b), in their turn, mirror the degradation sequence shown by the single molecules: TC disappears in a short-time scale, followed by PC, while even in the mixture CF disappears faster than AT. The mixture showed, also, a good final mineralization degree (Fig. 2.2a). After a steady decreasing trend, at the end of the photocatalytic test, a mineralization degree of 60% was achieved. For the sake of comparison, a well-known commercial oxide (Evonik P25) was also tested showing a better mineralization of the pollutant mixture (*ca.* 80% after 6 h

irradiation), possibly also due to its better dispersibility and stability in water. However, these characteristics make its removal from the suspension lengthy and complex, decreasing the global process efficiency[22] and introducing a possible source of errors in the analytical detection.

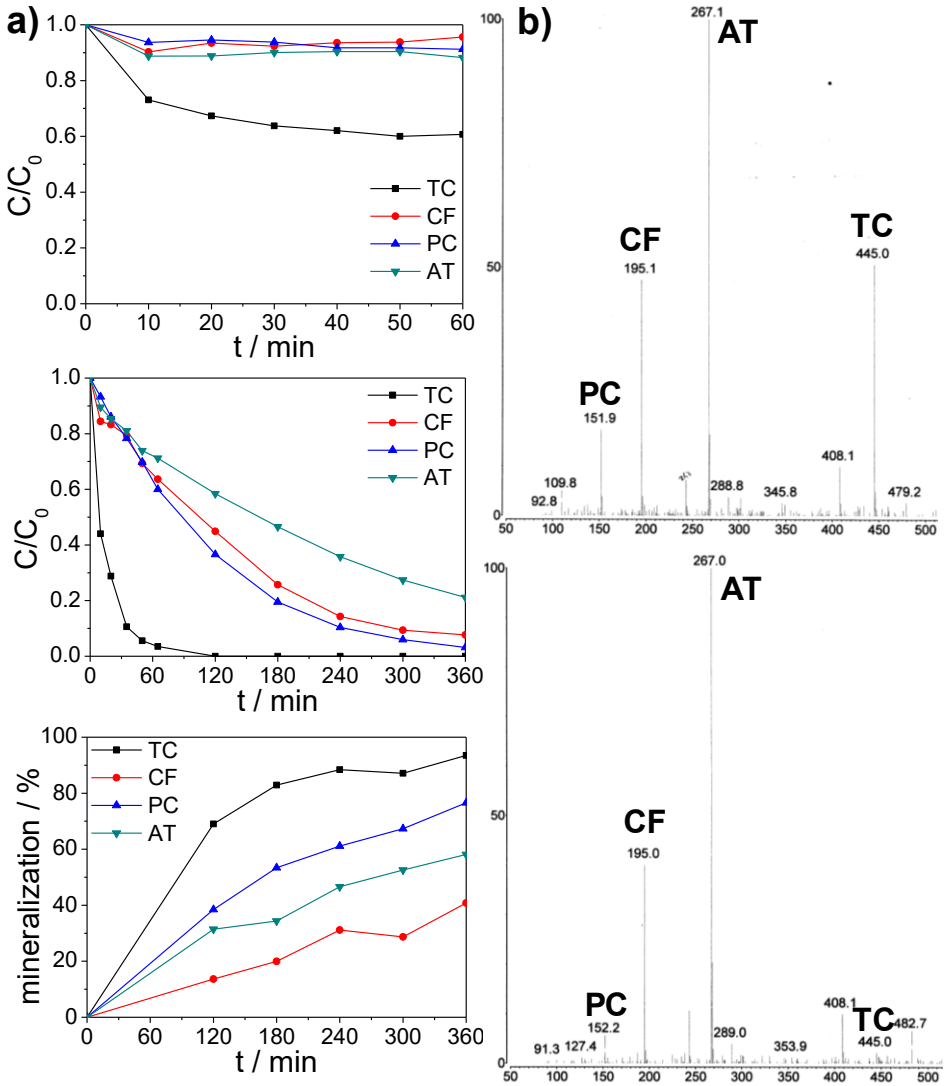

a) Adsorption (top), disappearance (middle) and mineralization (bottom) as a function of time in single pollutant tests (C_0 = 35 mg L^{-1}; 0.5 g L^{-1} TiO_2; ultrapure water matrix).

b) ESI-MS spectra of the photocatalytic tests with pollutant mixtures in ultrapure water at t = 0 (top) and t = 2 h (bottom).

Figure 2.1 – Results of the photocatalytic tests performed in ultrapure water.

Fig. 2.2a compares the mineralization degree obtained by home-made TiO_2 in the test in mixture with that of tests with single pollutants (using the same initial pollutant concentration) as a function of the irradiation time. At each reaction time, the left histogram represents the mineralization of the pollutant mixture measured by TOC determinations, while the right bars report the mineralization degree of each pollutant measured during single pollutant photocatalytic tests. The comparison between the two sets of data suggests that the mineralization rate of the mixture is fully comparable to the sum of the single pollutant ones. Figure 2.2a, together with results in Figure 2.1b, suggest that there are neither synergistic effects among the different molecules nor detrimental competition for the oxide surface sites or reactive radicals.

The tests using ultrapure water as a solvent were compared with tests using both simulated drinking water, prepared according to a standard protocol, and a commercial bottled mineral water (Tab. 2.2). The study of the effect of electrolytes on the photocatalytic activity has recently emerged as a crucial aspect in developing remediation treatments applicable to real effluents[22]. Electrolytes can adsorb onto the oxide surface, leading to a decrease of TiO_2 efficiency due to a competition for its active sites with the pollutant molecules[27,28]. Furthermore, some electrolytes have been reported to act as radical scavengers[26]. Figure 2.2b shows the effect of the presence of inorganic salts on the mineralization curve of photocatalytic tests of the pollutant mixture. In the case of the simulated drinking water, the mineralization decreases by about one third with respect to ultrapure water, although a 40% mineralization is achieved at the end of the test. Adsorption competition with the inorganic compounds seems limited (Fig. 2.2c), even in the case of TC where the adsorption of the molecule is significant. Interestingly, tests with single pollutants in this simulated water matrix (Fig. 2.2c) show different behaviours: both PC and AT show a marked decrease in the molecule disappearance, whereas the disappearance of both TC and CF is not appreciably inhibited. Again, as in the case of distilled water, neither synergistic nor detrimental competition effects are appreciable among the different molecules in the presence of the relatively high concentrations of different electrolytes (Fig. 2.2d). All molecules appear to be mineralized to a lower extent in the presence of electrolytes, except for CF. This molecule, which is the most recalcitrant to

mineralization among the here studied pollutants, is mineralized to a slightly larger extent in the presence of the electrolytes, possibly reflecting the formation of different intermediate species. The general marked decrease of the mineralization might be due to a scavenging effect of the electrolytes toward OH• radicals, which are involved in the photocatalytic degradation of all the studied molecules.[32,40-42]

In the case instead of the commercial bottled water, the mineralization decrease is much larger (about two thirds) with respect to ultrapure water. The two water samples (Tab. 2.2) show comparable conductivity and pH, while they differ in the saline components: the bottled water shows a bicarbonate content three-times larger than the simulated one, together with a lower content in sulphates and chlorides. The comparison between these two sets of data evidences a relevant role played by the content of carbonates/bicarbonates in the mixture. Their role as scavengers of •OH radicals can be suggested also on the grounds of literature results. Indeed, Rioja *et al.*[26] attributed the drastic decrease in the disappearance of clofibric acid, in the case of bottled mineral water, to the competition played by inorganic ions for free radicals.

	simulated drinking water	**bottled mineral water**
Ca^{2+} (mg L^{-1})	45	49
Na^{+} (mg L^{-1})	46	6
Mg^{2+} (mg L^{-1})	9	29
Cl^{-} (mg L^{-1})	79	2
SO_4^{2-} (mg L^{-1})	37	4
HCO_3^{-} (mg L^{-1})	122	301
conductivity (µS cm^{-1})	478	415
pH	7.0	7.5

Table 2.2 – Electrolyte concentrations and physicochemical parameters of simulated and commercial bottled drinking water.

The mineralization reaction was also studied under simulated solar irradiation thanks to a lamp whose emission extends for *ca.* 5% in the UV region[16]. Although the photocatalytic reaction appeared much slower than under UV irradiation, a limited degree of mineralization was induced,

achieving 8.5% after 7 h of irradiation. It should be underlined that the photocatalyst was not promoted in any way to favour light absorption in the visible region and that the effective power density of the lamp was much lower than in UV tests. Hence, only the UV tail of the lamp could activate the photocatalytic properties, since anatase TiO_2, having a band gap of 3.2 eV, has an absorption edge of 386 nm.

Finally, the photocatalytic degradation of the pollutant mixture was studied using a TiO_2-immobilized system. Immobilized systems are often studied for photocatalytic purposes as devices able to be up-scaled for field applications. The removal of the photocatalyst from the treated effluent stands out as one of the most crucial, difficult and expensive operations following water treatments, above all in the case of nanomaterials. On the contrary, immobilizing the photocatalyst avoids removing the powder from the water basin, provided that a robust, stable and efficient device is developed. In our case, a homogenous and stable TiO_2 layer, prepared from the laboratory-made TiO_2 powder and a stable TiO_2 sol, was deposited on a titanium mesh (Fig. 2.2e). The mineralization curve as a function of the irradiation time during tests with the immobilized system is reported in Figure 2.2b. Despite the decrease of the surface area due to the process of immobilization, the mineralization curve shows a good photocatalytic performance (50% mineralization after 6 h), without any loss of efficiency throughout the duration of the test. The ease of preparation, applicability to a broad range of substrate types and geometries, and high activity make this immobilization method a valid alternative for field applications.

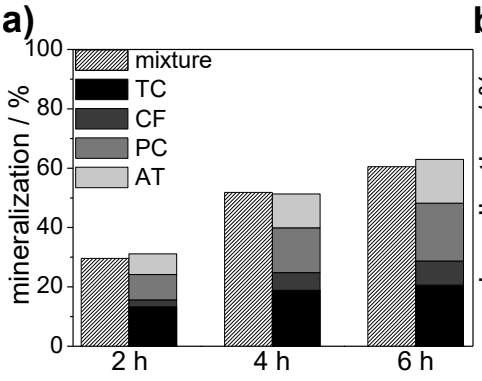

a) Mineralization degree of the tests in a mixture and that of single pollutant tests performed in ultrapure water, as a function of irradiation time.

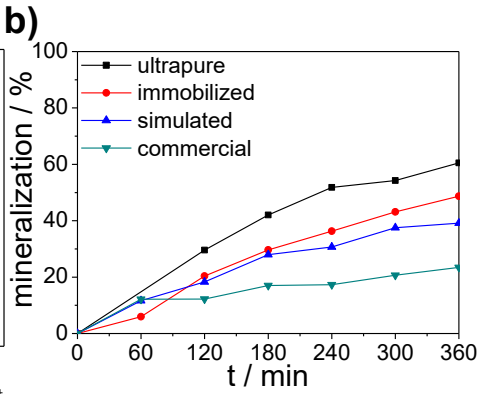

b) Mineralization rate during the pollutant mixture photocatalytic tests in the case of immobilized TiO_2 and TiO_2 slurry in ultrapure, simulated drinking and commercial bottled mineral water.

c)

		ads (%)	k (min^{-1})
TC	ultrapure	30	65 ± 3
	simulated	28	64 ± 6
PC	ultrapure	5	7.2 ± 0.1
	simulated	2	3.8 ± 0.1
CF	ultrapure	2	7.5 ± 0.8
	simulated	1	7.6 ± 0.1
AT	ultrapure	1	6.3 ± 0.5
	simulated	2	4.2 ± 0.2

c) Dark adsorption and kinetic constants, *k*, of the single pollutant degradation reactions in ultrapure and simulated drinking water matrices (C_0 = 35 mg L^{-1}; 0.5 g L^{-1} TiO_2).

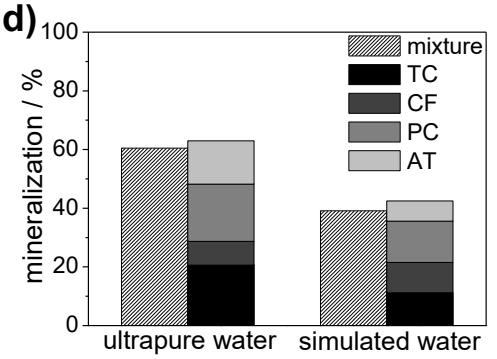

d) Comparison of the mineralization degree of the tests in mixture and that of single pollutant tests after 6 h irradiation, in ultrapure and simulated drinking water.

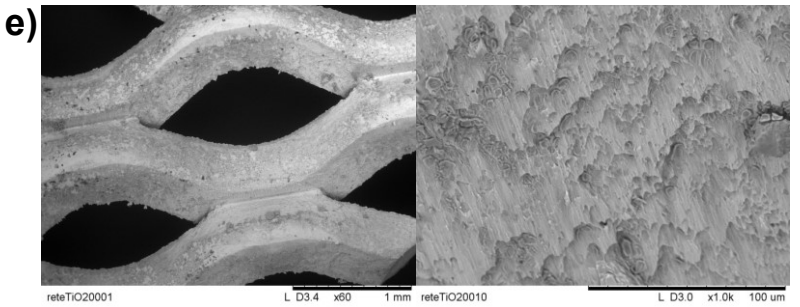

e) SEM images of the TiO_2-coated titanium mesh.

Figure 2.2 – Photocatalytic tests results in spiked waters and for the immobilized system.

2.2 Conclusions

A mixture of four emerging pollutants selected among the main contaminants found in Northern Italy surface waters, was submitted to photocatalytic treatments, both singularly and in mixture, under several different conditions. Both UV and simulated solar irradiation were employed using either nanosized TiO_2 suspensions and home-made immobilized systems. The role played by different water media was also investigated in detail.

For all compounds high degradation degrees were achieved in the case of TiO_2 slurries in ultrapure water: tetracycline removal occurred on a shorter-time scale (90% after 35 min), while paracetamol, caffeine and atenolol reached 80–90% of disappearance after 6 h with slower kinetics. Mineralization was obtained for all molecules as an evidence of complete transformation to harmless compounds. Caffeine was found to be the slowest to be mineralized, thus suggesting the production of highly recalcitrant reaction intermediates responsible for low mineralization degrees.

The degradation of the pollutants proceeded in the mixture with the same sequence observed in single molecules tests. Moreover, no lowering of the mineralization degree was observed, thus excluding the occurrence of interference or competition effects, typical of pollutant mixtures. However, it cannot be excluded that at trace or ultra-trace levels differences in the relative mineralization degrees might arise.

The degradation of a mixture of the four contaminants was also studied in a simulated drinking water matrix, by addition of selected electrolytes to ultrapure water, and in a fortified real water matrix (bottled mineral water). An inhibitory effect related to the presence of electrolytes was observed in both cases. However, the studied pollutants exhibited a different behaviour when tested singularly in the presence of electrolytes. Despite the presence of notable amounts of electrolytes with high affinity for oxide surfaces (*e.g.*, sulphates), all of the molecules showed a limited decrease in dark adsorption at the TiO_2 surface in simulated drinking water. Tests with a mineral water with comparable pH and conductivity but different electrolyte composition, seems to rule out the effect of pH and ionic strength as possible causes of the overall inhibitory effect. By comparing

the composition of the commercial and the simulated waters (Tab. 2.2), since Na^+ and Cl^- species have usually a detrimental effect on the photocatalytic activity of TiO_2 photocatalysts, the observed changes in the reaction kinetics can be mainly traced back to the presence of bicarbonates/carbonates, which are the sole electrolyte species present in a much larger amount in the commercial water than in the simulated one, and which might act as $OH^\bullet$ scavengers according to the mechanism:

$$HCO_3^- + {}^\bullet OH \rightarrow CO_3^{\bullet -} + H_2O \qquad (2.1)$$

The generated carbonate radical anions have an oxidation potential less positive than that of $^\bullet OH$ radicals. A modification of the reaction pathway of the different molecules can thus be expected in the presence of electrolytes.

Although our photocatalyst was not promoted to absorb in the visible region, tests under solar irradiation showed a slow but steady increase in time of the pollutant mineralization. This observation supports the absence of strongly adsorbing recalcitrant intermediates, which could have deactivated the surface of the photocatalyst in low irradiation conditions.

Eventually, we tested an immobilized-TiO_2 system prepared by depositing TiO_2 nanostructured particles and a TiO_2 sol on titanium meshes. This system gave rise to a 50% of mineralization of the pollutant mixture. Considering the relevant loss of surface area consequent immobilization, the device photocatalytic efficiency was high, revealing a perspective efficiency for field applications.

2.3 Specific procedures

Samples preparation. Reactants, purchased from Sigma-Aldrich, were used without further purification. Doubly distilled water obtained by a Milli-Q apparatus was used to prepare solutions and suspensions. TiO_2 nanostructured powders were prepared by a sol-gel synthesis. Water was added dropwise to a 1:1 mixture of titanium(IV) isopropoxide (TTIP) and acetic acid at 0 °C, while stirring vigorously. The water : TTIP molar ratio was fixed at 200. The as-prepared sol was aged for 24 h and successively dried at 70°C for 3 h, then 100°C overnight. Finally, the powder was calcined at 400 °C for 6 h under O_2 flux (9 NL h^{-1}).

Immobilized photocatalysts preparation. Immobilized titania system were prepared by brush casting on both sides of a titanium mesh (15 × 5 cm^2) a dispersion of the uncalcined laboratory-made TiO_2 particles in a stable sol, prepared according to a previously reported procedure, whose details can be found in Appendix A. The coated mesh was then calcined for 1.5 h at 400 °C under O_2 flux (9 NL h^{-1}). The deposition procedure was repeated twice.

Photocatalytic activity tests. The photocatalytic degradation of the studied pollutants was carried out under both UV and simulated solar irradiation in a jacketed batch reactor with a volume of 600 mL.

Photocatalytic tests were performed both on single molecules and on pollutant mixtures. Tests in different water media, besides ultrapure water, were performed: a simulated drinking water, prepared according to the Annex B2 of the Second Protocol of the French Norm NF P41-650 regarding the Specifications for Water Filter Pitchers, and a commercial bottled mineral water selected among the most diffuse Italian drinking waters.

In tests with single pollutants, two different initial concentrations were selected (C_0 = 8.75 and 35 mg L^{-1}); the TiO_2 surface area for pollutant molecule was kept constant by adopting a TiO_2 slurry concentration of 0.5 g L^{-1} for tests with high C_0 (35 mg L^{-1}) and of 0.125 g L^{-1} for tests with low C_0 (8.75 mg L^{-1}). In the case of pollutant mixtures, an initial concentration of 8.75 mg L^{-1} for each molecule and a slurry concentration of 0.5 g L^{-1} were adopted, in order to keep, in principle, the same photocatalyst surface area available for each pollutant molecule. The here adopted pollutant concentrations are well above the environmental levels; however, they were selected to allow a sound analytical approach, especially concerning the final mineralization of the pollutants.

Tests were carried out at 20 °C, using magnetic stirring and O_2 bubbling. In tests with ultrapure water, the solution pH was not corrected, being 5.5 in all cases except for the most concentrated TC solution, which had a pH of about 4 due to the nature of the salt. Before the test, the photocatalyst was pretreated with UV light for 1 h in order to promote surface hydroxylation, activation and cleaning. Then, it was dispersed in the pollutant solution and, before irradiation, the system was kept in the dark for 30 min until adsorption equilibrium was achieved. The photocatalytic

degradation was monitored for 6 h. Adsorption and photolysis kinetics were also performed.

The pollutant disappearance was monitored by UV-vis spectroscopy as well as high performance liquid chromatography (HPLC) analyses Acetonitrile (A) and phosphoric acid 0.1% (B) were used as eluents. A linear gradient elution was performed in 40 min from 90% A–10% B to 100% B. The detection of TC, CF, PC and AT was carried out by monitoring the absorption at 357, 277, 246, and 224 nm, respectively. Prior to analysis, the suspension was sampled with a syringe and filtered with a Millipore MF-membrane filter (0.45 μm-HA). In the case of the P25 photocatalyst, three subsequent filtration steps were needed to obtain a clear surnatant.

Further details about preparation and characterization methods can be found in Appendix A.

References

1 T. Heberer, *Toxicol. Lett.*, 2002, **131**, 5–17.

2 R. P. Schwarzenbach, *Science (80-.).*, 2006, **313**, 1072–1077.

3 A. B. A. Boxall, M. A. Rudd, B. W. Brooks, D. J. Caldwell, K. Choi, S. Hickmann, E. Innes, K. Ostapyk, J. P. Staveley, T. Verslycke, G. T. Ankley, K. F. Beazley, S. E. Belanger, J. P. Berninger, P. Carriquiriborde, A. Coors, P. C. DeLeo, S. D. Dyer, J. F. Ericson, F. Gagné, J. P. Giesy, T. Gouin, L. Hallstrom, M. V. Karlsson, D. G. J. Larsson, J. M. Lazorchak, F. Mastrocco, A. McLaughlin, M. E. McMaster, R. D. Meyerhoff, R. Moore, J. L. Parrott, J. R. Snape, R. Murray-Smith, M. R. Servos, P. K. Sibley, J. O. Straub, N. D. Szabo, E. Topp, G. R. Tetreault, V. L. Trudeau and G. Van Der Kraak, *Environ. Health Perspect.*, 2012, **120**, 1221–1229.

4 B. D. Blair, J. P. Crago, C. J. Hedman and R. D. Klaper, *Chemosphere*, 2013, **93**, 2116–2123.

5 E. N. Evgenidou, I. K. Konstantinou and D. A. Lambropoulou, *Sci. Total Environ.*, 2015, **505**, 905–926.

6 D. J. Lapworth, N. Baran, M. E. Stuart and R. S. Ward, *Environ. Pollut.*, 2012, **163**, 287–303.

7 T. Deblonde, C. Cossu-Leguille and P. Hartemann, *Int. J. Hyg. Environ. Health*, 2011, **214**, 442–448.

8 R. A. Palominos, M. A. Mondaca, A. Giraldo, G. Peñuela, M. Pérez-Moya and H. D. Mansilla, *Catal. Today*, 2009, **144**, 100–105.

9 X. D. Zhu, Y. J. Wang, R. J. Sun and D. M. Zhou, *Chemosphere*, 2013, **92**, 925–932.

10 F. Mazille, T. Schoettl, N. Klamerth, S. Malato and C. Pulgarin, *Water Res.*, 2010, **44**, 3029–3038.

11 R. Shen and S. A. Andrews, *Water Res.*, 2011, **45**, 944–952.

12 A. O. Kondrakov, A. N. Ignatev, F. H. Frimmel, S. Bräse, H. Horn and A. I. Revelsky, *Appl. Catal. B Environ.*, 2014, **160**–**161**, 106–114.

13 W.-K. Wang, J.-J. Chen, M. Gao, Y.-X. Huang, X. Zhang and H.-Q. Yu, *Appl. Catal. B Environ.*, 2016, **195**, 69–76.

14 S. Malato, in *Handbook of Environmental Chemistry*, Springer, Berlin, 2008, pp. 177–197.

15 L. Rimoldi, C. Ambrosi, G. Di Liberto, L. Lo Presti, M. Ceotto, C. Oliva, D. Meroni, S. Cappelli, G. Cappelletti, G. Soliveri and S. Ardizzone, *J. Phys. Chem. C*, 2015, **119**, 24104–24115.

16 A. Antonello, G. Soliveri, D. Meroni, G. Cappelletti and S. Ardizzone, *Catal. Today*, 2014, **230**, 35–40.

17 Z. Pan, E. A. Stemmler, H. J. Cho, W. Fan, L. A. LeBlanc, H. H. Patterson and A. Amirbahman, *J. Hazard. Mater.*, 2014, **279**, 17–25.

18 W. Lin, H. Zheng, P. Zhang and T. Xu, *Appl. Catal. A Gen.*, 2016, **521**, 75–82.

19 M. R. Eskandarian, H. Choi, M. Fazli and M. H. Rasoulifard, *Chem. Eng. J.*, 2016, **300**, 414–422.

20 C. Martínez, M. Canle L., M. I. Fernández, J. A. Santaballa and J. Faria, *Appl. Catal. B Environ.*, 2011, **107**, 110–118.

21 M. J. Arlos, M. M. Hatat-Fraile, R. Liang, L. M. Bragg, N. Y. Zhou, S. A. Andrews and M. R. Servos, *Water Res.*, 2016, **101**, 351–361.

22 J. Carbajo, M. Jiménez, S. Miralles, S. Malato, M. Faraldos and A. Bahamonde, *Chem. Eng. J.*, 2016, **291**, 64–73.

23 F. F. Sodré, M. A. F. Locatelli and W. F. Jardim, *Water. Air. Soil Pollut.*, 2010, **206**, 57–67.

24 L. Prieto-Rodriguez, S. Miralles-Cuevas, I. Oller, A. Agüera, G. L. Puma and S. Malato, *J. Hazard. Mater.*, 2012, **211**–**212**, 131–137.

25 X. Van Doorslaer, J. Dewulf, J. De Maerschalk, H. Van Langenhove and K. Demeestere, *Chem. Eng. J.*, 2015, **261**, 9–16.

26 N. Rioja, S. Zorita and F. J. Peñas, *Appl. Catal. B Environ.*, 2016, **180**, 330–335.

27 N. Klamerth, N. Miranda, S. Malato, A. Agüera, A. R. Fernández-Alba, M. I. Maldonado and J. M. Coronado, *Catal. Today*, 2009, **144**, 124–130.

28 T. Aarthi, P. Narahari and G. Madras, *J. Hazard. Mater.*, 2007, **149**, 725–734.

29 Agenzia Italiana del Farmaco AIFA, *Rapporto sull'uso dei farmaci antibiotici Analisi del consumo territoriale nelle regioni italiane*, 2009.

30 N. Czekalski, T. Berthold, S. Caucci, A. Egli and H. Bürgmann, *Front. Microbiol.*, 2012, **3**, 1–18.

31 E. Zuccato, D. Calamari, M. Natangelo and R. Fanelli, *Lancet*, 2000, **355**, 1789–1790.

32 I. Dalmázio, L. S. Santos, R. P. Lopes, M. N. Eberlin and R. Augusti, *Environ. Sci. Technol.*, 2005, **39**, 5982–5988.

This Chapter has been adapted with permission from Rimoldi *et al.*, *Photochem. Photobiol. Sci.*, 2017, **16**, 60−66. Published by The Royal Society of Chemistry (RSC) on behalf of the European Society for Photobiology, the European Photochemistry Association, and RSC.

Chapter 3

Impregnation *vs.* bulk synthesis: how the synthetic route affects the photocatalytic efficiency of Nb/Ta:N codoped TiO_2 nanomaterials

As already commented, titanium dioxide is one of the most studied photocatalysts in environmental remediation, owing to its stability, low cost and high activity[1,2]. However, its wide band gap (>3.0 eV) corresponds to light absorption in the UV region and prevents this material from being employed in several practical applications, including indoor usages, for which activity under solar light would be preferable. In recent years, considerable effort has been devoted to promoting the photocatalytic activity of TiO_2 under solar radiation by visible light sensitization.

Anion doping with p-block elements, such as nitrogen[3] has been widely studied in this context[4,5]. Nitrogen doping creates mid-gap states which strongly enhance visible light absorption[6–8]. However, dopants and doping-induced oxygen vacancies can also act as recombination centers and eventually reduce the lifetime of electron-hole (e^-/h^+) pairs, resulting in a neat decrease of quantum yields[9].

TiO_2 modification with transition metals (TMs) has been also proposed to produce defects beneficial for visible light harvesting. In recent years, theoretical[10] and experimental[11–14] studies have proposed niobium and tantalum as efficient dopants, thanks to the favorable location of the electronic states created by their 4d and 5d orbitals. For instance, Wang *et al.*[12] prepared Ta-doped macroporous titania photocatalysts with superior performance in the degradation of 4-nitrophenol at high Ta:Ti molar ratios.

Recently, codoping by metal and nonmetal species has attracted much attention as a possible solution to optimize light absorption while

preserving the quantum yield of titania. The simultaneous presence of electron donors (*e.g.*, a pentavalent metal like Nb or Ta) and acceptors (*e.g.*, N) might lead to charge compensation phenomena,[15] possibly beneficial to the photocatalytic activity[16–18]. The theoretical study by Zhu *et al.*[19] underlined the positive effects of compensated codoping in Nb,N- and Ta,N-copromoted titania systems, such as an increased amount of nitrogen species entering the TiO_2 lattice. However, Ta- and Ta,N-codoped TiO_2 was investigated to a lesser extent than Nb- and Nb,N-codoped[20] titania. A very recent theoretical work by Liu and coworkers[21] showed how Ta ion is promoted as a lattice guest thanks to the presence of a nonmetal species (sulfur). Obata *et al.*[22] first synthesized Ta,N-codoped films by magnetron sputtering, which showed enhanced photocatalytic activity under visible light. Furthermore, Wang *et al.*[23] demonstrated that even tri-doped Ta-N-F systems could be promising systems for visible-light applications. Based on EPR and XPS outcomes, they also found charge compensation effects and set an optimal Ta/Ti molar ratio as low as 1%. A further test of the photocatalytic activity was provided by Gong *et al.*[24] for Ta,B-codoped TiO_2, showing the beneficial effects of codoping with respect to single-doping in dye degradation tests. Consistently, other authors observed a better performance of co-promoted samples with respect to single-doped ones for photoelectrochemical water oxidation[25].

Given their proximity in the periodic table, a comparison between Nb- and Ta-containing TiO_2 nanomaterials is crucial to clarify what structure-properties relationships effectively contribute to determine a given photocatalytic performance. To the best of our knowledge, no previous experimental comparison between Nb,N- and Ta,N-codoped TiO_2 photocatalysts have been reported to date. The few works which compare Nb,N- and Ta,N-codoped titania are either theoretical[26,27] or involve single-doping strategies for electrochemical and DSSC applications[28–30].

Our approach not only combines experimental characterizations and Density Functional Theory (DFT) simulations, but also investigates the role played by the synthetic route on the final photocatalytic performance. This issue has a paramount importance, although being seldom discussed in the Literature. The synthetic procedure controls phase composition, crystallographic lattice distortions, nature and concentration of bulk defects, electronic band structure and surface properties, whose interplay

determines, *a fortiori*, crucial macroscopic properties such as the photocatalytic performance. Among other synthetic approaches, we will focus on bulk doping by classical sol-gel ('sy') routes and post-synthesis impregnation ('im'), since these two techniques are among the most frequently employed in modern catalytic applications.[31] While bulk doping generally leads to more homogeneous systems, impregnation is known to be a very effective method for the production of high performing catalysts[32].

In this Chapter, the photocatalytic performance of TiO_2 single-doped and codoped nanomaterials as a function of the doping method (either 'sy' or 'im') is compared. Niobium and tantalum were considered as TM dopants, while Nitrogen was selected as a possible nonmetal codopant. The photocatalytic efficiency was tested toward the degradation of ethanol – a pollutant model system – under UV and simulated solar light irradiation in the gas phase. The photodegradation ability of the various materials was related to their structural, morphological and electronic properties at various length scales as investigated by XRPD, BET, XPS, DRS and EPR characterizations. Experimental results were also complemented by bulk plane-wave DFT simulations. A tentative structural / electronic model was then proposed to account for the observed differences in the photocatalytic performance between the 'im' and 'sy' sample series. Eventually, implications on the suitability of the 'im' and 'sy' synthetic routes on the engineering of more efficient titania photocatalysts are discussed.

3.1 Results

3.1.1 Microstructure

Figure 3.1a shows typical recorded X-ray diffractograms, together with the corresponding least-squares fittings, for the codoped samples TTaN(im) and TTaN(sy).

As expected on the basis of the core synthetic procedure[8,15,33,34], all the materials here investigated are biphasic, with anatase TiO_2 (space group: $I4_1/amd$) being always the major polymorph in the mixture and brookite (space group: *Pbca*) the minority one. When the two 'im' and 'sy' sample series are compared (Fig. 3.1b), their trends as a function of the dopant are

qualitatively similar. Nevertheless, 'im' materials invariably bear a higher brookite content, while the 'sy' ones are richer in anatase and, in general, more similar to the undoped T reference.

On average, the brookite content turns out to be as high as 43±2% in impregnated specimens and 36±2% in the sol-gel ones. Interestingly, Nb,N-codoping seems to somewhat (weakly) favour the anatase phase with respect to single-doped powders[15], while the contemporary presence of Ta and N in the lattice has just the opposite effect. This holds true no matter the dopant feeding method, even though changes in the brookite content are more evident in the 'sy' nanostructured powders.

Also for what concerns the crystallite dimensions of the anatase phase (Fig. 1.1c), the 'im' samples are associated with a bit larger $<D_V>$ values (34±2 Å) than the 'sy' ones (31±1 Å). However, there are neither striking nor systematic deviations with respect to the reference T material and differences in $<D_V>$ between the two series are scarcely significant from a statistical viewpoint. This is even more true when the Williamson-Hall microstrain ε is taken into account (Fig. 3.1c). Rather, 'sy' and 'im' samples always bear very similar ε values and just a tendency toward higher lattice strain in codoped samples, no matter the doping strategy, could be inferred from Figure 3.1c. In turn, this likely implies that both Nb- and Ta-based doping somewhat increase the average concentration of defects in the nanomaterials here studied. It should be also noted that Ta-containing materials invariably bear higher Williamson-Hall microstrain parameters than the Nb-containing ones. This could be likely related to the longer ionic radius of tantalum, which implies greater lattice distortions.

In general, microstructural results for Nb- and Nb,N-(co)doped anatase are similar to previous investigations on similar materials[15], as the presence of both dopants discourages the brookite formation and leads to smaller anatase crystallites. Probably, such a behavior can be traced back to the strong thermodynamic driving force toward the $I4_1/amd$ phase, which results in smaller critical radii of the crystal nuclei and speeds up nucleation over the growth process[35]. However, this is no longer true when Tantalum is considered: Ta,N-codoping is associated with larger anatase crystallites and invariably imply a ≈ + 5 % increment in the brookite content (Fig. 3.1b,c). Assuming the validity of the simple nucleation model above sketched, such a difference might be due to a lower ability of the tetragonal

lattice in hosting the larger Ta^{5+} ions (for the sake of comparison, ionic radii of Ti^{4+}, Nb^{5+} and Ta^{5+} in 6-fold coordination[36] are 0.605 Å, 0.640 Å and 0.780 Å).

More quantitative information on the amount of distortion to which the crystallographic long-range structure is subject upon doping can be obtained by following the changes of the anatase cell edges as a function of the dopant (Fig. 3.1d).

At the quite low nominal dopant concentration here employed, the relative changes of the crystallographic anatase cell edges are generally immaterial in terms of their estimated standard deviations. More in details, both the **c** and the symmetry-equivalent **a**,**b** cell edges have length equal to those shown by the reference sample T within ± 0.1%. The two codoped impregnated TNbN(im) and TTaN(im) samples are the only patent outliers, as they show a significant lengthening (up to ≈ + 0.3 %) of the |**c**| vector module with respect to the reference compound.

In conclusion, the following take-home messages can be derived by our microstructural XRD analysis. First, the dopant feeding strategy mainly affects the phase composition, with 'im' materials showing a higher brookite content than the 'sy' ones. Second, other average microstructural parameters such as crystallite dimensions and microstrain, are very similar between the two sample series, with the 'im' one possibly showing a small tendency toward larger $<D_v>$. Moreover, Ta-containing materials show higher microstrain, ε, than Nb-containing ones. Third, the crystallographic lattice parameters are scarcely affected by the dopant nature and the synthetic route, with the only exception of impregnated codoped materials, which undergo a ≈ +0.2, 0.3 % increment of the cell along the unique axis. In general, structural distortions and compositional differences are enhanced by both Nb,N- and Ta,N-codoping, no matter how the dopants are added to the material, a fact that mirrors metal/non-metal synergic effects already detected in previous works on similar systems[15].

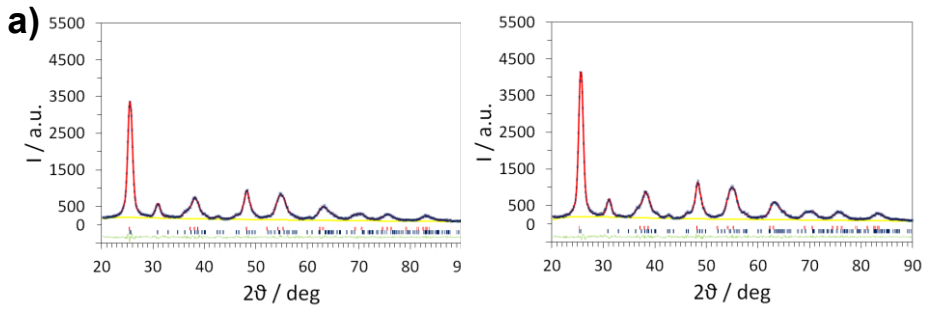

a) Collected XRPD patterns of the TTaN(sy) (left) and TTaN(im) (right) samples. The least-squares fitting curves are in red, the $y_{obs} - y_{calc}$ point-by-point differences in green and the refined background function in yellow. The diffractions for the anatase and brookite phases are shown as red and blue markers, respectively.

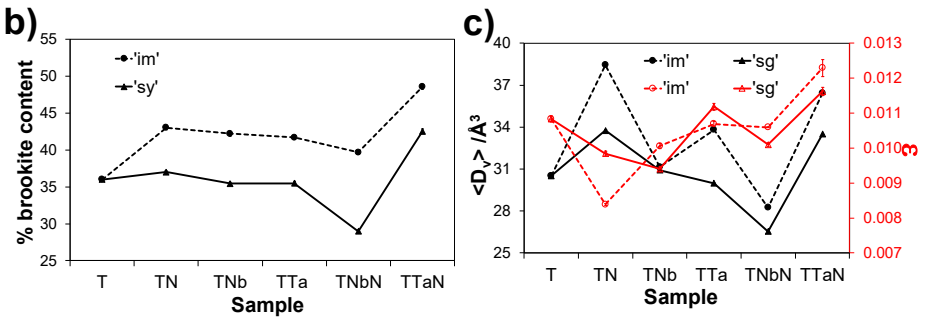

b) Brookite content for the 'im' and 'sy' samples, as estimated from the Rietveld refinement against the XRPD data.

c) Average crystallite dimensions of anatase (<D_γ>, black) and lattice microstrain values (ε, red).

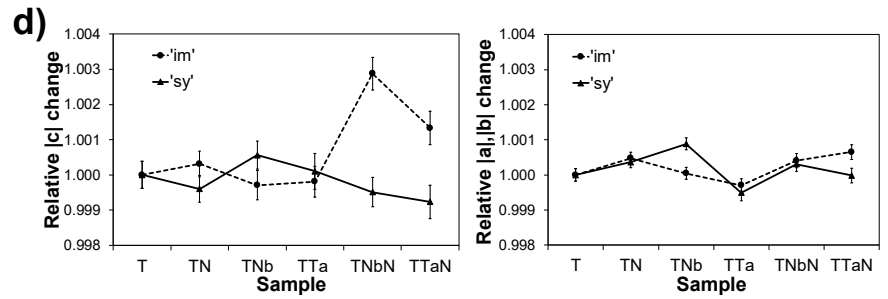

d) Relative changes of the |c| (left) and |a|,|b| (right) anatase cell axis modules of the 'im' and 'sy' sample series with respect to the reference material T.

Figure 3.1 – Microstructure analysis results.

3.1.2 Morphological features

The adsorption-desorption isotherms of N_2 in subcritical conditions of single- and codoped samples are reported in Figure 3.2a. All the samples show hysteresis loops characteristic of a mesoporosity. The two doping approaches have markedly different effects on the morphological features of the resulting materials (Fig. 3.2a).

As for 'sy' materials, both doped and codoped samples generally show lower surface areas, together with a relevant decrease of the total pore volume (Tab. 3.1 and Fig. 3.2b), with respect to the reference T. Furthermore, the presence of either Nb or Ta species induces a shift of the hysteresis loop to lower pressures (Fig. 3.2a), indicating a decrease in the average pore size. The shape of the hysteresis loop is also modified upon metal doping, becoming more typical of H2-type (bottleneck shape). On the contrary, N-doping has an almost negligible effect on the morphological features of TiO_2, in agreement with previous reports[15].

Sample	S_{BET} ($m^2\ g^{-1}$)	V_{pores} ($mL\ g^{-1}$)	D_{BET} (nm)	E_g (eV)
T	149	0.277	10.2	3.23
Bulk synthesis				
TN(sy)	132	0.291	11.6	3.18
TNb(sy)	119	0.166	12.8	3.09
TNbN(sy)	161	0.223	9.5	3.13
TTa(sy)	135	0.187	11.3	3.16
TTaN(sy)	111	0.169	13.8	3.09
Impregnation				
TN(im)	165	0.390	9.3	3.22
TNb(im)	133	0.328	11.5	3.22
TNbN(im)	150	0.268	10.2	3.22
TTa(im)	124	0.281	12.3	3.24
TTaN(im)	123	0.325	12.4	3.23

Table 3.1 - Specific surface area (S_{BET}), total pore volume (V_{pores}), average grain diameter calculated from S_{BET} values (D_{BET}) and band-gap value (E_g) for the doped and undoped samples of the two series.

The presence of both dopants has a different effect with respect to both single dopant. N,Nb-codoping results in an appreciable increase in surface area while the total pore volume remains unchanged, a fact that might be related to the smaller crystallites and smaller pores (Fig. 3.2b). N,Ta-codoping gives rise instead to a decrease of the surface area, which may be traced back to the larger average pore size and bigger crystallites.

With respect to bulk doping, the impregnation method leads to higher total pore volumes and to larger average pore sizes (Fig. 3.2b), although no clear trends can be appreciated by comparing the specific surface areas of the samples obtained by the two doping approaches. Furthermore, impregnation does not give rise to appreciable effects on the shape of the hysteresis loop of the adsorption/desorption isotherms (Fig. 3.2a). 'im' samples doped with Nb and Ta have lower surface areas with respect to the undoped reference but have a higher total pore volume and larger pores, as appreciable from the shift of the hysteresis loop to higher pressures. Finally, the addition of nitrogen, both in single- and codoped samples, seems to increase the surface area.

A roughly inverse correlation between the surface area (S_{BET}) and the average crystallite size ($<D_v>$) obtained by XRPD refinements can be envisaged. The only exception is the sample TN(im), which presents a large surface area together with the largest crystallite size. However, this specimen also bears the largest total pore volume (0.390 mL g^{-1}), which determines a significant increment of the corresponding surface area.

According to the following equation[37]

$$S_{BET} = \frac{6\times10^4}{\rho\times D_{BET}} \qquad (3.1)$$

the BET surface area can be written as the total surface area of the powder population divided by the powder mass, where ρ is the density of the sample (3.9 g cm^{-3}, as calculated by XRPD results for the anatase phase). The factor 6 applies for spherical as well as for cubic particles. D_{BET} (Tab. 3.1) could be therefore taken as a rough estimate of the average particle size in the assumption that both porosity and surface roughness are negligible. It can be observed that for all samples the D_{BET} value is larger than the crystallite data obtained from X-ray elaboration (Fig. 3.1c), possibly indicating the occurrence of aggregation phenomena among the crystallites.

3.1.3 Electronic structure

The left part of Figure 3.2c reports the electronic density of states (DOSs) of TM single-doped TiO_2. Both substitutional and interstitial Ta-doping lead to quite different DOSs. In the case of substitutional doping, the Fermi

energy of the system lies at the bottom of the conduction band and the 5d states of the dopant are located deep into the conduction band. This opens the possibility for enhanced UV absorption. Instead, when Ta is located interstitially, mid-gap states are injected into the band gap roughly at the bottom of the conduction band, as shown by the Ta 5d projected DOS. Considering that the Fermi energy is in both cases just below the conduction band, we can deduce that Ta acts in any case as an electron-donor. Taking into account that titania is highly defective[38–40], we simulated oxygen defective and Ta-doped supercells. Clearly, the vacancies act as electron donors and the Fermi energy is pinned at the bottom of the conduction band. A comparison between these four panels shows that the Ta orbital location is left unchanged upon oxygen vacancy generation.

To better rationalize the experimental results, we report on the two lower panels (Fig. 3.2c) the DOSs relative to oxygen defective Nb substitutional and interstitial doping. In the case of Nb dopant, Nb 4d orbitals act as electron donors as Ta 5d ones, but Nb states are just below the conduction band and potentially available for visible light excitation.

We have reported for sake of documentation both substitutional and interstitial TMs doping. However, in the present case only substitutional doping is considered plausible.[15] DFT+U calculations show that both Nb[15,38] and Ta are preferentially accommodated in substitutional Ti sites. The possibility for an interstitial TMs doping site was excluded by comparing the crystallographic strains obtained by the XRD refinements and the DFT+U simulations results.

Finally, the codoping scenarios to complete the description of the experimental samples are presented in the right part of Figure 3.2c. To avoid rare configurations, we placed the TM doping site away from the nitrogen one[15]. We have considered all possible substitutional and interstitial codoping combinations, even though, as stated above, the TM interstitial location is quite improbable. Figure 3.2c shows an electron transfer from the 5d Ta electronic states to the partially empty N orbitals located above the valence band, as it was reported also for the 4d Nb states[15]. This electron transfer closes the electronic shell and shifts the Fermi energy toward mid-gap values. The occurrence of this phenomenon is confirmed by EPR experiments. Clearly, this charge compensation effect

generates extra stability for the doping process and possibly enhances the photocatalytic performances.

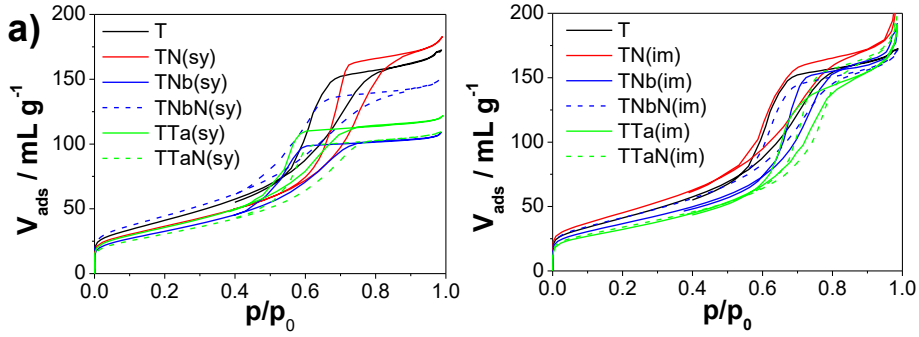

a) Adsorption–desorption N_2 isotherms in subcritical conditions of the bulk doped (left) and the impregnated samples (right), with respect to the reference material T.

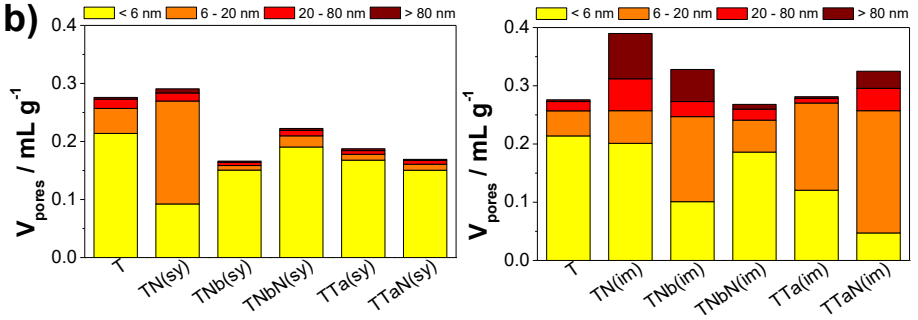

b) Pore size distribution of the bulk doped (left) and impregnated (right) samples.

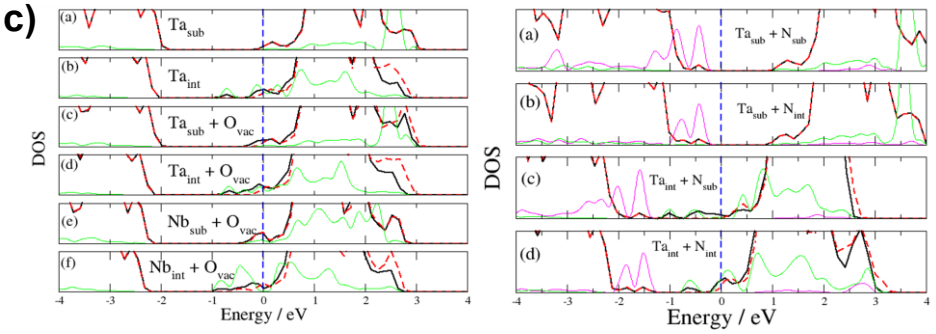

c) Total spin-up (black continuous line) and spin-down (dashed red lines) DOSs, together with TM (green lines) and N (pink lines) PDOS, for doped (left) and codoped (right) systems.

Figure 3.2 – Morphological characterization and DFT simulation results.

3.1.4 Visible absorption properties

DRS results of single-doped and codoped samples provide direct insight into the mutual role of the guest species in modifying the photoabsorption properties of TiO_2.

The undoped reference T has the characteristic absorption behavior of anatase TiO_2, showing a band gap value of 3.2 eV. Bulk doping with either N or metal species (Fig. 3.3a) gives rise to both an absorption in the UV region and to a visible sensitization of TiO_2. N-doping causes a visible light absorption at 450−500 nm, in agreement with previous reports about TiO_2 doped with ammonia salts[7,15,18]. Such a localized visible light absorption can be traced back, on the grounds of DFT calculations, to the formation of shallow intragap states located above the valence band of TiO_2[33,41]. Bulk doping with either Nb or Ta leads instead to a red shift of the absorption edge, which is comparable for both samples and results in a reduction of the observed band gap of about 0.1 eV (Tab. 3.1)[42]. Similar red shift effects have previously been reported for Nb-doped TiO_2[15,18,43,44] and can be attributed to the formation of donor levels located close to the conduction band of TiO_2[15,19]. With respect to Nb-doping, the Ta-doped sample shows also a broader absorption in the blue-green region, which can be attributed to the presence of the 5d state localized into the conduction band. Interestingly, codoped samples display the characteristic features of the absorption spectra of both N- and Nb/Ta-doped samples. As reported previously[15], N,Nb-codoping enhances the visible absorption at 450 nm with respect to nitrogen single-doped samples. Such an effect is even more marked in the case of the N,Ta-codoped sample. Theoretical calculations[19] have shown that transition metals (Nb, Ta) might facilitate the insertion of p-type dopants (N and C) in the TiO_2 lattice. Therefore, the observed enhanced visible absorption at 450 nm might be related to a higher amount of N entering the TiO_2 lattice in codoped samples.

The adopted doping strategy remarkably affects the optical properties of the resulting materials. DRS experiments show that impregnation with TMs (Nb, Ta) does not give rise to appreciable effects on the absorption features of TiO_2 (Fig. 3.3a). In particular, no shifts of the absorption edge are observed upon either Nb- or Ta-doping with respect to the undoped reference. On the contrary, impregnated N atoms lead to a visible light

absorption around 450 nm, which is fully comparable to what it is observed for bulk doped samples. It is noteworthy that impregnated codoped samples do not shift the absorption edge and the visible absorption localized around 450 nm has a lower intensity with respect to the N-doped sample.

3.1.5 Photocatalytic activity

The photocatalytic activity of the doped and codoped samples was tested toward the gas phase degradation of ethanol as a model volatile organic compound (VOC). Ethanol and its main degradation intermediate, acetaldehyde, are indeed important atmospheric and indoor pollutants[45–48]. During photocatalytic tests, the concentrations of ethanol, acetaldehyde, and of the product of complete mineralization (CO_2) were monitored by a gas-chromatographic system. Besides acetaldehyde, no other intermediate compounds were determined due to the difficulty in quantifying trace amounts. The carbon balance was always complete at the end of the reaction. Photocatalytic tests were carried out under both UV and simulated solar light irradiation. The emission spectrum of the UV lamp contains small visible tails, but these are not expected to significantly contribute to the generation of e^-/h+ pairs with respect to the main UV peaks. Actually, the latter are able to dig electrons from deeper valence states, while the visible tail might involve at most near-edge regions, where the density of states is much lower. On the contrary, the solar lamp contains an UV component analogously to the natural solar emission spectrum. Photolysis tests under both irradiation sources showed negligible ethanol degradation.

Ethanol degradation was completed for all samples within 120 min of UV irradiation. Acetaldehyde showed the typical bell-shaped curve of a reaction intermediate and a significant degree of mineralization was obtained for all samples. Figure 3.3b compares the CO_2 formation for the bulk doped and impregnated samples under UV irradiation. Bulk doping with either Nb or Ta has a clear detrimental effect on the TiO_2 photocatalytic behavior. Conversely, nitrogen bulk doping gives rise to a very limited enhancement of the photocatalytic activity with respect to undoped TiO_2. Interestingly, codoping with nitrogen significantly improves the performance of Nb- and Ta-doped materials, although they still remain less active than the nitrogen single-doped sample. Impregnated samples largely outperform their bulk doped counterparts under UV light.

All impregnated samples are indeed more active than the undoped reference and give rise to complete mineralization of the pollutant in less than 120 min, with the only exception of TNb(im) whose photocatalytic activity is comparable to that of the undoped reference. The most active sample is TTa(im), followed by TN(im), TTaN(im), TNbN(im) and TNb(im). Table 3.2 reports the initial rates of ethanol degradation under UV light determined using the method of initial decay[7], and the CO_2 percentage after 60 min reaction time. The initial rates of ethanol degradation show the same trends in photocatalytic activity than the CO_2 formation percentage, although mineralization trends are, as expected, more evident.

sample	UV $k_{p.f.o.}$ (min^{-1})	UV %CO_2 (t = 60 min)	Solar $k_{p.f.o}$ (min^{-1})	Solar %CO_2 (t = 210 min)
T	0.053	37.7	0.0032	0.6
TN(sy)	0.057	47.6	0.0031	1.1
TNb(sy)	0.039	14.8	0.0051	2.5
TNbN(sy)	0.056	44.4	0.0057	2.6
TTa(sy)	0.052	23.2	0.0009	0.3
TTaN(sy)	0.052	36.5	0.0007	0.3
TN(im)	0.060	80.6	0.0020	0.0
TNb(im)	0.051	37.9	0.0032	0.9
TNbN(im)	0.063	54.6	0.0023	0.7
TTa(im)	0.060	88.5	0.0018	0.5
TTaN(im)	0.066	74.6	0.0009	0.2

Table 3.2 – Pseudo-first order kinetic constants ($k_{p.f.o.}$) and percentage of mineralization (%CO_2) in UV and simulated solar tests for all samples.

The scenario is quite different for simulated solar tests. For all samples, ethanol degradation was not completed under simulated solar irradiation during the reaction time (Fig. 3.3c) and mineralization percentages were extremely low (Tab. 3.2). Acetaldehyde was the main reaction product for all the tested samples. Fig. 3.3c reports the ethanol disappearance curves for bulk doped and impregnated samples under simulated solar irradiation. As for the UV light tests, nitrogen bulk doped TiO_2 has a behavior similar

to the undoped reference, while Ta-doping plays a detrimental role on the TiO_2 photocatalytic activity. On the contrary, Nb-doped and codoped samples exhibit an enhanced photocatalytic performance with respect to the reference, with the codoped sample being the most active. These results are in agreement with the electronic structure calculations in Figure 3.2c and also with previous reports[17], showing improved photocatalytic activity of Nb,N-codoped samples under visible-light irradiation.

Strikingly, all the impregnated samples are less active than the undoped reference (Fig. 3.3c), with the only exception of TNb(im) which still presents a comparable behavior with respect to the undoped TiO_2. It is noteworthy that Ta-doped and codoped samples are the least active under solar irradiation.

To fully rationalize the above highlighted results is important to investigate the amount of paramagnetic defects in our samples. A tentative model to understand the behavior of the materials here investigated under photoactivity tests is given in the Discussion section below.

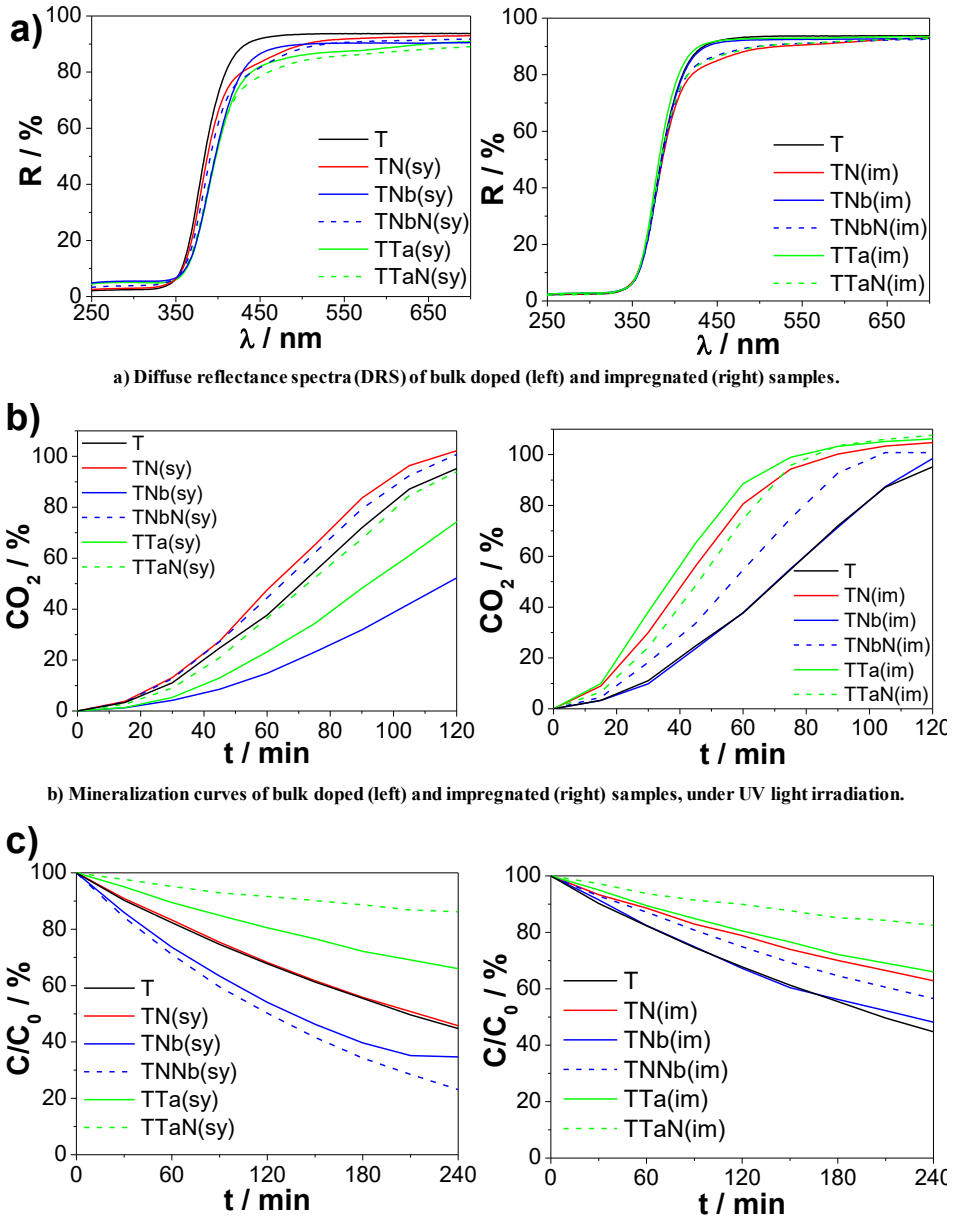

a) Diffuse reflectance spectra (DRS) of bulk doped (left) and impregnated (right) samples.

b) Mineralization curves of bulk doped (left) and impregnated (right) samples, under UV light irradiation.

c) Ethanol disappearance curves of bulk doped (left) and impregnated (right) samples, under simulated solar light irradiation.

Figure 3.3 – Optical characterization and photocatalytic tests results.

3.1.6 EPR analyses

Several paramagnetic features, introduced by the dopants, can be appreciated in EPR spectra obtained at 77 K. The features A and B can be

related to paramagnetic radical oxygen species, while the lines C, D and E to Ti^{3+} in different environments. Line F can be attributed to F^+ paramagnetic defects.

TN(sy) and TN(im) have the same chemical nominal composition and indeed show the same EPR features. However, the same lines have different intensities in the two EPR spectra. Specifically, we can compare the intensity ratio, *R*, between the most intense $N^{\bullet}_b$ (star-labeled) line and that of B, which is the most intense line due to oxygen radical species. This ratio is very different for the two spectra, being $R(\text{TN(sy)}) \cong 0.44$ and $R(\text{TN(im)}) \cong 2.1$. Furthermore, the E line attributed to Ti^{3+} is observed only in the case of TN(sy) but not in the case of N(im). The two adopted doping procedures apparently give rise to a different balance between paramagnetic defects.

The role played by the metal (Nb, Ta) in modifying N-induced defects can be now examined, starting from the codoped samples obtained by impregnation.

Only oxygen radicals as well as F^+ and Ti^{3+} species (except for the one producing the E line) are appreciable in the TNbN(im) codoped sample (Fig. 3.4a). Several authors reported the occurrence of bulk Ti^{3+} species also in Nb-doped TiO_2[15,43,44], whose formation was attributed to a mechanism of valence induction[17,19].

The disappearance of $N_b^{\bullet}$ paramagnetic species in the TNbN(im) sample supports the occurrence of charge compensation phenomena between Nb (acting as an electron donor) and N (acting as an electron acceptor), as already reported elsewhere[15,19].

In the case, instead, of TTaN(im), the compensation mechanism is not as complete as for sample TNbN(im), since low intensity $N_b^{\bullet}$ lines add to the F^+ and Ti^{3+} paramagnetic species in the spectrum (Fig. 3.4a). The intensity ratio *R* pertaining to TTaN(im) is about 0.21, to be compared with $R \cong 0$ for N,Nb-codoped, impregnated sample.

In the case of the codoped samples obtained by bulk synthesis (sy) the compensation effects are less significant than for the impregnated samples (Fig. 3.4b). As for TNbN(sy), the only relevant effect due to the presence of the metal is the disappearance of the E line attributed to Ti^{3+} species, while no other significant difference can be appreciated. The *R* value is around 0.47.

The picture is slightly different in the case of TTaN(sy). The R(TTaN(sy)) ≅ 0.25 ratio is almost half with respect to the value of TN(sy) and suggests that the presence of Ta in the synthesis modifies the balance between $N_b^{\bullet}$ and of the oxygen-based radical species.

3.2 Discussion

XPS results are affected by a large noise, possibly due to the low amount of the provided dopants. However, as a general trend, XPS results point out that 'im' samples invariably bear an apparent higher amount of dopants with respect to the 'sy' ones, as reported in Table 3.3.

	'im'	**'sy'**
TNb	0.14	0.03
TTa	0.06	0.01
TNbN	0.05	0.01
TTaN	0.02	0.01

Table 3.3 – Apparent concentrations of transition metal (TM) dopants within the 'im' and 'sy' nanostructured powders, as retrieved from the area ratios of the Nb/Ti and Ta/Ti XPS peaks and expressed as TM/Ti atomic ratios.

This was quite an unexpected result, as the reaction mixtures were always fed with the same amount of precursor reagents within the experimental error. The two sample series were calcined under identical thermodynamic control conditions and non-volatile TM species should have been granted the same chances of entering the nanoparticles. Besides, no evidences of segregated Nb- and Ta-based phases were found by the XRD analysis. To explain the detected differences (Tab. 3.3), we hypothesize that 'im' samples are less homogeneous than the 'sy' ones. Actually, it is reasonable to assume that the distribution of point defects differs depending on the adopted doping procedure. In the 'sy' case, guest ions are supplied when the TiO_2 crystalline phase is growing, and it is probable that they spread out quite uniformly throughout most of the anatase lattice structure[15]. On the contrary, in 'im' materials the dopants are supplied after the bulk phases are formed and prior to the calcination step. With this procedure, the dopants must first diffuse through grain pores

and interstitial voids to enter the crystallites. This diffusion needs to occur when the amorphous-to-crystalline transition is taking place. Consequently, a radial concentration gradient is set up within large aggregates of crystallites (grains), and the extrinsic impurities are more concentrated within crystallites near the boundaries and less at the core of each grain (Fig. 3.4c). This defect modeling could explain the differences that we have detected in the XPS signals (Tab. 3.3). Indeed, higher concentrations of dopants in crystallites at the grain surface produce more intense signals, as less photoelectrons are available from inner crystallites. Actually, photoelectrons generated from regions buried in depth within the grain have a higher probability of being inelastically scattered prior to escaping from the surface.

In Fig. 3.4d, the two sample series show very different trends. For the 'im' materials, the ratio among paramagnetic defects is high in TN and then undergoes an abrupt reduction when metal species are also present, while the apparent band gap is invariant. Quantum mechanical calculations show that a reduction of the band gap is mostly associated with shallow mid-gap states created by oxygen vacancies[8]. Otherwise, E_g is expected to undergo a slight reduction in N (and TM,N co-) doped samples, as occupied valence N states lie just at the valence band edge[15].

Combined EPR, DRS and DFT results provide compelling evidence that the 'im' method does not change the concentration of host defects, *i.e.* the denominator in the $[N_b^\bullet]/[O^\bullet]$ ratio. The abrupt reduction of this ratio (Fig. 3.4d, circles) can be explained by the reduction of the amount of paramagnetic $N_b^\bullet$ species, that in turn can be related to the occurrence of an internal electron transfer[15] from TM to N. When considering the 'sy' samples, we observe a very different behavior (Fig. 3.4d, triangles). First, the $[N_b^\bullet]/[O^\bullet]$ ratio is always low and constant, while E_g is systematically smaller than those of 'im' materials. This latter evidence suggests that in these cases the concentration of host defects is always higher. This is also in accordance with the increased absorption efficiency detected for these powders in the visible range.

We can now tentatively interpret these experimental results at the light of the measured photocatalytic activity of the two 'im' and 'sy' sample series. Under UV irradiation, 'im' samples perform better than 'sy' ones, with Ta-doped powders being significantly more efficient than the Nb-

doped ones. The first observation can be explained by invoking the anisotropic guest defect distribution at the mesoscale we have hypothesized, as near-surface crystallites should bear a higher amount of extrinsic guest species and are therefore expected to be more efficient in light harvesting. Also, the higher UV activity of Ta-doped specimens, can be traced back to the electronic states injected by Ta ions within the conduction band, since these orbitals improve the probability to allocate the photoexcited carries.

When subjected to simulated solar light irradiation, 'sy' Nb,N-codoped and Nb-doped materials are the most active ones, while *all* the impregnated samples are even less performing than the undoped reference T. It should be remarked that the spectrum of the solar lamp mostly bears longer-wavelength components, which penetrate more deeply than shorter UV ones. Therefore, it is reasonable that larger portions of the grains are involved in the process of creating photogenerated carriers. Consequently, differences in the defect distributions at the mesoscale (Fig. 3.4c) are expected to be less important and the electronic structure, as resulting from the cooperative interplay between guest and host defects, becomes determinant. In general, the less defective 'im' samples do not exploit any enhancement of the photocatalytic activity with respect to the T reference. Instead, the 'sy' materials, which contain a higher amount of paramagnetic host defects, do enhance the photocatalytic activity. This implies that a strict correlation exists, as expected, between such defects and the visible-light activity of the photocatalyst. At the same time, the synergic role of Nb and N codopants[15] is confirmed, as the TNbN material is absolutely the best performing one. Also, 'sy' Ta-doping performs worse than Nb-doping possibly because of kinetic effects. More specifically, an increased charge recombination is likely to occur since larger Ta^{5+} ions induce a bit higher lattice strain than the corresponding Nb^{5+}-containing materials, *i.e.* more lattice defects are present in Ta-doped systems. A too high defect concentration is detrimental to photocatalysis, as it favors recombination of the charge carriers.[5] It is also worth noting that the worst performing TTaN specimen is associated with the highest ε and to the lowest E_g estimates.

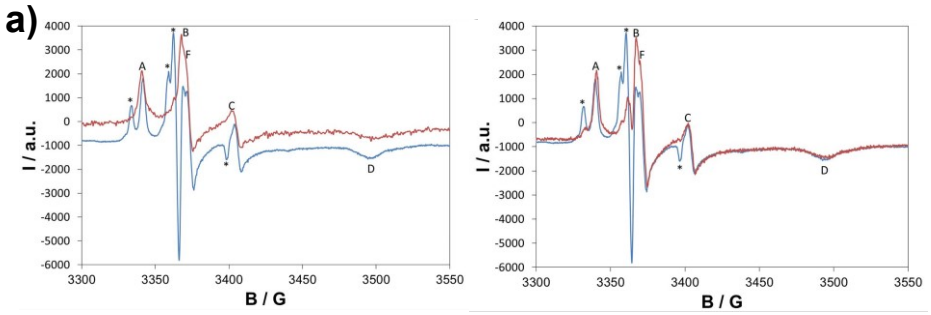

a) Experimental EPR spectra collected at 77 K of TNbN(im) (left, red curve) and TTaN(im) (right, red curve) with respect to TN(im) (blue curves).

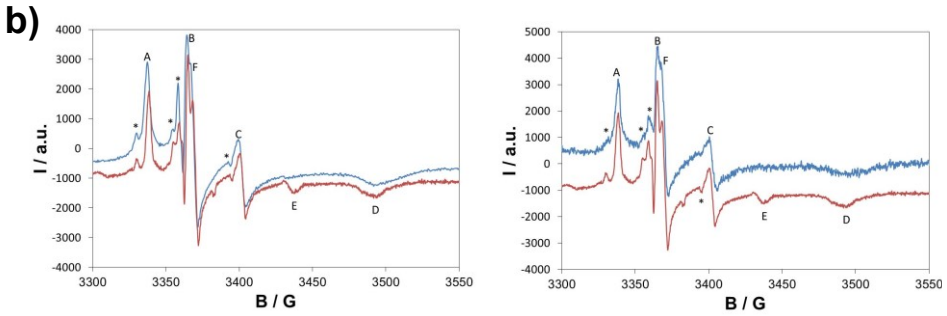

b) Experimental EPR spectra collected at 77 K of TNbN(sy) (left, blue curve) and TTaN(sy) (right, blue curve) with respect to TN(sy) (red curves).

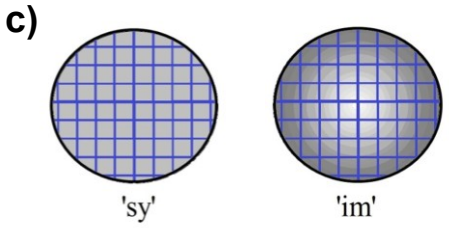

c) Sketch of the mesoscale defect model proposed to explain compositional differences detected by XPS spectroscopy. The ellipsoids represent TiO_2 grains, blue boxes differently oriented crystallites and darker regions imply a higher concentration of extrinsic defects.

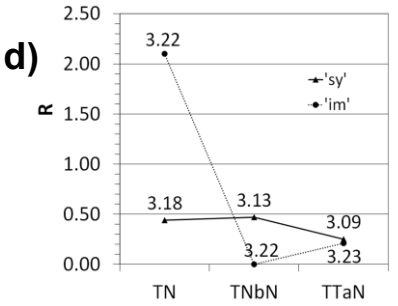

d) EPR-derived $[N_b\bullet]/[O\bullet]$ ratios R for "im" and "sy" TN, TNbN, and TTaN materials. The band gap width in eV, estinmated by the Kubelka−Munk elaboration, is also shown.

Figure 3.4 – Defectivity properties of the samples, as a function of the preparation method.

3.3 Conclusion

In this work, a thorough multi-disciplinary experimental (XRPD, BET, XPS, DRS, EPR) and theoretical (plane-wave DFT) study was undertaken on both single-doped and codoped TM,N (TM = Nb, Ta) nanostructured

TiO_2 materials. The photocatalytic performances of the synthesized powders were tested towards the gas phase degradation of ethanol under both UV and simulated solar light irradiation. This work mainly focused on relating the efficiency of the photocatalytic process to the synthetic route employed to feed titania nanocrystals with guest species, *i.e.* impregnation ('im') *vs.* bulk synthesis ('sy').

We found that the main absorption features of the 'im' samples are unchanged with respect to the undoped TiO_2 reference, whereas the 'sy' ones show a significant apparent reduction of the band gap. Accordingly, upon solar light irradiation 'sy' materials are the most active ones, while *all* the 'im' samples performing worse than the undoped TiO_2 reference. These differences can be understood on the grounds of the different amount of host defects within the two sample series. 'sy' materials are more defective and the lattice microstrain of Ta-containing nanoparticles are always higher than the corresponding Nb-containing ones. In other words, the macroscopic photocatalytic activity in this energy range is mainly correlated with the presence of host defects. The more defective Ta-doped materials show worse performances due to a higher likelihood of charge recombination.

Under UV irradiation, the picture is very different. Here 'im' samples perform better than 'sy' ones, with Ta-doped powders being significantly more efficient than the Nb-doped ones. To account for this reversed behavior, we developed an anisotropic defect distribution model at the mesoscale. In few words, we observe that in 'im' powders the crystallites near the grain surface bear a higher amount of guest species. Therefore, they are more efficient in light harvesting. Ta-doped specimens, on the other hand, degrade ethanol more efficiently than Nb-doped ones as guest Ta ions inject 5d-like states within the TiO_2 conduction band, enhancing the number of e^-/h^+ pairs available to promote redox reactions at the grain surface.

As a possible take-home message, we would like to point out that fine details of the selected synthetic procedure, such as just the moment when the guest species are provided to the reaction mixture, might have a dramatic effect on several crucial macroscopic properties of the resulting material. A thoughtful selection of the doping strategy should allow one to control the photocatalytic response even without changing nature and

amount of the extrinsic dopants. In turn, this could help in developing novel strategies to engineer nanomaterials for tailored applications.

3.4 Specific procedures

Samples preparation. Two series of titania samples were synthesized, differing in the doping procedure: either addition during the sol-gel synthesis ('sy') or impregnation ('im'). Each series consisted of five samples: N-doped (TN), Nb-doped (TNb), Ta-doped (TTa), Nb,N-codoped (TNbN) and Ta,N-codoped (TTaN) TiO_2. The nominal dopant/Ti molar ratio was fixed at 1%. Solutions of NH_4OH, $NbCl_5$ and $TaCl_5$ were employed as dopant precursors. For the TNbN specimens, the two dopants were provided at the same time by $NH_4[NbO(C_2O_4)_2(H_2O)]\cdot nH_2O$, whereas NH_4Cl and $TaCl_5$ were employed as precursors for the TTaN samples. '(sy)' or '(im)' symbols are added to the various sample labels to specify whether each specific material was respectively obtained either from the 'sy' or the 'im' procedure. An undoped titania sample (T) was also synthesized as a reference for both series.

The same sol-gel procedure was employed throughout as the basic synthetic route. More in detail, 0.063 mol of titanium(IV) isopropoxide was mixed with 24 mL of 2-propanol in order to obtain a molar ratio of 1:5. The solution was stirred for 10 min at 300 rpm. Then, 113 mL of a HCl aqueous solution at pH 3 was added drop-wise while stirring vigorously to obtain a final Ti/H_2O molar ratio of 1:100. The mixture was stirred continuously for 90 min to complete the hydrolysis. Then, the solvent was removed drying in oven at 80 °C.

The first series ('sy') of samples was prepared by adding the dopant precursors directly during the sol-gel synthesis in the 2-propanol solution. A NH_4OH solution was mixed to the aqueous solution for the preparation of the N-doped (TN(sy)) sample. The powders were then dried in oven at 80 °C and calcined at 400 °C for 6 h in O_2 flux (9 NL h^{-1}).

The second series ('im') of photocatalysts was prepared by suspending 1.5 g of the uncalcined powder in 15 mL of an ethanol:water (2:1) solution (or 15 mL of an aqueous solution for the TN(im) sample) containing the dopant precursors. After 90 min, the material was dried in oven at 90 °C and calcined at 400 °C for 6 h in O_2 flux (9 NL h^{-1}).

Photocatalytic activity tests. All samples were tested under both UV and simulated solar irradiation in the gas phase photocatalytic degradation of ethanol, as a pollutant model for volatile organic compounds (VOCs). 50 mg of TiO_2 powder, drop casted on a 78 cm^2 Petri dish, were employed in conjunction with a starting ethanol concentration in the range 198–238 ppm. The disappearance of the pollutant molecule, the formation of the main intermediate (acetaldehyde) and its complete mineralization to CO_2 were monitored during photocatalytic tests by means of a gas-chromatographic system. Further details can be found in Appendix A.

DFT modeling. To simulate doped TiO_2 anatase, we performed DFT+U calculations[49] using VASP suite of codes[50–55]. The U parameter was fixed at 3.3 eV. The Projector augmented wave (PAW) pseudopotentials were employed[51,53], considering the spin-polarization. The Generalized Gradient Approximation (GGA) was used[56] with the Perdew-Burke-Ernzerhof parametrization[54]. A 3x3x3 anatase bulk supercell was built by reproduction of the primitive cell. Given the 162 atoms supercell, sampling was limited only around the Γ point in reciprocal space. The energy cutoff was set at 400 eV. The conjugated gradient scheme[S7-8] was employed for optimization with a threshold for convergence equal to 0.001 eV for the change in total energy between two consecutive steps and 0.01 eV/Å for the forces.

Further details about the preparation and characterization methods can be found in Appendix A.

References

1 A. Fujishima, X. Zhang and D. A. Tryk, *Surf. Sci. Rep.*, 2008, **63**, 515–582.

2 N. Serpone and A. V. Emeline, *J. Phys. Chem. Lett.*, 2012, **3**, 673–677.

3 N. Serpone, *J. Phys. Chem. B*, 2006, **110**, 24287–24293.

4 R. Asahi, T. Morikawa, H. Irie and T. Ohwaki, *Chem. Rev.*, 2014, **114**, 9824–9852.

5 F. Spadavecchia, M. Ceotto, L. Lo Presti, C. Aieta, I. Biraghi, D. Meroni, S. Ardizzone and G. Cappelletti, *Chinese J. Chem.*, 2014, **32**, 1195–1213.

6 R. Asahi, *Science (80-.).*, 2001, **293**, 269–271.

7 D. Meroni, S. Ardizzone, G. Cappelletti, C. Oliva, M. Ceotto, D. Poelman and H. Poelman, *Catal. Today*, 2011, **161**, 169–174.

8 M. Ceotto, L. Lo Presti, G. Cappelletti, D. Meroni, F. Spadavecchia, R. Zecca, M. Leoni, P. Scardi, C. L. Bianchi and S. Ardizzone, *J. Phys. Chem. C*, 2012, **116**, 1764–1771.

9 J. Zhang, Y. Wu, M. Xing, S. A. K. Leghari and S. Sajjad, *Energy Environ. Sci.*, 2010, **3**, 715.

10 R. Long and N. J. English, *Chem. Phys. Lett.*, 2009, **478**, 175–179.

11 L. R. Sheppard, S. Hager, J. Holik, R. Liu, S. Macartney and R. Wuhrer, *J. Phys. Chem. C*, 2015, **119**, 392–400.

12 C. Wang, A. Geng, Y. Guo, S. Jiang and X. Qu, *Mater. Lett.*, 2006, **60**, 2711–2714.

13 M. Altomare, K. Lee, M. S. Killian, E. Selli and P. Schmuki, *Chem. - A Eur. J.*, 2013, **19**, 5841–5844.

14 S. M. Bawaked, S. Sathasivam, D. S. Bhachu, N. Chadwick, A. Y. Obaid, S. Al-Thabaiti, S. N. Basahel, C. J. Carmalt and I. P. Parkin, *J. Mater. Chem. A*, 2014, **2**, 12849.

15 C. Marchiori, G. Di Liberto, G. Soliveri, L. Loconte, L. Lo Presti, D. Meroni, M. Ceotto, C. Oliva, S. Cappelli, G. Cappelletti, C. Aieta and S. Ardizzone, *J. Phys. Chem. C*, 2014, **118**, 24152–24164.

16 T. M. Breault and B. M. Bartlett, *J. Phys. Chem. C*, 2012, **116**, 5986–5994.

17 J. Lim, P. Murugan, N. Lakshminarasimhan, J. Y. Kim, J. S. Lee, S.

H. Lee and W. Choi, *J. Catal.*, 2014, **310**, 91–99.
18 T. Breault and B. Bartlett, *J. Phys. Chem. C*, 2013, **117**, 8611–8618.
19 Y. Zhu, Y. Wu, Y. Lu, J. Xu, Y. Wang and X. Ma, *J. Phys. Chem. C*, 2011, **115**, 16963–16969.
20 T. Cottineau, N. Béalu, P.-A. Gross, S. N. Pronkin, N. Keller, E. R. Savinova and V. Keller, *J. Mater. Chem. A*, 2013, **1**, 2151.
21 Q.-L. Liu, Z.-Y. Zhao and Q.-J. Liu, *Mater. Sci. Semicond. Process.*, 2015, **33**, 94–102.
22 K. Obata, H. Irie and K. Hashimoto, *Chem. Phys.*, 2007, **339**, 124–132.
23 W. Wang, C. Lu, Y. Ni, M. Su, W. Huang and Z. Xu, *Appl. Surf. Sci.*, 2012, **258**, 8696–8703.
24 Y. Gong, C. Fu, L. Ting, J. Chenu, Q. Zhao and C. Li, *Appl. Surf. Sci.*, 2015, **351**, 746–752.
25 S. Hoang, S. Guo and C. B. Mullins, *J. Phys. Chem. C*, 2012, **116**, 23283–23290.
26 J. Huang, S. Wen, J. Liu and G. He, *J. Nat. Gas Chem.*, 2012, **21**, 302–307.
27 W. J. Yin, H. Tang, S. H. Wei, M. M. Al-Jassim, J. Turner and Y. Yan, *Phys. Rev. B - Condens. Matter Mater. Phys.*, 2010, **82**, 1–6.
28 J. Liu, Y. Duan, X. Zhou and Y. Lin, *Appl. Surf. Sci.*, 2013, **277**, 231–236.
29 X. Liu, X. Wu and K. Scott, *Catal. Sci. Technol.*, 2014, **4**, 3891–3898.
30 P. Mazzolini, P. Gondoni, V. Russo, D. Chrastina, C. S. Casari and A. Li Bassi, *J. Phys. Chem. C*, 2015, **119**, 6988–6997.
31 H. Ay and D. Üner, *Appl. Catal. B Environ.*, 2015, **179**, 128–138.
32 A. Minguzzi, C. Locatelli, G. Cappelletti, C. L. Bianchi, A. Vertova, S. Ardizzone and S. Rondinini, *J. Mater. Chem.*, 2012, **22**, 8896.
33 L. Lo Presti, M. Ceotto, F. Spadavecchia, G. Cappelletti, D. Meroni, R. G. Acres and S. Ardizzone, *J. Phys. Chem. C*, 2014, **118**, 4797–4807.
34 F. Spadavecchia, G. Cappelletti, S. Ardizzone, M. Ceotto, M. S. Azzola, L. Lo Presti, G. Cerrato and L. Falciola, *J. Phys. Chem. C*, 2012, **116**, 23083–23093.
35 J. W. Mullin, *Crystallization*, Oxford U.K., 2001.

36 R. Shannon, *Acta Cristal. Sect. A Found. Adv.*, 1976, **32**, 751–767.
37 S. Ardizzone, C. L. Bianchi, G. Cappelletti, S. Gialanella, C. Pirola and V. Ragaini, *J. Phys. Chem. C*, 2007, **111**, 13222–13231.
38 Z. Zhao and Q. Liu, *Catal. Letters*, 2008, **124**, 111–117.
39 F. Spadavecchia, G. Cappelletti, S. Ardizzone, M. Ceotto and L. Falciola, *J. Phys. Chem. C*, 2011, **115**, 6381–6391.
40 H. Irie, Y. Watanabe and K. Hashimoto, *J. Phys. Chem. B*, 2003, **107**, 5483–5486.
41 S. Livraghi, M. C. Paganini, E. Giamello, A. Selloni, C. Di Valentin and G. Pacchioni, *J. Am. Chem. Soc.*, 2006, **128**, 15666–15671.
42 V. N. Kuznetsov and N. Serpone, *J. Phys. Chem. C*, 2009, **113**, 15110–15123.
43 J. Biedrzycki, S. Livraghi, E. Giamello, S. Agnoli and G. Granozzi, *J. Phys. Chem. C*, 2014, **118**, 8462–8473.
44 L. De Trizio, R. Buonsanti, A. M. Schimpf, A. Llordes, D. R. Gamelin, R. Simonutti and D. J. Milliron, *Chem. Mater.*, 2013, **25**, 3383–3390.
45 H. T. H. Nguyen, N. Takenaka, H. Bandow, Y. Maeda, S. T. De Oliva, M. M. F. Botelho and T. M. Tavares, *Atmos. Environ.*, 2001, **35**, 3075–3083.
46 K. D. Kwon, W. K. Jo, H. J. Lim and W. S. Jeong, *Environ. Sci. Pollut. Res.*, 2008, **15**, 521–526.
47 L. S. R. Brickus, J. N. Cardoso and F. R. De Aquino Neto, *Environ. Sci. Technol.*, 1998, **32**, 3485–3490.
48 J. S. Gaffney and N. A. Marley, *Atmos. Environ.*, 2009, **43**, 23–36.
49 S. L. Dudarev, S. Y. Savrasov, C. J. Humphreys and A. P. Sutton, *Phys. Rev. B*, 1998, **57**, 1505–1509.
50 G. Kresse and J. Hafner, *Phys. Rev. B*, 1994, **49**, 14251–14269.
51 G. Kresse, *Phys. Rev. B*, 1996, **54**, 11169–11186.
52 G. Kresse, *Phys. Rev. B*, 1999, **59**, 1758–1775.
53 G. Kresse and J. Hafner, *Phys. Rev. B - Condens. Matter*, 1993, **47**, 558−561.
54 J. P. Perdew, K. Burke, M. Ernzerhof, D. of Physics and N. O. L. 70118 J. Quantum Theory Group Tulane University, *Phys. Rev. Lett.*, 1996, **77**, 3865–3868.
55 P. E. Blöchl, *Phys. Rev. B*, 1994, **50**, 17953–17979.

56 J. P. Perdew and Y. Wang, *Phys. Rev. B*, 1992, **45**, 13244–13249.
57 M. Teter, M. Payne and D. Allan, *Phys. Rev. B*, 1989, **40**, 255–263.
58 D. M. Bylander, L. Kleinman and S. Lee, *Phys. Rev. B*, 1990, **42**, 1394–1403.

This Chapter has been adapted with permission from Rimoldi *et al.*, *J. Phys. Chem. C*, 2015, **119**, 24104−24115.

Chapter 4

The role played by different TiO_2 features on the photocatalytic degradation of paracetamol

In the case of TiO_2 applications in photocatalysis, both bulk and surface oxide features can differently, or even divergently, affect the final performance of the reaction. The choice of the synthetic route to obtain the oxide is often crucial in this respect, as also highlighted by the results presented in the previous Chapter.

The temperature of the oxide preparation, for instance, is one of the key parameters to be controlled or modulated in the synthesis of a photocatalyst[1]. In fact, on one side, high temperature promotes crystallinity and surface regularity reducing recombination between charge carriers; at the same time, however, the growth of the crystallites and their aggregation may support loss of surface area and porosity, lowering the active photocatalyst surface.

Recently the use of metal species was proposed to promote TiO_2 efficiency in photocatalytic applications[2–4]. The introduction of metal species may relevantly modify the structural, electronic, optical and morphological properties of the material. Besides metals of the first transition series, the doping by niobium and tantalum was recently suggested, on the grounds of both theoretical and experimental results, to promote the oxide photocatalytic activity, due to the electronic configuration of their 4 and 5 d orbitals[5]. In the case of Nb/N codoped materials, the choice of the procedure adopted to dope the oxide by the guest species appeared to be decisive: the sample obtained by including the dopants during the oxide synthesis showed the best performance under solar irradiation while the sample obtained by impregnation appeared to be the slowest photocatalyst even with respect to undoped TiO_2[6,7].

Apart from modifications of the bulk and electronic features of a material, the surface acidity of a photocatalyst can be expected to appreciably affect the course of the reaction. These aspects are not extensively debated in the literature and several apparent diverging results can be found. Both enhancement[8–10] and decreasing[11–14] of the photocatalytic performance due to a stronger surface acidity were reported in the case of TiO_2 materials. Yamazaki *et al.* also described a decrease of activity of the photocatalyst due to the transformation of Lewis sites to Brønsted, during the reaction[15].

In the present Chapter, results concerning the synthesis and the characterization of two pristine TiO_2 nanostructured samples showing different phase composition and the two relative Ta-doped samples obtained by impregnation are presented. A comparative analysis of the intrinsic surface acidity of the nanomaterials by acid-base titration with adsorption of 2-phenylethylamine (PEA) probe was performed[16,17]. The results of the different characterizations are discussed in the light of the samples photocatalytic performance in the oxidative degradation of paracetamol. The choice of the target molecule is to be considered in the context of emerging contaminants pollution of surface, ground and wastewaters, which attracted much attention in the scientific community in the last few years[18–20].

4.1 Results

4.1.1 Characterization results

For all samples the phase composition was assessed by Rietveld refinement by adopting the Quanto software[1]. XRPD analyses revealed the predominant polymorph to be anatase for all synthesized samples (Fig. 4.1a). The series of samples prepared by hydrolysis with HCl solution (T and TTa) contained both anatase and brookite (*ca.* 60% anatase and 40% brookite), with small variations between the Ta-doped and the undoped samples (Tab. 4.1). Differently, the nanostructured materials synthesized in the presence of acetic acid (TAC and TTaAC) are mainly composed by anatase, due to the action of acetic acid as promoting species, as reported elsewhere[21]. In both cases, the presence of Ta did not seem to modify the

phase composition of the samples, while more significant effects are obtained under the morphological point of view (Fig. 4.1b). Conversely, the effect of the guest species is clear on the average crystallite dimensions, calculated by applying the Scherrer equation to (101) anatase reflections: while pristine samples had a crystallite diameter of *ca.* 7 nm, Ta-doped nanomaterials reached slightly bigger dimensions (*ca.* 9 nm) (Tab. 4.1). TEM images allowed to recognize a certain aggregation among the crystallites, found to be comparable for all samples. HR-TEM analyses confirmed the information retrieved by XRPD about the crystallites dimension and the trend upon impregnation treatment (Tab. 4.1). We reported both the average and the mode of the equivalent crystallites diameter, because the mode represents the more probable value and it is more representative of the morphology of the nanocrystals. Anyway, it is not worthless to consider also the mean size because this parameter was fully comparable with the results obtained by the Scherrer equation (Tab. 4.1). The phase composition of the different samples previously obtained by XRPD analyses, was confirmed also by the electron diffraction (ED) powder pattern (Fig. 4.2a). Both anatase and brookite monocrystals were identified for the T and TTa biphasic samples, by applying Fast Fourier Transform, clearly exhibiting the typical patterns of the two titania polymorphs (Fig. 4.1c).

Sample	Phase composition (%)	d_{101} XRPD (nm)	Mode d TEM (nm)	Average d TEM (nm)	S_{BET} ($m^2\ g^{-1}$)	V_{pores} ($mL\ g^{-1}$)
T	62 A – 38 B	7	6 ± 2	6	153	0.317
TTa	59 A – 41 B	9	8 ± 3	8	114	0.119
TAC	100 A	7	6 ± 2	7	173	0.227
TTaAC	100 A	9	8 ± 3	8	137	0.263

Table 4.1 – Structural and morphological information about the synthesized samples: phase composition (A: anatase; B: brookite), average crystallites diameter calculated by Scherrer equation, mode and average crystallites diameter retrieved by TEM images, specific surface area (S_{BET}) and pores total volume (V_{pores}).

N_2 adsorption-desorption isotherms of all samples present the typical profile of mesoporous materials, classified as IV-type according to the IUPAC classification (Fig. 4.1b). The BET calculation revealed higher specific surface area for the TAC sample (173 m^2 g^{-1}), with respect to the corresponding mixed phase powder, T (153 m^2 g^{-1}). In both cases, the doping procedures affect the surface area parameter by a decrease of *ca.* 40 m^2 g^{-1} (Tab. 4.1), in agreement with the increase of the crystallite sizes observed by XRD and with particle aggregation shown by TEM images. Regarding hysteresis loop shapes, TAC exhibited a strong H2-type shape, characteristic of bottle-neck shaped pores. This profile is less marked for T, even if characterized by H2 hysteresis loop, in its turn. Under this point of view, no significant difference was found upon Ta-doping. The position of the hysteresis loop revealed TAC sample to have smaller pores with respect to T. Moreover, the total porosity of the samples is observed to decrease appreciably upon Ta impregnation in the case of the mixed phase T sample (Fig. 4.1b).

In the case of the Ta-impregnated samples the amount of Ta was analysed by XPS. For the doped samples the experimental atomic Ta/Ti ratio was found in the range 0.02–0.06 indicating a surface Ta enrichment due to impregnation procedure.

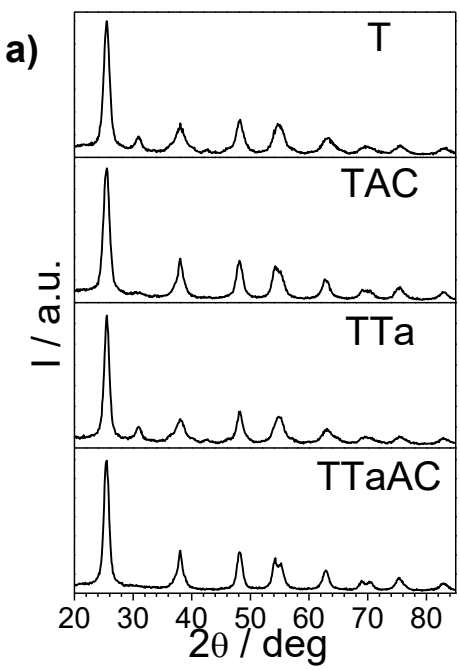

a) XRPD patterns of the four synthesized samples.

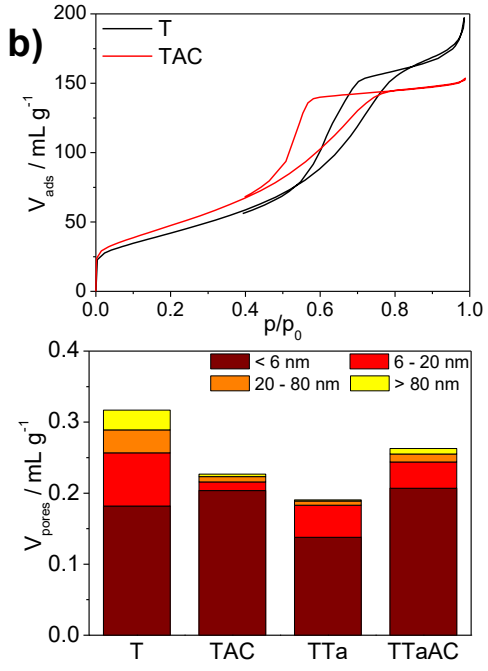

b) N_2 adsorption–desorption isotherms of T and TAC (top) and pore size distribution of all samples (bottom).

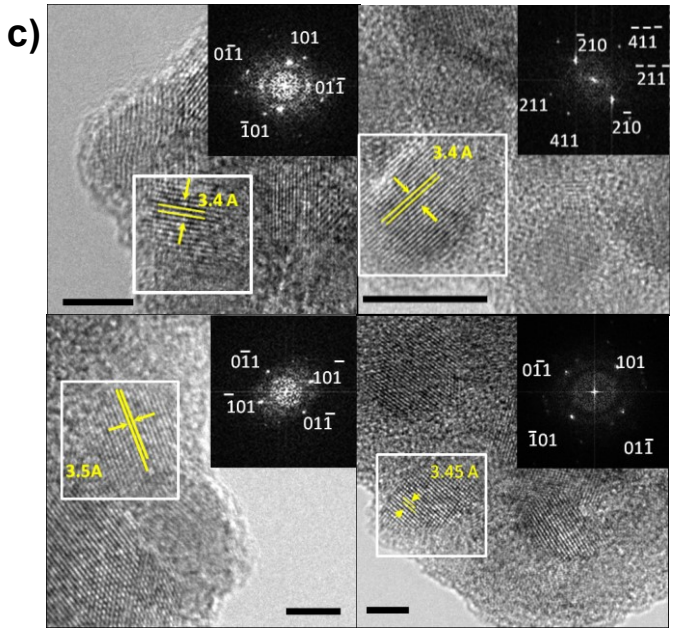

c) HR-TEM images of the T, together with the FFT pattern of anatase (top, left) and brookite (top, right) in inset, the TTa (bottom, left) and the TTaAC (bottom, right) samples; the bar is equal to 5 nm.

Figure 4.1 – Structural and morphological characterization results.

The surface acidity of the four samples was evaluated by liquid-solid acid-base titration by using PEA as basic probe. All the obtained results are collected in Figure 4.2b, in which the adsorbed PEA is reported for all samples (1st run adsorption) as a function of the injected PEA. The collected curves have hyperbolic shape with attainment of a *plateau* value for the adsorbed PEA, which corresponds to saturation of all surface acid sites. In particular, the three samples, TAC, TTa, and TTaAC showed high acidity, while T sample did not possess acid surface. As expected, the most acidic samples correspond to those synthesized in the presence of acetic acid (TTaAC and TAC); also, the Ta-doped sample (TTa) showed a well-developed surface acidity. Table 4.2 reports the results in terms of total acid sites (meq g^{-1}) including the strong acid sites which correspond to 84%, for TTa, 77% for TAC, and 90% for TTaAC, evaluated comparing the 1st and 2nd runs of PEA adsorption. In other words, in the 1st run all strong and weak acid sites are measured, while upon elution of pure solvent ideally removing only the weakly adsorbed PEA molecules, the weak acid sites are titrated and quantified by the 2nd run. As the samples have different surface area values, the acid site density of the samples, calculated for surface unity (μeq m^{-2}), does not follow the same ranking (Tab. 4.2).

The suspension stability in water was evaluated by spectrometry. All samples give rise to relatively stable suspensions, the absorbance decreasing at maximum by about 6% after 1 h. The T sample revealed to be the most stable photocatalyst. The Ta-doping procedure resulted in an increased instability in aqueous suspension, the more so for the TTaAC sample (Fig. 4.2c).

Sample	Total acid sites (μeq m^{-2})	Total acid sites (meq g^{-1})	Strong acid sites (meq g^{-1}) (%)
T	$48.60 \cdot 10^{-3}$	0.00744	-
TTa	1.407	0.1603	0.1341 (84%)
TAC	0.8113	0.1820	0.1403 (77%)
TTaAC	1.604	0.2198	0.1971 (90%)

Table 4.2 – Surface acidity of the four prepared samples.

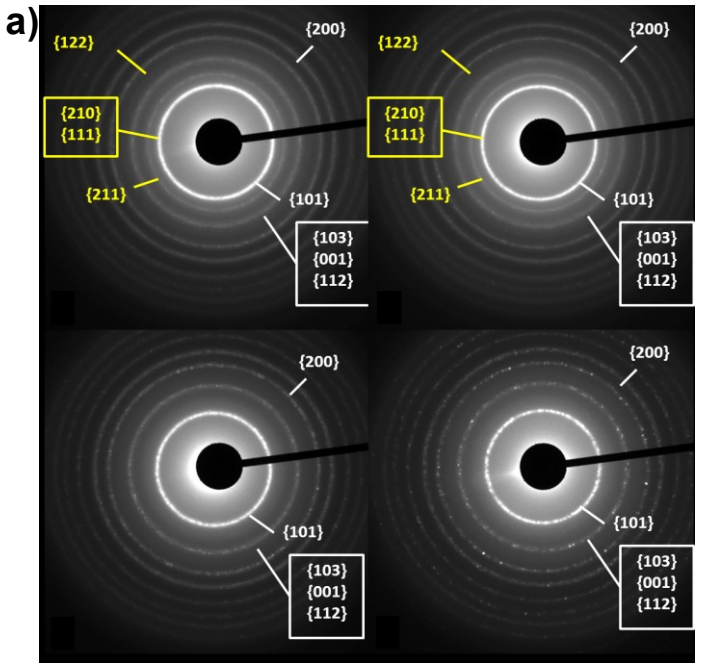

a) Electron diffraction of the nanostructured powder samples. The T (top, left) and the TTa (top, right) samples show well defined anatase and brookite ED patterns. The diffraction planes corresponding to the anatase phase are reported in white, while the planes corresponding to the brookite phase are reported in yellow. In the TAC (bottom, left) and the TTaAC (bottom, right) samples only the anatase phase is present.

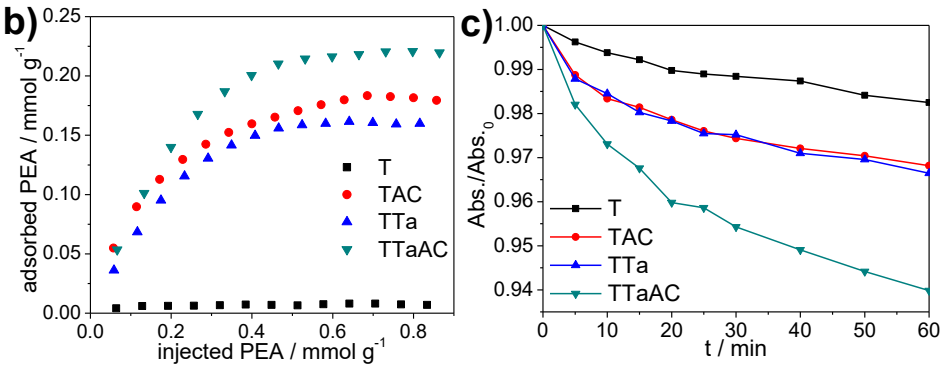

b) Evaluation of the surface acidity of the studied samples by the pulse titration technique with PEA probe. The 1st run adsorption on fresh samples is reported.

c) Suspension stability of the samples with respect to time, by spectrophotometric measurements (λ = 500 nm).

Figure 4.2 – Powder characterization results.

4.1.2 Photocatalytic results

While most of the literature uses dyes as model water pollutants[22,23], the present samples were tested in the photocatalytic degradation of paracetamol under UV irradiation. In a short time-scale (2 h) 70–80% of

degradation was achieved, together with high mineralization degrees, between 44 and 59%, depending on the sample (Fig. 4.3a, Tab. 4.3). T sample revealed to be the most efficient regarding both molecule disappearance and mineralization, although not showing the highest surface area among the different samples. The oxidative photodegradation proceeded more slowly for the other three samples, with small differences concerning the molecule disappearance. Under the mineralization point of view, the TTa sample showed the lowest performance (44%), while the other two samples exhibited similar behaviour in terms of mineralization.

While the molecule disappearance reaches values of 70–80% at the end of the photocatalytic test, TOC data showed that only 40–60% of the organic carbon is fully mineralized in the considered reaction time, suggesting significant presence of reaction intermediates. ESI-MS analyses upon 120 min light irradiation proved the presence of peaks at m/z = 79, 95, 108 and 130; these peaks, which are in good agreement with the literature, may represent reaction intermediates, although their attribution is difficult due to their low concentrations[24]. No significant differences in the detected peaks could be observed between the different samples, although their relative concentration varies. GC-MS analyses were also carried out to identify the degradation intermediates of the reaction for the two undoped samples after 0, 65 and 120 min of irradiation. Figure 4.3b reports the MS fragmentation profiles of the main identified intermediates which are in good agreement with previous investigations of paracetamol degradation by TiO_2/UV and UV/H_2O_2[24–27]. The contemporary presence of aminophenol and acetamide suggests the parallel occurrence of competitive reaction pathways involving $^{\bullet}OH$ radicals. In particular, the presence of acetamide suggests an early cleavage of the $–NHCOCH_3$ moiety of the paracetamol molecule, possibly following the attack of hydroxyl radicals at a para position with respect to the –OH group of paracetamol[24,27,28]. The resulting hydroquinone intermediate is known to produce p-benzoquinone by successive $^{\bullet}OH$ oxidation, which is known to be unstable and tends to undergo ring rupture giving rise to open ring dicarboxylic acids[29]. The detection of aminophenol supports instead the alternative degradation mechanism proposed by Moctezuma *et al.*[25], involving a deacylation reaction pathway.

4.2 Discussion

The synthetic procedure adopted to prepare the present TiO_2 samples is found to markedly affect the final oxide features and, consequently, their photocatalytic activity. The sol-gel T sample obtained in the presence of HCl shows the best activity, although presenting a specific surface area of 20 m^2 g^{-1} lower than TAC (largest surface area of all samples). The photocatalytic activity is often due to an interplay of different properties[30]. In the present case, morphological properties alone cannot explain the observed activity sequence, as shown by the comparison of the photocatalytic performance of the two undoped samples. The sol-gel T sample obtained in the presence of HCl shows the best activity. Several factors can be invoked to interpret these finding. The oxide is composed by both anatase and brookite and the presence of different polymorphs has often been invoked to reduce recombination due to charge separation effects [31]. Moreover, the T aqueous suspension shows the best stability in time, supporting a fast approach by the pollutant and its intermediates. A relevant role is played by the acidity features of the present samples. The T sample is definitely the sample showing the lowest content of acid sites. The relevant acidity of TAC may be traced back to the large amount of acetic acid adopted to promote the anatase structure. The selective promotion of a given structural crystalline lattice is the result of strong chemisorption phenomena occurring at given facets[32]. In the case instead of the Ta-promoted samples, the pentavalent guest species promote the formation of Lewis acid Ti^{3+} moieties, thus enhancing the surface acidity. On the grounds of XPS results, the prevailing surface enrichment of Ta species supports an appreciable modification of the surface properties of the metal doped samples. The acidic features, together with the lowest value of the specific surface area, may be invoked to be responsible for the low photocatalytic efficiency of the TTa sample. The role played by the acid features of a photocatalyst is poorly discussed in the literature with controversial results. For example, Kozlov *et al.* reported promotion of acetone photodegradation in the gas phase by increasing the acidity of sulphate-doped TiO_2[10]. Conversely, in the case of the photodegradation of phenol in the liquid phase, Colón *et al.* showed a decreasing performance by increasing the acidity of sulphated TiO_2[14]. The degradation of

paracetamol may show similarities with that of phenol supporting the agreement between the present results and those by Colón *et al.*. The paracetamol molecule shows a pK_a of 9.38 and therefore at the pH adopted in the present experiment (pH = 5.5) the molecule is neutral and simple electrostatic effects can be excluded. No indications of different reaction routes among the different samples are given by GC-MS and ESI results. Since the increasing acid features affect to a larger extent the final mineralization than the molecule disappearance (Tab. 4.3), we can suggest that basic intermediates (*p*-aminophenol, acetamide, *etc.*) may remain strongly bound at the photocatalyst acid surface sites, thus blocking the access at the active surface.

On the grounds of the mass characterizations, the parallel reaction pathways reported in Figure 4.3c can be proposed, also according to previous reports concerning TiO_2/UV and H_2O_2/UV degradation of paracetamol[25,28].

This suggested mechanism may allow us to interpret the different role played by Ta-doped TiO_2 on the photocatalytic degradation of different pollutants under UV irradiation. In a previous work, Ta-promoted samples showed an improved performance with respect to pristine TiO_2 in the gas phase degradation of ethanol, which proceeds by acidic intermediates[6].

Sample	k (10^{-3} min^{-1})	Mineralization (2 h) (%)
T	12.4 ± 0.2	59 ± 1
TTa	9.4 ± 0.1	44 ± 1
TAC	9.3 ± 0.1	54 ± 1
TTaAC	10.4 ± 0.1	50 ± 1

Table 4.3 – Pseudo-first order kinetic constants (*k*) and mineralization degrees for the photocatalytic degradation of paracetamol of the four samples.

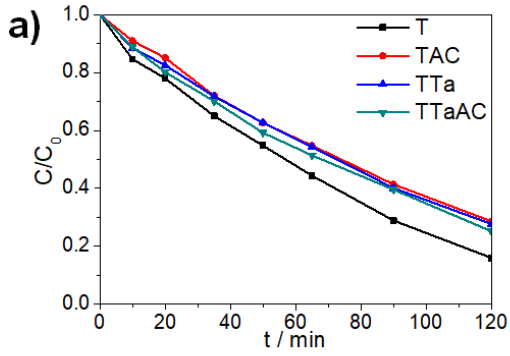

a) Paracetamol disappearance for the prepared photocatalysts.

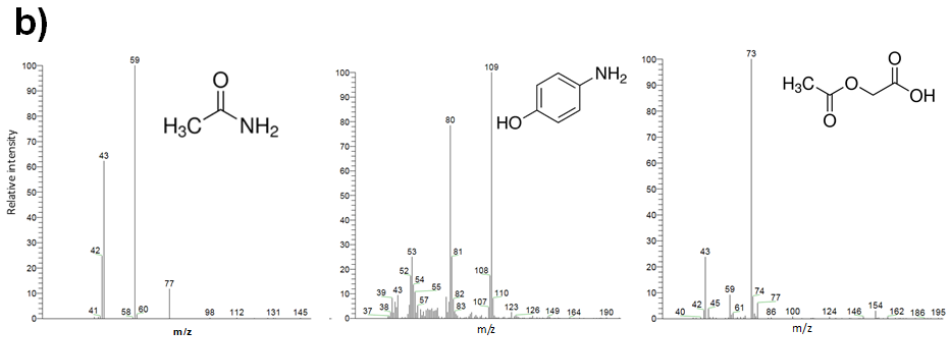

b) Mass spectra of the main identified intermediates by GC–MS analyses: acetamide (left), p-aminophenol (middle) and acetoxyacetic acid (tentative identification) (right).

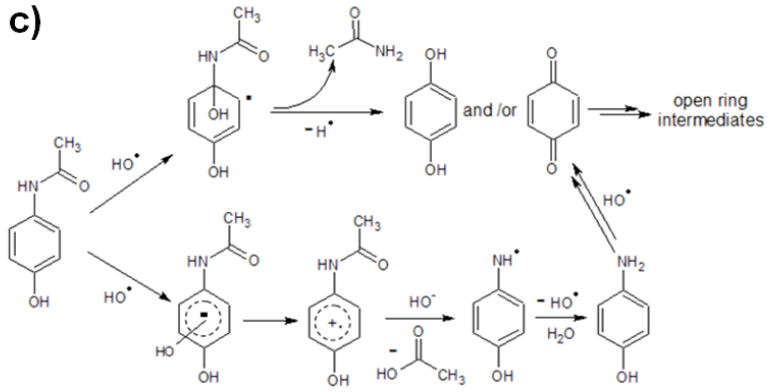

c) Proposed reaction pathways of paracetamol degradation.

Figure 4.3 – Photocatalytic tests results.

4.3 Conclusions

Different TiO_2 samples, both pristine and Ta-doped, were obtained in the laboratory by sol-gel procedures combined with mild calcinations. The two pure TiO_2 samples are composed either by an anatase/brookite mixture or by pure anatase. The addition of Ta species by impregnation does not modify the phase composition with respect to the relative pure oxide but it provokes an increase in the crystallite sizes with an ensuing decrease of the specific surface area and an increase of the surface acidity.

All samples give rise to relatively stable suspensions in water the more so in the case of the pristine anatase/ brookite mixture. This latter sample is the one showing the lowest content of acidic groups, while all other samples show markedly acidic features.

The photocatalytic degradation of paracetamol, an emerging pollutant, was studied in aqueous suspensions of the photocatalysts. A balance of different factors can be proposed as the origin of the best performance shown by the anatase/brookite pristine sample:

- highly accessible surface sites (large surface area and pore volume, excellent stability in water);
- the presence of the two TiO_2 polymorphs which can reduce charge carrier recombination effects;
- the very low content of acid sites.

The first two points can be considered to bear a general significance in the case of photocatalytic reactions performed in aqueous media. The effects, instead, introduced by the surface acidity, appear to be more strictly related to the physicochemical pollutant features and, mainly, to its degradation intermediates. In fact, the study of the reaction pathway suggests the occurrence of basic intermediate species which might remain strongly adsorbed at the oxide acid sites, thus reducing the total mineralization of the process.

4.4 Specific procedures

Samples preparation. The nanostructured powders were prepared by two different sol-gel procedures.

The first procedure was already reported in the previous Chapter. In brief, in a three-necked flask, isopropanol and Ti(IV)isopropoxide were mixed and then the Ti precursor was hydrolyzed by dropping a HCl aqueous solution at pH = 3 in 30 min under vigorous stirring. The sol was kept under stirring for 1 h and successively put in an oven at 90 °C to dry. The recovered powder was finally calcined at 400 °C for 6 h under O_2 flux (9 NL h^{-1}). The sample was labelled T. An impregnation method in a $TaCl_5$ water-ethanol solution was adopted before the calcination step to obtain the corresponding Ta-doped sample, with a molar ratio Ti/Ta = 1 %. The Ta-doped sample was labelled TTa.

The second procedure, adopted also in Chapter 1, implied the formation of a Ti(IV)isopropoxide and acetic acid mixture in a three-necked flask and a successive drop-by-drop hydrolysis with water under vigorous stirring, for 30 min at 0 °C. The sol was kept under stirring for 1 h and later put in an oven at 70 °C for 3 h and then at 100 °C to dry. Finally, the amorphous powder was calcined at 400 °C for 6 h under O2 flux (9 NL h^{-1}). The sample was labelled TAC. The same impregnation procedure described above was adopted to obtain the sample doped with Ta. The Ta-doped sample was named TTaAC.

Surface acidity measurements. Experiments were performed in a modified liquid chromatograph (HPLC), equipped with a UV detector coupled to a personal computer for the collection, storage and processing of the data, especially set-up for realizing acid-base titrations in liquid-solid phase[17]. For each experiment, a weighed amount (*ca.* 0.1 g) of fresh sample was introduced into the sample holder maintained in an oven for 4 h at 150 °C under flowing air, then evacuated and filled with cyclohexane under vacuum. In each adsorption test performed at 25 °C, pulses (50 μL) of 2-phenyethylamine (PEA) solution in cyclohexane of known concentration were sent at fixed time intervals (10 min) onto the sample at a constant solvent flow rate (5 mL min^{-1}). The non-adsorbed amounts of PEA after each pulse were detected up to sample saturation, corresponding to the obtainment of chromatographic peaks of equal area.

The amount of amine adsorbed on the catalyst sample after the i-th pulse was calculated via the following equation:

$$(\text{amine adsorbed})_i\ [\text{meq g}^{-1}] = (V\ C/w)\ (A_{av} - A_i)\ A_{av} \qquad (4.1)$$

where V (mL) corresponds to the volume a single pulse, C (mol L^{-1}) is the concentration of the amine solution, w (g) is the mass of the sample, A_{av} is

the mean chromatographic area at saturation and A_i is the area corresponding to the i-th pulse.

If a 1:1 adsorption stoichiometry is assumed, the total number of acidic sites corresponds to the total amount of amine adsorbed on the sample surface.

$$\text{acidic sites [meq g}^{-1}\text{]} = \Sigma_i \text{ (amine adsorbed)}_i \text{ [meq g}^{-1}\text{]} \qquad (4.2)$$

After the 1st run adsorption on the fresh sample, a 2nd run was performed after elution of pure solvent for 30 min, to determine the strong acidity of the samples by subtracting the acid sites titrated in the 2nd run (weak acid sites) from those of the 1st run adsorption (total acid sites).

Photocatalytic activity tests. All samples were tested in the photocatalytic degradation of paracetamol in ultrapure water, under UV irradiation. A 600 mL jacketed reactor termostated at 20 °C was used. An initial paracetamol concentration of 35 mg L^{-1} and a catalyst amount of 0.5 g L^{-1} were selected. An O_2 flux was bubbled in the reactor during the reaction (9 NL h^{-1}). The molecule degradation was followed by UV-vis spectroscopy by detecting the decreasing intensity of the typical absorption peak of paracetamol at 243 nm with respect to time, while Total Organic Carbon (TOC) measurements allowed the mineralization degree to be calculated. The reaction was followed for 2 h.

Further details about the preparation and characterization methods can be found in Appendix A.

References

1 L. Rimoldi, D. Meroni, G. Cappelletti and S. Ardizzone, *Catal. Today*, 2017, **281**, 38–44.

2 A. Sengele, D. Robert, N. Keller, V. Keller, A. Herissan and C. Colbeau-Justin, *J. Catal.*, 2016, **334**, 129–141.

3 R. Long and N. J. English, *Chem. Phys. Lett.*, 2009, **478**, 175–179.

4 X. Yan, C. Xue, B. Yang and G. Yang, *Appl. Surf. Sci.*, 2017, **394**, 248–257.

5 L. R. Sheppard, S. Hager, J. Holik, R. Liu, S. Macartney and R. Wuhrer, *J. Phys. Chem. C*, 2015, **119**, 392–400.

6 L. Rimoldi, C. Ambrosi, G. Di Liberto, L. Lo Presti, M. Ceotto, C. Oliva, D. Meroni, S. Cappelli, G. Cappelletti, G. Soliveri and S. Ardizzone, *J. Phys. Chem. C*, 2015, **119**, 24104–24115.

7 C. Marchiori, G. Di Liberto, G. Soliveri, L. Loconte, L. Lo Presti, D. Meroni, M. Ceotto, C. Oliva, S. Cappelli, G. Cappelletti, C. Aieta and S. Ardizzone, *J. Phys. Chem. C*, 2014, **118**, 24152–24164.

8 K. K. Akurati, A. Vital, J. Dellemann, K. Michalow, T. Graule, D. Ferri and A. Baiker, *Appl. Catal. B Environ.*, 2008, **79**, 53–62.

9 J. Papp, S. Soled, K. Dwight and A. Wold, *Chem. Mater.*, 1994, 496–500.

10 D. Kozlov, D. Bavykin and E. Savinov, *Catal. Letters*, 2003, **86**, 169–172.

11 J. Yu, J. C. Yu, M. K.-P. Leung, W. Ho, B. Cheng, X. Zhao and J. Zhao, *J. Catal.*, 2003, **217**, 69–78.

12 M. D. Hernández-Alonso, A. R. Almeida, J. A. Moulijn and G. Mul, *Catal. Today*, 2009, **143**, 326–333.

13 L. Zhang, V. M. Menendez-Flores, N. Murakami and T. Ohno, *Appl. Surf. Sci.*, 2012, **258**, 5803–5809.

14 G. Colón, M. C. Hidalgo, J. A. Navío, A. Kubacka and M. Fernández-García, *Appl. Catal. B Environ.*, 2009, **90**, 633–641.

15 S. Yamazaki, K. Ichikawa, A. Saeki, T. Tanimura and K. Adachi, *J. Phys. Chem. A*, 2010, **114**, 5092–5098.

16 P. Carniti and A. Gervasini, in *Calorimetry and Thermal Methods in Catalysis*, ed. A. Auroux, Springer Berlin Heidelberg, Berlin, Heidelberg, Springer-V., 2013, vol. 154, pp. 543–551.

17 P. Carniti, A. Gervasini and S. Biella, *Adsorpt. Sci. Technol.*, 2005, **23**, 739–749.
18 T. Deblonde, C. Cossu-Leguille and P. Hartemann, *Int. J. Hyg. Environ. Health*, 2011, **214**, 442–448.
19 D. J. Lapworth, N. Baran, M. E. Stuart and R. S. Ward, *Environ. Pollut.*, 2012, **163**, 287–303.
20 F. Mazille, T. Schoettl, N. Klamerth, S. Malato and C. Pulgarin, *Water Res.*, 2010, **44**, 3029–3038.
21 M. A. Behnajady, H. Eskandarloo, N. Modirshahla and M. Shokri, *Photochem. Photobiol.*, 2011, **87**, 1002–1008.
22 B. Lin, C. Xue, X. Yan, G. Yang, G. Yang and B. Yang, *Appl. Surf. Sci.*, 2015, **357**, 346–355.
23 B. Lin, G. Yang, B. Yang and Y. Zhao, *Appl. Catal. B Environ.*, 2016, **198**, 276–285.
24 I. Dalmázio, T. M. A. Alves and R. Augusti, *J. Braz. Chem. Soc.*, 2008, **19**, 81–88.
25 E. Moctezuma, E. Leyva, C. A. Aguilar, R. A. Luna and C. Montalvo, *J. Hazard. Mater.*, 2012, **243**, 130–138.
26 L. Yang, L. E. Yu and M. B. Ray, *Water Res.*, 2008, **42**, 3480–3488.
27 R. Andreozzi, V. Caprio, R. Marotta and D. Vogna, *Water Res.*, 2003, **37**, 993–1004.
28 D. Vogna, R. Marotta, A. Napolitano and M. D'Ischia, *J. Org. Chem.*, 2002, **67**, 6143–6151.
29 L. Yang, L. E. Yu and M. B. Ray, *Environ. Sci. Technol.*, 2009, **43**, 460–465.
30 O.-O. Prieto-Mahaney, N. Murakami, R. Abe and B. Ohtani, *Chem. Lett.*, 2009, **38**, 238–239.
31 D. C. Hurum, A. G. Agrios, K. A. Gray, T. Rajh and M. C. Thurnauer, *J. Phys. Chem. B*, 2003, **107**, 4545–4549.
32 H. G. Yang, C. H. Sun, S. Z. Qiao, J. Zou, G. Liu, S. C. Smith, H. M. Cheng and G. Q. Lu, *Nature*, 2008, **453**, 638–641.

This Chapter has been adapted with permission from Rimoldi *et al.*, *Appl. Surf. Sci.*, 2017, **424**, 198−205.

Chapter 5

Concurrent role of metal (Sn, Zn) and N species in enhancing the photocatalytic activity of TiO_2 under solar light

Among non-metal species, starting from the pioneering work of Asahi *et al.*[1], nitrogen has been the focus of extensive research (as also reported in Chapter 3) since it proved able to promote titanium dioxide (TiO_2) visible light absorption. Nonetheless, as already discussed, the introduction of N as guest species in the TiO_2 lattice generates localized intra gap states that can promote electron/hole recombination phenomena, thus decreasing the photocatalytic efficiency[2].

A viable strategy to improve the photocatalytic activity of N-doped TiO_2 is the development of mixed oxide structures and heterojunctions able to limit recombination phenomena by enhancing the charge separation[3,4]. Due to their band structure, SnO_2 and ZnO have been frequently adopted to develop SnO_2/TiO_2 and ZnO/TiO_2 heterojunctions[5–12], although reports of the formation of heterojunctions with N-doped TiO_2 have been much more scarce.

Codoping of TiO_2 with nitrogen and a metal species has also emerged as a promising strategy to boost the photocatalytic efficiency of N-doped materials. Several transition elements have been reported as efficient codopants of N-doped TiO_2[13–15], leading in some cases to synergistic effects in the visible light absorption[16,17]. Few articles can be found in the literature regarding codoping of TiO_2 with N and Zn or Sn[18]. Zhuang *et al.* reported an enhanced activity of Sn and N-codoped TiO_2 systems with respect to both photocatalytic hydrogen evolution and Rhodamine B degradation[19]. Kaur *et al.*, studying a series of metal,N codoped titania

systems, suggested Zn as an efficient species able to promote photocatalysis reducing the recombination centres[20]. The improved photocatalytic activity of Zn,N-codoped TiO_2 was confirmed by Hu *et al.* for samples prepared by nitridation and hydrogenation with high oxygen vacancies content[21].

In this Chapter, the modifications provided by Sn and Zn species on the physicochemical features and the photocatalytic activity of N-doped TiO_2 systems were studied. High metal contents were investigated to favour the occurrence of partial segregation of the metal oxides. The obtained samples were characterized from the structural, morphological, optical and spectroscopic point of view. Their photocatalytic activity was tested both under UV and simulated solar irradiation toward the degradation of tetracycline (TC). Further, the photocatalytic degradation mechanism of Sn- and Zn-modified titania samples were identified and related to the modifications of the physicochemical features induced by metal species.

5.1 Results and discussion

5.1.1 Materials characterization

Figure 5.1a reports the XRPD patterns of the investigated samples. Sharp differences in terms of phase composition and average crystallite size are appreciable depending on the nature and nominal amount of the guest species (Tab. 5.1). The undoped sample is an anatase-brookite composite in a *ca.* 2:1 ratio, as clearly appreciable from the presence of the brookite (121) reflection. N-doping promotes the anatase content (space group: $I4_1/amd$; tetragonal structure) and crystal growth (Tab. 5.1), in agreement with previous reports about N-doped TiO_2[22,23].

The presence of Sn seems instead to result in lower crystallinity and anatase content with respect to TiN sample. In particular, TiNSn5 showed *ca.* 22% of brookite (space group: *Pbca*; orthorhombic structure) and smaller crystallites, whereas the higher Sn content promotes the rutile phase (space group: $P4_2/mnm$; tetragonal structure), which is the only phase clearly appreciable. These phenomena can be explained on the grounds of the structural similarity of rutile TiO_2 and SnO_2-cassiterite (space group: $P4_2/mnm$; tetragonal structure), which can favour the growth of rutile at

low temperatures (< 500–600 °C). Interestingly, XRPD analyses show no well-defined peaks related to SnO_2 segregated phases.

Zn-promoted samples show a marked decrease in crystallinity, which is already clear from the XRPD pattern of TiNZn5 (Fig. 5.1a). This phenomenon can be rationalized considering the sharp difference among the crystalline habits of TiO_2 polymorphs and ZnO wurtzite (the most likely ZnO polymorph to form in the adopted synthetic conditions, space group: $P6_3mc$; hexagonal structure), which might inhibit the TiO_2 crystal growth in the presence of Zn species. As in the case of Sn-modified samples, no well-defined peaks related to segregated phases (ZnO polymorphs) are appreciable from XRPD patterns, even at the highest Zn content.

The structural modification in terms of anatase cell distortion is highlighted by the shift of the anatase (101) diffraction peak towards lower 2θ values for both N- and metal-modified samples with respect to the pristine Ti material (Fig. 5.1a). A shift of 0.05° was recorded in the case of N- and N,Zn-modified samples, with respect to the pristine material. A distortion of the anatase cell was previously reported by Lo Presti and co-authors[22] in the case of N-doped samples. A more marked shift (0.1°) was recorded in the case of TNSn5. It is worth noting that the TiNSn20 sample shows a phase transition to rutile.

These results suggest a higher affinity of Sn species for the titania lattice with respect to the Zn species, due to either the same oxidation state of Ti or its tendency to form the same tetragonal polymorphic structure. Differently, the presence of Zn, characterized by lower valence and its growth in hexagonal wurtzite, mostly decreases the sample crystallinity.

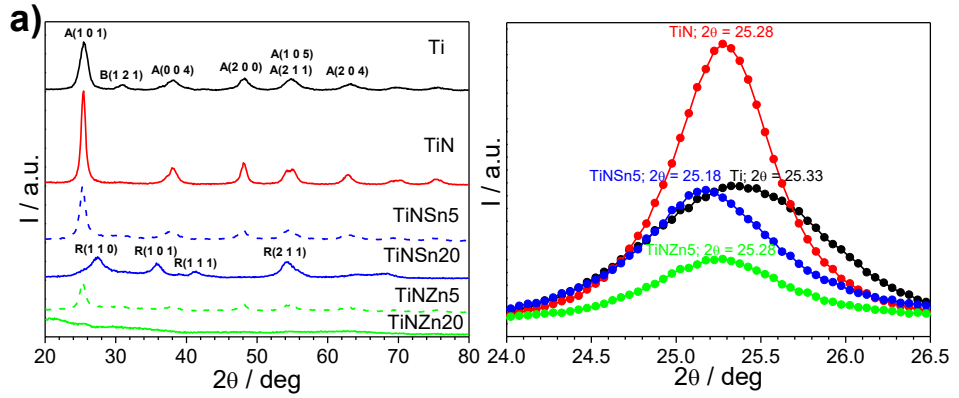

a) XRPD patterns of the synthesized samples (left) (the main peaks of anatase, brookite and rutile are highlighted); together with highlighting of the anatase (101) peak shift for selected samples (right).

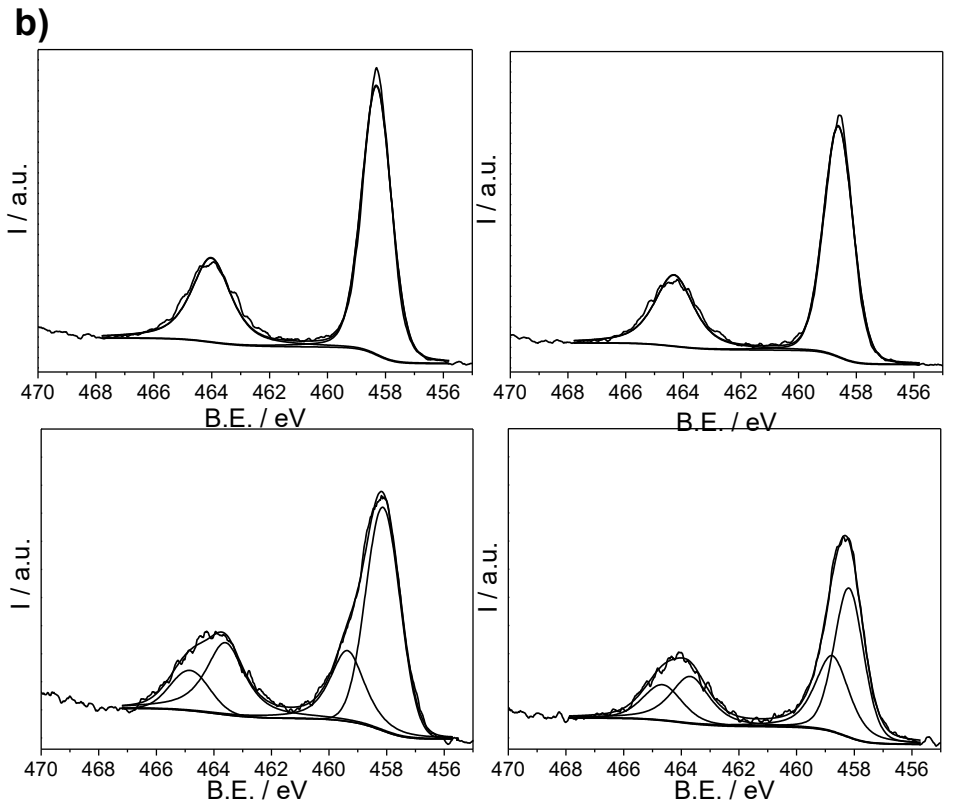

b) XPS spectra of the Ti 2p region for the Ti (top, left), TiN (top, right), TiNSn5 (bottom, left) and TiNZn5 (bottom, right) samples.

Figure 5.1 – Structural (XRPD) and spectroscopic (XPS) results.

In order to corroborate XRPD outcomes, XPS spectra were acquired. All samples show the presence of Ti(IV) (Fig. 5.1b, Ti $2p_{3/2}$ and Ti $2p_{1/2}$ peaks

at 458.5 and 464.0 eV, respectively), while Sn(IV) (3d region at 486.1 and 494.8 eV) and Zn(II) (2p region at 1021.5 and 1044.0 eV) peaks were detected in metal-modified samples (Fig. 5.2a). Slightly higher Sn/Zn contents with respect to the nominal amounts were measured by XPS, possibly indicating the occurrence of surface segregation phenomena of metal guest species. On the other hand, Sn/Ti and Zn/Ti molar ratios, retrieved by EDX analyses, are comparable to the theoretical amount, within experimental error, for all metal-modified samples. It should be noted that EDX analyses have a local character and results might not be indicative of the whole sample elemental composition. Furthermore, in the case of Sn- and Zn-modified samples, peak components ascribable to Ti(IV+δ) species (459.1 and 464.8 eV) were appreciable[24]. The Ti(IV+δ)/Ti(IV) ratios (*ca.* 0.4 and 0.7 for TiNSn5 and TiNZn5, respectively) support a higher surface defectivity in the case of Zn-modified systems (Fig. 5.1b). The O 1s region (Fig. 5.2b) exhibits for all samples a multi-component signal, presenting a main peak at around 529.6 eV (peak I in Fig. 5.2b), attributable to lattice O species, and two minor components centred at ~ 530.8 eV (peak II) and ~ 532.0 eV (peak III), which can be related to surface hydroxyls and chemisorbed oxygen species, respectively[25,26]. While no significant differences in the O 1s peak positions were appreciable, the relative intensities of peak components markedly vary among the samples. In particular, the components at higher B.E. were significantly more intense in the metal-modified samples with respect to Ti and TiN, also supporting a higher defectivity of these samples.

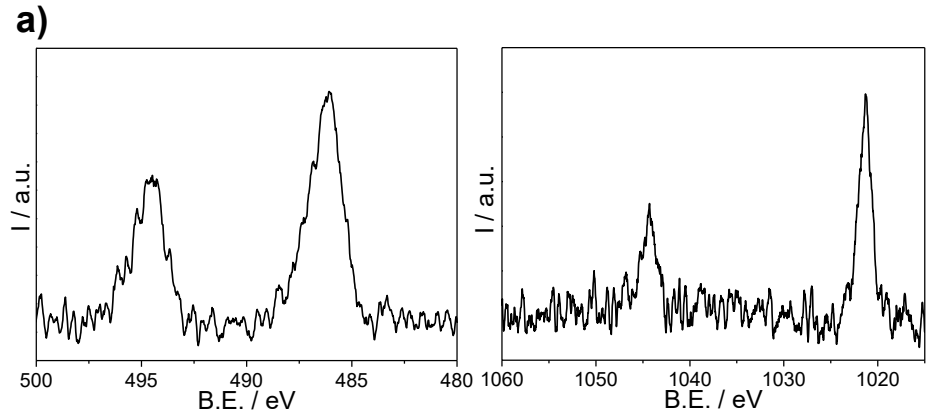

a) XPS spectra of the Sn 3d region for TiNSn5 (left) and of the Zn 2p region for TiNZn5 (right).

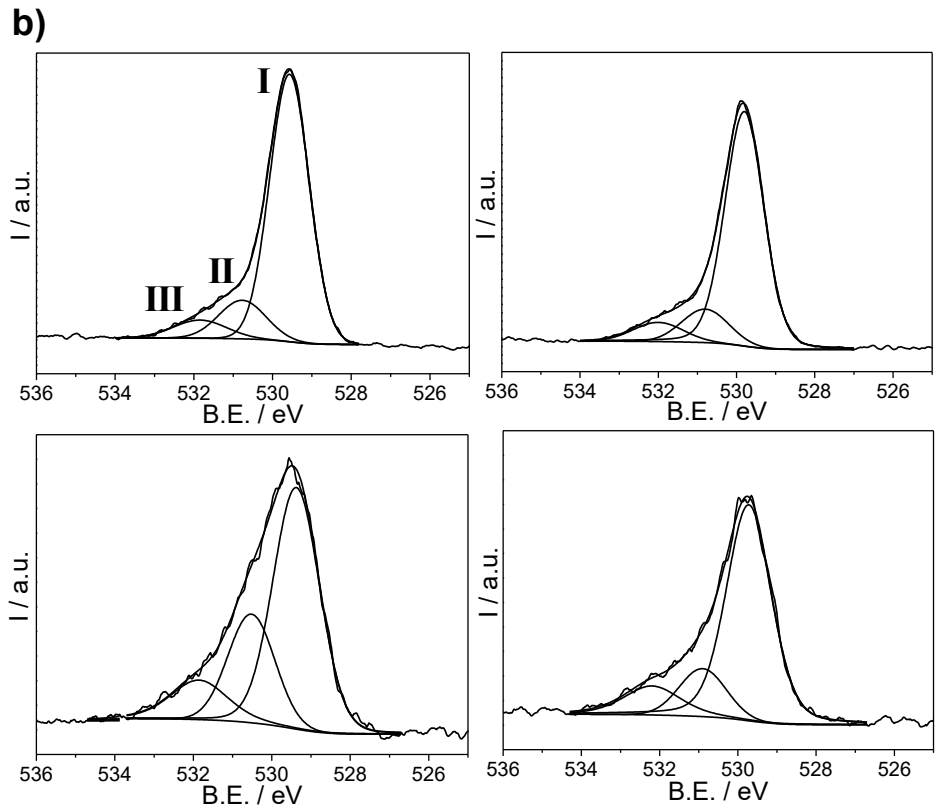

b) XPS spectra of the O 1s region for the Ti (top, left), TiN (top, right), TiNSn5 (bottom, left) and TiNZn5 (bottom, right) samples.

Figure 5.2 – Further X-ray photoelectron spectroscopy characterization.

Figure 5.3 reports HR-TEM micrographs of bare and promoted TiO_2. Both Ti and TiN samples show pseudo-spherical crystallites with a good degree of crystallinity and interplanar distances characteristics of anatase TiO_2 (d_{101} = 0.339–0.342 nm), in good agreement with XRPD findings. The TiNSn5 sample shows crystalline particles (3–6 nm) in which both anatase (d_{101} = 0.339–0.342 nm) and brookite (d_{211} = 0.291–0.294 nm) interplanar distances are recognizable. However, with respect to XRPD results, a small content of SnO_2 cassiterite (d_{111} = 0.223–0.227 nm; inset of Fig. 3c) is appreciable. In the case of TiNSn20, crystalline particles with a broader size distribution (showing also particles over 10 nm) are appreciable. Interplanar distances reveal the presence of rutile (d_{101} = 0.246–0.249 nm), as well as of SnO_2 cassiterite (d_{101} = 0.260–0.263 nm). The addition of Zn leads to a broader size distribution and poorer sample crystallinity, as well as to a higher amorphous content, in agreement with XRPD findings. However, also in the case of Zn, HR-TEM analyses show the presence of a guest oxide phase (ZnO wurtzite, d_{101} = 0.290–0.293 nm), which was not detected by XRPD, possibly due to both the low amount and the oxide preferential segregation at the photocatalyst surface.

Sample	phase composition (%)	$<D_v>$ (nm)	guest/Ti (EDX) (at. %)	S_{BET} ($m^2\ g^{-1}$)	V_{pores} ($mL\ g^{-1}$)	E_g (eV)	ζ potential (mV)
Ti	66 A – 34 B	6	-	188	0.308	3.26	+ 23.7
TiN	88 A – 12 B	12	-	115	0.096	3.22	+ 26.5
TiNSn5	78 A – 22 B	9	5.8	215	0.079	3.11	+ 14.7
TiNSn20	100 R *	11	26.1	197	0.104	3.12	+ 9.7
TiNZn5	100 A ‡	9	5.7	272	0.087	3.13	+ 18.2
TiNZn20	-	-	19.9	311	0.108	3.17	+ 14.2

* A small amount of anatase cannot be excluded. ‡ Amorphous phase is also appreciable.

Table 5.1 – Phase composition (A: anatase, B: brookite, R: rutile) and average crystallite size of the most abundant phase, estimated from XRPD analyses, $<D_v>$; guest/Ti molar ratios determined from EDX analyses; specific surface area, S_{BET}, and total pore volume, V_{pores}; apparent band gap values determined by Kubelka-Munk approach, E_g; ζ-potential values at pH 4.

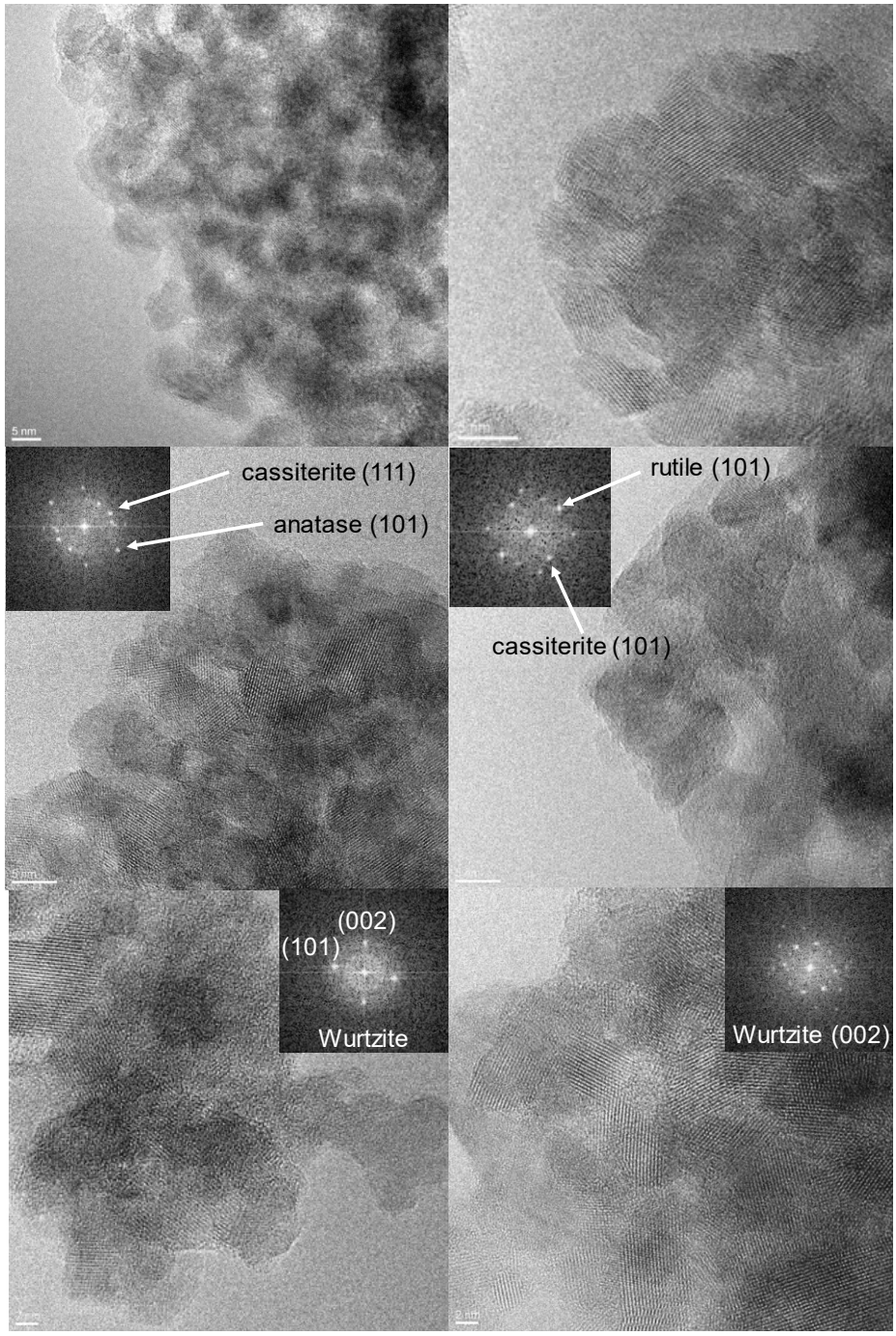

Figure 5.3 – HR-TEM images of Ti (top, left), TiN (top, right), TiNSn5 (middle, left), TiNSn20 (middle, right), TiNZn5 (bottom, left), and TiNZn20 (bottom, right). Insets: FFT patterns of the investigated polymorphs.

N_2 adsorption-desorption isotherms under subcritical conditions (T = –196 °C) of all samples are characteristic of mesoporous materials (Fig. 5.4a). While the undoped sample presents an H2-type hysteresis loop with high total porosity, N-doping sharply decreases the total porosity for all the sensitized samples (Tab. 5.1). In this regard, all the prepared powders exhibit invariably a notable decrease of the average pore size with respect to the pristine TiO_2, as well as a drop in the total pore volume (Tab. 5.1), when either N or metal species are introduced. The sole N-doping also leads to a notable decrease in surface area with respect to the undoped reference, as a result of lower total porosity and larger crystallites. On the other hand, metal addition invariably resulted in larger surface areas, more so in the case of Zn-modified samples, as expected on the grounds of their higher amorphous content. The higher specific surface area of Zn-modified samples might favour a TC degradation pathway involving a direct attack of photogenerated holes to the adsorbed pollutant molecule.

Moreover, the photocatalyst surface features were characterized by ζ-potential measurements performed at the pH conditions of photocatalytic tests (pH *ca.* 4). All samples show a positive value of the ζ-potential, *i.e.* a positive surface charge. The highest values were found for the pristine and the N-doped samples, while the introduction of the metal species decreases the surface charge of the material, more so in the case of Sn and of higher metal content (Tab. 5.1). The lower surface charge of metal-modified samples might favour the adsorption of TC, due to its partial speciation as positively charged species at the photocatalytic test conditions[27].

DRS spectra revealed the typical sigmoidal shape for undoped TiO_2 (Fig. 5.4b). Band gap values of the prepared materials were evaluated by applying the Kubelka-Munk elaboration. The band gap of the Ti sample was determined to be 3.26 eV, as expected on the grounds of its phase composition (anatase and brookite have a reported band gap of 3.2 and *ca.* 3.3 eV, respectively[28,29]). N-doping led to a localized light absorption in the visible region in the 400–550 nm range, which resulted in a slight decrease of the apparent band gap (3.22 eV). This absorption has been previously reported in the case of N-doped samples[28,30–33] and attributed to mid-gap states introduced by interstitial nitrogen[2], often related to enhanced recombination effects.

Sn- and Zn-modified samples show different behaviours in terms of light absorption (Fig. 5.4b). Sn-modified samples behave similarly to N-doped TiO_2. With respect to the latter, however, Sn-modified samples present a slight redshift of the absorption edge and a more marked absorption in the 400–600 nm range. Both effects are more appreciable increasing the Sn content. A similar effect was reported in the case of Nb,N-codoped samples[16,17] and attributed to charge compensation phenomena taking place between the two guest species. In the case of the Sn-promoted samples, the observed visible sensitization cannot be explained by the presence of segregated oxide, due to the large band gap of SnO_2 (3.6 eV). It is therefore indicative of the formation of intragap states as a consequence of the introduction of defects/heteroatoms in the TiO_2 lattice. Zn-promoted samples show a redshift of the absorption edge as well, resulting in a decrease of the apparent band gap (Tab. 5.1). However, the N-doping characteristic absorption in the visible region is less appreciable in these samples and does not vary with the Zn-content. This effect might be indicative of a lower N content introduced in the TiO_2 lattice, due to the lower crystallinity and higher amorphous content of Zn-modified samples.

5.1.2 Photocatalytic tests

The prepared photocatalysts were tested toward the degradation of an emerging water pollutant, tetracycline, under both UV and simulated solar light irradiation. A photocatalytic time of 3 h was selected to obtain an almost complete disappearance of the TC molecule (Tab. 5.2) for all the tested photocatalysts under UV light in the adopted experimental conditions. Initial kinetic constants under UV irradiation (Tab. 5.2) revealed the most performing photocatalyst to be Ti, while guests introduction resulted in a decrease of the molecule degradation rate, in particular for metal (Sn and Zn)-modified samples. Undoped Ti shows a higher TC disappearance kinetic constant also with respect to TiN, in agreement with its larger surface area. Fig. 5.4c compares the mineralization degrees of the synthesized samples at the end of the photocatalytic tests. An incomplete mineralization is observed in all cases, even under UV irradiation, reaching the highest value (73%) for the Ti sample. The undoped Ti and TiN present a fully comparable mineralization degree due to the balancing of morphological and structural effects: on one

side, the undoped Ti sample presents a higher surface area, while TiN shows a higher content in anatase, often regarded as the most active TiO_2 crystal phase. These two effects can partly balance off and lead to comparable mineralization degrees for the two samples under a high intensity UV light (*i.e.*, in favourable reaction conditions). The mineralization trend under UV irradiation (Fig. 5.4c) shows invariably a worse performance for metal-modified samples with respect to Ti and TiN, more so for Zn-doped photocatalysts and in the case of the highest metal content (guest metal/Ti molar ratio of 20%).

The scenario is completely different for photocatalytic tests performed under simulated solar light irradiation. As expected on the grounds of the lower effective power density and broader wavelength range, a slower TC disappearance is appreciable under simulated solar irradiation than under UV light (Tab. 5.2) leading to an incomplete molecule disappearance in the investigated reaction time (Tab. 5.2 and Fig. 5.4d) and lower mineralization degrees (Fig. 5.4c) are observed with respect to UV tests. Furthermore, all the metal-modified samples present higher mineralization with respect to the undoped and N-doped samples (Fig. 5.4c). TiNSn5 showed the best overall performance. The TiNZn20 sample presents a similar mineralization degree with respect to TiNSn5, even though the kinetic constant (Tab. 5.2) is far lower, suggesting differences in the reaction pathways between the two samples. With respect to N-doped TiO_2, whose visible light absorption does not result in an improved visible light activity, Sn,N- and Zn,N-copromoted samples show a synergistic effect in terms of both visible light absorption and photocatalytic activity, as also reported in previous literature reports[19–21].

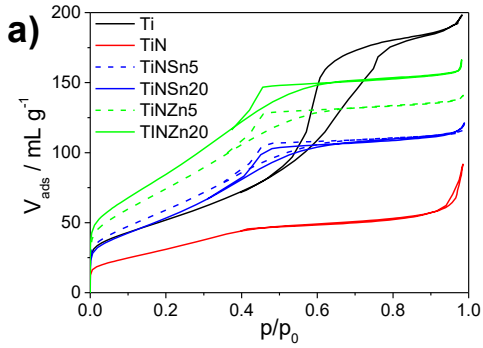

b) N_2 adsorption–desorption isotherms under subcritical conditions for all samples.

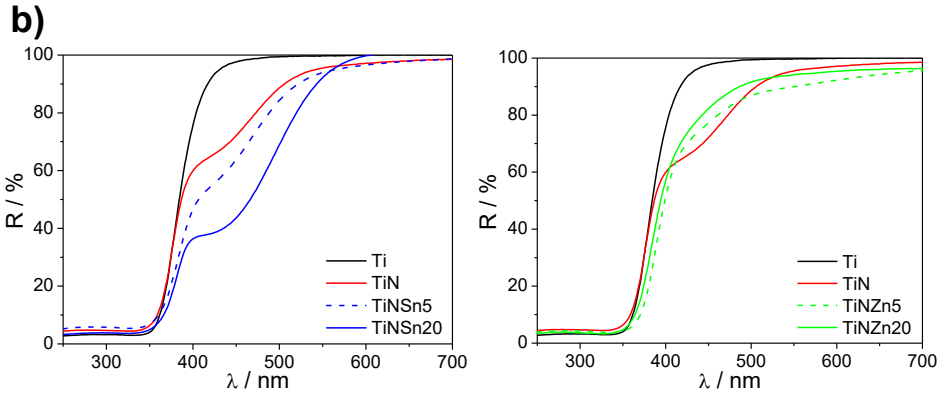

b) Diffuse reflectance spectra for Sn (left) and Zn (right) modified samples.

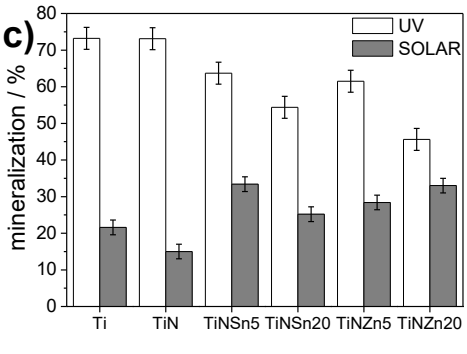

c) Mineralization degrees at the end of the photocatalytic test under UV and simulated solar irradiation.

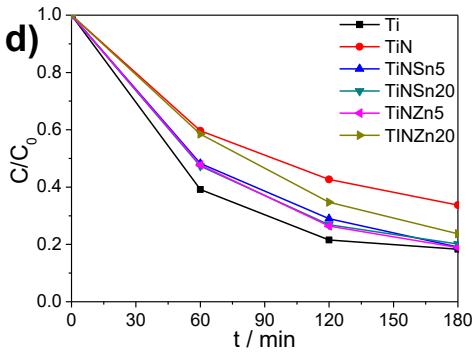

d) Tetracycline disappearance with respect to time simulated solar photocatalytic tests.

Figure 5.4 – Morphological, optical and photocatalytic results.

On the grounds of these results, the tetracycline photocatalytic degradation mechanisms reported in Figure 5.5 can be proposed in the case of pure, N-doped and metal-modified samples, after 35 minutes of UV

irradiation. The reported by-products have been identified by evaluating the *m/z* values from MS spectra. Starting from the pristine TC molecule ($[TC+H]^+$, *m/z* 445) and its relative Na-adduct ($[TC+Na]^+$, *m/z* 467), two diverse attacks could be hypothesized, mediated by either OH radicals (route a) or photogenerated holes, h^+ (route b), on the grounds of literature results[34–36]. In the former, the degradation may imply several steps consisting in dehydroxylations, loss of the $–N(CH_3)_2$ group and formation of a carboxylic termination eventually leading to product A ($[A+H]^+$, *m/z* 371)[37]. Then, a ring opening occurs ($[B+H]^+$, *m/z* 297) followed by oxidation reactions and the loss of the methyl group ($[C+H]^+$, *m/z* 242). This latter compound was identified by Niu *et al.* in the case of tetracycline photodegradation by TiO_2[34]. Further degradation products, with *m/z* 203 and 172 ($[D+H]^+$ and $[E+H]^+$, respectively) come from the progressive breakage of the aromatic rings[38]. MS analyses were carried out also after longer irradiation time (65 min). With respect to the relative spectrum at 35 min, the same main peaks were appreciable although with different relative intensities. In particular, the peaks associated with the TC molecule ($[TC+H]^+$, *m/z* 445, and the Na-adduct $[TC+Na]^+$, *m/z* 467) markedly decrease in intensity, in agreement with the kinetic and mineralization data. Route b, on the contrary, assumes the dealkylation of the tertiary amine ($[F+H]^+$, *m/z* 417)[34], the subsequent loss of $–NH_2$ and the reduction of the amide group to a ketone moiety ($[G+H]^+$, *m/z* 301). Nevertheless, no other lower molecular weight intermediates can be detected.

By detecting these intermediates in the MS spectra, Ti, TiN, and TiNSn20 seem to follow path a, whereas with the Zn-modified sample (TiNZn20), route b has to be preferred. In the latter case, the formation of F and G by-products might hinder any further oxidation steps: actually, TiNZn20 shows lower photocatalytic performance (Tab. 5.2) and mineralization degree.

In the case of solar light tests, the data concerning 3 h reaction time were selected, due to the lower degradation rate with respect to UV irradiation. In this case, the lower signal to noise ratios in the case of the metal-modified samples with respect to the pristine Ti sample indicated the presence of a lower amount of by-products, due to their higher photocatalytic efficiency under solar light with respect to the undoped sample. Moreover, lighter by-products were also detected ascribable to

both pathways. While the pristine and Sn-promoted samples exhibit the same main degradation intermediates under both UV and similar solar irradiation, Zn,N-modified samples exhibit different by-products in the two series of tests. Hence, the possibility of different degradation pathways prevailing under simulated solar irradiation cannot be excluded. It is noteworthy that both pristine and Sn-promoted samples show a relatively fast TC disappearance but a comparatively lower mineralization degree, whereas Zn-promoted samples despite the slower kinetic constant (Tab. 5.2) show appreciable mineralization.

Sample	UV		Simulated solar	
	disapp. (%)	k (10^{-3} min^{-1})	disapp. (%)	k (10^{-3} min^{-1})
Ti	100	78 ± 4	82	13.4 ± 0.8
TiN	100	56 ± 1	66	7.4 ± 0.4
TiNSn5	100	43 ± 1	81	10.7 ± 0.5
TiNSn20	99	53 ± 2	80	11.3 ± 0.4
TiNZn5	99	38 ± 1	81	11.3 ± 0.4
TiNZn20	95	51 ± 5	76	8.8 ± 0.1

Table 5.2 – TC disappearance after 3 h of irradiation and initial pseudo-first order kinetic constants of TC disappearance, k, for photocatalytic tests under UV and simulated solar irradiation.

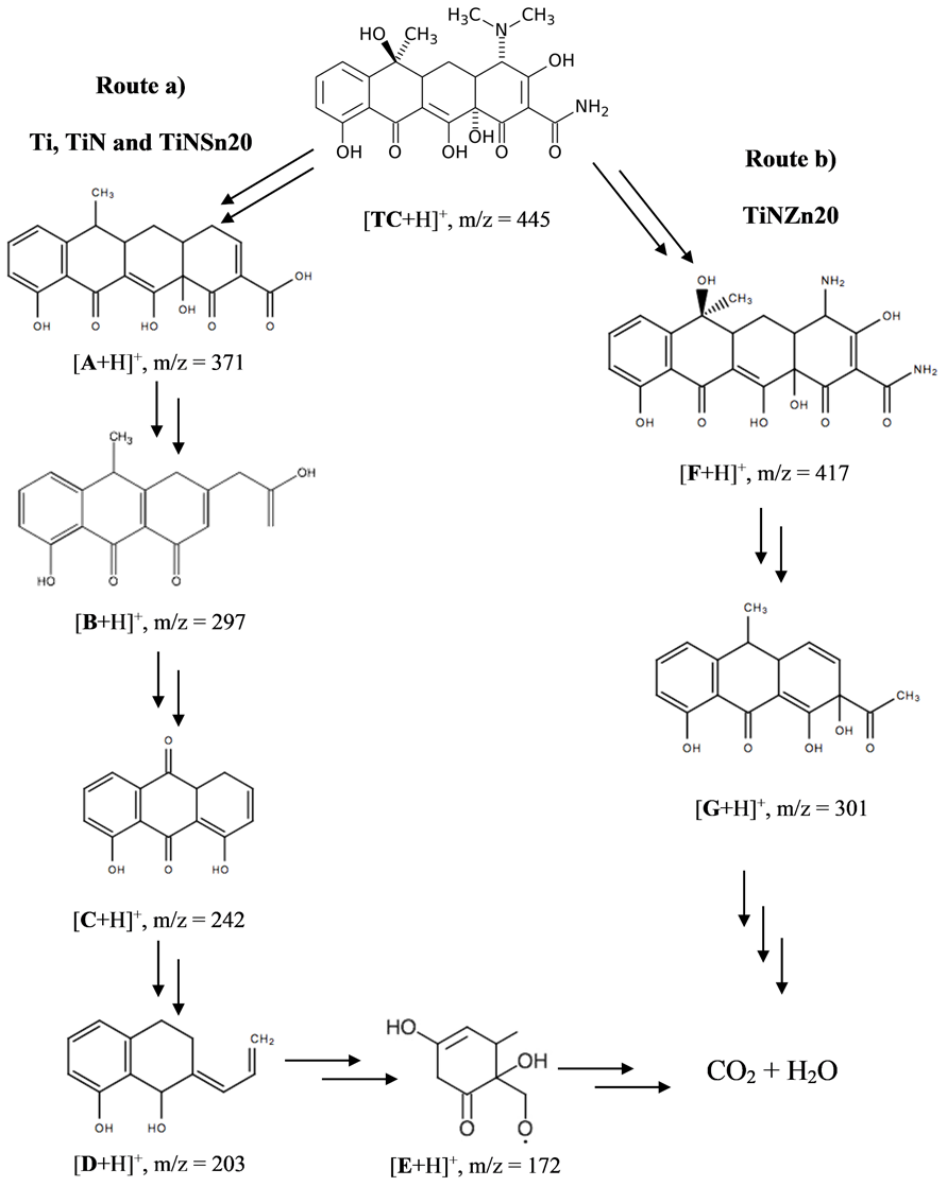

Figure 5.5 – Proposed initial photocatalytic degradation mechanisms of TC under UV irradiation source.

5.2 Conclusions

In this work, the modifications imparted by Sn and Zn species on the physicochemical properties and photocatalytic activity of N-doped TiO_2

photocatalysts are presented. The metal (Sn, Zn) addition leads to significant variations of the structural, morphological, spectroscopic and surface properties with respect to both the pristine and the N-doped titania.

Metal promoters are present as Sn(IV) and Zn(II) species within the samples, as shown by Sn 3d and Zn 2p XPS spectra. HR-TEM images show the presence of crystalline phases of Sn and Zn oxides. However, despite the high metal contents investigated, no segregated SnO_2/ZnO phases are appreciable from XRPD patterns. Considering the higher surface content of metal species shown by XPS analyses, and the marked change in surface charge shown by ζ-potential measurements, a preferential location of the segregated metal species at the sample surface can be proposed. The addition of both metals leads to a general increase in the TiO_2 defectivity, as appreciable from Ti 2p and O 1s XPS spectra. However, the two metal species seem to have instead two different effects on the TiO_2 lattice. Sn promotes the formation of rutile TiO_2, which can be expected on the grounds of the structural similarity of TiO_2 rutile ($P4_2/mnm$, a = 4.5937 Å, c = 2.9587 Å) and SnO_2 cassiterite ($P4_2/mnm$, a = 4.7382 Å, c = 3.1871 Å). Considering the similar ionic radii of Ti(IV) and Sn(IV) species[39], Sn species could partially substitute Ti in the TiO_2 lattice, as also supported by the observed shift of XRPD peak position for Sn-modified samples. On the other hand, the introduction of Zn leads mainly to a loss of TiO_2 crystallinity (appreciable in both XRPD patterns and HR-TEM images), which can be rationalized considering the marked structural diversity of ZnO wurtzite ($P6_3mc$; hexagonal structure a = 3.82, c = 6.26) with respect to the main TiO_2 polymorphs. These structural differences might explain the observed electronic features of the two sets of metal-promoted materials: DRS spectra show the formation of intragap states for Sn-promoted samples, possibly due to heteroatoms[19], whereas in the case of Zn-modified samples, the observed optical features (such as, a redshift of the absorption edge) could be related to the increased TiO_2 defectivity[40].

At the investigated metal content, partial segregation of the guest oxides is appreciable only by HR-TEM, while other marked structural changes are observed by XRPD: favoured rutile formation for Sn-modified samples and higher amorphous content for Zn-modified ones. The higher defectivity of metal-modified samples, shown not only by XRPD analyses but also by the relevant changes in the surface properties (XPS and ζ-potential

measurements), crucially affects the samples' optical and electronic features (DRS). Both sets of metal-promoted samples display a redshift of the absorption edge with respect to both pure and N-doped TiO_2, and a light absorption component at longer wavelength which can be attributed to intragap states related to lattice defects. The higher surface defectivity and the lower ζ-potential values with respect to both pristine and N-doped TiO_2, together with the enhanced surface area, can promote TC adsorption and subsequent degradation in the case of the metal-modified photocatalysts. In agreement with previous reports[16,30], the sole N-doping, despite the increased visible light harvesting, fails to enhance the photocatalytic activity under simulated solar irradiation with respect to the pristine sample. This phenomenon has been attributed to favoured recombination pathways of photogenerated charges due to mid-gap states generated by N doping, particular interstitial one[16,30]. The addition of metal species, instead, bestowed enhanced photocatalytic performance in the tetracycline mineralization under simulated solar light with respect to both the pristine and N-doped samples. As the formation of segregated guest oxide phases comes along with the modification of the host lattice, it is complex to single out the effect of a specific photocatalyst feature on its photocatalytic activity. However, the better performance of the metal-modified photocatalysts under simulated sunlight can be related to their optical and electronic features, arising from the higher defectivity with respect to both pure and N-doped samples. Moreover, it is worth noting that, as already reported by other researchers[41,42], the detrimental effect of crystallinity loss, as here observed in particular for Zn-modified samples, can be overcome by a surface area enhancement and a major defectivity of the sample, beneficial for the photocatalytic efficiency under solar or visible light.

The modifications of the physicochemical features induced by metal species also stand at the basis of the differences in the photocatalytic degradation mechanism of Sn- and Zn-modified samples which were identified here for the first time. In particular, the prevalence of a direct attack mechanism in Zn-modified samples was related to their higher surface areas and surface defectivity, arising from the low structural compatibility between ZnO and TiO_2 species.

5.3 Specific procedures

Samples preparation. Reactants were purchased from Sigma-Aldrich and used without further purification. Solutions and suspensions were prepared with doubly-distilled water, passed through a Milli-Q apparatus.

In a typical synthesis, carried out at 60 °C, 10.7 g of titanium(IV) isopropoxide and 11.3 g of 2-propanol were mixed for 15 min. In the case of the metal modified samples, the required amount of $SnCl_4 \cdot 5H_2O$ or $ZnCl_2$ was dissolved in the mixture. Successively, 65 mL of either NH_4OH (N/Ti molar ratio = 0.5) or KOH aqueous solution for N-doped and undoped samples, respectively, was added drop-by-drop while stirring vigorously (300 rpm). In both cases, the base solution concentration was adjusted in order to obtain a final pH of 9. The reaction mixture was then stirred for 90 min to complete the hydrolysis. The resulting precipitate was washed three times by centrifugation-resuspension cycles and later dried at 80 °C overnight. Finally, the xerogel was calcined at 400 °C for 6 h under oxygen flux (9 NL h^{-1}). TiO_2 samples were labelled as Ti, TiN, TiNSnx, and TiNZn*x* for undoped, N-doped and N,metal co-promoted samples, respectively, where *x* identifies the metal/Ti molar ratio (5 or 20%).

Photocatalytic activity tests. All samples were tested toward the photocatalytic degradation of tetracycline hydrochloride in water under both UV and simulated solar light irradiation. Photocatalytic experiments were performed at 20 °C in a 300-mL jacketed reactor using an initial TC concentration of 35 mg L^{-1} and a photocatalyst concentration of 0.5 g L^{-1}. An oxygen flux (9 NL h^{-1}) was bubbled in the reactor during the photocatalytic experiments. Before light irradiation, samples were left in the dark for 30 min in order to reach the adsorption equilibrium. Photolysis tests were also conducted to quantify the molecule degradation in the absence of photocatalyst, leading to less than 5% mineralization. Initial kinetic constants (pseudo-first order) were calculated within 35 min and 120 min of irradiation in the case of UV and solar irradiation, respectively.

Further details about the preparation and characterization methods can be found in Appendix A.

References

1 R. Asahi, T. Morikawa, T. Ohwaki and Y. Taga, *Science (80-.).*, 2001, **293**, 269–271.

2 R. Asahi, T. Morikawa, H. Irie and T. Ohwaki, *Chem. Rev.*, 2014, **114**, 9824–9852.

3 P. V Kamat, *J. Phys. Chem. Lett.*, 2012, **3**, 663–672.

4 G. Liu, L. Wang, H. G. Yang, H.-M. Cheng and G. Q. (Max) Lu, *J. Mater. Chem.*, 2010, **20**, 831–843.

5 X. Li, C. Gao, H. Duan, B. Lu, Y. Wang, L. Chen, Z. Zhang, X. Pan and E. Xie, *Small*, 2013, **9**, 2005–2011.

6 A. Enesca, M. Baneto, D. Perniu, L. Isac, C. Bogatu and A. Duta, *Appl. Catal. B Environ.*, 2016, **186**, 69–76.

7 F. Xie, Y. Li, J. Dou, J. Wu and M. Wei, *J. Power Sources*, 2016, **336**, 143–149.

8 H. Cao, S. Huang, Y. Yu, Y. Yan, Y. Lv and Y. Cao, *J. Colloid Interface Sci.*, 2017, **486**, 176–183.

9 M. Kwiatkowski, R. Chassagnon, O. Heintz, N. Geoffroy, M. Skompska and I. Bezverkhyy, *Appl. Catal. B Environ.*, 2017, **204**, 200–208.

10 L. Lv, X. Bai and Z. Ye, *CrystEngComm*, 2016, **18**, 7580–7589.

11 E. A. Floriano, L. V. A. Scalvi, M. J. Saeki and J. R. Sambrano, *J. Phys. Chem. A*, 2014, **118**, 5857–5865.

12 R. Wang, H. Tan, Z. Zhao, G. Zhang, L. Song, W. Dong and Z. Sun, *J. Mater. Chem. A*, 2014, **2**, 7313.

13 J. J. Brancho and B. M. Bartlett, *Chem. Mater.*, 2015, **27**, 7207–7217.

14 X. Ma, Y. Wu, Y. Lu, J. Xu, Y. Wang and Y. Zhu, *J. Phys. Chem. C*, 2011, **115**, 16963–16969.

15 Q. Meng, T. Wang, E. Liu, X. Ma, Q. Ge and J. Gong, *Phys. Chem. Chem. Phys.*, 2013, **15**, 9549–61.

16 L. Rimoldi, C. Ambrosi, G. Di Liberto, L. Lo Presti, M. Ceotto, C. Oliva, D. Meroni, S. Cappelli, G. Cappelletti, G. Soliveri and S. Ardizzone, *J. Phys. Chem. C*, 2015, **119**, 24104–24115.

17 C. Marchiori, G. Di Liberto, G. Soliveri, L. Loconte, L. Lo Presti, D. Meroni, M. Ceotto, C. Oliva, S. Cappelli, G. Cappelletti, C. Aieta

and S. Ardizzone, *J. Phys. Chem. C*, 2014, **118**, 24152–24164.
18 E. Wang, T. He, L. Zhao, Y. Chen and Y. Cao, *J. Mater. Chem.*, 2011, **21**, 144–150.
19 H. Zhuang, Y. Zhang, Z. Chu, J. Long, X. An, H. Zhang, H. Lin, Z. Zhang and X. Wang, *Phys. Chem. Chem. Phys.*, 2016, **18**, 9636–9644.
20 N. Kaur, S. K. Shahi and V. Singh, *Photochem. Photobiol.*, 2016, **92**, 69–75.
21 Y. Hu, G. Chen, C. Li, Y. Yu, J. Sun and H. Dong, *New J. Chem.*, 2015, **39**, 2417–2420.
22 L. Lo Presti, M. Ceotto, F. Spadavecchia, G. Cappelletti, D. Meroni, R. G. Acres and S. Ardizzone, *J. Phys. Chem. C*, 2014, **118**, 4797–4807.
23 M. Ceotto, L. Lo Presti, G. Cappelletti, D. Meroni, F. Spadavecchia, R. Zecca, M. Leoni, P. Scardi, C. L. Bianchi and S. Ardizzone, *J. Phys. Chem. C*, 2012, **116**, 1764–1771.
24 E. Pargoletti, G. Cappelletti, A. Minguzzi, S. Rondinini, M. Leoni, M. Marelli and A. Vertova, *J. Power Sources*, 2016, **325**, 116–128.
25 S. Ardizzone, C. L. Bianchi and D. Tirelli, *Colloids Surfaces A Physicochem. Eng. Asp.*, 1998, **134**, 305–312.
26 L. Jing, B. Xin, F. Yuan, L. Xue, B. Wang and H. Fu, *J. Phys. Chem. B*, 2006, **110**, 17860–17865.
27 M. Brigante and P. C. Schulz, *J. Hazard. Mater.*, 2011, **192**, 1597–1608.
28 V. N. Kuznetsov and N. Serpone, *J. Phys. Chem. C*, 2009, **113**, 15110–15123.
29 A. Di Paola, M. Bellardita and L. Palmisano, *Catalysts*, 2013, **3**, 36–73.
30 D. Meroni, S. Ardizzone, G. Cappelletti, C. Oliva, M. Ceotto, D. Poelman and H. Poelman, *Catal. Today*, 2011, **161**, 169–174.
31 N. Serpone, *J. Phys. Chem. B*, 2006, **110**, 24287–24293.
32 G. Liu, G. Y. Hua, X. Wang, L. Cheng, J. Pan, Q. L. Gao and H. M. Cheng, *J. Am. Chem. Soc.*, 2009, **131**, 12868–12869.
33 S. Livraghi, M. C. Paganini, E. Giamello, A. Selloni, C. Di Valentin and G. Pacchioni, *J. Am. Chem. Soc.*, 2006, **128**, 15666–15671.
34 J. Niu, S. Ding, L. Zhang, J. Zhao and C. Feng, *Chemosphere*, 2013,

93, 1–8.
35 R. A. Palominos, M. A. Mondaca, A. Giraldo, G. Peñuela, M. Pérez-Moya and H. D. Mansilla, *Catal. Today*, 2009, **144**, 100–105.
36 X. D. Zhu, Y. J. Wang, R. J. Sun and D. M. Zhou, *Chemosphere*, 2013, **92**, 925–932.
37 M. Cao, P. Wang, Y. Ao, C. Wang, J. Hou and J. Qian, *J. Colloid Interface Sci.*, 2016, **467**, 129–139.
38 L. Jinhai, M. Han, Y. Guo, F. Wang, L. Meng, D. Mao, S. Ding and C. Sun, *Appl. Catal. A Gen.*, 2016, **524**, 105–114.
39 J. C. Slater, *J. Chem. Phys.*, 1964, **41**, 3199–3204.
40 V. N. Kuznetsov, V. K. Ryabchuk, A. V. Emeline, R. V. Mikhaylov, A. V. Rudakova and N. Serpone, *Chem. Mater.*, 2013, **25**, 170–177.
41 Y. Li, T. Sasaki, Y. Shimizu and N. Koshizaki, *J. Am. Chem. Soc.*, 2008, **130**, 14755–14762.
42 D. Zywitzki, H. Jing, H. Tüysüz and C. K. Chan, *J. Mater. Chem. A*, 2017, **5**, 10957–10967.

This Chapter has been adapted with permission from Rimoldi *et al.*, *Catal. Today*, 2018, **313**, 40−46.

Chapter 6

Insights on the photocatalytic degradation processes supported by TiO_2/WO_3 systems. The case of ethanol and tetracycline

As already described in the previous Chapters, titanium dioxide (TiO_2) despite being the most adopted semiconductor in the field of photocatalysis, suffers from high e^-/h^+ recombination rates and a large band gap, which significantly decrease its performance especially under solar or visible irradiation. In order to increase the performance of TiO_2, one of the most common techniques is semiconductor engineering. In this sense, semiconductors coupling is commonly adopted for decreasing the recombination rate by exploiting charge separation effects. In this context, the band gap alignment between the coupled semiconductors is pivotal for efficient charge separation. WO_3 has been proposed as a promising semiconductor which can promote longer wavelength absorption with respect to TiO_2 thanks to its lower band gap (2.8 eV)[1] and disfavour charge recombination in composite systems. In fact, the conduction band edge of WO_3 is placed at a more positive potential than the one of TiO_2 behaving, therefore, as a sink for the photogenerated electrons while the holes remain in the TiO_2 valence band.

WO_3 has been adopted in several works for creating composite materials together with TiO_2, mainly for water splitting, fuel production, (photo)electrochemical and electrochromic applications[2–6]. The use of TiO_2/WO_3 systems for the photocatalytic degradation of organic pollutants has been described by several authors with regards to both air and water pollutants[3,7–9]. Numerous synthetic procedures have been adopted to obtain TiO_2/WO_3 both by bulk mixing of the components[3,6,10] and by surface

deposition[4,11–13] showing controversial effects of the coupling. Several authors report an increase in the composite photocatalytic activity with respect to both pure oxides. Other authors obtained conflicting results[11,12]. Tada *et al.*, in the case of TiO_2/WO_3 films, show that the photocatalytic activities for both the oxidation of CH_3-CHO in the gas phase and the liquid oxidation of 2-naftol decreased significantly with the composites[14]. This effect was rationalized as due to the decrease of the electron transfer from the semiconductors to O_2. Similarly, Miyauchi *et al.* reported no beneficial effects introduced by the coupling of TiO_2 and WO_3 in photocatalytic oxidation processes[15].

The aim of the work presented in this Chapter is to gather new insights pertaining the role of surface properties of TiO_2/WO_3 systems on their photocatalytic behaviour, with special attention to their reaction mechanisms. A precipitation procedure over TiO_2 sol-gel powder precursors was developed to obtain a preferential surface location of the tungsten oxide. Also on the basis of the results presented in Chapter 4, the surface location of tantalum oxide, displaying increased acidity, was observed to promote the UV degradation of ethanol in the gas phase. In the case of WO_3, its surface acidity has been related to higher pollutant adsorption at the photocatalyst surface, better dispersibility in water and enhanced $^{\bullet}OH$ radical production[11,12]. The role played by the sample composition on the structural, optical and surface features was carefully analysed. The photocatalytic performance was tested both in the liquid and the gas phase towards two pollutants which were extensively studied by us[16–19]: an emerging pollutant (tetracycline) and ethanol as a model molecule for VOCs.

6.1 Results and discussion

6.1.1 Materials characterization

The morphological features of the TW samples were investigated via N_2 adsorption-desorption isotherms collected in subcritical conditions (Fig. 6.1a). All of the TW samples, as well as the T reference, revealed type IV profiles, typical of mesoporous materials. The hysteresis loop, centred around $p/p_0 = 0.5$, can be classified as H2 type, according to the IUPAC

classification, usually referred to the presence of bottleneck-shaped pores. The W addition lead to a progressive increase in the specific surface area and total pore volume (Tab. 6.1), the latter mainly related to pores > 6 nm (Fig. 6.1a). Previous studies[12] have reported similar increases in surface areas at low W concentrations, which were related to the formation of a thin layer of WO_x species hindering the growth and sintering of TiO_2 particles.

The XRPD patterns of the TW samples (Fig. 6.1b) as well as the reference T sample show a good degree of crystallinity and the typical reflections of anatase and a brookite TiO_2 polymorphs. All of the samples are composed by anatase TiO_2 as the main polymorph, while brookite is present as a minor component (Tab. 6.1). The TW samples show a slight increase in the brookite content, although no significant trends in the phase composition were observed with respect to the W content. No reflection peaks attributable to WO_3 phases were detected in the TW samples. Nonetheless, the XRPD pattern of the reference pristine WO_3 sample, prepared by the same precipitation route from H_2WO_4 in the absence of the TiO_2 xerogel, shows the formation of WO_3 in its monoclinic crystalline habit (Fig. 6.1b) with hexagonal WO_3 impurities. The lack of reflections characteristic of WO_3 in TW samples reveals either the presence of highly dispersed WO_x clusters or of an amorphous WO_3 layer on TiO_2, as reported by several authors [11,12].

The average crystallite dimensions were calculated by applying the Scherrer equation on the most intense (101) reflection of anatase (Tab. 1). A slight decrease of the crystallite size is appreciable for increasing W content, in agreement with BET findings.

Sample	S_{BET} ($m^2\ g^{-1}$)	V_{pores} ($mL\ g^{-1}$)	Phase composition	d_a^{101} (nm)	W/Ti at ratio (%)	E_g (eV)
T	141	0.280	75A–25B	8	-	3.25
TW4	151	0.296	65A–35B	7	3.1 ± 0.3	3.23
TW6	158	0.354	64A–36B	6	4.8 ± 0.4	3.23
TW8	170	0.333	68A–32B	6	5.3 ± 0.1	3.24

Table 6.1 – Specific surface area (S_{BET}), total pore volume (V_{pores}), percentage phase composition (A: anatase; B: brookite), anatase average crystallite dimensions (d_a^{101}), W/Ti atomic ratios, and apparent band gap (E_g) of all samples.

The HRTEM inspection of the TW samples (Fig. 6.1c) show small crystallites, in the 4–6 nm interval, exhibiting smooth contours and closed packed nature. These values compare well with the average crystallite size obtained by elaboration of the XRPD peaks. All particles exhibit a highly ordered habit, as it is quite simple to single out fringe patterns confirming the high crystallinity of the materials. The detailed inspections of the distances of the fringe patterns, and the parallel analysis of the diffraction patterns as well, indicate that the crystallites exhibit, with very high frequency, the 0.357 nm distance, corresponding to the (101) family planes of TiO_2 anatase; this is also confirmed by the diffraction patterns marked with nr. 1 in Figure 6.1c. The presence of WO_x species is confirmed by the inspection of the portions of images (marked with nr. 2 in Figure 6.1c), in which both direct image and diffraction indicate the 0.259 nm distance, corresponding to the (131) family planes of WO_3 tungstite (ICDD card n. 00-018-1418 tungstite).

The presence of WO_3 species is also confirmed by the EDS analyses carried out for all the samples in many different portions of the grids. The resulting W/Ti atomic ratios (Tab. 6.1) appear slightly lower than the stoichiometric ratios adopted in the synthetic reaction.

Micro-Raman spectra are reported in Figure 6.2a. Peaks at 149, 190, 402, 517, and 638 cm^{-1} can be attributed to the 1-Eg, 2-Eg, B1g, A1g and 3-Eg modes typical of the anatase tetragonal structure[3,20], in agreement with XRPD results. All spectral components suffer of a slight shift, which can be related to the presence of brookite[21]. Moreover, an additional peak located at *ca.* 970 cm^{-1} is appreciable in TW samples. This band is ascribable, on the basis of both its spectral features and literature data[22], to the W=O mode of surface tungsten-containing species in which W is present with +6 oxidation state. A preferential surface location of WO_x species can be expected as it has been reported that at least 3 mol% of WO_3 is needed to cover in a complete monolayer the much lower surface area of TiO_2 P25[11]. It should be noted the absence of peaks at *ca.* 810 cm^{-1} representative of the O–W–O stretching mode of three-dimensional crystalline WO_3[3,23] and of components in the 1050-1075 cm^{-1} range indicative of WO_x species in tetrahedral coordination[12]. These observations are in good agreement with HRTEM findings[24].

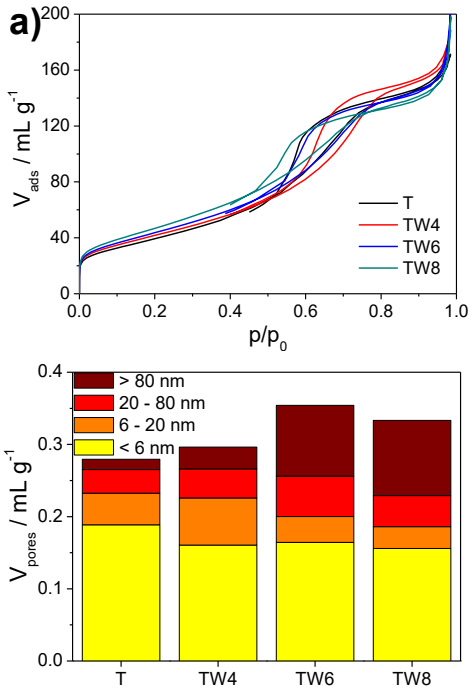

a) N_2 adsorption-desorption isotherms (top) and pore size distribution (bottom) for TW and T samples.

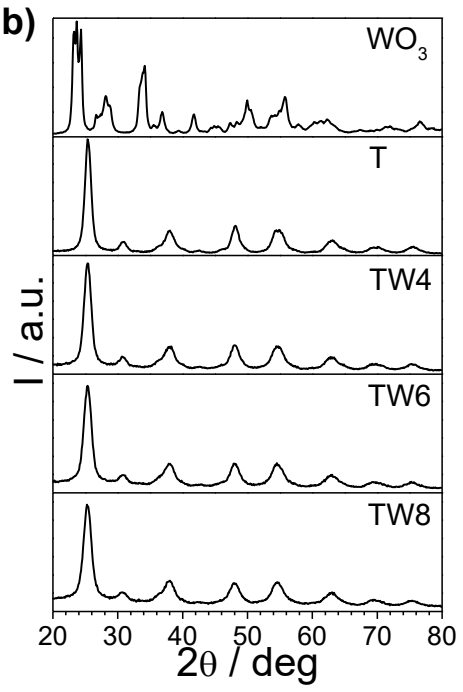

b) XRPD patterns of the TW samples. The diffractograms of the pristine TiO_2 and WO_3 samples are added for the sake of comparison.

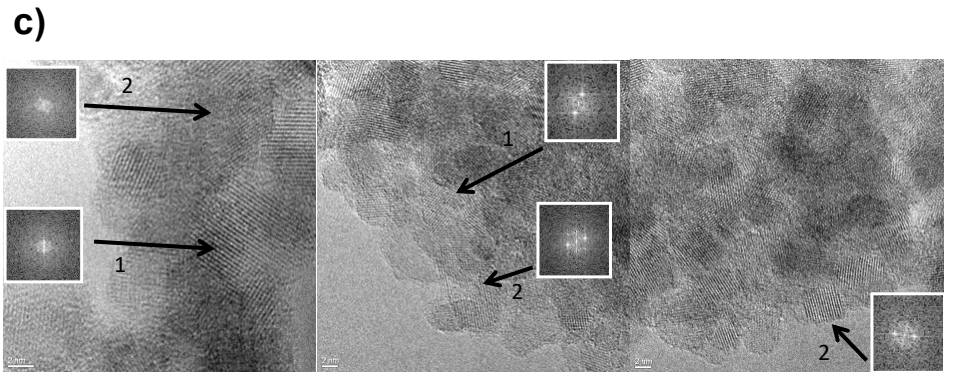

c) HRTEM images and FFT patterns of TW4 (left), TW6 (middle) and TW8 (right).

Figure 6.1 – Structural and morphological characterization results.

The main surface nature of the WO_3 species is also corroborated by DRS spectra (Fig. 6.2b). With respect to the reference T sample, the W addition does not significantly modify the absorption edge of the spectra nor the band gap value (Tab. 6.1). The main difference between the reference and

the TW samples is a visible light absorption in the 400–500 nm range, which can be traced back to intragap states located above the TiO_2 valence band maximum due to N-doping[25,26]. As the intensity of this spectral absorption is irrespective of the sample W content, this absorption feature can be attributed to the NH_4OH used during the TW synthesis and it seems instead unrelated with the W addition.

The surface features of the materials were investigated by zeta potential measurements as a function of pH in order to determine the isoelectric point (iep) of the samples (Fig. 6.2c). The bare TiO_2 material displays a slightly acidic iep (*ca.* 5.5), in accordance with the literature values for TiO_2[27], especially when synthesized in acidic environment. The TW samples exhibited significant shifts of the iep towards more and more acidic values by increasing the W content. This effect can be traced back to the strongly acidic values of WO_3 which is reported to fall around or below pH 2[27]. Specifically, the TW4 sample showed an iep around pH 3, while TW6 and TW8 showed negatively charged surface in the whole range of investigated pH. These results are in complete agreement with micro-Raman results supporting the prevailing surface location of WO_3 species.

The surface features of the samples were further investigated by FTIR spectroscopy (Fig. 6.2d). Besides the broad absorption in the 450–850 cm^{-1} range attributed to Ti–O stretches and Ti–O–Ti vibrational modes[28], all spectra exhibit a broad band in the 3600−3000 cm^{-1} spectral range characteristic of OH stretching vibration of surface hydroxyl groups[29] and its spectral partner, the in plane H–O–H bending mode of undissociated water molecules at *ca.* 1630 cm^{-1}. It should be noted that the surface hydroxylation seems promoted in the case of TW, in agreement with previous reports[3]. Interestingly, the TW samples display two distinctive features with respect to pristine TiO_2: a shoulder peak at 954 cm^{-1}, attributable to stretching vibrations of W=O[30,31], and a peak at 1438 cm^{-1}, barely visible in the case of TW4 and increasing in intensity as a function of the W content. The latter can be ascribed to NH_4^+ species, probably residues from the synthesis, coordinated to Brønsted acid sites[32,33]. This component cannot be observed in pristine TiO_2 also when NH_4OH is added during synthesis. The addition of WO_3 is known to impart Brønsted and Lewis acidity to WO_3/TiO_2 composites[11], which explains the higher surface hydroxylation[3]. It has been reported that WO_3 addition extends the

desorption peak of NH_3 species toward higher temperature compared to pristine TiO_2[12].

6.1.2 Photocatalytic activity

Samples were tested in the liquid phase towards the photocatalytic degradation of tetracycline under UV irradiation. Dark adsorption data are reported in Tab. 6.2: with the exception of TW4, an increase in TC adsorption is appreciable for TW samples with respect to the pristine TiO_2, even when normalized with respect to the specific surface area. Tetracycline is an organic molecule which presents as a mixture of its neutral and positively charged forms at spontaneous pH conditions. Hence, according to the results obtained by electrophoretic measurements, the adsorption of tetracycline on the photocatalyst surface is favoured by electrostatic effects in the case of TW samples, which are negatively charged in the adopted experimental conditions. Moreover, the presence of WO_3 induced acidic sites, clearly appreciable from FTIR results in the case of TW6 and TW8, should favour TC adsorption, as reported by the literature[3,11,34].

The reaction rates of TC disappearance together with mineralization data are reported in Tab. 6.2. The TW samples show slightly lower disappearance rates with respect to the reference sample and no clear trends are appreciable as a function of the W content. The most striking difference is related to the final mineralization: a clear drop of the mineralization degree is observed for increasing WO_3 amount. To better understand this striking behaviour, tests with radical scavengers were carried out on both the pristine TiO_2 and the sample with the highest W content (Fig. 6.2e). In the case of pristine TiO_2, a main role of h^+ is apparent as shown by tests with EDTA. This is in agreement with previous reports from the literature[16,35,36]. Moreover, N_2 purging experiments showed that O_2 plays a significant role, in agreement with the literature[37,38] which has been related to a pivotal role of $O_2^{-\bullet}$ radicals in TC degradation. In the case of TW8, a more balanced effect between $^{\bullet}OH$ and h^+ species is observed, whereas O_2 species contribute to the same extent to both the T and TW8 photocatalytic reactions. Indeed, it has been previously suggested that WO_3 could be able to generate more hydroxyl radicals thanks to its higher surface hydroxylation[11,12]. It should be noted that EDTA, besides an h^+ depletion

effect, also competes for adsorption at the photocatalyst surface, as observed in the present case for both T and TW8. A different reaction mechanism can thus be hypothesized, also on the grounds of solution speciation of the reaction intermediates. UV-vis spectra show in the case of pristine TiO_2 a parallel disappearance of the absorption peaks at *ca.* 357 and 270 nm (Fig. 6.3a), which has been related to reaction mechanisms involving h^+ species[35]. Instead, the TW8 sample displays the progressive growth of the peak at 270 nm along with the disappearance of the characteristic peak of TC (Fig. 6.3a). The selective decrease of the peak at 357 nm is generally attributed to an initial 1,3-dipolar cycloaddition towards the C11a-C12 double-bond of a $^{\bullet}OH$ radical and a consequent rearrangement with the OH at the position C12[35,39,40]. These results are in agreement with ESI-MS spectra of TC during photocatalytic tests with TW samples upon different times of irradiation (Fig. 6.3b), mainly showing intermediates related to $^{\bullet}OH$ attack. Interestingly, a few peaks (m/z 297, 459, 475 and 477) were previously reported by us in the case of TC photocatalysis by pristine TiO_2 and attributed on the grounds of the photocatalytic mechanism reported by Zhu et al. to successive $^{\bullet}OH$ attacks on the pollutant molecule[35]. In the present case, however, several more peaks can be appreciated that are generally not reported in the case of photocatalytic removal of TC by TiO_2. It is worth noting that most of them have been reported in the case of tetracyclines degradation by other advanced oxidation processes (AOPs), such as UV/H_2O_2 and catalytic ozonation[40,41]: the peaks at 413, 429, 431 m/z were attributed to the formation of TC intermediates upon alcohol oxidation mechanism, while the presence of peak 443 m/z can be traced back to the occurrence of dehydration path; the peaks at 465, 497 m/z were attributed to the influence of consecutive decarbonylation and hydroxylation paths; finally, 509 m/z peak, along with the already cited peaks at 459 and 477 m/z were attributed to progressive hydroxylations of TC. For all these degradation routes, the role of $^{\bullet}OH$ is prevailing, suggesting the more important role of hydroxyl radicals for the TW composite sample, with respect to pristine TiO_2.

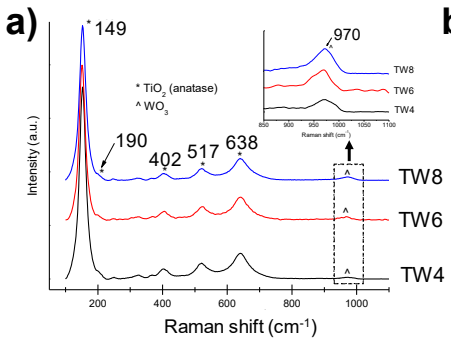

a) Micro-Raman spectra of the TW materials.

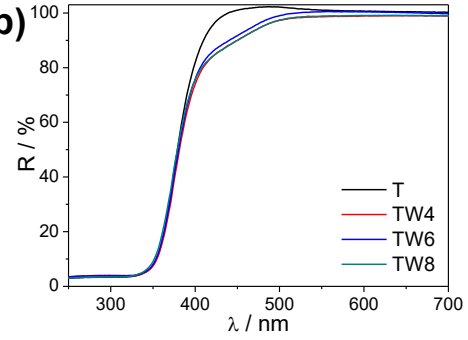

b) DRS spectra of the TW samples. The T spectrum is also reported as reference.

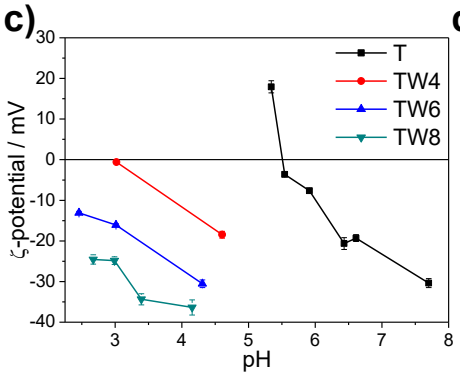

c) ζ-potential measurements of the samples as a function of pH.

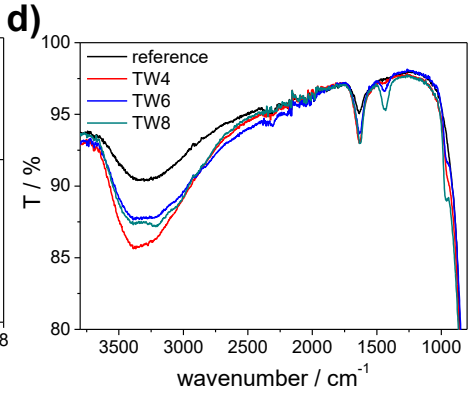

d) FTIR spectra of the TW samples and of a reference pristine TiO_2 sample treated with NH_4OH during synthesis.

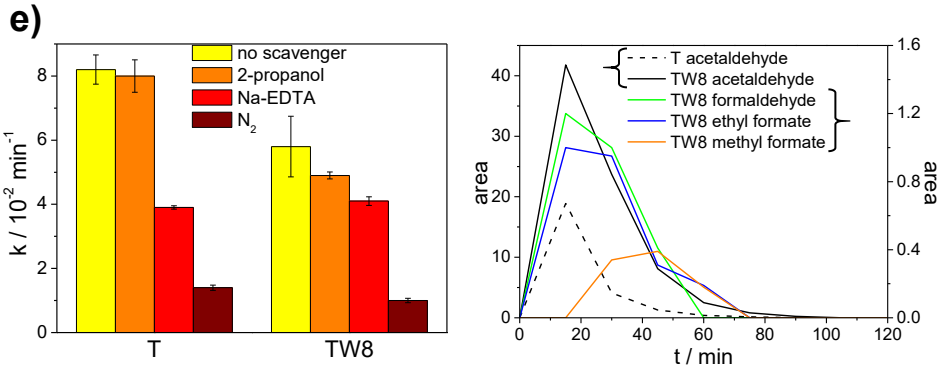

e) Tetracycline degradation rate constants in tests with radical scavengers and N_2 purging (left); concentration profiles for ethanol degradation intermediates under UV irradiation for T and TW8 samples (right).

Figure 6.2 – Further characterization and photocatalytic results.

Samples were also tested towards the degradation of ethanol in the gas phase. Dark adsorption data show an opposite trend with respect of TC: the ethanol adsorption decreases as a function of W content, more so when normalized with respect to the surface area. This observation can be rationalized considering the reported competitive adsorption at the photocatalyst surface of water and alcohols[42,43], and higher surface hydration of TiO_2-WO_3 as shown in FTIR spectra (Fig. 6.2d). Under UV irradiation, all samples were able to completely degrade ethanol and its main intermediate (acetaldehyde) within the reaction time (2 h). At least 90% ethanol was degraded in 30 min for all samples. From the ethanol disappearance point of view, whose rate was calculated and expressed in terms of pseudo-first order kinetic constant, all samples behave similarly (Tab. 6.2). The variation of the rate constant among the different samples stay within the experimental error. Nonetheless, for the composite samples the production of acetaldehyde and, thus, the final conversion to CO_2 appear to be slower. In the case of TW samples, other species besides acetaldehyde, showing the typical intermediate profile, can be appreciated (Fig. 6.2e): they were identified by calibration with standards as formaldehyde, ethyl formate and methyl formate. Interestingly, these intermediates were never observed in our experimental setup in the case of T sample, also when a less powerful irradiation was adopted. The concentration profile of the detected reaction intermediates shows that formaldehyde forms at a similar reaction stage compared to acetaldehyde, reaching a peak concentration before 20 min of irradiation for all of the investigated samples. Formaldehyde reached its maximum concentration at similar reaction time with respect to acetaldehyde, but its degradation appears slower. Methyl formate and ethyl formate are detected later on in the reaction (up to 75 min of irradiation). It is noteworthy that WO_3 adsorbs ethanol in a dissociative mode ($CH_3CH_2O^-_{(ad)}$), due to the presence of acidic sites promoting the dissociation of H^+ from the ethanol molecule[44,45]. As previously reported by Coronado et al., with respect to molecular adsorption, the dissociative adsorption of ethanol promotes the direct formation of carboxylic acids (acetic acid and formic acid) which successively bring to oxidized species as formates[42].

The effect of the increased light absorption in the visible region leads to an enhanced visible light activity for the TW samples, especially for TW4, whose degradation kinetics almost doubled that of the reference sample (Tab. 6.2). In this case, a solar lamp with emission both in the UV and in the visible region but equipped with a filter able to cut off wavelengths shorter than 400 nm was adopted. As a matter of fact, the significantly lower power density with respect to the UV lamp and the limited spectral range exploited considerably decrease the ethanol degradation kinetics. The ethanol conversion was not complete within the reaction time, but in all cases, acetaldehyde was produced and the ethanol degradation proceeded along the whole reaction time, thus suggesting the possibility to complete the photocatalytic oxidation reaction by prolonging the reaction time.

	Tetracycline			Ethanol		
Sample	**k (min^{-1})**	**Ads. (%)**	**Min. (%)**	**k_{UV} (10^{-2} min^{-1})**	**k_{vis} (10^{-4} min^{-1})**	**Ads. (%)**
T	8.2 ± 0.5	27	78	7.8 ± 0.4	3.6 ± 0.2	38
TW4	5.4 ± 0.1	23	35	7.8 ± 0.2	6.5 ± 0.1	32
TW6	6.2 ± 0.1	33	15	7.6 ± 0.2	3.4 ± 0.3	27
TW8	5.8 ± 0.9	45	7	7.7 ± 0.1	4.5 ± 0.1	26

Table 6.2 – Photocatalytic tests results for tetracycline (2^{nd}-4^{th} column) and ethanol (5^{th}-7^{th} column) degradation reactions: pseudo first order kinetic constants, *k*, dark adsorption, *Ads.*, and mineralization degree, *Min.*.

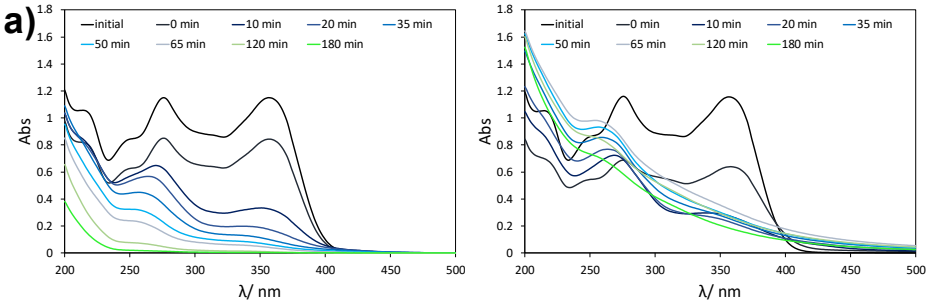

a) UV-vis absorption spectra of TC solution with respect to time of irradiation during photocatalytic tests of T (left) and TW8 (right) photocatalysts.

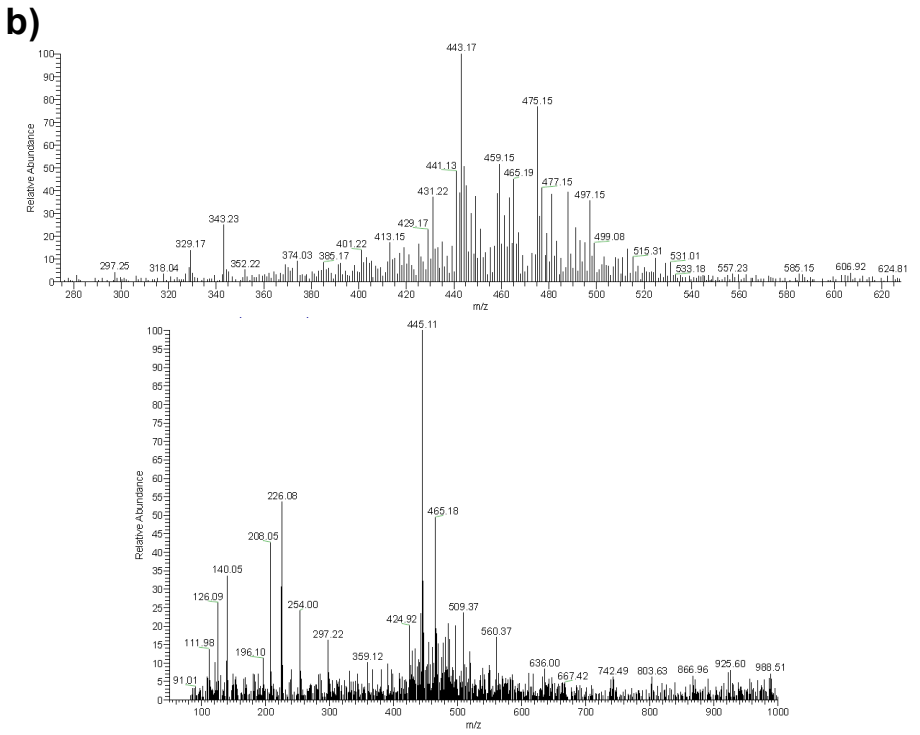

b) ESI-MS spectra of the TW8 sample, as a representative example, after 35 min (top) and 50 min (bottom) UV irradiation.

Figure 6.3 – Results regarding tetracycline degradation path.

6.2 Conclusions

In this Chapter, TiO_2/WO_3 samples prepared by sol-gel/precipitation multistep synthesis were presented. Evidence from electrophoretic measurements, Raman and FTIR spectroscopies proved a preferential location of WO_3 on the surface of TiO_2. DRS spectra supported the absence

of bulk effects induced by WO_3 on the optical properties of the composites. A promoted visible light absorption due to the presence of nitrogen species, imparted slightly enhanced photocatalytic activity under visible irradiation. Thanks to the WO_3 surface acidity, TW samples showed higher adsorption of tetracycline with respect to the bare TiO_2, although lower degradation kinetics and much lower mineralization were achieved. ESI-MS analyses supported the parallel occurrence of several TC degradation pathways in the case of TW samples, in which $^{\bullet}OH$ radicals play a major role. These findings are supported also by tests with radical scavengers showing a more marked effect of $^{\bullet}OH$ radicals for TW samples with respect to TiO_2. Some of the observed reaction intermediates, not previously detected in the case of TiO_2 photocatalysis, have been reported in the case of other oxidation processes, such as catalytic ozonation and UV/H_2O_2, characterized by lower mineralization degrees. It is noteworthy that the presence of O_2 in the reaction environment plays a key role on the reaction rate for both pristine and modified TiO_2; O_2 is well known to act as electron acceptor in photocatalysis, generating $O_2^{-\bullet}$ for electron transfer by the TiO_2 conduction band ($O_2 + e^- \rightarrow O_2^{-\bullet}{}_{(aq)}$, −0.33 V NHE) and H_2O_2 for electron transfer from the WO_3 conduction band ($O_2 + 2H^+ + 2e^- \rightarrow H_2O_{2(aq)}$, +0.682 V NHE). H_2O_2 could further react with e^- to give rise to hydroxyl radicals.

Reactions in the gas phase proved how the photocatalyst surface acidity can have a detrimental role also on its adsorption features, since the competition between water and the model pollutant led to a decrease in the ethanol adsorption at the TW surface. Also in this case different reaction intermediates between TW and TiO_2 were observed. Different reaction pathways arising from the adsorption mode of the pollutant molecule were hypothesized.

6.3 Specific procedures

Samples preparation. The TiO_2 xerogel was prepared by sol-gel according to the following procedure. 18.4 g of titanium tetraisopropoxide (TTIP) dissolved in 24 mL of 2-propanol at 25°C was hydrolysed by adding drop by drop 113 mL of an HCl aqueous solution (pH 3) while stirring at 300 rpm. The hydrolysis was completed by stirring for other 90 min. The solid was then recovered and washed with water by five centrifugation-

reprecipitation cycles. The xerogel was obtained by drying the collected solid at 90°C in an oven. TiO_2/WO_3 composites were synthesized by precipitating WO_3 on the prepared TiO_2 xerogel by a modification of a previously reported procedure[46]. The selected amount of tungstic acid (H_2WO_4) was suspended in 50 mL of water and then dissolved by addition of a 25% NH_4OH aqueous solution. Complete dissolution was typically achieved by the addition of *ca.* 1.2 mL of NH_4OH solution, when the pH value was *ca.* 10. Successively, the solution was acidified by 0.5 M HCl till pH 4 was achieved. Then, 10 mL of a 0.1 M oxalic acid solution was added (pH around 2.5), followed by the addition of 1.10 g of the prepared TiO_2 xerogel. The suspension was heated at 90°C under reflux for 6 h while stirring. The sample was then dried at 80°C and finally calcined at 450°C in O_2 flux (9 NL h^{-1}) for 6 h. The samples were labelled as TWx, where x indicate the percentage Ti/W nominal ratio (4%, 6% or 8%). This concentration range was investigated on the grounds of previous reports about optimum photocatalytic activity [3,11,46].

A pure WO_3 sample was prepared by adopting the same synthetic procedure without the addition of the TiO_2 xerogel. A reference TiO_2 sample was prepared by calcining the TiO_2 xerogel as previously described, without the addition of W salts.

Photocatalytic tests. The photocatalytic degradation of ethanol in the gas phase was tested under both UV and visible irradiation. Photocatalytic tests were carried out adopting the experimental setup reported in Appendix A, using 50 mg of sample drop casted on a Petri dish (d = 10 cm) and a starting ethanol concentration of 198 ppm.

The degradation of tetracycline hydrochloride (TC) in water was tested under UV irradiation in the experimental setup already described in Chapter 1. Before irradiation, the suspension was kept in the for 30 min to achieve an adsorption equilibrium.

Further details about the preparation and characterization methods can be found in Appendix A.

References

1 C. Di Valentin and G. Pacchioni, *Acc. Chem. Res.*, 2014, **47**, 3233–3241.

2 I. A. Castro, G. Byzynski, M. Dawson and C. Ribeiro, *J. Photochem. Photobiol. A Chem.*, 2017, **339**, 95–102.

3 H. Khan, M. G. Rigamonti, G. S. Patience and D. C. Boffito, *Appl. Catal. B Environ.*, 2018, **226**, 311–323.

4 N. O. Balayeva, M. Fleisch and D. W. Bahnemann, *Catal. Today*, 2018, **313**, 63–71.

5 J. Georgieva, E. Valova, S. Armyanov, N. Philippidis, I. Poulios and S. Sotiropoulos, *J. Hazard. Mater.*, 2012, **211**–**212**, 30–46.

6 F. Riboni, M. V. Dozzi, M. C. Paganini, E. Giamello and E. Selli, *Catal. Today*, 2017, **287**, 176–181.

7 S. A. K. Leghari, S. Sajjad, F. Chen and J. Zhang, *Chem. Eng. J.*, 2011, **166**, 906–915.

8 J. Y. Lee and W. Jo, *J. Hazard. Mater.*, 2016, **314**, 22–31.

9 G. Wang, Q. Chen, Y. Liu, D. Ma, Y. Xin, X. Ma and X. Zhang, *Chem. Eng. J.*, 2018, **337**, 322–332.

10 A. Cordero-García, G. Turnes Palomino, L. Hinojosa-Reyes, J. L. Guzmán-Mar, L. Maya-Teviño and A. Hernández-Ramírez, *Environ. Sci. Pollut. Res.*, 2017, **24**, 4613–4624.

11 Y. Tae Kwon, K. Yong Song, W. In Lee, G. Jin Choi and Y. Rag Do, *J. Catal.*, 2000, **191**, 192–199.

12 K. K. Akurati, A. Vital, J.-P. Dellemann, K. Michalow, T. Graule, D. Ferri and A. Baiker, *Appl. Catal. B Environ.*, 2008, **79**, 53–62.

13 J. Han, Y. Li, L. Yang, T. Li, Y. Luo, L. Yang and S. Luo, *J. Hazard. Mater.*, 2018, **358**, 44–52.

14 H. Tada, A. Kokubu, M. Iwasaki and S. Ito, *Langmuir*, 2004, **20**, 4665–4670.

15 M. Miyauchi, A. Nakajima, K. Hashimoto and T. Watanabe, *Adv. Mater.*, 2000, **4095**, 1923–1927.

16 L. Rimoldi, D. Meroni, G. Cappelletti and S. Ardizzone, *Catal. Today*, 2017, **281**, 38–44.

17 L. Rimoldi, E. Pargoletti, D. Meroni, E. Falletta, G. Cerrato, F. Turco and G. Cappelletti, *Catal. Today*, 2018, **313**, 40–46.

18 L. Rimoldi, C. Ambrosi, G. Di Liberto, L. Lo Presti, M. Ceotto, C. Oliva, D. Meroni, S. Cappelli, G. Cappelletti, G. Soliveri and S. Ardizzone, *J. Phys. Chem. C*, 2015, **119**, 24104–24115.
19 A. Antonello, G. Soliveri, D. Meroni, G. Cappelletti and S. Ardizzone, *Catal. Today*, 2014, **230**, 35–40.
20 H. Khan and D. Berk, *Appl. Catal. A Gen.*, 2015, **505**, 285–301.
21 M. N. Iliev, V. G. Hadjiev and A. P. Litvinchuk, *Vib. Spectrosc.*, 2013, **64**, 148–152.
22 M. Picquart, S. Castro-Garcia, J. Livage, C. Julien and E. Haro-Poniatowski, *J. Sol-Gel Sci. Technol.*, 2000, **18**, 199–206.
23 W. Smith and Y. Zhao, *J. Phys. Chem. C*, 2008, **112**, 19635–19641.
24 M. Ahmadi and M. J.-F. Guinel, *Acta Mater.*, 2014, **69**, 203–209.
25 D. Meroni, S. Ardizzone, G. Cappelletti, C. Oliva, M. Ceotto, D. Poelman and H. Poelman, *Catal. Today*, 2011, **161**, 169–174.
26 R. Asahi, T. Morikawa, H. Irie and T. Ohwaki, *Chem. Rev.*, 2014, **114**, 9824–9852.
27 M. Kosmulski, *Adv. Colloid Interface Sci.*, 2016, **238**, 1–61.
28 D. Guerrero-Araque, D. Ramírez-Ortega, P. Acevedo-Peña, F. Tzompantzi, H. A. Calderón and R. Gómez, *J. Photochem. Photobiol. A Chem.*, 2017, **335**, 276–286.
29 G. Soliveri, V. Pifferi, R. Annunziata, L. Rimoldi, V. Aina, G. Cerrato, L. Falciola, G. Cappelletti and D. Meroni, *J. Phys. Chem. C*, 2015, **119**, 15390–15400.
30 J. Polleux, M. Antonietti and M. Niederberger, *J. Mater. Chem.*, 2006, **16**, 3969.
31 X.-X. Zou, G.-D. Li, P.-P. Wang, J. Su, J. Zhao, L.-J. Zhou, Y.-N. Wang and J.-S. Chen, *Dalt. Trans.*, 2012, **41**, 9773.
32 K. A. Michalow-Mauke, Y. Lu, K. Kowalski, T. Graule, M. Nachtegaal, O. Kröcher and D. Ferri, *ACS Catal.*, 2015, **5**, 5657–5672.
33 J. J. Murcia, M. C. Hidalgo, J. A. Navío, J. Araña and J. M. Doña-Rodríguez, *Appl. Catal. B Environ.*, 2013, **142**–**143**, 205–213.
34 K. K. Akurati, A. Vital, J. Dellemann, K. Michalow, T. Graule, D. Ferri and A. Baiker, *Appl. Catal. B Environ.*, 2008, **79**, 53–62.
35 X. D. Zhu, Y. J. Wang, R. J. Sun and D. M. Zhou, *Chemosphere*, 2013, **92**, 925–932.

36 R. A. Palominos, M. A. Mondaca, A. Giraldo, G. Peñuela, M. Pérez-Moya and H. D. Mansilla, *Catal. Today*, 2009, **144**, 100–105.
37 F. Chen, Q. Yang, J. Sun, F. Yao, S. Wang, Y. Wang, X. Wang, X. Li, C. Niu, D. Wang and G. Zeng, *ACS Appl. Mater. Interfaces*, 2016, **8**, 32887–32900.
38 D. Jiang, T. Wang, Q. Xu, D. Li, S. Meng and M. Chen, *Appl. Catal. B Environ.*, 2017, **201**, 617–628.
39 Y. Wang, H. Zhang, J. Zhang, C. Lu, Q. Huang, J. Wu and F. Liu, *J. Hazard. Mater.*, 2011, **192**, 35–43.
40 Y. Wang, H. Zhang and L. Chen, *Catal. Today*, 2011, **175**, 283–292.
41 Y. Liu, X. He, Y. Fu and D. D. Dionysiou, *Chem. Eng. J.*, 2016, **284**, 1317–1327.
42 J. M. Coronado, S. Kataoka, I. Tejedor-Tejedor and M. A. Anderson, *J. Catal.*, 2003, **219**, 219–230.
43 P. Pichat, *Appl. Catal. B Environ.*, 2010, **99**, 428–434.
44 A. Labidi, C. Lambert-Mauriat, C. Jacolin, M. Bendahan, M. Maaref and K. Aguir, *Sensors Actuators B Chem.*, 2006, **119**, 374–379.
45 W. Yu-De, C. Zhan-Xian, L. Yan-Feng, Z. Zhen-Lai and W. Xing-Hui, *Solid. State. Electron.*, 2001, **45**, 639–644.
46 V. Iliev, D. Tomova, S. Rakovsky, A. Eliyas and G. L. Puma, *J. Mol. Catal. A Chem.*, 2010, **327**, 51–57.

This Chapter has been adapted with permission from Rimoldi *et al.*, *Catal. Today*, DOI: 10.1016/j.cattod.2018.11.035, in press.

Chapter 7

TiO_2-SiO_2-PMMA ter-polymer floating device for the photocatalytic remediation of water and gas phase pollutants

Polymer/TiO_2 micro and nano-composites have raised a great deal of interest in recent years due to their broad range of applications, including the enhancement of thermal, dielectric and mechanical properties of polymers[1–4], water purification[5,6], biomaterials[7] and anti-bacterial surfaces[8], energy conversion and storage such as in solar and fuel cells, lithium batteries and electrochemical capacitors[9–12].

In the field of surface water and wastewater treatment by photocatalytic oxidation[13,14], TiO_2/polymer composites benefit from the high durability, light-weight, controlled surface properties and ease-of-processing of the polymeric component[15]. One major challenge in this field is the development of photoactive and durable floating devices for the remediation of large, polluted areas, such as water basins[16]. With respect to powder photocatalysts, floating systems enable an easy retrieval of the photocatalyst as well as a more efficient light usage, since light, especially UV, attenuates rapidly in water (less than 1% of the UV light or *ca.* 20% of visible light irradiated on the water surface reaches a depth of 0.5 m[17]. The use of inorganic coatings and polymer substrates aims at filling this gap by combining the unique photocatalytic properties deriving from TiO_2 and the excellent polymer processability for an easy scalable technology. Key to the success of such composite devices is the engineering of the fabrication materials and of the device design. Tu *et al.* described the development of a ternary system made of polypropylene, TiO_2 and activated carbon for the adsorption and degradation of phenol[18]. Sponge-

like polyurethane composite foams were adopted by Ni *et al.* for surface water remediation[19]. Han *et al.* coated commercial polypropylene with different TiO_2 layers for the degradation of methyl orange[20]. However, an unresolved issue for nano/microcomposites is represented by their poor photochemical, thermal and mechanical stability. As a matter of fact, the mechanical stability of composite devices is limited by the inherent low compatibility between the polymer and the oxide layers[21]. Moreover, the device stability under prolonged irradiation depends on the photostability of the polymer component as well as on the possible occurrence of polymer degradation due to the TiO_2 photocatalytic activity[22]. Overall, a relatively fast loss of photocatalytic performance is often reported[8,18].

In order to increase the mechanical and photochemical stability of the composite, the properties of the device are to be carefully tailored. In particular, the wetting properties of the polymer surface have to be modified to promote the adhesion of the oxide film by increasing the polymer surface hydrophilicity[23]. However, the bottom side of the floating device should present good hydrophobic properties in order to display stable buoyancy. In this respect, the addition of fluorinated chains to enhance hydrophobicity can reduce the photostability of the polymer. The tailoring of the wetting features of the polymer is thus a critical issue for the creation of stable polymer/oxide composites.

Most of the literature uses commercial polymers as substrates for the oxide deposition due to their flexibility, availability and lower cost[21]. However, the poor thermal stability of common commercial polymers (*e.g.*, polyesters and polyacrylates) severely restricts the range of available stabilization treatments that can be used to improve the oxide layer adhesion. The UV resistance and mechanical properties are also critical issues when commercial polymers like polypropylene and polyesters are employed. Moreover, a good transparency in the UV-vis range and high oxygen permeability are also required for the application in open water basins, limiting the applicability of polyurethanes and polyacrylonitriles, respectively.

To solve these issues, in the work presented in this Chapter a tailored ter-polymer based on methylmethacrylate, MMA, α-methylstyrene and perfluoroctyl methacrylate (POMA) co-monomers was synthesized to be

adopted as substrate for the photoactive layer, to achieve good buoyancy, transparency and high mechanical, UV and thermal stability. The TiO_2 layer adhesion was ensured via a surface pretreatment of the polymer aimed at enhancing its hydrophilicity as well as via addition of an intermediate SiO_2 layer, which also protects the polymer from the TiO_2 generated radicals. The device showed good stability under prolonged irradiation in working conditions. The photocatalytic performance was tested towards the degradation of VOCs in the gas phase and of an emerging pollutant in water, showing good recyclability.

7.1 Results and discussion

7.1.1 Synthesis and characterization of MMA_α-methylstyrene_POMA ter-polymer

Poly(methyl methacrylate) is the lightweight and shatter-resistant alternative to glass *par excellence* due to its optimal transparency. It is widely used for outdoor applications thanks to its UV resistance and excellent mechanical properties. However, this polymer suffers from a relatively low thermal stability (glass transition temperature, T_g, 105.0 °C) that makes it unsuitable for the present application.

In this work, a new type of methacrylic ter-polymer was prepared via free radical polymerization among MMA, α-methylstyrene and POMA, according to the reaction scheme represented in Figure 7.1a. The ^{1}H NMR spectra of the synthesized fluorinated comonomer and of the ter-polymer are reported in Figure 7.1b, respectively. The addition of α-methylstyrene in a molar ratio of 20% with respect to MMA significantly enhanced the thermal properties of the material, leading to a T_g of 123.9 °C (Fig. 7.1a) and furthermore, the corresponding polymer foils are characterized by mechanical properties (Fig. 7.1a) comparable with industrial films of polyacrylates[24] and excellent oxygen permeability (oxygen transmission rate, OTR: 314 $cm^3\ m^{-2}\ d^{-1}$)[25] with high homogeneity of the film casted.

a)

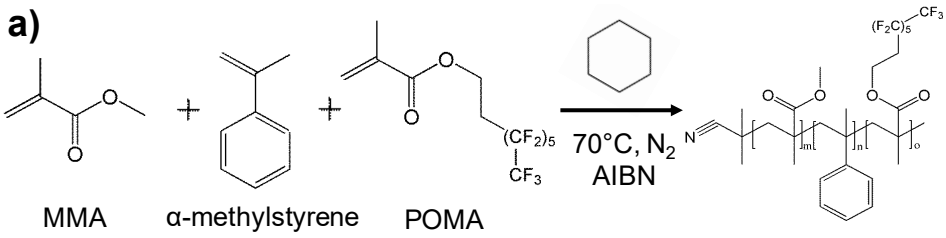

	T_g (°C)	M_n (Da)	D	wCA air-side (°)	wCA mould-side (°)	Elastic modulus (GPa)	Tensile strength (MPa)	Elongation at break (%)
Before UV test	123.9	28100	2.1	67±2	114±3	3.1	70	2.3
After UV test	124.0	28000	2.1	66±3	116±2	2.9	68	1.9

a) Synthetic route (top) and main physicochemical (glass transition temperature, T_g; number average molecular weight, M_n; molecular weight distribution, D; water contact angles, wCA) and mechanical properties (elastic Young's tensile modulus, tensile strength, elongation at break) (bottom) of the ter-polymer before and after the UV stability test.

b)

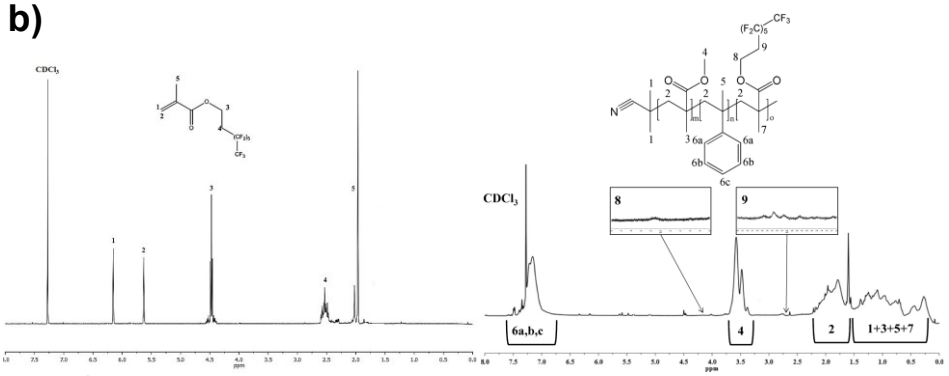

b) ^{1}H NMR spectrum of POMA monomer (left) and MMA_ α-methylstyrene_POMA polymer (right).

c)

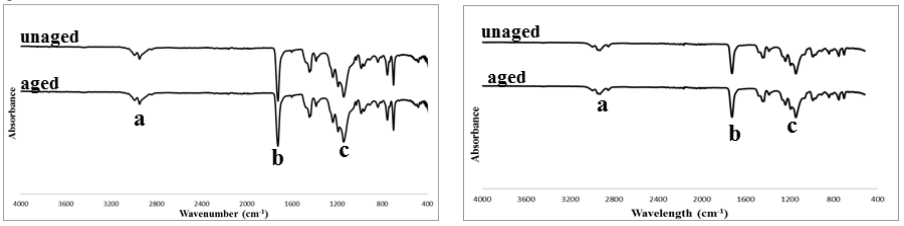

c) FT-IR spectra of MMA_α-methylstyrene_POMA collected before and after the UV stability test at the air (left) and PTFE (right) side.

Figure 7.1 – Polymer characterization results.

The wetting features of the polymer films were tailored by the addition of a new fluorinated methacrylic monomer, POMA, which was synthesized via esterification reaction between methacryloyl chloride and *1H,1H,2H,2H*-Perfluoro-1-octanol. The fluorinated monomer, together with the adopted solvent casting deposition technique, allowed us to achieve different wetting features on the two sides of the polymer film. As described in previous works[26,27], during the drying process the apolar fluorinated chains of the polymer tend to reorganize orienting towards the hydrophobic mould surface due to the higher affinity with PTFE with respect to the solvent. This gives rise to a polymer film characterized by a hydrophobic side (PTFE-side), and a hydrophilic one (air-side), as appreciable from water contact angle measurements (Fig. 7.1a).

The POMA content was selected in order to impart the desired hydrophobic properties while preserving the UV stability of the polymer, as determined by stability tests upon prolonged UV irradiation (100 h). FT-IR spectra collected at the air and the PTFE sides of the polymer film before and after UV exposure (Fig. 7.1c) show the same features: peaks in the ~3100–2800 cm^{-1} range, which can be attributed to stretching modes of C–H aliphatic bonds[28], the stretching of carbonyl ester groups (C=O) between ~1750 cm^{-1} and ~1600 cm^{-1}[28], and the characteristic absorption band for the symmetric stretching vibration of C–O conjugated to carbonyl ester groups, which appear between ~1350 cm^{-1} and ~1100 cm^{-1}[28]. The shape of these peaks does not change upon the UV exposure test, testifying the preservation of the polymeric bonds in correspondence of the aliphatic and carbonyl groups[29,30]. The presence of $–CH_3$ groups in alpha position to carbonyl groups, which are deriving from the methacrylic co-monomers, inhibits the photo-chemical degradation of the polymer[31]. Moreover, the main physicochemical properties of the polymer do not change upon UV irradiation (Fig. 7.1a), also in terms of wetting features of the two film sides. Thus, upon UV irradiation the ter-polymer maintains not only its overall structure but also the organization of the fluorinated chains, responsible for the wetting properties of the polymer foils. In their turn, the thermal and mechanical properties remained totally unchanged upon UV stability test.

7.1.2 Device preparation and characterization

For the preparation of the composite photocatalytic device, firstly the hydrophilic side of the polymer film was corona treated in order to increase its wettability and promote the adhesion of the deposited oxide layers. Then, a SiO_2 layer was deposited by spray coating a stable home-made silica sol. Successively, a TiO_2 layer was deposited onto the dried silica layer by spray coating a titania sol containing a commercial anatase powder. Finally, a wet and a mild thermal treatments were performed to promote condensation reactions and improve adhesion.

Figure 7.2 shows top SEM images of the different components of the photocatalytic device, *i.e.* of the device layers in each stage of its assembly. The relative water contact angles are also reported in inset. The air side and the mould side of the as-deposited polymeric foil present notable differences both in terms of wetting and morphological features. While the air side (Fig. 7.2, top left) appears highly homogeneous and smooth, the mould side (Fig. 7.2, top right) is characterized by micrometric roughness due to Teflon mould adopted for the deposition. The two sides of the as-deposited polymer foil show different wettability thanks to the orientation of the fluorinated chains of POMA towards the Teflon mould side. The corona treatment increases the hydrophilicity of the polymer surface (reaching a value of 44±1° right after the treatment) surface and imparts a morphological change in the polymer foils (Fig. 7.2, middle left). Micrometric cavities can be detected, in agreement with the literature[32], which are excavated by the energy particles bombardment. These micro pits concur to improve the adhesion of the inorganic layers due to a larger potential bond area[32]. The silica layer spray-deposited onto the polymer surface is crack-free and homogeneously covers the whole foil surface (Fig. 7.2, middle right) and further increases the hydrophilicity of the surface (32±6°). Upon deposition of the TiO_2 layer, the presence of titania particles leads to an appreciable surface roughness (Fig. 7.2, bottom, left) and to a slight increase of the water contact angle (63±2°) for the unirradiated sample. Even after prolonged irradiation in water, the morphology of the film remains comparable with the one of pristine sample (Fig. 7.2, bottom right).

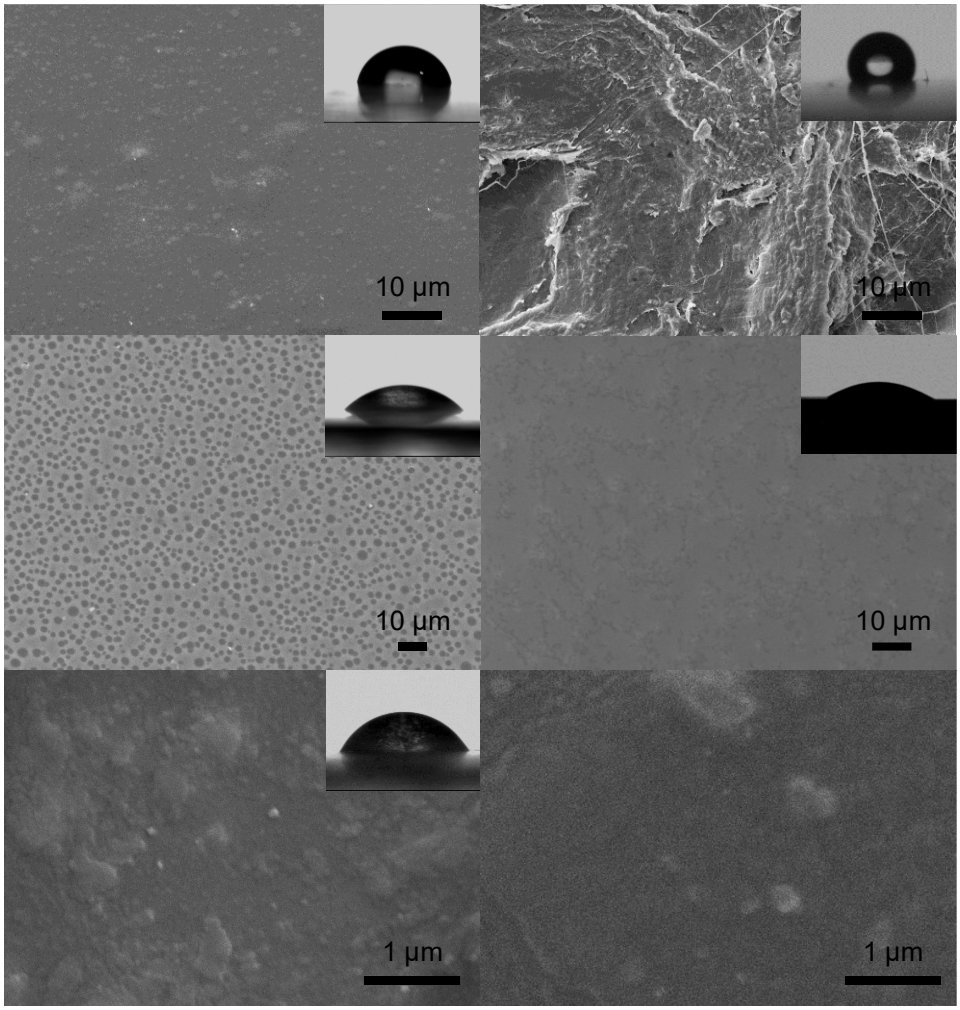

Figure 7.2 – SEM images of the air side (top, left) and the mould side (top, right) of the polymer foil, of the air side after corona treatment (middle, left), of the silica layer (middle, right) and of the final device before (bottom, left) and after (bottom, right) prolonged irradiation under working conditions, together with the relative water contact angles (in insets).

Cross-sectional SEM images of the bare polymer foil and of the final composite device are reported in Figure 7.3a. The left part of the figure shows that the polymer foil has a porous morphology, induced by the choice of the casting solvent, which is at the basis of the lightness of the foil and enhances its floating capabilities. The thickness of the foil was measured to be *ca.* 200 µm. The right part of the figure shows instead the thickness and the morphology of the inorganic layers (SiO_2 and TiO_2)

deposited onto the polymer substrate in the complete device. A micrometric silica layer with a very compact morphology favours the protection the organic substrate from the photocatalytically produced radical species. The top titania layer is instead much thinner, in agreement with previous reports[33]; moreover, the active TiO_2 layer displays a rough and porous morphology, as also shown by the top view micrographs, which can be beneficial for the photocatalytic application by enhancing the actual surface area extension and by increasing photon absorption[34].

The transmittance spectra of the device before and after the deposition of the TiO_2 layer are reported in Figure 7.3b together with the spectrum of the bare polymer, for the sake of comparison. The bare polymer foil presents high transparency in the whole visible range (constant transmittance of *ca.* 80% between 400 and 800 nm). This is a highly desirable feature for application in natural settings as water basins. In the UV region, the transmittance shows a good degree of transparency, presenting a transmittance >60% up to 285 nm, enabling an efficient use of sunlight by the TiO_2 layer in the full device even when the device is capsized. The deposition of the silica layer leads to a further slight enhancement of transmittance in the visible range, owing to the antireflective properties of the silica film[35], while in the UV region a minor decrease of transmittance is observed, due to the characteristic light absorption of SiO_2, remaining however >55% up to 285 nm. The complete photocatalytic device still presents a good transparency (transmittance *ca.* 70%) in the whole visible region, as also revealed by the photograph reported in Figure 7.3b. In the UV region, the characteristic absorption of TiO_2 is appreciable, due to the top titania layer. It should be noted that up to 340 nm the device shows substantial transparency (transmittance > 50%), which guarantees the photoactivation of the titania layer also with back illumination. The device can thus be used for both the degradation of water pollutants and gaseous organic compounds present in the atmosphere. In fact, as appreciable from Figure 7.3c, the device revealed high floating capabilities, which remained stable in time, owing to the lightness of the polymer, together with the enhanced hydrophobicity of the bottom side provided by the use of the fluorinated comonomer.

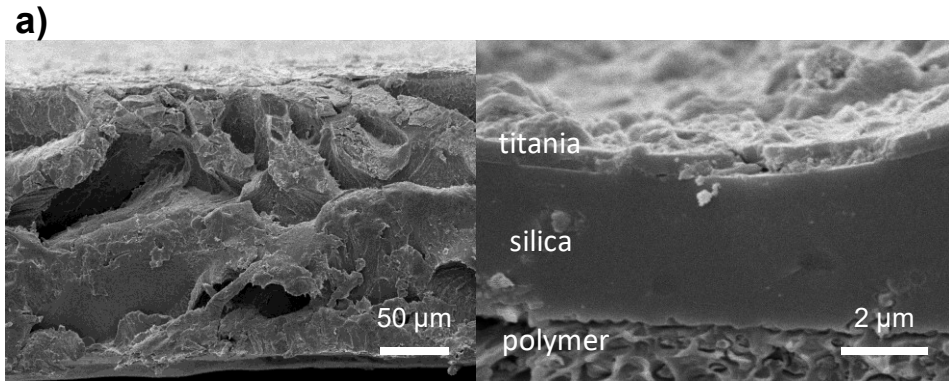

a) Cross-sectional SEM images of the deposited polymeric foil (left) and of the final device (right).

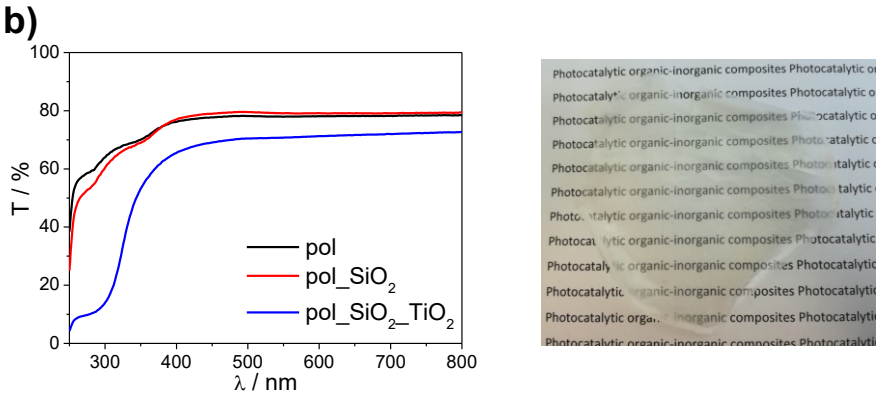

b) UV-vis transmittance spectra (left) and photographs proving the transparency (right) of the composite device.

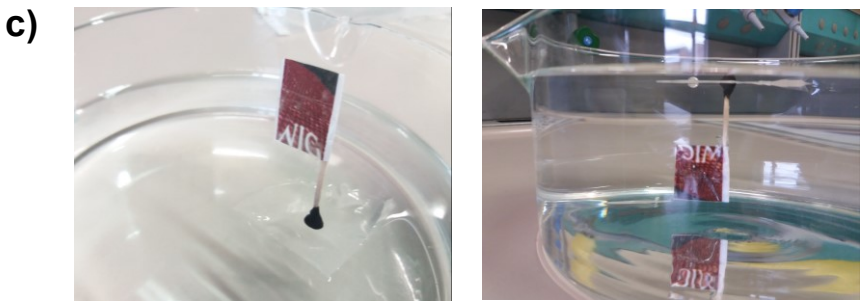

c) Photographs proving the buoyancy of the composite device on both the mould (left) and air sides (right); a flag was attached on top of the air side of the transparent device to make it more easily detectable.

Figure 7.3 – Further ter-polymer and composite device characterization results.

7.1.3 Photocatalytic activity

The photocatalytic activity of the device was firstly tested in the gas phase degradation of VOCs, mimicking the use of the device for degrading vapours of volatile organic molecules dissolved in the water basins and/or present on their surface. In this respect, ethanol was selected as model molecule on the grounds of a previous work[36]. The present device proved to be effective in the degradation of ethanol vapour, achieving complete disappearance of the target molecule after 4 h of irradiation (Fig. 7.4a) despite the high pollutant concentration (200 ppm) and the low irradiated TiO_2 amount (*ca.* 9 mg). Moreover, the main intermediate (acetaldehyde) was almost entirely removed after 6 h, leading to CO_2 and water as final products (Fig. 7.4a). The present result is thus comparable with previous reports of ethanol gas phase degradation using a similar amount of P25 free powder[37]. However, with respect to previous reports showing substantial deactivation just upon three recycle tests[37], in the present case the device maintained its photocatalytic activity after three consecutive photocatalytic runs (Fig. 7.4b), as appreciable from the pollutant pseudo-first order disappearance rates. In all cases, the mineralization (complete oxidation to CO_2) was larger than 75%, proving the stability and the reusability of the prepared photocatalytic device.

The photocatalytic activity of the device was also evaluated towards the degradation of tetracycline. Tetracyclines are the best-selling antibiotics[38] and have been classified as emerging pollutants[39,40]. Due to their large usage in both humans and animals, tetracyclines are among the most frequently detected micropollutants both in wastewaters[41] and in large water basins as the lakes of Northern Italy[42], leading to increased levels of tetracycline-resistant bacteria[43]. Under simulated solar light with back irradiation, the floating device achieved a tetracycline degradation of 50% after 14 h of irradiation, without any decrease of the performance during the reaction time (Fig. 7.4c), suggesting the possibility to completely degrade the target molecule by prolonging the irradiation. A pseudo-zero order kinetics of 7.0 ± 0.3 ppb min^{-1} was observed. Only few studies reported the photocatalytic degradation of pollutants by floating devices under solar light[21]. Although comparisons are difficult to draw due to the different experimental conditions, the presently reported floating device

shows promising performance with respect to previous reports as several literature studies obtain similar degradation rates using much larger TiO_2 actual contents[20,44,45].

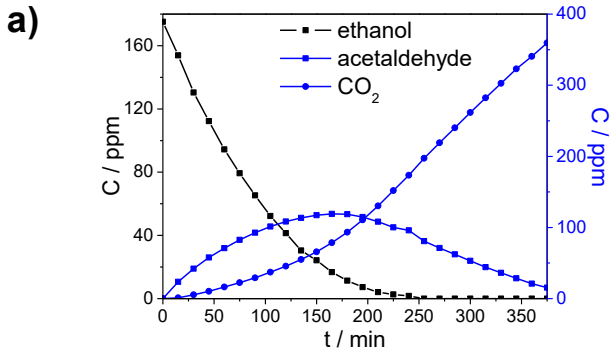

a) Ethanol disappearance and acetaldehyde and CO_2 formation during the photocatalytic test under UV irradiation.

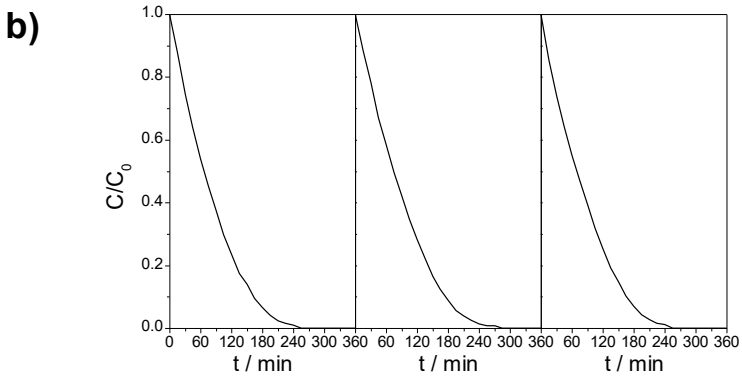

b) Ethanol disappearance under UV irradiation and the relative rate constant in the recycle tests.

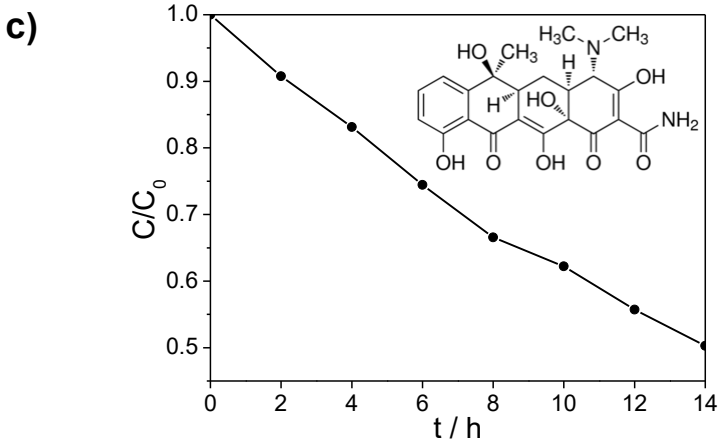

c) Tetracycline disappearance under solar simulated irradiation together with tetracycline molecular structure.

Figure 7.4 – Photocatalytic tests results.

7.2 Conclusions

In this Chapter, a floating photocatalytic device based on TiO_2 photocatalyst immobilized over an *ad hoc* synthesized ter-polymer was presented. The developed methylmethacrylate, α-methylstyrene and perfluoroctyl methacrylate ter-polymer is characterized by a highly porous morphology and inherent hydrophobicity, which enable a stable buoyancy. Furthermore, the support, displaying the characteristic optical transparency and oxygen permeability of PMMA, was engineered to possess enhanced thermal stability, mechanical resistance and photostability, in order to promote the device durability. The compatibility of the inorganic top coating was enhanced by a series of strategies: 1) an *ad hoc* polymer casting method leading to reorganization of the hydrophobic chains and dual wetting features of the opposite film sides; 2) the corona treatment of the polymer surface aimed at increasing hydrophilicity and creating surface pitting to bolster adhesion of the inorganic coating; 3) the deposition of an intermediate SiO_2 layer, which improves the adhesion of the TiO_2 top layer and protects the polymer support from the radical species generated by photocatalytic oxidation. The adopted TiO_2 layer contains commercial nanoparticles with high photocatalytic activity bound together by a titania sol promoting adhesion. The final device showed promising results in photocatalytic degradation tests of both water and gas phase pollutants, also in recycle tests. Tests were carried out under both UV and simulated solar irradiation, with either front or back irradiation, confirming the ability of the device to work also when capsized. Future work will further optimize the TiO_2 amount to boost the photocatalytic activity of the device by both increasing the nanoparticles content in the top layer and using fibres and sponge architectures as an alternative to polymer films.

7.3 Specific procedures

Synthesis of POMA. The reaction was carried out under inert atmosphere using a 100 mL three-neck round bottom flask equipped with a nitrogen inlet adapter, an internal thermometer adapter, an overhead magnetic stirrer and a reflux condenser. Firstly, 20 mL of methylene chloride, methacryloyl chloride (2.8 g) and *1H,1H,2H,2H*-Perfluoro-1-octanol (9.8 g) were mixed.

Then, 2.9 g of TEA was added to neutralize HCl formed during the esterification reaction. The solution was carefully cooled down to 0 °C and then stirred for 16 h. Afterwards, it was gradually brought back to room temperature. The solution was washed several times with an aqueous solution of HCl at 5% w/w and then with $NaHCO_3$ 5% w/w to remove traces of TEA and HCl, respectively. Water traces were removed with Na_2SO_4 and the salt was removed via filtration. The resulting solution was dried under vacuum (*ca.* 4 mbar) at 40°C for 1 h (96% yield). The structure of POMA was confirmed via ^{1}H NMR spectroscopy.

Synthesis of MMA_α-methylstyrene_POMA ter-polymer. The reaction was performed under inert atmosphere in a 100 mL two-necked round bottom flask equipped with a nitrogen inlet adapter, a reflux condenser and an overhead magnetic stirrer. 40 mL of cyclohexane was mixed with MMA (14.6 g) and α-methylstyrene (4.3 g) POMA (0.8 g) and AIBN (0.3 g), used as free radical initiator. The resulting molar ratios were 8:2 MMA:α-methylstyrene, 1% mol*mol^{-1} POMA:(MMA and α-methylstyrene), and 1% mol*mol^{-1} AIBN:(MMA, α-methylstyrene and POMA). The solution heated in an oil bath at 70°C for 24 h, then gradually cooled down to room temperature. A white solid was precipitated by addition of a large excess of methanol. After recovering the solid by filtration, the polymer was washed with methanol for several days under stirring to remove unreacted methacrylic monomers. After washing, the polymer was dried in a vacuum oven (*ca.* 4 mbar) at 40°C for 48 h. The structure of the product was confirmed via ^{1}H NMR spectroscopy.

Silica and titania sols preparation. The silica sol was prepared by a modification of the procedure reported by Soliveri *et al.*[33]. Firstly, 10 g of TEOS was added to a solution of 4.5 g of 0.1 M HCl and 25 g of ethanol. The mixture was stirred at room temperature for 120 min and then refluxed at 60°C for 60 min. After cooling down, a solution prepared by dissolving 2 g of Lutensol ON 70 (BASF) in 25 g of ethanol, was added to the reaction mixture and stirred for 1 h. A stable, transparent sol was obtained.

For the preparation of the titania sol, 28.4 g of titanium isopropoxide was dissolved in 79 g of ethanol and 0.9 mL of HCl 37% was added while stirring. Then, a solution of 0.47 g of Lutensol ON 70 in 79 g of ethanol was added. The resulting stable and transparent sol was stirred at 1 h at room temperature.

Device preparation. Polymer films were prepared via solution casting: 1.8 g of polymer was dissolved in 10 mL of CH_2Cl_2 and the resulting solution was cast onto a PTFE mould (7 cm in diameter). The films were dried overnight at 25°C and atmospheric pressure. The air side of the polymer film was corona treated (Aslan Machinery, voltage: 0.43 kW; exposition time: 5 min) in order to promote the adhesion of the oxide layers. Then, the SiO_2 layer was deposited by spray coating the silica sol (nozzle diameter: 0.5 mm, target-nozzle distance *ca.* 30 cm; spraying time *ca.* 1 s, 3 layers). After drying at room temperature, the TiO_2 layer was deposited by spray coating a suspension of Hombikat UV100 in the prepared titania sol (2 mg of commercial TiO_2 + 1 mL of ethanol + 0.3 mL titania sol), in the same conditions adopted for the silica layer. The prepared device was immediately dried in oven at 90°C for 20 h. A further treatment was performed by immersing the device in water for 10 min at 70°C and finally in 10^{-4} M HNO_3 for 20 min at 70°C. Finally, the device was dried in an oven and irradiated for 3 h under UV light.

Photocatalytic tests. The photocatalytic activity of the device was tested under both UV and simulated solar irradiation. Tests were carried out both in the gas phase and in water. The gas phase degradation of ethanol was carried out using the setup reported in Appendix A. An active surface area of 38 cm^2 and an initial pollutant concentration of 198 ppm were employed; the pollutant disappearance, and the formation of acetaldehyde (main reaction intermediate) and CO_2 were followed by gas chromatography. Three consecutive photocatalytic tests were performed in the same conditions to test the stability and the reusability of the device. Photolysis tests showed an ethanol disappearance rate of 1.2×10^{-3} min^{-1}. The degradation of a tetracycline hydrochloride (TC) in water was conducted in an open reactor, with a total active surface of 60 cm^2 and an initial pollutant concentration of 12 ppm (V = 300 mL). The reaction was carried out at spontaneous pH and oxygen saturation was maintained via air bubbling. Before irradiation, the device was kept in the dark for 30 min in order to achieve adsorption-desorption equilibrium. Tests performed in the absence of the device showed a photolysis rate of 2.4 ± 0.2 ppb min^{-1}.

Further details about the preparation and characterization methods can be found in Appendix A.

References

1 M. Crippa, A. Bianchi, D. Cristofori, M. D'Arienzo, F. Merletti, F. Morazzoni, R. Scotti and R. Simonutti, *J. Mater. Chem. C*, 2013, **1**, 484–492.

2 S. Zhang, J. Cao, Y. Shang, L. Wang, X. He, J. Li, P. Zhao and Y. Wang, *J. Mater. Chem. A*, 2015, **3**, 17697–17703.

3 W. Li, H. Li and Y.-M. Zhang, *J. Mater. Sci.*, 2009, **44**, 2977–2984.

4 T. E. Motaung, A. S. Luyt, F. Bondioli, M. Messori, M. L. Saladino, A. Spinella, G. Nasillo and E. Caponetti, *Polym. Degrad. Stab.*, 2012, **97**, 1325–1333.

5 B. Pan, B. Pan, W. Zhang, L. Lv, Q. Zhang and S. Zheng, *Chem. Eng. J.*, 2009, **151**, 19–29.

6 M. Wang, G. Yang, P. Jin, H. Tang, H. Wang and Y. Chen, *Sci. Rep.*, 2016, **6**, 19148.

7 A. M. Díez-Pascual and A. L. Díez-Vicente, *ACS Appl. Mater. Interfaces*, 2015, **7**, 5561–5573.

8 A. Salabat and F. Mirhoseini, *Photochem. Photobiol. Sci.*, 2015, **14**, 1637–1643.

9 P. Ravirajan, S. A. Haque, J. R. Durrant, D. D. C. Bradley and J. Nelson, *Adv. Funct. Mater.*, 2005, **15**, 609–618.

10 H. J. Lee, H. C. Leventis, S. A. Haque, T. Torres, M. Grätzel and M. K. Nazeeruddin, *J. Power Sources*, 2011, **196**, 596–599.

11 R. Wen, J. Guo, C. Zhao and Y. Liu, *Adv. Mater. Interfaces*, 2018, **5**, 1701088.

12 J. Cao, L. Wang, X. He, M. Fang, J. Gao, J. Li, L. Deng, H. Chen, G. Tian, J. Wang and S. Fan, *J. Mater. Chem. A*, 2013, **1**, 5955–5961.

13 Y.-H. Chen, Y.-Y. Liu, R.-H. Lin and F.-S. Yen, *J. Hazard. Mater.*, 2009, **163**, 973–981.

14 Y.-H. Chen, L.-L. Chen and N.-C. Shang, *J. Hazard. Mater.*, 2009, **172**, 20–29.

15 Y. Xu, W. Wen and J.-M. Wu, *J. Hazard. Mater.*, 2018, **343**, 285–297.

16 X. Zhou, C. Shao, S. Yang, X. Li, X. Guo, X. Wang, X. Li and Y. Liu, *ACS Sustain. Chem. Eng.*, 2018, **6**, 2316–2323.

17 J. Krýsa, G. Waldner, H. Měšťánková, J. Jirkovský and G. Grabner, *Appl. Catal. B Environ.*, 2006, **64**, 290–301.
18 W. Tu, Y.-P. Lin and R. Bai, *J. Environ. Chem. Eng.*, 2016, **4**, 230–239.
19 L. Ni, Y. Li, C. Zhang, L. Li, W. Zhang and D. Wang, *J. Appl. Polym. Sci.*, 2016, **133**, 43400.
20 H. Han and R. Bai, *Sep. Purif. Technol.*, 2010, **73**, 142–150.
21 Z. Xing, J. Zhang, J. Cui, J. Yin, T. Zhao, J. Kuang, Z. Xiu, N. Wan and W. Zhou, *Appl. Catal. B Environ.*, 2018, **225**, 452–467.
22 M. Yang, Z. Di and J.-K. Lee, *J. Colloid Interface Sci.*, 2012, **368**, 603–607.
23 G. Soliveri, V. Sabatini, H. Farina, M. A. Ortenzi, D. Meroni and A. Colombo, *Colloids Surfaces A Physicochem. Eng. Asp.*, 2015, **483**, 285–291.
24 J. Z. Ma, J. Hu and Z. J. Zhang, *Eur. Polym. J.*, 2007, **43**, 4169–4177.
25 A. C. McLaren, S. G. McLaren and M. K. Hickmon, *Clin. Orthop. Relat. Res.*, 2007, 60–63.
26 V. Sabatini, H. Farina, A. Montarsolo, S. Ardizzone and M. A. Ortenzi, *Polym. Plast. Technol. Eng.*, 2017, **56**, 296–309.
27 V. Sabatini, C. Cattò, G. Cappelletti, F. Cappitelli, S. Antenucci, H. Farina, M. A. Ortenzi, S. Camazzola and G. Di Silvestro, *Prog. Org. Coatings*, 2018, **114**, 47–57.
28 W. Huang, J.-B. Kim, M. L. Bruening and G. L. Baker, *Macromolecules*, 2002, **35**, 1175–1179.
29 O. Chiantore, L. Trossarelli and M. Lazzari, *Polymer (Guildf).*, 2000, **41**, 1657–1668.
30 I. C. McNeill and S. M. T. Sadeghi, *Polym. Degrad. Stab.*, 1990, **29**, 233–246.
31 V. V. Zuev, F. Bertini and G. Audisio, *Polym. Degrad. Stab.*, 2006, **91**, 512–516.
32 A. Carradò, O. Sokolova, B. Donnio and H. Palkowski, *J. Appl. Polym. Sci.*, 2011, **120**, 3709–3715.
33 G. Soliveri, V. Pifferi, G. Panzarasa, S. Ardizzone, G. Cappelletti, D. Meroni, K. Sparnacci and L. Falciola, *Analyst*, 2015, **140**, 1486–1494.

34 I. Arabatzis, S. Antonaraki, T. Stergiopoulos, A. Hiskia, E. Papaconstantinou, M. Bernard and P. Falaras, *J. Photochem. Photobiol. A Chem.*, 2002, **149**, 237–245.
35 V. Pifferi, L. Rimoldi, D. Meroni, F. Segrado, G. Soliveri, S. Ardizzone and L. Falciola, *Electrochem. commun.*, 2017, **81**, 102–105.
36 A. Antonello, G. Soliveri, D. Meroni, G. Cappelletti and S. Ardizzone, *Catal. Today*, 2014, **230**, 35–40.
37 E. Piera, J. A. Ayllón, X. Doménech and J. Peral, *Catal. Today*, 2002, **76**, 259–270.
38 U.S. Food and Drug Administration, *Summary Report On Antimicrobials Sold or Distributed for Use in Food-Producing Animals*, Washington, DC, USA, 2016.
39 L. Rimoldi, E. Pargoletti, D. Meroni, E. Falletta, G. Cerrato, F. Turco and G. Cappelletti, *Catal. Today*, 2018, **313**, 40–46.
40 R. A. Palominos, M. A. Mondaca, A. Giraldo, G. Peñuela, M. Pérez-Moya and H. D. Mansilla, *Catal. Today*, 2009, **144**, 100–105.
41 R. Wei, F. Ge, S. Huang, M. Chen and R. Wang, *Chemosphere*, 2011, **82**, 1408–1414.
42 D. Calamari, E. Zuccato, S. Castiglioni, R. Bagnati and R. Fanelli, *Environ. Sci. Technol.*, 2003, **37**, 1241–1248.
43 N. Czekalski, T. Berthold, S. Caucci, A. Egli and H. Bürgmann, *Front. Microbiol.*, 2012, **3**, 1–18.
44 F. Magalhães and R. M. Lago, *Sol. Energy*, 2009, **83**, 1521–1526.
45 F. Magalhães, F. C. C. Moura and R. M. Lago, *Desalination*, 2011, **276**, 266–271.

L.R. contribution: physicochemical analyses, photocatalytic tests, data curation, manuscript preparation.

Part II
Tailoring of surface and porosity features of oxidic films

Part II – Introduction

Silicon dioxide (SiO_2) and titanium dioxide (TiO_2) are two of the most adopted oxides. Since the wide applicability of TiO_2 has been already discussed in Part I of this Thesis, I will more deeply dwell on the characteristics of silicon dioxide, but also on the theme of wettability. In fact, in this part of the Thesis, mainly silicon dioxide films and their surface and morphology modification were studied, making extensive use of wettability characterizations. The surface properties of the films were not only studied by water contact angle measurements, but also properly tailored for the final scope. Moreover, electrochemical characterization techniques were adopted to better comprehend the surface features of bare, morphology modified and surface modified films.

In recent years, both SiO_2 and TiO_2, despite their very different characteristics (insulating properties for SiO_2 and semiconductor properties for TiO_2) were deeply employed in the field of surface science, thanks to advantageous characteristics of their surfaces. For example, the high reactivity of the typical hydroxylated surfaces of SiO_2 and TiO_2 allowed surface modifications by organic molecules, often referred as *functionalizing agents*, to be performed[1,2].

This kind of recently developed materials are usually constituted by an inorganic surface on which an organic molecule is allowed to react to form an organic/inorganic hybrid material. This way, the surface properties can be fully modified (and tailored), with respect to that of the bare oxide. In this field, *self-assembled monolayers* (SAM) have attracted much attention in the last few years[3–5]. By means of advanced techniques and fine control of the experimental conditions, the functionalizing molecule can form a thin layer with the thickness of one single molecule which is able to orderly arrange onto the oxide surface.

The possibility to modulate important surface properties, such as wettability, adhesion and conductivity, is responsible for the great number of application fields: nanotechnology, opto-electronics, protective

coatings, patterned surfaces, chemical sensors and biosensors, protein adsorption and cell adhesion[3].

The most adopted functionalizing molecules for preparing organic-SiO_2/TiO_2 hybrids in films are alkylsilanes. These compounds are highly reactive with the hydroxyl groups present on the oxidic surfaces, on which they tend to self-assemble and polymerize, and allow the wettability of the oxides to be drastically modified, even achieving superhydrophobicity. Superhydrophobic surfaces are extensively studied in materials and surface science for their self-cleaning, anti-stain, anti-corrosion and low adhesion/friction applications[6–8]. Alkylsilanes are suitable for engineering (super)hydrophobic surfaces, due to their amphiphilic nature. Together with a polar moiety (which reacts with the inorganic surface), they are characterized by an apolar chain which can impart the commonly called *water repellency*. Alkylsilanes with fluorinated apolar chains more easily permit to achieve superhydrophobicity.

Moreover, due to its semiconductor properties, in the case of TiO_2 the functionalization by organic molecules can also be exploited for photocatalytic applications. Chemisorbed or physisorbed molecules can be degraded by irradiating the modified surface with light. The degradation proceeding can be followed by means of different techniques, among which water contact angle measurements. In fact, in the case of functionalizing agents imparting hydrophobicity, with the progress of the degradative process, the progressive restoring of the TiO_2 surface hydrophilicity can be followed. Further, TiO_2-based hybrid surfaces are often exploited for patterning applications. The so-called *photocatalytic lithography* allows patterned surfaces, *i.e.* patch-wise surfaces characterized by wettability contrasts, to be developed. In contrast to photochemical lithography, which usually needs powerful and high energy ($\lambda < 185$ nm) light sources and has been performed on a wide range of substrates (silicon, polymers, metals), photocatalytic lithography allows less demanding experimental conditions.

Patch-wise superhydrophobic-(super)hydrophilic surfaces find application for electronic devices, cells and metals selective adsorption, drug delivery systems, electrolytes and gas transport[9–13].

Another strategy for developing engineered oxidic films is the modification of the morphology. 2D and 3D morphology engineering has

been exploited by means of many different strategies and for a wide range of applications[14–17]. One of these is the study of wettability modification for the understanding of the mechanism which stand at the basis of superhydrophobic and/or (super)oleophobic surfaces. Multiscale roughness, as well as complex micro and nano structures, mimicking natural surfaces such as lotus leaves and gecko skin are often able to create devices with specific wetting features[8,13,18,19].

Moreover, in recent years, the morphology tuning, especially concerning porosity, has attracted much attention in the field of electrochemical sensing. On the grounds of the pioneering work by Kresge on mesoporous silica macrostructures developed by Mobil® for application in heterogeneous catalysis[20], SiO_2 films have been extensively studied, also in electrochemistry[21–23]. Regarding the sensing of molecules of environmental or biological/biomedical concern, electrochemical characterization techniques performed on modified electrodes encountered recent interest[24–26].

In this area, but also in the field of the above-mentioned hybrid surfaces, researchers are still involved in the understanding of the fundamental phenomena which govern the surface and bulk properties, the wetting features and the mass transport and charge transfer phenomena. Moreover, regarding electrochemical sensing, the lowering of the detection and quantification limits, the selectivity for the effective use in complex matrices, and the durability and reusability of the electrode are felt as the most urgent needs[27–29]. In the last years, the theme of electroactive surface engineering by means of nanomaterials received particular attention[30]. More recently, the problem of surface (bio)fouling involved a lot of research[26,31–33]. Fouling prevents the durable use of electrode, due to irreversible adsorption of active or inactive species, scarce reproducibility, low robustness and stability. Nanotechnology and materials science stand out as interesting and promising tools for overcoming these issues, especially by developing new engineered device and architectures, able to maintain high activity while promoting electrode usability and even selectivity[24,34–36].

During my PhD, I devoted to the preparation of differently modified SiO_2 and TiO_2 films, mainly prepared by depositing colloidal solutions or powders on different substrates. Both surface functionalization for

wettability modification purposes and porosity tunability were performed by chemical vapour deposition, spin-coating and hard templating techniques were studied. Especially, after comprehending the mass transport and the charge transfer phenomena occurring at an electroactive surface modified by different layers of silica, and the variation of the electrochemical response with respect the surface wettability, I dedicate myself to the developing of an electrochemical sensor based on a mesoporous hard-templated silica architecture. The morphology of the electrode, together with its charge and wetting properties allowed its effective use in the detection of dopamine (a neurotransmitter involved in the diagnosis of Parkinson's disease) in a complex matrix, upon size-excluding and interferent rejecting effects. In the second part of this Thesis these studies with different applications (understanding of fundamental properties and phenomena, electrochemical sensing and development of self-cleaning, anti-stain, anti-fogging and patterned surfaces) are presented.

II.1 Silicon dioxide (SiO_2)

Silicon dioxide is one of the most abundant chemical compounds on Earth. It is widely adopted for both research and industrial purposes. It mainly finds application as components in a lot of manufactures, in the construction industry, in the glass and ceramics production. It is also used as additive in pharmaceutics, cosmetics and foods, as support in heterogeneous catalysis, while its hydrophobic derivatives are used as defoamer components. The native oxide layer growing on silicon substrates has an important role for its insulating character (its band gap is *ca.* 9 eV wide) in microelectronics.

Silicon dioxide is usually found in nature as quartz, its most common crystalline structure. Nonetheless, silicon dioxide has a lot of other polymorphic forms: cristobalite, tridymite, stishovite, seifertite are just some of the structural form and minerals of silica. Interestingly, silica is very common and adopted in its amorphous form, mainly for research aims. SiO_2, in fact, usually crystallizes at high temperature (or pressure) conditions. Moreover, mesoporous silica is a form of SiO_2, generally amorphous, which has been recently developed in nanotechnology deserving particular attention[37,38]. They were firstly developed for

application in heterogeneous catalysis, where MCM-41 and SBA-15 are the most famous examples. The porosity in the range of mesoporosity, usually obtained by means of soft or, more rarely, hard templating agents, allows many interesting properties to be exploited[39–41]. The increase of the surface area, the pore dimensions-dependent accessibility of molecules and particles of different nature, the higher availability of the active acid sites are responsible for the use of mesoporous silica also for molecular sieving, engineered (bio)sensors, energy storage and drug delivery[37,42–48]. In this field, the reactivity of its surface also allows modifications by organic molecules with specific properties to be performed[23,49,50].

II.2 Basic principles of wettability

When a drop of liquid falls on a solid surface, it can behave in different ways, in terms of spreading, as a result of the physicochemical characteristics of both the liquid and the surface. In this way, three different interfaces (liquid-solid, liquid-gas and solid-gas) are formed, together with a *triple interface point* in which the three phases are in contact and the force given by the three interface surface tensions are balanced.

Basically, the higher the spreading of the drop, the higher its affinity with the solid surface, primarily upon the polar or apolar character of the two components and their chemical nature. This is particularly true in the case of ideal, *i.e.* smooth, surfaces.

The study of the triple interface formed is usually studied by *contact angle* measurements to comprehend the surface physicochemical properties. The so-called contact angle, generally referred as θ, is the angle formed, in equilibrium conditions, between the solid surface and the tangent to the liquid-gas interface, measured at the triple interface point and, conventionally, in the liquid phase. In general, and for the most common measurements performed by using water, it discriminates between hydrophilic ($\theta < 90°$) and hydrophobic ($\theta > 90°$) surfaces.

In the case of ideal surfaces, the contact angle value is governed by Young equation, which describes the contact angle, θ, as a function of the interfacial tension, γ:

$$\gamma_s = \gamma_{ls} + \gamma_l \cos\theta \qquad \text{(I.1)}$$

where γ_s, γ_{ls} and γ_l are the solid-gas, liquid-solid and liquid-gas interfaces surface tensions.

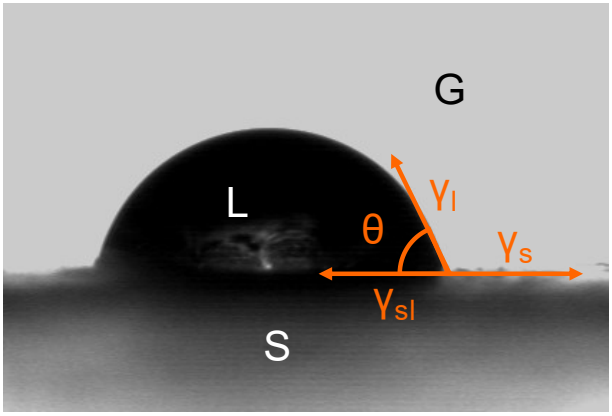

Figure II.1 – Schematic representation of the forces acting in the triple interface point.

Nonetheless, due to the hypotheses of the Young model, no contact angle hysteresis is expected. For real surfaces instead, often not a single value of contact angle is observed, mainly upon dynamic measurements. In other words, due to surface roughness, surface deformations and chemical heterogeneity and depending on the liquid drop size, a $\Delta\theta$ value between the so-called advancing (the maximum measured angle, θ_a) and receding (the minimum measured angle, θ_r) contact angles can be observed[51].

In order to better describe the effects provided by the deviation from the ideal case, a different wettability model taking into account the surface roughness was described by Wenzel[52]. In this model, a roughness factor, *r*, described as the ratio between the real and the geometric surface is introduced to weight the effect of roughness.

From the Wenzel equation

$$\cos\theta^* = r\cos\theta \qquad \text{(I.2)}$$

where θ^* is the contact angle according to the Wenzel model and θ is the contact angle according to the Young model as described above, it can be traced back how surface roughness tends to enhance the character of the surface both in the case of hydrophilicity ($\theta < 90°$) and hydrophobicity ($\theta < 90°$), since in any case it can be considered that $r > 1$.

However, the Wenzel equation should be considered mainly as a qualitative relation between the surface wetting features and its roughness. In fact, no limitation to complete wetting ($\cos\theta^* > 1$) or complete drying

($\cos\theta^* < -1$) is hypothesized in the case of highly rough surfaces ($r >> 1$). Despite this, these extreme conditions cannot trivially be achieved just by making the roughness arbitrarily large.

For explaining the behaviour of highly rough hydrophobic surfaces, a further wettability theory was conceived by Cassie and Baxter[53]. This model implies that in the case of specific morphologies and asperities, the liquid drop is most likely to be in contact with the solid just on the surface asperities. In this way, air pockets under the liquid drop are formed, responsible for enhanced hydrophobicity, even allowing superhydrophobicity to be achieved. This model is based on the following equation:

$$\cos\theta^* = -1 + \varphi_s(\cos\theta + 1) \qquad \text{(I.3)}$$

where φ_s is the fraction of solid actually in contact with the liquid and θ is Young contact angle. Thus, if φ_s = 10%, *i.e.* if the liquid has very little interaction with the solid and 90% of the drop base contacts air, a surface with a contact angle of 110° in the ideal case (Young's model) will reach about 160°. In other words, the smaller the φ_s value, the closer the situation of no contact between the solid and the liquid, the extreme case in which θ = 90°.

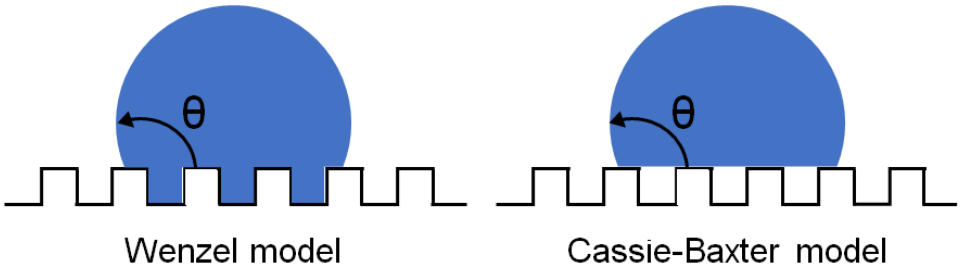

Figure II.2 – The two models of the wettability of rough surfaces.

II.3 TiO_2 photo-induced superhydrophilicity

The wettability of TiO_2 can be tuned adopting UV light irradiation by exploiting its behaviour as a photocatalyst.

The native surface of TiO_2 is scantly hydrophilic (*ca.* 70°) due to the crystallographic structure of the oxide, characterized by Ti–O repeated chemical bonds. Upon UV light irradiation, the surface become more and more hydrophilic till complete spreading (θ = 0°), often referred as

superhydrophilicity. The causes of this switchable and reversible behaviour are still debated in the literature[6]. Briefly, the photoreduction of Ti^{4+} centres to Ti^{3+} which promotes oxygen vacancies, together with the chemisorption of hydrophilic hydroxyl groups on surface defect sites are responsible for the enhanced surface hydrophilicity induced by light irradiation. As reported by Liu *et al.*, the surface reconstruction is probably initiated by photopromoted electron hole trapped by a surface oxygen atom resulting in an oxygen defect[6]. Then, water molecules spontaneously adsorb at the defect sites dissociatively[6]. Moreover, the degradation of adventitious organic molecules adsorbed on the surface further promotes hydrophilicity, although contamination and light induced decontamination is not the most relevant effect. Conversely, in prolonged dark conditions, the TiO_2 surface come back to the native geometric and chemical structure by desorption of hydroxyl groups and water molecules, restoring the slight hydrophilicity.

References

1 F. Milanesi, G. Cappelletti, R. Annunziata, C. L. Bianchi, D. Meroni and S. Ardizzone, *J. Phys. Chem. C*, 2010, **114**, 8287–8293.

2 S. A. Kulkarni and K. P. Vijayamohanan, *Surf. Sci.*, 2007, **601**, 2983–2993.

3 C. Haensch, S. Hoeppener and U. S. Schubert, *Chem. Soc. Rev.*, 2010, **39**, 2323.

4 S. A. Di Benedetto, A. Facchetti, M. A. Ratner and T. J. Marks, *Adv. Mater.*, 2009, **21**, 1407–1433.

5 S. Kobayashi, T. Nishikawa, T. Takenobu, S. Mori, T. Shimoda, T. Mitani, H. Shimotani, N. Yoshimoto, S. Ogawa and Y. Iwasa, *Nat. Mater.*, 2004, **3**, 317–322.

6 K. Liu, M. Cao, A. Fujishima and L. Jiang, *Chem. Rev.*, 2014, **114**, 10044–10094.

7 A. Fujishima, X. Zhang and D. A. Tryk, *Surf. Sci. Rep.*, 2008, **63**, 515–582.

8 D. Quéré, *Annu. Rev. Mater. Res.*, 2008, **38**, 71–99.

9 M. Moxey, A. Johnson, O. El-Zubir, M. Cartron, S. S. Dinachali, C. N. Hunter, M. S. M. Saifullah, K. S. L. Chong and G. J. Leggett, *ACS Nano*, 2015, **9**, 6262–6270.

10 D. Meroni, S. Ardizzone, U. S. Schubert and S. Hoeppener, *Adv. Funct. Mater.*, 2012, **22**, 4376–4382.

11 Q. Wang, Q. Meng, P. Wang, H. Liu and L. Jiang, *ACS Nano*, 2015, **9**, 4362–4370.

12 G. Panzarasa, G. Soliveri, K. Sparnacci and S. Ardizzone, *Chem. Commun.*, 2015, **51**, 7313–7316.

13 G. Soliveri, R. Annunziata, S. Ardizzone, G. Cappelletti and D. Meroni, *J. Phys. Chem. C*, 2012, **116**, 26405–26413.

14 S. Nagarajan, M. Li, R. A. Pai, J. K. Bosworth, P. Busch, D.-M. Smilgies, C. K. Ober, T. P. Russell and J. J. Watkins, *Adv. Mater.*, 2008, **20**, 246–251.

15 P. C. A. Alberius, K. L. Frindell, R. C. Hayward, E. J. Kramer, G. D. Stucky and B. F. Chmelka, *Chem. Mater.*, 2002, **14**, 3284–3294.

16 A. Enesca, M. Baneto, D. Perniu, L. Isac, C. Bogatu and A. Duta, *Appl. Catal. B Environ.*, 2016, **186**, 69–76.

17 W. Zhang, M. Saliba, D. T. Moore, S. K. Pathak, M. T. Hörantner, T. Stergiopoulos, S. D. Stranks, G. E. Eperon, J. A. Alexander-Webber, A. Abate, A. Sadhanala, S. Yao, Y. Chen, R. H. Friend, L. A. Estroff, U. Wiesner and H. J. Snaith, *Nat. Commun.*, 2015, **6**, 6142.
18 A. Fujishima, X. Zhang and D. Tryk, *Surf. Sci. Rep.*, 2008, **63**, 515–582.
19 E. Martines, K. Seunarine, H. Morgan, N. Gadegaard, C. D. W. Wilkinson and M. O. Riehle, *Nano Lett.*, 2005, **5**, 2097–2103.
20 C. T. Kresge, *Nature*, 1992, **359**, 710–712.
21 A. Walcarius, *Chem. Soc. Rev.*, 2013, **42**, 4098.
22 A. Walcarius, E. Sibottier, M. Etienne and J. Ghanbaja, *Nat. Mater.*, 2007, **6**, 602–608.
23 G. Giordano, N. Vilà, E. Aubert, J. Ghanbaja and A. Walcarius, 2017, **237**, 227–236.
24 S. Chandra, A. D. Miller and D. K. Y. Wong, *Electrochim. Acta*, 2013, **101**, 225–231.
25 M. Silvestrini, P. Schiavuta, P. Scopece, G. Pecchielan, L. M. Moretto and P. Ugo, *Electrochim. Acta*, 2011, **56**, 7718–7724.
26 G. Di Carlo, A. Trani, D. Zane, G. M. Ingo, M. Pasquali, A. Dell'Era and A. Curulli, *Electroanalysis*, 2014, **26**, 1409–1418.
27 C. M. A. Brett and A. M. Oliveira-Brett, *J. Solid State Electrochem.*, 2011, **15**, 1487–1494.
28 G. Soliveri, V. Pifferi, G. Panzarasa, S. Ardizzone, G. Cappelletti, D. Meroni, K. Sparnacci and L. Falciola, *Analyst*, 2015, **140**, 1486–1494.
29 V. Pifferi, G. Soliveri, G. Panzarasa, G. Cappelletti, D. Meroni and L. Falciola, *Anal. Bioanal. Chem.*, 2016, **408**, 7339–7349.
30 C. M. Welch and R. G. Compton, *Anal. Bioanal. Chem.*, 2006, **384**, 601–19.
31 J. Patel, L. Radhakrishnan, B. Zhao, B. Uppalapati, R. C. Daniels, K. R. Ward and M. M. Collinson, *Anal. Chem.*, 2013, **85**, 11610–11618.
32 P. Daggumati, Z. Matharu, L. Wang and E. Seker, *Anal. Chem.*, 2015, **87**, 8618–8622.
33 A. Fagan-Murphy, F. Watt, K. A. Morgan and B. A. Patel, *J.*

Electroanal. Chem., 2012, **684**, 1–5.

34 G. Soliveri, V. Pifferi, G. Panzarasa, S. Ardizzone, G. Cappelletti, D. Meroni, K. Sparnacci and L. Falciola, *Analyst*, 2015, **140**, 1486–1494.

35 B. Hoyer and N. Jensen, *Electrochem. commun.*, 2003, **5**, 257–261.

36 P. Daggumati, Z. Matharu and E. Seker, *Anal. Chem.*, 2015, **87**, 8149–8156.

37 C. Perego and R. Millini, *Chem. Soc. Rev.*, 2013, **42**, 3956–3976.

38 A. Walcarius and M. M. Collinson, *Annu. Rev. Anal. Chem.*, 2009, **2**, 121–143.

39 E. W. S. J. C. Vartuli, K. D. Schmitt, C. T. Kresge, W. J. Roth, M. E. Leonowicz, S. B. McCullen, S. D. Hellring, J. S. Beck, J. L. Schlenker, D. H. Olson, *Chem. Mater.*, 1994, **6**, 2317–2326.

40 A. H. Yuwono, Y. Zhang, J. Wang, X. H. Zhang, H. Fan and W. Ji, *Chem. Mater.*, 2006, **18**, 5876–5889.

41 W. Li and D. Zhao, *Adv. Mater.*, 2013, **25**, 142–149.

42 S. Y. Tan, C. Teh, C. Y. Ang, M. Li, P. Li, V. Korzh and Y. Zhao, *Nanoscale*, 2017, **9**, 2253–2261.

43 D. Fattakhova-Rohlfing, M. Wark and J. Rathouský, *Chem. Mater.*, 2007, **19**, 1640–1647.

44 M.-S. Wu, X.-T. Sun, M.-J. Zhu, H.-Y. Chen and J.-J. Xu, *Chem. Commun.*, 2015, **51**, 14072–14075.

45 Y. Zhang, Z. Zhang, W. Yan, B. Zhang, Y. Feng, A. M. Asiri, M. K. Nazeeruddin and P. Gao, *J. Mater. Chem. A*, 2017, **5**, 1415–1420.

46 W. Cheng, C. Liang, X. Wang, H. Tsai, G. Liu, Y. Peng, J. Nie, L. Huang, L. Mei and X. Zeng, *Nanoscale*, 2017, **9**, 17063–17073.

47 M. Saadaoui, I. Fernández, G. Luna, P. Díez, S. Campuzano, N. Raouafi, A. Sánchez, J. M. Pingarrón and R. Villalonga, *Anal. Bioanal. Chem.*, 2016, **408**, 7321–7327.

48 Z. Liu, X. Zhang, T. Murakami and A. Fujishima, *Sol. Energy Mater. Sol. Cells*, 2008, **92**, 1434–1438.

49 S. Huh, H.-T. Chen, J. W. Wiench, M. Pruski and V. S.-Y. Lin, *Angew. Chemie Int. Ed.*, 2005, **44**, 1826–1830.

50 M. Laskowska, I. Kityk, M. Dulski, J. Jędryka, A. Wojciechowski, J. Jelonkiewicz, M. Wojtyniak and Ł. Laskowski, *Nanoscale*, 2017, **9**, 12110–12123.

51 H. Y. Erbil, G. McHale, S. M. Rowan and M. I. Newton, *Langmuir*, 1999, **15**, 7378–7385.
52 R. N. Wenzel, *Ind. Eng. Chem.*, 1936, **28**, 988–994.
53 A. B. D. Cassie and S. Baxter, *Trans. Faraday Soc.*, 1944, **40**, 546.

Chapter 8

Electrochemical characterization of insulating silica-modified electrodes: transport properties and physicochemical features

The modification of electrodes by deposition of electroinactive layers (*e.g.* insulating oxides or non-conductive polymers), in which analytes can dissolve and diffuse, is a field of great interest for electrochemical (fuel cells, batteries, …) and electroanalytical (sensors) applications due to the possibility to tune diffusion, transport and reactivity properties[1–5]. Starting from the pioneering works by Gileadi *et al.* and Amatore *et al.* about partially blocked electrodes[6,7], theoretical and computational models have been proposed to rationalize these phenomena[1,4,8–11]. However, experimental studies aiming at verifying such theoretical models have been scarce[12,13]. Furthermore, the inactive layer morphology and physicochemical features have been often disregarded in the complete understanding of the electrochemical performance. In this context, the development of electrodes modified with tailored electroinactive layers is crucial to clarify the mechanisms of diffusion, mass transport and charge transfer in these systems.

In the work presented in this Chapter, planar ITO-coated glass electrodes were modified by the deposition of a silica sol and the role of film thickness was studied by depositing subsequent layers. The modified electrodes were characterized by field emission scanning electron microscopy (FE-SEM), atomic force microscopy (AFM), UV-vis transmittance and water contact angle measurements to investigate their morphological and physicochemical properties. Electrochemical

measurements by both cyclic voltammetry (CV) and electrochemical impedance spectroscopy (EIS), adopting both negatively and positively charged electrochemical probes, allowed diffusion and transport phenomena to the electrode to be understood.

8.1 Results and discussion

8.1.1 Morphological properties

FE-SEM images show that all samples exhibited high homogeneity and complete substrate coverage (Fig. 8.1a), with a morphology characterized by nanometric silica domains (Fig. 8.1a, inset), with no significance differences regarding the number of the deposited layers. The nanometric features at the film surface can be traced back to the colloidal silica sol: DLS measurements performed on the sol before deposition show that the transparent hydroalcoholic solution contained silica nuclei of *ca.* 5 ± 2 nm size (Fig. 8.1b). The homogeneity of the silica films was confirmed by AFM images (Fig. 8.1c), showing low surface roughness (RMS for SiO_2_1: 0.7 nm).

The optical properties of the silica films were studied by UV-vis transmittance spectroscopy. The ITO-coated glass shows a typical spectrum characterized by an absorption edge at about 320 nm. The deposition of silica sol does not shift the absorption edge of the films. However, with respect to the ITO-coated substrate, the silica coated samples exhibit higher transmittance in the 350–600 nm region due to the larger refractive index of ITO with respect to SiO_2 (Fig. 8.1d). Successive depositions of SiO_2 further increase the optical transparency, consistently with the formation of a thicker homogeneous anti-reflective layer.

The wetting properties of the different samples were investigated measuring water contact angles, θ_w[14]. While ITO is hydrophobic (θ_w *ca.* 90°) with a moderate hysteresis between advancing and receding angles (*ca.* 30°), all silica modified electrodes are characterized by lower θ_w, *i.e.* a higher hydrophilicity, and by a large hysteresis between advancing and receding angles (hysteresis starting from 55 and up to 69° for the different samples), compatible with a Wenzel state[15,16]. SiO_2_3 shows a lower value of θ_w as an evidence of an appreciably increased hydrophilic character of the electrode (Fig. 8.2a). Contact angle values further decrease for

successive depositions, reaching about 40° with 5 layers. This latter effect can be interpreted as due to the increased water chemisorption ensuing the growth of the film nanostructure with its thickness, as proposed by Ganesh *et al.* for TiO_2 layers[17].

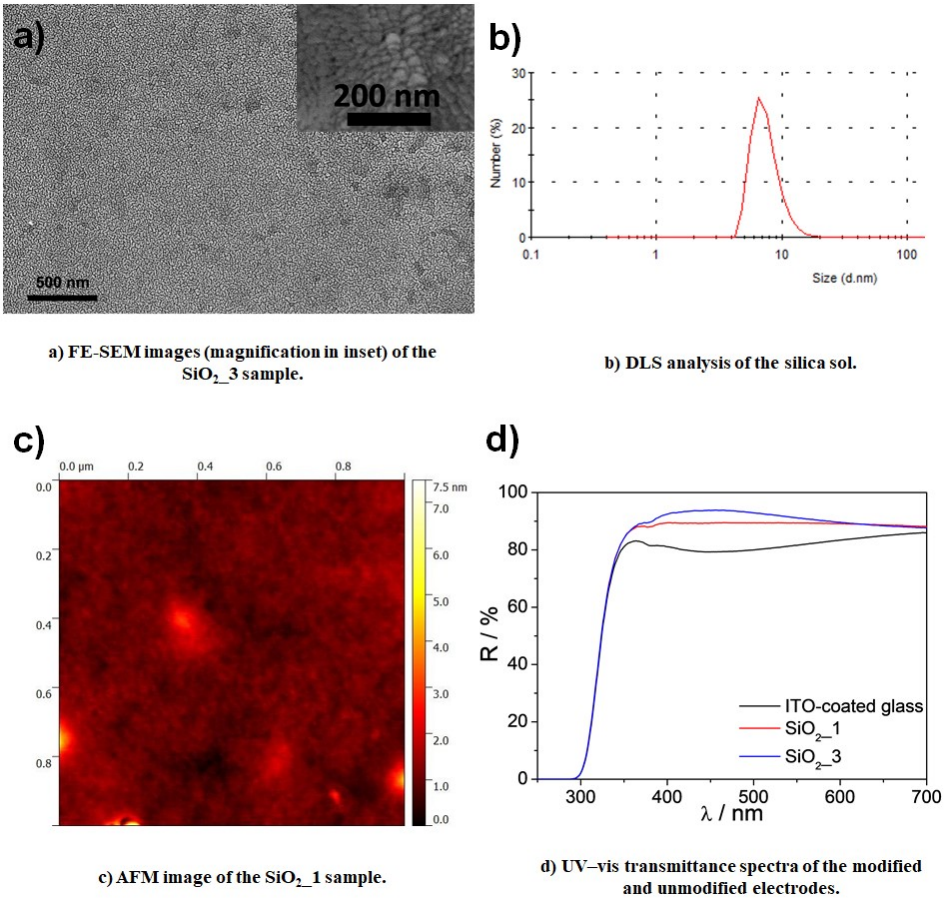

a) FE-SEM images (magnification in inset) of the SiO_2_3 sample.

b) DLS analysis of the silica sol.

c) AFM image of the SiO_2_1 sample.

d) UV–vis transmittance spectra of the modified and unmodified electrodes.

Figure 8.1 – Morphological and optical properties results.

8.1.2 Electrochemical properties

CV and EIS were employed with two commonly adopted redox probes: $[Fe(CN)_6]^{4-}/[Fe(CN)_6]^{3-}$ and $[Ru(NH_3)_6]^{3+}/[Ru(NH_3)_6]^{2+}$, which present the same dimensions being different by their opposite charge[18–20]. Therefore, the two probes are supposed to behave differently with respect to SiO_2, which is negatively charged in the working conditions (pH 5 – 6 aqueous KCl solution), having an isoelectric point very close to 3[21,22].

The deposition of SiO_2 layers on ITO drastically decreases the probes electrochemical response in comparison with the bare support (Fig. 8.2a), due to the insulating properties of the oxide, confirming the homogeneity and complete coverage found by FE-SEM characterization. The present electrodes can be considered non-porous electroinactive materials as the measured electrochemical response can be ascribed to the diffusion of the active species through the material. The current decrease, by about one order of magnitude with respect to ITO, is more evident in the case of the negatively charged iron probe, as expected by the charge repulsion from SiO_2. However, the study of SiO_2_n samples revealed an unexpected behaviour with both probes: while the peak current decreases passing from one to two insulating layers, we observed an unforeseen increase when the third layer is added (Fig. 8.2b). Moreover, the voltammogram shape undergoes a remarkable change during the layer transition, which is dependent on the scan rate. In particular, in the case of SiO_2_1 (curve A), the voltammogram presents a quasi-step shape for low scan rates transforming in a peak for higher scan rates (not shown). When two SiO_2 layers are deposited (SiO_2_2, curve B), a step is obtained for the entire scan rate range. The addition of a third layer (SiO_2_3, curve C) always results in a peak-shaped voltammogram, regardless of the scan rate. The deposition of further layers increases the capacitive currents and the background noise for the insulating properties of silica, making the probes undetectable (curve D).

This trend is confirmed by the slopes obtained from the Randles-Sevčik plot (Fig. 8.2a). Furthermore, the very low slope values ($<< 0.5$) of ln i *vs.* ln v plots for all silica samples, support the evidence of a remarkable modification of the probe diffusion mode, which cannot be described anymore only by the classical planar diffusion phenomenon[1].

Furthermore, EIS measurements (Fig. 8.2b) show that the highest and the lowest impedance values are observed for the 2 and 3 layers samples, respectively. Also the charge transfer resistance values, obtained by the fitting of impedance data (Fig. 8.2a), follow the same trend.

The characteristic electrochemical behaviour shown by the SiO_2_n samples can be examined on the grounds of literature results relative to simulated voltammetric patterns, theorized by Compton *et al.* for non-porous electroinactive materials[1,4]. Compton *et al.* ascribed the different

shapes of the voltammetric response to the change of probe diffusion coefficient inside the insulating layer in comparison with that of the bulk solution (Fig. 8.2b)[1]. According to their simulations, under the adopted experimental conditions, a transition from step-shaped to peak-shaped voltammograms by increasing the scan rate should be recorded (red line) considering the conventional diffusion coefficients of the two probes in solution. Actually, this behaviour was found only for SiO_2_1. An increase of the material diffusion coefficient must be invoked when only step-shaped voltammograms are recorded in the investigated scan rate range (green line). This corresponds, in the present case, to SiO_2_2. Moreover, peak-shaped voltammograms independent of scan rate may be due to a further increase of the diffusion coefficients in the insulating layer (blue line). This might mirror the behaviour of SiO_2_3. Therefore, an increase of the diffusion coefficient with layers in the silica-based electrodes should be invoked.

The overall electrochemical behaviour shown by the present layers are closely related to the physicochemical features of the electrode[4,23]. The apparent diffusion coefficient increase with the number of silica layers, together with the observed peak current behaviour, can be the result of a complex balance between diverging effects. The progressive decrease in water contact angle of the layers produces a higher affinity between the electrolyte solution and the electrode surface, with an ensuing promotion of the diffusion coefficient. On the other hand, the silica insulating properties cause competing detrimental effects on the electrochemical performance with increasing film thickness. The optimal balance of these two diverging effects was found in the present case for SiO_2_3, which shows the highest peak current density and the lowest impedance values.

a)

Sample	Wettability	Electrochemical characterization				
	Contact angle	CV Fe probe		CV Ru probe		EIS
	θ_w / °	Slope i_a vs $v^{0.5}$ / (mA cm^{-2} V$^{-0.5}$ s$^{0.5}$)	Slope ln i_a vs. ln v	Slope i_c vs $v^{0.5}$ / (mA cm^{-2} V$^{-0.5}$ s$^{0.5}$)	Slope ln i_c vs. ln v	R_{CT} / (kΩ cm^2)
ITO	90	2.16 ± 0.08	0.50 ± 0.01	- 1.30 ± 0.02	0.45 ± 0.01	-
SiO_2_1	76	(2.14 ± 0.03) · 10^{-2}	0.31 ± 0.01	(- 7.3 ± 0.2) · 10^{-2}	0.28 ± 0.02	29 ± 3
SiO_2_2	69	(0.48 ± 0.04) · 10^{-2}	0.18 ± 0.03	(- 1.07 ± 0.03) · 10^{-2}	0.21 ± 0.02	71 ± 1
SiO_2_3	51	(7.94 ± 0.09) · 10^{-2}	0.36 ± 0.01	(- 18.0 ± 0.3) · 10^{-2}	0.36 ± 0.02	6.6 ± 0.1

a) Static water contact angles (±5°), CV parameters for both electrochemical probes, and charge transfer resistances, R_{CT}, obtained by EIS measurements.

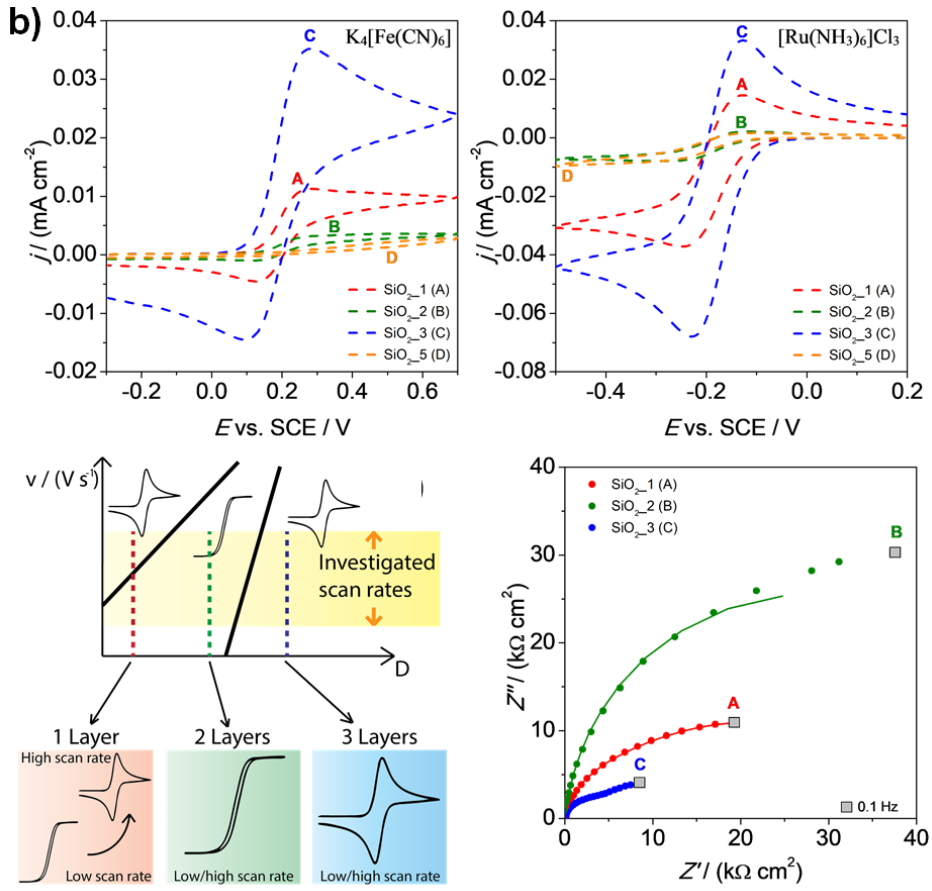

b) Cyclic voltammograms registered at 100 mV s^{-1} for electrodes modified with different numbers of layers of silica in the presence of 3 mM $K_4[Fe(CN)_6]$ (top, left) and $[Ru(NH_3)_6]Cl_3$ (top, right). Schematic representation of the evolution of the CV pattern, according to Compton's theoretical model (adapted from [1]) (bottom, left). Complex plane plot in the presence of 3 mM $K_4[Fe(CN)_6]$ registered at +0.25 V (bottom, right).

Figure 8.2 – Electrochemical characterization results.

8.2 Conclusions

The consecutive deposition of insulating silica layers onto an ITO electrode was analysed with the aim of providing experimental evidence to theoretical models concerning electroinactive layer-modified electrodes. Both FE-SEM, AFM and UV-vis spectroscopy show that the conductive support is covered by a continuous and homogeneous layer. The electrochemical characterizations revealed a scan rate-dependent variation of the CV shape with the number of insulating layers, which was attributed, on the grounds of previous theoretical models, to a progressive increase of the diffusion coefficient. In the present case, the progressive enhancement of film hydrophilicity is proposed as a possible origin of this diffusion coefficient increase. The balance between the diffusion coefficient increase and the insulating effect produced by consecutive silica layer addition, is proposed to interpret the overall electrochemical behaviour. The present results can offer an interpretative framework to better understand diffusion and transport properties in a number of electroinactive layer-modified electrodes, such as sensors, batteries and fuel cells.

8.3 Specific procedures

Samples preparation. Indium tin oxide (ITO) supports (15-25 Ω-sq^{-1}, 2.5 × 2 cm^2) were used as substrates for film deposition. Before deposition, they were sonicated in a 50:50 water/isopropanol mixture and in water, then dipped in H_2SO_4 98% for 30 s, rinsed with water and dried under N_2 flux.

A silica sol was prepared by mixing 16.8 mL of water, 25.4 mL of ethanol, 2.2 mL of HCl 1 M and 4.9 mL of tetraethyl orthosilicate. The sol was stirred for 1 h, then aged at room temperature for 24 h before use.

Silica films were prepared by spin coating the silica sol (3000 rpm, 30 s, 500 rpm s^{-1}) on the ITO glass, repeating the deposition procedure to obtain multilayers. Each layer was *ca.* 100 nm-thick, as determined by FE-SEM cross sectional images. Finally, films were dried at room temperature overnight. Each film was re-synthesized at least 3 times. Samples were labelled "SiO_2_n", where *n* is the number of deposited silica layers.
Further details about the preparation and characterization methods can be found in Appendix A.

References

1 D. Menshykau and R. G. Compton, *Langmuir*, 2009, **25**, 2519–2529.

2 G. Giordano, C. Durante, A. Gennaro and M. Guglielmi, *J. Phys. Chem. C*, 2016, **120**, 28820–28824.

3 C. Song and G. Villemure, *Microporous Mesoporous Mater.*, 2001, **44**–**45**, 679–689.

4 S. Eloul, C. Batchelor-McAuley and R. G. Compton, *J. Solid State Electrochem.*, 2014, **18**, 3239–3243.

5 M. Saadaoui, I. Fernández, G. Luna, P. Díez, S. Campuzano, N. Raouafi, A. Sánchez, J. M. Pingarrón and R. Villalonga, *Anal. Bioanal. Chem.*, 2016, **408**, 7321–7327.

6 H. Reller, F. Kirowa-Eisner and E. Gileadi, *J. Electroanal. Chem. Interfacial Electrochem.*, 1982, **138**, 65–77.

7 C. Amatore, J. M. Savéant and D. Tessier, *J. Electroanal. Chem. Interfacial Electrochem.*, 1983, **147**, 39–51.

8 K. Neyts, M. Karvar, O. Drobchak, T. Brans, F. Strubbe and F. Beunis, *Colloids Surfaces A Physicochem. Eng. Asp.*, 2014, **440**, 101–109.

9 F. G. Chevallier, N. Fietkau, J. del Campo, R. Mas, F. X. Muñoz, L. Jiang, T. G. J. Jones and R. G. Compton, *J. Electroanal. Chem.*, 2006, **596**, 25–32.

10 F. G. Chevallier, T. J. Davies, O. V. Klymenko, L. Jiang, T. G. J. Jones and R. G. Compton, *J. Electroanal. Chem.*, 2005, **580**, 265–274.

11 F. G. Chevallier, T. J. Davies, O. V. Klymenko, L. Jiang, T. G. J. Jones and R. G. Compton, *J. Electroanal. Chem.*, 2005, **577**, 211–221.

12 A. Walcarius, E. Sibottier, M. Etienne and J. Ghanbaja, *Nat. Mater.*, 2007, **6**, 602–608.

13 A. Vuorema, M. Sillanpää, K. J. Edler, R. Jaber, S. E. C. Dale, S. Bending, Y. Gu, K. Yunus, A. C. Fisher and F. Marken, *Electroanalysis*, 2012, **24**, 1296–1305.

14 G. Soliveri, V. Pifferi, R. Annunziata, L. Rimoldi, V. Aina, G. Cerrato, L. Falciola, G. Cappelletti and D. Meroni, *J. Phys. Chem. C*, 2015, **119**, 15390–15400.

15 D. Quéré, *Annu. Rev. Mater. Res.*, 2008, **38**, 71–99.
16 D. Meroni, S. Ardizzone, G. Cappelletti, M. Ceotto, M. Ratti, R. Annunziata, M. Benaglia and L. Raimondi, *J. Phys. Chem. C*, 2011, **115**, 18649–18658.
17 V. A. Ganesh, a. S. Nair, H. K. Raut, T. M. Walsh and S. Ramakrishna, *RSC Adv.*, 2012, **2**, 2067.
18 V. Pifferi, M. M. Barsan, M. E. Ghica, L. Falciola and C. M. A. Brett, *Electrochim. Acta*, 2013, **98**, 199–207.
19 V. Pifferi, G. Cappelletti, C. Di Bari, D. Meroni, F. Spadavecchia and L. Falciola, *Electrochim. Acta*, 2014, **146**, 403–410.
20 T. Doneux, A. de Ghellinck, E. Triffaux, N. Brouette, M. Sferrazza and C. Buess-Herman, *J. Phys. Chem. C*, 2016, **120**, 15915–15922.
21 S. Schwarz, K. Lunkwitz, B. Keßler, U. Spiegler, E. Killmann and W. Jaeger, *Colloids Surfaces A Physicochem. Eng. Asp.*, 2000, **163**, 17–27.
22 M. Kosmulski, *Colloids Surfaces A Physicochem. Eng. Asp.*, 2003, **222**, 113–118.
23 M. E. Orazem and B. Tribollet, *Electrochemical Impedance Spectroscopy*, John Wiley & Sons, Inc., Hoboken, NJ, USA, 2008.

This Chapter has been adapted with permission from Pifferi *et al.*, *Electrochem. Commun.*, 2017, **81**, 102−105. Copyright 2017 Elsevier.

L.R. contribution: samples preparation, DLS and UV-vis transmittance analyses, manuscript preparation.

Chapter 9

Three-dimensional mesoporous silica networks with improved diffusion and interference-abating properties for electrochemical sensing

Mesoporous silica-based architectures are attracting a great deal of interest in numerous fields of materials chemistry[1–6]. Templated silicas, either as hollow microparticles[7–9] or porous films[10–13], have recently drawn much attention for sensing and biosensing[14–20], photocatalytic and optical devices[21–23], composites and inorganic-organic hybrids[24–27], drug-delivery and cancer cell detection[28–30], energy conversion and storage systems[31,32] and environmental remediation[33–35]. In this context, the tuneability of the porous network structure and dimension is of primary importance[1]. For instance, the transport of active species such as analytes, probes, reactants through the oxide network to the catalytic support or the modified electrode surface strictly depends on the dimension and the permeability of the porous structure. In this respect, the traditional approach firstly proposed by Mobil Oil Company[36,37], adopting ionic surfactant liquid crystals as templating agents, provided systems with a rather limited pore range. Anionic or cationic surfactant micelles are able to build well-ordered structures with a pore diameter varying in the range 5–10 nm[38].

In order to create a larger porosity, both non-ionic surfactants and solid templates started to be adopted[39–42]. Polystyrene (PS) monodispersed latex proved to be a useful tool to produce meso- or macro-porous silica with pore dimensions tuneable from about 30 nm to micrometric dimensions. Nonetheless, PS latex has been mostly adopted as template for the preparation of macroporous systems. Kanungo *et al.* focused on the morphological aspects of macroporous silica films by varying experimental

parameters and the silica sol composition[43]. Etienne *et al.* studied the electrochemical assisted deposition of hierarchical macro/mesoporous silica films by using 100 nm PS latex and cationic surfactant micelles[44]. The stability of macroporous silica films was investigated by Aluri *et al.*[45], while the possibility to obtain self-supporting membranes was explored by Han *et al.*, once more in the range of macroporosity[46]. All of these studies involved the use of PS latex with a diameter of 0.1–1 μm. On the contrary, the preparation of silica materials with pores larger than those obtained using surfactant micelles, but still in the mesoporosity range, has been scarcely reported in the literature. The preparation of silica films with pores up to 100 nm would represent a pivotal step towards the development of high-performing electrochemical modified electrodes to be adopted in complex matrices.

In this respect, in recent years, an increased attention has been devoted to the preparation of sensors with antifouling properties[47–49]. Electrode fouling is considered as one of the main issues in the field of sensors, since it prevents the electrode on-line and on-site use due to a decrease of its sensing properties[50,51]. In particular, the analysis of biological matrices greatly suffers from fouling phenomena, due to the complexity of biological fluids and the interferent variety and high concentrations with respect to the analyte[52,53]. In this respect, large proteins and colloidal aggregates (*e.g.* tannin, lecithin, casein micelles) represent widespread interferents which often prevent a reliable determination of trace compounds in real matrices, such as body fluids, food and beverages. Porous architectures with tailored surfaces acting as interference-abating layers are promising in this field, as they improve selectivity by blocking the access of the interferent to the active electrode surface[18,54–58]. Apart from a few notable exceptions[59], these layers, generally with a pore size <10 nm, can significantly hamper the device response by limiting the analyte diffusion.

In this Chapter, an engineered electrochemical sensor based on negatively charged mesoporous silica films characterized by a 3D network with much larger pore sizes (up to 75 nm) is described. This device proved effective against colloidal interference while preserving good analyte sensitivity. Porous silica films deposited on conductive glass were prepared

by adopting PS latex as the templating agent, with a diameter in the 30–100 nm range. The role played by the template dimension and by the number of the deposited layers on the electrochemical and sensing properties was investigated. The modified electrodes were characterized from the morphological, optical and wettability point of view. Electrochemical measurements adopting both negatively- and positively-charged electrochemical probes shed light on diffusion and transport phenomena to the electrode, found to be strictly related to the geometry of the 3D structure. Finally, the present device is successfully applied for the detection of dopamine, a neurotransmitter whose quantification in biofluids is pivotal for the early diagnosis of the Parkinson's disease, also in the presence of mucin protein as interferent. By a careful tailoring of the pore size, devices with optimal selectivity were prepared while preserving their sensitivity.

9.1 Results and discussion

9.1.1 Films deposition

Mesoporous SiO_2 films were prepared by spin coating a mixture composed by a hydroalcoholic silica sol containing colloidal SiO_2 nuclei and a hard template suspension (PS latex spheres) on an ITO-coated glass. After drying, the PS spheres embedded into the silica matrix were removed by dissolution in chloroform producing a mesoporous architecture made of interconnected cavities (Fig. 9.1a). Differently sized PS latex spheres were adopted to tune the morphology of the porous architecture reflecting in differently dimensioned paths to the electroactive support. DLS measurements of the PS latex suspension (Fig. 9.1b) show a single population with a mean size of 34, 59 and 105 nm for PS beads of 30, 60 and 100 nm nominal diameter, respectively.

All samples exhibited high mechanical stability as proved by ISO 2409 adhesion tests. Samples were firstly crisscrossed with a razor blade forming small squares. Then, an adhesive tape was pressed on the surface of the film and removed applying a constant force under an angle of 60°. Neither appreciable detachment of the SiO_2 layers from the substrate (Fig. 9.1c), nor difference between mono- and multi-layered samples could be appreciated.

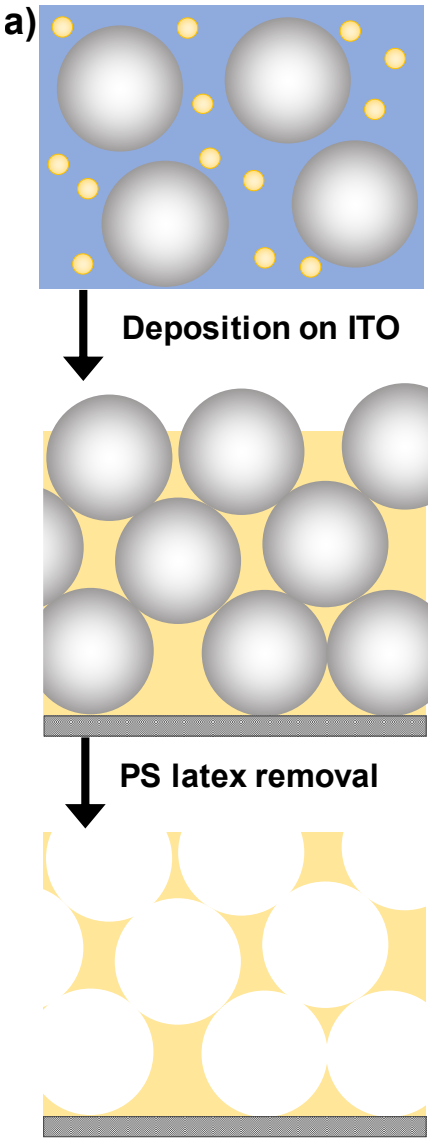

a) Schematic representation of the mesoporous silica films preparation procedure (small yellow circles = colloidal silica nuclei; grey circles = PS latex beads).

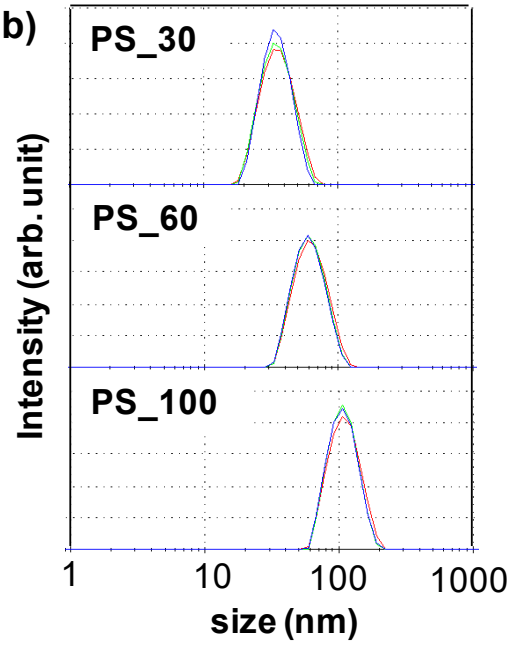

b) Particle size distribution of the adopted PS latex spheres.

c) Adhesion test performed on the SiO_2_30_3 sample highlighting no detachment of the film from the substrate; magnification: 30x.

Figure 9.1 – Information about materials and samples preparation.

9.1.2 Morphological properties

The samples morphology was investigated by FE-SEM images (Fig. 9.2a,b). Before the template removal, the presence of PS latex spheres embedded in the silica matrix is clearly appreciable (Fig. 9.2a). Upon

template removal, SiO_2_30_**n** and SiO_2_60_**n** samples show porosity in the mesopores range (2–50 nm, Fig. 9.2b). The homogeneity of the films varies with the PS latex size: while 30 and 60 nm templates lead to continuous films characterized by a homogenously distributed porosity and no observable cracking, also in the case of multilayers (Fig. 9.2a), the 100 nm PS latex resulted in heterogeneous films with macro- and microporous areas (Fig. 9.2b). The heterogeneity of this sample can be traced back to agglomeration phenomena occurring in the 100 nm PS-SiO_2 sol mixture. The effect of these agglomerates is amplified by the fact that the diameter of the 100 nm PS spheres is comparable to the thickness of a single layer deposition. The average pore size and pore size distribution also depend on the template size (Fig. 9.2b): all samples exhibited an average pore size (d_{median}: 22–24 nm, 40–45 nm and 70–75 nm for SiO_2_30_1, SiO_2_60_1 and SiO_2_100_1, respectively) *ca.* 30% smaller than the dimension of the corresponding PS latex spheres used as templates. This phenomenon is likely the result of the different embedding degrees of latex spheres within the silica matrix, *i.e.* the nanometric spheres may be completely or only partially embedded into the silica matrix after the deposition. The silica network retained its stability upon removal of the PS latex spheres.

The film morphology was also investigated using AFM measurements (Fig. 9.3a). AFM images show that the film has nanometric features, that can be related to silica particles. The mesoporosity induced by PS latex spheres is also clearly appreciable, leading to an increase in the sample roughness of about one order of magnitude with respect to the reference samples (RMS: 0.14, 6.3 and 5.6 nm for SiO_2_1, SiO_2_30_1 and SiO_2_60_1, respectively).

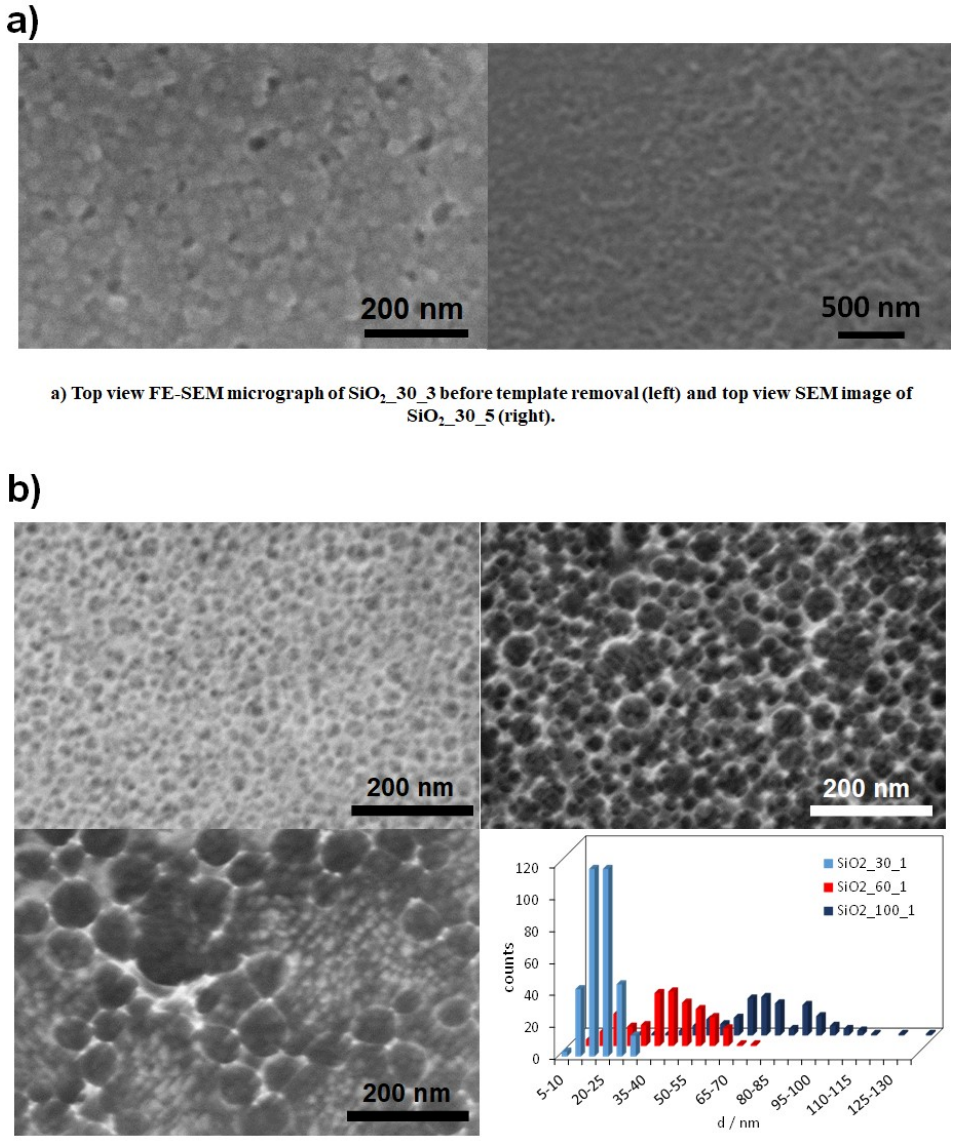

a) Top view FE-SEM micrograph of SiO_2_30_3 before template removal (left) and top view SEM image of SiO_2_30_5 (right).

b) FE-SEM images of SiO_2_30_1 (top, left), SiO_2_60_1 (top, right) and SiO_2_100_1 (bottom, left) samples. Pore size distributions as retrieved from FE-SEM images for the different samples (bottom, right).

Figure 9.2 – Morphological characterization by SEM and FE-SEM.

The film thickness was determined by cross-sectional SEM images (Fig. 9.3b) and it was found to be *ca.* 100 nm for each layer, although at increasing the number of layer the thickness becomes more irregular. In this context, the dimension of the PS latex adopted was not found to appreciably influence the thickness of the silica films. In high-resolution

cross-section micrographs acquired using FE-SEM, the porous network of the samples is clearly appreciable over the whole film thickness (Fig. 9.3b). It should be noted that the maximum resolution of these micrographs was limited by the insulating nature of both the sample and the support (in cross section mostly the bare glass is more exposed than the ITO coating).

The presence of pores leads to a capillary pull effect, which is stronger in the case of smaller and more hydrophilic pores, as predicted by the Young-Laplace equation[60]:

$$h\rho g = \frac{2\gamma \cos\theta}{r_{pore}} \qquad (9.1)$$

where h is the height of the liquid column in the pore, ρ is the density of the solution, g is the gravitation coefficient, γ is the surface tension of the solution, θ is the contact angle, and r_{pore} is the radius of the pore.

9.1.3 Optical and wetting properties

The analysis of the optical properties of the samples and of the non-covered substrate show the antireflective properties of the silica films. Similar spectra were obtained for samples synthesized by means of PS latex with a diameter of 30 and 60 nm as an evidence of the samples homogeneity. On the contrary, SiO_2_100_1 sample showed a lower transmittance in the 320–700 nm range, due to macroscopic heterogeneity mirrored in an increased opacity (Fig. 9.3c). Multi-layered samples did not exhibit significant difference with respect to the corresponding single-layered ones.

The wetting properties of the silica films were analysed by water contact angle measurements (Fig. 9.3d and Tab. 9.1). The deposition of a silica layer causes a decrease of the observed water contact angle with respect to bare ITO (θ_w *ca.* 90°), as an indication of the higher hydrophilicity of silica with respect to ITO, probably related to a higher surface hydroxylation[61]. Two trends are appreciable: on one hand, increasing the number of layers invariably causes a decrease in water contact angles, more marked in the case of porous films. This behaviour can be explained on the grounds of enhanced water chemisorption resulting from the increased film thickness[62]. Wettability is also affected by the variation of the pore size. Large pores (SiO_2_100_1) show θ_w values comparable to ITO. In this case, both the microscopic and the macroscopic heterogeneity of the film is responsible for the partial exposure of the ITO-coated glass, due to an

incomplete substrate coverage, leading to wetting features comparable with those of the bare substrate. More interestingly, smaller pores (SiO_2_30_**n**) give rise to a higher apparent hydrophilicity than the non-porous silica layer, the more so for increasing number of layers. Intermediate pores (SiO_2_60_**n**) present wetting properties more similar to the non-porous silica layer, in the case of the deposition of the first layer, while θ_w values progressively decrease with increasing the number of layers. The superimposition of different layers of not aligned, randomly distributed 60 nm pores yields to a final porosity which resembles that of the smaller pores. In the case of SiO_2_30_**n** and SiO_2_60_**n** (with n>1), the observed higher hydrophilicity with respect to the non-porous silica layers can be related to hemiwicking (*i.e.* spreading of a liquid drop on rough hydrophilic surfaces driven by capillarity)[63], arising from the interconnected network of pores[64].

n° layers	**water contact angles (°)**			
	d = 0 nm	*d = 30 nm*	*d = 60 nm*	*d = 100 nm*
1	72 ± 5	42 ± 2	73 ± 9	91 ± 9
2	71 ± 4	43 ± 1	62 ± 7	n.a.
3	48 ± 1	36 ± 9	32 ± 3	n.a.
5	41 ± 13	29 ± 5	15 ± 1	n.a.

Table 9.1 – Water contact angles, in degrees, of silica films as a function of the number of layers and of the size of PS latex spheres, *d*, used during synthesis (0 stands for the non-porous silica films).

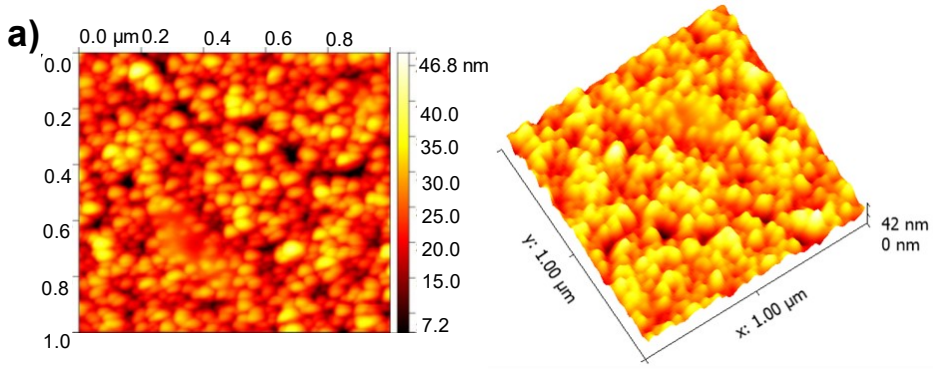

a) AFM images of SiO_2_30_1 (left) and SiO_2_60_1 (right) samples.

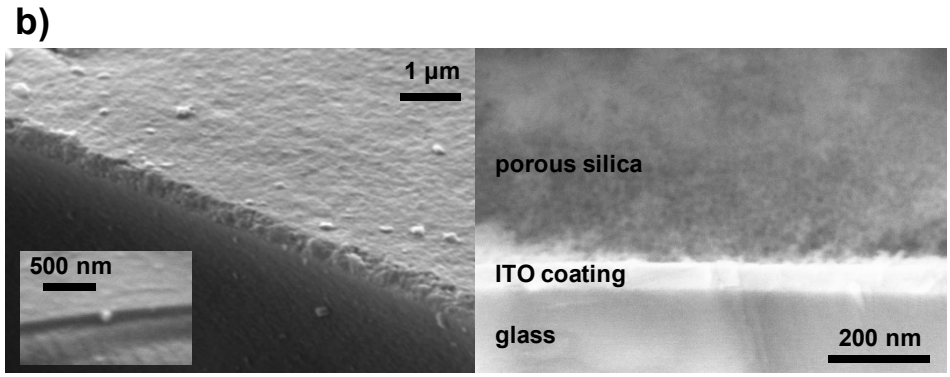

b) Cross-sectional SEM images of SiO_2_30_3 and of SiO_2_30_1 (inset) (left) and high resolution cross-sectional FE-SEM micrograph of SiO_2_30_3 (right).

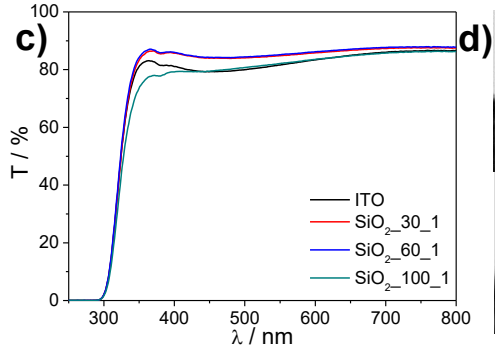

c) Transmittance spectra for SiO_2_30_1, SiO_2_60_1 and SiO_2_100_1.

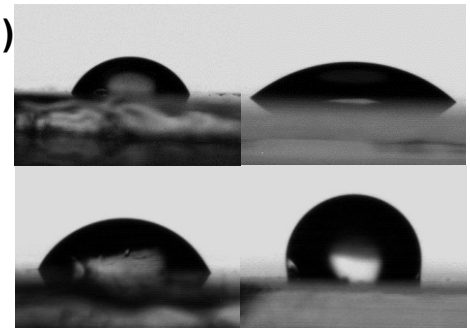

d) Water contact angles for SiO_2_1 (top, left), SiO_2_30_1 (top, right), SiO_2_60_1 (bottom, left) and SiO_2_100_1 (bottom, right).

Figure 9.3 – Further morphological, optical and surface characterization results.

9.1.4 Voltammetric characterization

Figure 9.4a reports the cyclic voltammograms of the SiO_2_**d**_1 samples, of the reference bare ITO and of the non-porous SiO_2_1 in the presence of the positively charged $[Ru(NH_3)_6]^{3+}/[Ru(NH_3)_6]^{2+}$ redox probe. With respect to bare ITO (black continuous line), the non-porous SiO_2_1 sample (black dashed line) shows a drastic decrease of the current response, due to the insulating character of the homogeneous SiO_2 coating[65]. Mesoporous SiO_2_**d**_1 samples show peak shaped voltammograms, implying that pores are diffusionally dependent, as expected on the grounds of the lower distance between adjacent pores with respect to their diameters[66], and that completely convergent diffusion is not present.

Despite the insulating properties of the deposited material, the peak currents of mesoporous structures are comparable (SiO_2_100_1) or even higher (SiO_2_30_1 and SiO_2_60_1) with respect to the bare ITO substrate, with higher values for SiO_2_30_1, due to the presence of smaller pores, which leads to a more intense capillary pull effect (as commented above). The same trends are appreciable in the presence of the negatively charged $[Fe(CN)_6]^{4-}/[Fe(CN)_6]^{3-}$ redox probe (Fig. 9.4b): in this case, all peaks of the SiO_2_**d**_1 samples are an order of magnitude higher with respect to non-porous silica, although remaining lower with respect to the bare ITO peak. The different response of the two probes is due to the attractive or repulsive electrostatic interactions between the two differently charged probes and the silica surface: the deposited oxide (SiO_2) possesses an isoelectric point close to pH 3[67], resulting in a negatively charged surface when immersed in a KCl solution at pH 5–6, whereas in the case of bare ITO the surface can be considered neutral or slightly positive (isoelectric point around pH 6)[68].

Figures 9.4a,b report the CV response of SiO_2_30_**n** samples as a function of the number of deposited silica layers: by increasing the number of layers from 1 to 3, a monotonous growth of the peak current was registered for both probes. By contrast, when five layers of silica are deposited, the peak intensity decreases, since in this case the silica insulating properties probably begin to contrast the favourable effects provided by the mesoporous architecture. Similar results were obtained for the SiO_2_60_**n** samples (Fig. 9.5a).

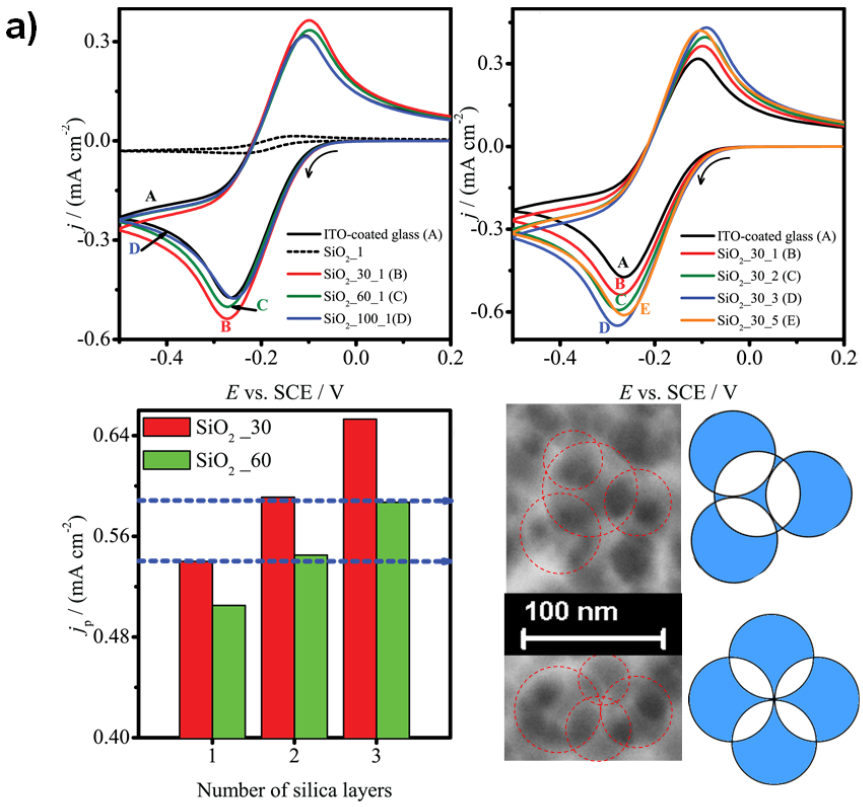

a) Cyclic voltammograms of SiO_2_d_1 (top, left) and SiO_2_30_n (top, right) samples in the presence the Ru probe (3mM) in 0.1M KCl; current values for SiO_2_30_n and SiO_2_60_n series (bottom, left); SEM image (SiO_2_60_2) and scheme illustrating the shrinking of pore channels from the overlap of different layers of PS spheres (bottom, right).

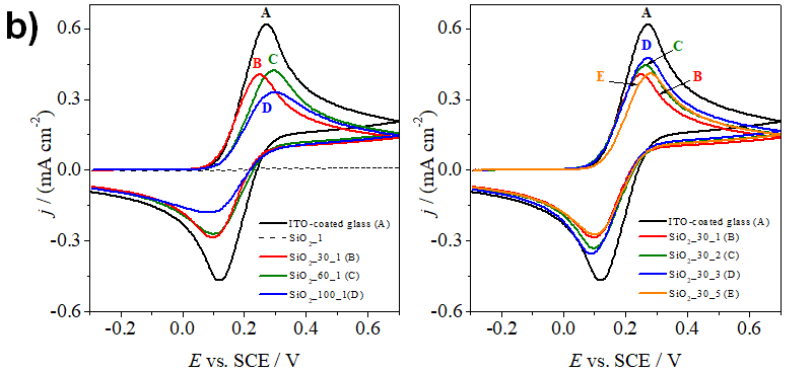

b) Cyclic voltammograms of (a) SiO_2_d_1 and (b) SiO_2_30_n samples in the presence of 3 mM $[Fe(CN)_6]^{4-}$/$[Fe(CN)_6]^{3-}$ in 0.1M KCl, in comparison with ITO and SiO_2_1 as references.

Figure 9.4 – Cyclic voltammetry characterization results.

The above-reported trends are confirmed by the elaboration of the cyclic voltammetric results by means of the Randles-Sevčik equation (see Table 9.2), whose applicability to the present cases is supported by the values of the slope of ln*i vs.* ln*v*, which are always close to the theoretical value (0.5) for a diffusive controlled regime[69]. By either decreasing pore size or increasing the number of deposited layers, a progressive increase of the absolute value of the slope of the i_p *vs.* $v^{0.5}$ curve is observed, overcoming the ITO values in the case of the positive probe. Since depositing an insulating layer of mesoporous silica on bare ITO cannot result in an increase of the electroactive area (*A*), the only parameter which can produce this build-up in the slope value is the increase of the probe diffusion coefficient inside the porous layer (*D)*. Moreover, the increase of the peak to peak separation (Fig. 9.4a) supports a partial loss of electrochemical reversibility of the system in comparison with bare ITO, going from 1 to 3 layers and mainly for the smallest pore diameter (SiO_2_30_**n**). This phenomenon can also be related to an increase of the mass transport coefficient, thus confirming a growth of the probe diffusion coefficient[69].

Sample	$[Ru(NH_3)_6]^{3+/2+}$		$[Fe(CN)_6]^{4-/3-}$	
	Slope ln i_p *vs.* ln v	Slope i_p *vs.* $v^{0.5}$ (mA cm^{-2} V$^{-0.5}$ s$^{0.5}$)	Slope ln i_p *vs.* ln v	Slope i_p *vs.* $v^{0.5}$ (mA cm^{-2} V$^{-0.5}$ s$^{0.5}$)
ITO	0.45	- 1.30	0.50	2.16
SiO_2_30_1	0.45	- 1.54	0.46	1.09
SiO_2_60_1	0.43	- 1.29	0.44	1.06
SiO_2_100_1	0.44	- 1.32	0.40	0.74
SiO_2_30_2	0.45	- 1.75	0.45	1.16
SiO_2_60_2	0.43	- 1.37	0.44	1.01
SiO_2_30_3	0.46	- 1.95	0.45	1.22
SiO_2_60_3	0.43	- 1.42	0.44	1.23

Table 9.2 – CV parameters recorded in the presence of 3 mM $[Ru(NH_3)_6]Cl_3$ and $K_4[Fe(CN)_6]$ in 0.1M KCl and elaborated according to the Randles-Sevčik equation.

The increase of the probe diffusion within the capillaries can be correlated to the analyte concentration enrichment due to the previously cited capillary pull effect. This phenomenon was previously reported in the Literature by other authors on the grounds of experimental evidence[18,19,70].

Apart from the diffusion coefficient change, it should be underlined that a modification of the diffusion mechanism (from fully planar to a mixed planar-radial) has also to be considered due to the presence of shallow pores (*i.e.* pores in which the depth of the pore - nanometers range - is smaller than the size of the diffusion layer - micrometers range)[69]. This morphological characteristic may contribute to the enhancement of the current signal in the presence of porosity.

The comparison among samples with different pore size gives rise to other interesting findings. Figure 9.4a shows that the current values reached by SiO_2_60_2 are comparable with those obtained for SiO_2_30_1, while the peak current of the SiO_2_60_3 nearly coincide with that of SiO_2_30_2, suggesting a decrease of the pore diameter when the number of silica layers is increased. Probably, the random disposition of PS spheres, when successive layers are deposited, produces more tortuous and narrower paths for the electrochemical probe, as can be deduced from Figure 9.4a and as supported by wetting data.

9.1.5 Electrochemical impedance analysis

Fig. 9.5b shows the EIS trends for SiO_2_30_**n** samples registered at – 0.1 V (other potentials give fully comparable results) in the absence of any redox probe. Bare ITO and SiO_2_1 present the same trend, with a straight line covering the entire range of frequencies in the Nyquist plot and phase values very close to 90° for low frequencies. In the case of SiO_2_30_**n** samples, the straight line is replaced by a semicircle and phase values at low frequencies deviate from 90°, giving rise to a sort of peak in the Bode phase plot. Both phenomena are accentuated increasing the number of silica layers.

EIS data can be rationalized in terms of two different equivalent circuits (Fig. 9.5b). In the case of the bare ITO support and of non-porous silica samples, the ohmic resistance, $R_{\Omega,}$ is in series with a capacitance C which include the ITO, the double layer and, when present, the silica layer. In other words, these samples behave as pure capacitors. Differently, in the

case of mesoporous silica-based samples, an additional resistance R_{pore} in parallel with the capacitance has to be added. Actually, R_{pore} indicates the resistance of the solution into the pores, which strongly differs from that in the bulk due to the contribute of radial diffusion and to the capillary pull effect previously mentioned.

The resulting EIS parameters are reported in Tab. 9.3. R_Ω values are higher in the case of silica-covered electrodes with respect to bare ITO, more so for non-porous samples, due to the intrinsic insulating character of SiO_2. In general, the capacitances are smaller when silica is deposited on the electrodes, since the deposition of an insulating material ideally distances the plates of a capacitor, and when pores are not present the lowest values are reached, since these plates are better spaced. All the α values are very close to 1 for all samples (ranging from 0.95 to 0.97), meaning that the surfaces are macroscopically uniform, also in the case of porous materials[71]. Furthermore, it should be underlined that the smaller the pores, the lower the values of the solution resistance into the pores R_{pore} (Tab. 9.3) for the same numbers of layers. Moreover, considering equal pore dimensions, the increase of the number of silica layers reflects in lower resistances, confirming the increase of the diffusion coefficient previously discussed.

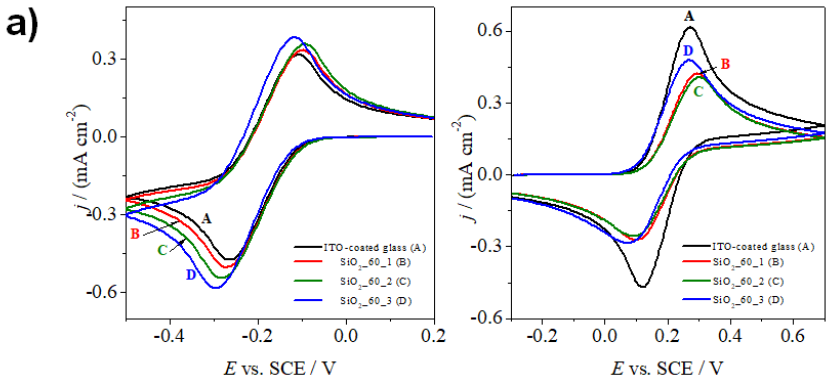

a) Cyclic voltammograms SiO_2_60_n samples in the presence of 3 mM $[Ru(NH_3)_6]^{3+}/[Ru(NH_3)_6]^{2+}$ (left) and $[Fe(CN)_6]^{4-}/[Fe(CN)_6]^{3-}$ in 0.1M KCl (b).

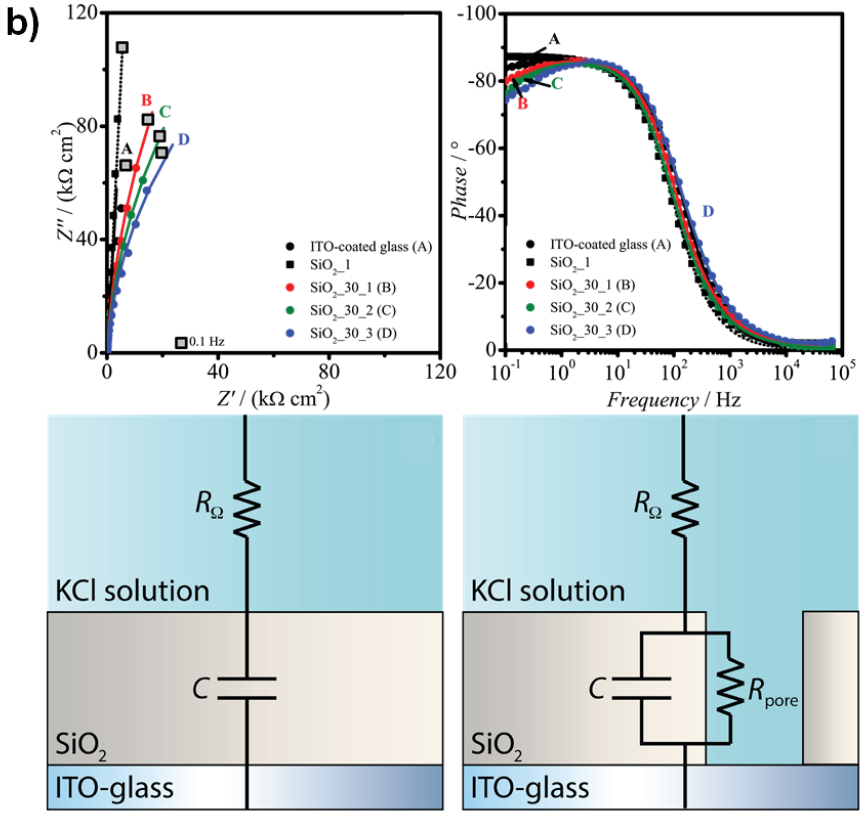

b) Complex plane (top, left) and Bode phase (top, right) plots for bare ITO support, SiO_2_1 and SiO_2_30_n samples recorded at – 0.1 V in 0.1M KCl; equivalent circuits and schematic representation for non-porous silica modified-ITO (and ITO itself) (bottom, left) and mesoporous silica modified-ITO (bottom, right).

Figure 9.5 – Further cyclic voltammetry and impedance results.

EIS data registered in the presence of $[Ru(NH_3)_6]^{3+}/[Ru(NH_3)_6]^{2+}$ (the probe with the best results in cyclic voltammetry thanks also to its positive charge) are not here considered, since the mass transport and the reaction[72] of this molecule are too quick to allow the differences among the electrodes to be appreciated. By contrast, EIS spectra obtained in the presence of $[Fe(CN)_6]^{4-}/[Fe(CN)_6]^{3-}$ redox couple (Fig. 9.6a), with a slower mass transport due to the negative charge and a slower reaction due to the change in the solvation sphere[72], allow to discriminate among the different samples. In the case of ITO, a Randles circuit typical of flat conductive electrodes (Fig. 9.6b) can be used to fit data: an ohmic resistance R_Ω in series with the double layer capacitance C_{dl}, in parallel with the charge transfer resistance R_{ct} and the resistance to the mass transport Z_W, represented with a Warburg element. For the mesoporous electrodes, the circuit (Fig. 9.6b) is more complicated[71], with the addition of the solution resistance inside the pores R_{pore}, in series with the ITO Randles circuit and the film capacitance C_{film} in parallel. Obviously, the values of R_{ct} (9.80 **Ω** cm^2) and C_{dl} (0.10 mF cm^{-2} $s^{\alpha-1}$) remain the same than those of ITO (the electrochemical reaction takes place on the surface of ITO also for mesoporous silica electrodes), while values of Z_W can be affected by the modification of the mass transport phenomenon for the presence of the mesoporous layer.

Increasing the pore diameter from 30 to 100 nm and the number of layers, the film capacitance C_{film} decreases depending on the homogeneity and on the thickness of the deposited silica, respectively. Pore resistance R_{pore} and mass transport resistance Z_W values follow a complex behaviour due to a counterbalance of the pull capillary effect and the repulsive electrostatic component brought by the silica layer, confirming the behaviour observed in cyclic voltammetry for the $[Fe(CN)_6]^{4-}/[Fe(CN)_6]^{3-}$ probe (Fig. 9.5a).

Sample	R_Ω (Ω cm^2)	CPE (μF cm^{-2} s$^{\alpha-1}$)	R_{pore} (kΩ cm^2)
ITO	58	20.5	-
SiO_2_1	132	13.2	-
SiO_2_2	103	13.7	-
SiO_2_3	96	13.4	-
SiO_2_30_1	67	16.4	522
SiO_2_60_1	82	15.7	685
SiO_2_100_1	78	13.5	1352
SiO_2_30_2	89	15.5	307
SiO_2_60_2	95	16.3	472
SiO_2_30_3	86	15.1	173
SiO_2_60_3	63	17.0	399

Table 9.3 – Values obtained from the fitting of EIS data registered in 0.1 M KCl for all tested samples: R_Ω = ohmic resistance; CPE = constant phase element; R_{pore} = pore resistance.

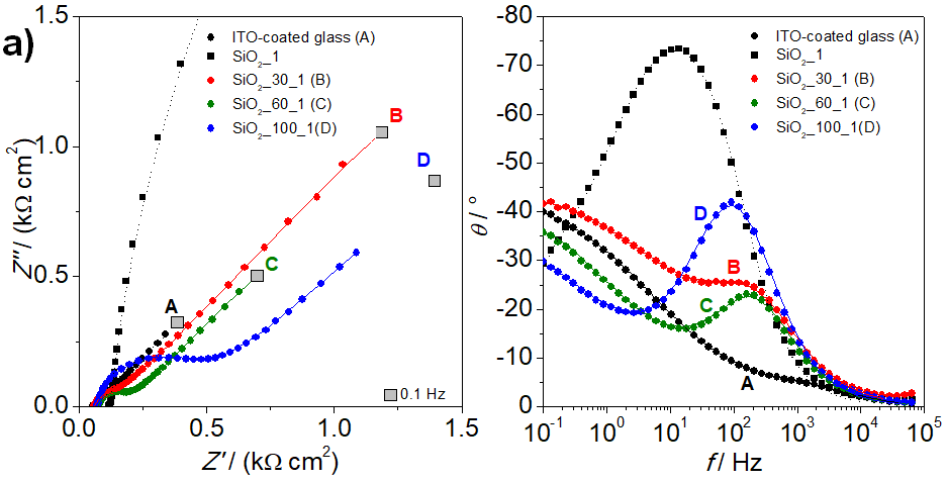

a) Complex plane (left) and Bode phase (right) plots for bare ITO support, SiO_2_1 and mpSiO_2_n_1 samples recorded at + 0.25 V in 0.1 M KCl in the presence of 3 mM $K_4[Fe(CN)_6]$.

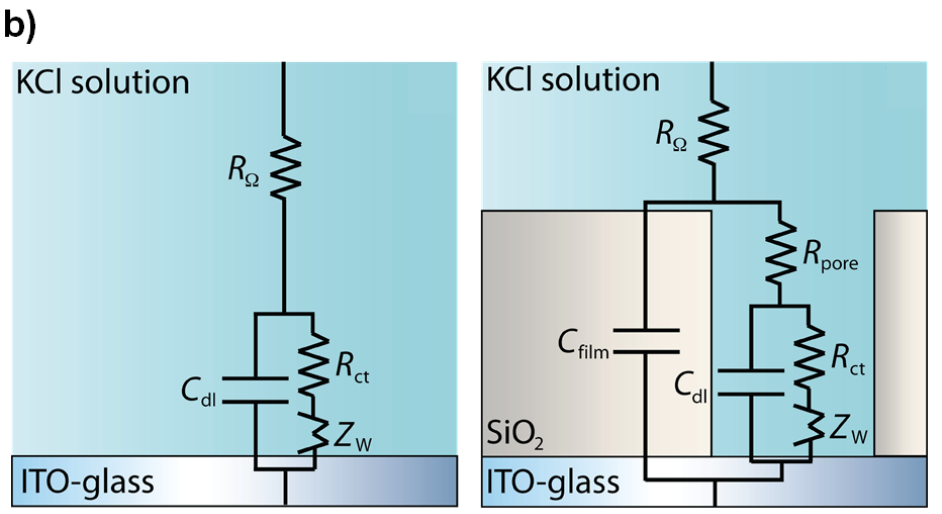

b) Equivalent circuits and schematic representation for ITO (left) and mesoporous silica modified-ITO (right) obtained for measurements in the presence of 3 mM $[Fe(CN)_6]^{4-}$/$[Fe(CN)_6]^{3-}$ at + 0.25 V in 0.1 M KCl.

Figure 9.6 – Impedance spectroscopy results in the presence of Fe probe.

9.1.6 Application in the detection of dopamine

Our samples were tested for the determination of dopamine, an important neurotransmitter widely studied in the field of neurodegenerative diseases, also in the presence of mucin as interferent species. Mucin is a high

molecular weight glycoprotein that is a component of mucus and as a result, can be found in a variety of bodily fluids; it is easily adsorbed on electrode surfaces, giving rise to biofouling effects[73,74].

The electroanalytical determination of dopamine in the absence of mucin shows good performances in the case of porous silica electrodes in terms of sensitivity (comparable with that of bare ITO, Fig. 9.7a) and lower detection limit (Fig. 9.7b). These results are in accordance with what observed in the first part of the manuscript, *i.e.* the promotion of the electrochemical response of the insulating layer due to its tailored porous structure. The electrostatic attractive interactions between the negatively charged silica layers and the monovalent cationic dopamine are presumably less significant than in the case of the multivalent $[Ru(NH_3)_6]^{3+}/[Ru(NH_3)_6]^{2+}$ probe.

The porous structure becomes fundamental in the presence of interferents. When interfering mucin is present, the determination of dopamine at low concentration is not possible on bare ITO, since the strong protein adsorption prevents the electron transfer at the electrode surface (Fig. 9.7a). On the other hand, dopamine is detected in the presence of mucin on SiO_2_30_3 electrodes and a good calibration plot with slight changes in sensitivity and detection limits is obtained (Figs. 9.7a,b). The porous structure of silica (with a median pore size of 22–24 nm) allows dopamine (molecule dimension *ca.* 0.8 nm) to reach the active electrode surface underneath the pores (ITO), whilst acting as a barrier for mucin (Fig. 9.7a) due to both charge repulsion (same charge of silica) and to size exclusion (molecule diameter around 50 nm, as demonstrated by DLS measurements, Fig. 9.7a).

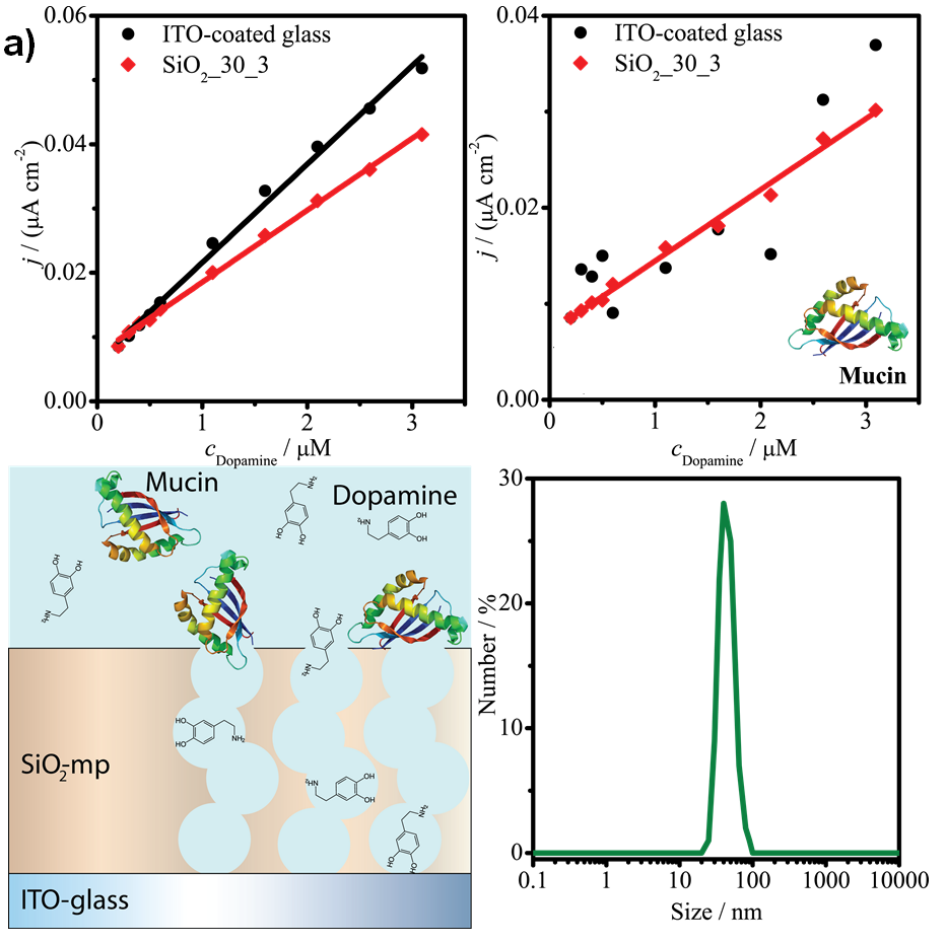

a) Calibration plots for dopamine detection in the absence (top, left) and in the presence (top, right) of interfering mucin; schematic representation of the selectivity properties in the mesoporous silica detection system (bottom, left); DLS of interfering mucin (bottom, right).

b)

Sample	S (mA cm^{-2} M^{-1})	R^2	LoD (μM)	LoQ (μM)
ITO	15.3 ± 0.4	0.994	0.271	0.824
SiO_2_30_3	11.2 ± 0.2	0.998	0.156	0.476
ITO + Mucin	-	-	-	-
SiO_2_30_3 + Mucin	7.4 ± 0.2	0.993	0.310	0.944

b) Analytical parameters obtained from the elaboration of the calibration plot for dopamine in the absence and in the presence of mucin: sensitivity (*S*), correlation coefficient (R^2), limit of detection (*LoD*), limit of quantification (*LoQ*).

Figure 9.7 – Results concerning the use of the device as a sensor for dopamine.

9.2 Conclusions

The tailored structure of mesoporous electrodes can represent the answer to sensor problems arising in real systems. As evidenced by Compton *et al.*[75], the efforts invested in preparing tailored insulating porous layers should be rewarded by the solution of complex problems.

In the present study, the growth of hard-templated mesoporous silica layers onto ITO electrodes has led to comparable or even improved voltammetric responses with respect to the bare electrode, notwithstanding the insulating character of the material. These effects are interpreted as due to the positive combination of tailored morphology, wetting properties and electrostatic effects, resulting in enhanced diffusion/accumulation of the analyte at the electrode surface.

EIS measurements provide an overall framework representing the combination of the different effects, permitting a deep comprehension of the material architecture.

Moreover, the silica mesoporous layer enables a smart control of interfering species during dopamine determination in a complex matrix, permitting its reliable detection. The enhanced selectivity (in terms of the capability of determining particular analyte(s) in a complex mixture without interference from other components in the mixture), which is obtained by the presence of an insulating layer, could have led to a dramatic decrease of the device performance in terms of sensitivities and detection limits. Instead, by tailoring the mesoporous network, an optimal selectivity was achieved while preserving the electrode sensitivity.

The presented approach paves the way to the detection of a wide range of analytes in real matrices, such as body fluids, food and beverages, where interferents such as large proteins and colloidal components often prevent a reliable determination of trace compounds. Its applicability can be further extended by changing the chemical nature of the adopted porous materials. For example, other oxides with different isoelectric points (*e.g.* TiO_2, Al_2O_3) can be selected to promote the exclusion of specific fouling agents.

9.3 Specific procedures

Samples preparation. Reactants were purchased from Sigma-Aldrich and adopted without any further purification. Non-functionalized polystyrene (PS) latex suspensions (10% m/v) of three different average diameters (30, 60, and 100 nm) were purchased from Magsphere Inc. (Pasadena, CA, USA). Indium tin oxide (ITO) covered glass slides (15–25 Ω/sq, Sigma-Aldrich, 2.5 cm × 2 cm) were used as substrates for film depositions. Solutions were prepared using doubly-distilled water, passed through a Milli-Q apparatus.

ITO-covered supports cleaning and silica sol preparation were performed according to the procedures already reported in the previous Chapter. Right before the deposition, 1 mL of silica sol was mixed with 0.83 mL of a PS latex suspension. Silica films were deposited by spin coating the PS-silica mixture on pretreated ITO supports (spin time: 30 s, rate: 3000 rpm, ramp: 500 rpm s^{-1}), repeating the procedure for the deposition of multilayers. After drying at room temperature, films were dipped in chloroform for 3 h to remove the PS latex by dissolution, thus creating the sought porosity. Finally, films were rinsed with ethanol and dried at room temperature overnight. At least 3 repetitions of each sample were prepared to verify the reproducibility of the results. The as prepared samples are labelled "*SiO_2_d_n*", where *d* is the diameter of the adopted PS latex expressed in nanometers, and *n* is the number of deposited layers. Non-porous films were prepared as reference by adopting the same procedure without the addition of PS spheres. Reference non-porous samples are labelled "*SiO_2_n*", where *n* is the number of spin coated layers. A pristine ITO-coated glass was also tested as a reference after washing by sonication in H_2O/isopropanol.

Dopamine determination. The electrochemical cell was the same described in the electrochemical characterization paragraph and phosphate buffer 0.1 M pH = 7.4 was used as supporting electrolyte (K_2HPO_4 and NaH_2PO_4). In selected measurements, mucin was added to the electrolyte solution in a concentration of 0.4% w/w. Consecutive additions of 1 mM dopamine were performed to obtain the calibration plots, using differential pulse voltammetry as the electroanalytical technique (Modulation time: 0.05 s; Interval time: 0.5 s; Step Potential: 0.005 V; Modulation Amplitude:

0.05 V). The sensitivity *S* is represented by the slope of the calibration plot, while LoD and LoQ were calculated by using the following equations: LoD = 3.29 $s\ S^{-1}$ and LoQ = 10 $s\ S^{-1}$, where *s* is the standard deviation of the calibration plot.

Further details about the preparation and characterization methods can be found in Appendix A.

References

1 C. Perego and R. Millini, *Chem. Soc. Rev.*, 2013, **42**, 3956–3976.

2 Y. Deng, Y. Cai, Z. Sun, J. Liu, C. Liu, J. Wei, W. Li, C. Liu, Y. Wang and D. Zhao, *J. Am. Chem. Soc.*, 2010, **132**, 8466–8473.

3 A. Walcarius, D. Mandler, J. A. Cox, M. Collinson and O. Lev, *J. Mater. Chem.*, 2005, **15**, 3663.

4 A. Vuorema, M. Sillanpää, K. J. Edler, R. Jaber, S. E. C. Dale, S. Bending, Y. Gu, K. Yunus, A. C. Fisher and F. Marken, *Electroanalysis*, 2012, **24**, 1296–1305.

5 A. Walcarius, *Chem. Soc. Rev.*, 2013, **42**, 4098.

6 M. Ogawa, *Chem. Rec.*, 2017, 17, 217–232.

7 P. Xu, J. Liang, X. Cao, J. Tang, J. Gao, L. Wang, W. Shao, Q. Gao and Z. Teng, *J. Colloid Interface Sci.*, 2016, **474**, 114–118.

8 J. Mielby, A. J. Kunov-Kruse and S. Kegnæs, *J. Catal.*, 2017, **345**, 149–156.

9 W. Li and D. Zhao, *Adv. Mater.*, 2013, **25**, 142–149.

10 S. Nagarajan, M. Li, R. A. Pai, J. K. Bosworth, P. Busch, D.-M. Smilgies, C. K. Ober, T. P. Russell and J. J. Watkins, *Adv. Mater.*, 2008, **20**, 246–251.

11 M. M. Collinson, D. A. Higgins, R. Kommidi and D. Campbell-Rance, *Anal. Chem.*, 2008, **80**, 651–656.

12 D. Zhao, P. Yang, N. Melosh, J. Feng, B. F. Chmelka and G. D. Stucky, *Adv. Mater.*, 1998, **10**, 1380–1385.

13 M. Kobayashi, K. Susuki, T. Otani, S. Enomoto, H. Otsuji, Y. Kuroda, H. Wada, A. Shimojima, T. Homma and K. Kuroda, *Nanoscale*, 2017, **9**, 8321–8329.

14 A. Walcarius and M. M. Collinson, *Annu. Rev. Anal. Chem.*, 2009, **2**, 121–143.

15 D. Sun, Y. Zhang, F. Wang, K. Wu, J. Chen and Y. Zhou, *Sensors Actuators B Chem.*, 2009, **141**, 641–645.

16 M. Saadaoui, I. Fernández, G. Luna, P. Díez, S. Campuzano, N. Raouafi, A. Sánchez, J. M. Pingarrón and R. Villalonga, *Anal. Bioanal. Chem.*, 2016, **408**, 7321–7327.

17 F. Yan, Y. He, L. Ding and B. Su, *Anal. Chem.*, 2015, **87**, 4436–4441.

18 T. Nasir, G. Herzog, M. Hébrant, C. Despas, L. Liu and A. Walcarius, *ACS Sensors*, 2018, **3**, 484–493.
19 F. Yan, X. Lin and B. Su, *Analyst*, 2016, **141**, 3482–3495.
20 S. Y. Tan, C. Teh, C. Y. Ang, M. Li, P. Li, V. Korzh and Y. Zhao, *Nanoscale*, 2017, **9**, 2253–2261.
21 Z. Liu, X. Zhang, T. Murakami and A. Fujishima, *Sol. Energy Mater. Sol. Cells*, 2008, **92**, 1434–1438.
22 C. He, B. Tian and J. Zhang, *Microporous Mesoporous Mater.*, 2009, **126**, 50–57.
23 M. Laskowska, I. Kityk, M. Dulski, J. Jędryka, A. Wojciechowski, J. Jelonkiewicz, M. Wojtyniak and Ł. Laskowski, *Nanoscale*, 2017, **9**, 12110–12123.
24 M. Faustini, L. Nicole, C. Boissière, P. Innocenzi, C. Sanchez and D. Grosso, *Chem. Mater.*, 2010, **22**, 4406–4413.
25 N. Vilà and A. Walcarius, *Electrochim. Acta*, 2015, **179**, 304–314.
26 N. Vilà, J. Ghanbaja, E. Aubert and A. Walcarius, *Angew. Chemie Int. Ed.*, 2014, **53**, 2945–2950.
27 M. Etienne and A. Walcarius, *Electrochem. commun.*, 2005, **7**, 1449–1456.
28 B.-H. Shen, M.-L. Hsieh, H.-Y. Chen and J.-Y. Wu, *J. Polym. Res.*, 2013, **20**, 220.
29 M.-S. Wu, X.-T. Sun, M.-J. Zhu, H.-Y. Chen and J.-J. Xu, *Chem. Commun.*, 2015, **51**, 14072–14075.
30 W. Cheng, C. Liang, X. Wang, H. Tsai, G. Liu, Y. Peng, J. Nie, L. Huang, L. Mei and X. Zeng, *Nanoscale*, 2017, **9**, 17063–17073.
31 R. Liu, J. Duay and S. B. Lee, *Chem. Commun.*, 2011, **47**, 1384–1404.
32 Y. Zhang, Z. Zhang, W. Yan, B. Zhang, Y. Feng, A. M. Asiri, M. K. Nazeeruddin and P. Gao, *J. Mater. Chem. A*, 2017, **5**, 1415–1420.
33 P. Shinde, S. Sen Gupta, B. Singh, V. Polshettiwar and B. L. V. Prasad, *J. Mater. Chem. A*, 2017, **5**, 14914–14921.
34 M. Okamoto, H. Satake and H. Seki, *J. Mater. Chem. A*, 2017, **5**, 24425–24432.
35 K. Fujiwara, Y. Kuwahara, Y. Sumida and H. Yamashita, *J. Mater. Chem. A*, 2017, **5**, 25431–25437.
36 C. T. Kresge, *Nature*, 1992, **359**, 710–712.

37 J. S. Beck, J. C. Vartuli, W. J. Roth, M. E. Leonowicz, C. T. Kresge, K. D. Schmitt, C. T. W. Chu, D. H. Olson, E. W. Sheppard, S. B. McCullen, J. B. Higgins and J. L. Schlenker, *J. Am. Chem. Soc.*, 1992, **114**, 10834–10843.
38 Z. Teng, G. Zheng, Y. Dou, W. Li, C. Mou, X. Zhang, A. M. Asiri and D. Zhao, *Angew. Chemie Int. Ed.*, 2012, **51**, 2173–2177.
39 P. C. A. Alberius, K. L. Frindell, R. C. Hayward, E. J. Kramer, G. D. Stucky and B. F. Chmelka, *Chem. Mater.*, 2002, **14**, 3284–3294.
40 R. Fan, S. Huh, R. Yan, J. Arnold and P. Yang, *Nat. Mater.*, 2008, **7**, 303–307.
41 M. Kanungo and M. M. Collinson, *Chem. Commun.*, 2004, 548.
42 C. Ma, L. Han, Z. Jiang, Z. Huang, J. Feng, Y. Yao and S. Che, *Chem. Mater.*, 2011, **23**, 3583–3586.
43 M. Kanungo, P. N. Deepa and M. M. Collinson, *Chem. Mater.*, 2004, **16**, 5535–5541.
44 M. Etienne, S. Sallard, M. Schröder, Y. Guillemin, S. Mascotto, B. M. Smarsly and A. Walcarius, *Chem. Mater.*, 2010, **22**, 3426–3432.
45 H. Aluri and M. M. Collinson, *J. Electroanal. Chem.*, 2011, **651**, 143–149.
46 C. Han, M.-Y. Li, Y. Li, H. Liu, P. Wang, M. M. Collinson and Z.-X. Lu, *RSC Adv.*, 2015, **5**, 19182–19189.
47 G. Soliveri, V. Pifferi, G. Panzarasa, S. Ardizzone, G. Cappelletti, D. Meroni, K. Sparnacci and L. Falciola, *Analyst*, 2015, **140**.
48 V. Pifferi, G. Soliveri, G. Panzarasa, S. Ardizzone, G. Cappelletti, D. Meroni and L. Falciola, *RSC Adv.*, 2015, **5**, 71210–71214.
49 V. Pifferi, G. Soliveri, G. Panzarasa, G. Cappelletti, D. Meroni and L. Falciola, *Anal. Bioanal. Chem.*, 2016, **408**, 7339–7349.
50 C. M. a. Brett, *Pure Appl. Chem.*, 2001, 73, 1969–1977.
51 C. M. Welch and R. G. Compton, *Anal. Bioanal. Chem.*, 2006, **384**, 601–19.
52 S. Chandra, A. D. Miller and D. K. Y. Wong, *Electrochim. Acta*, 2013, **101**, 225–231.
53 W. Harreither, R. Trouillon, P. Poulin, W. Neri, A. G. Ewing and G. Safina, *Electrochim. Acta*, 2016, **210**, 622–629.
54 Y. Qian, J. Zhu and Y. Li, *ChemElectroChem*, 2018, **5**, 292–299.
55 A. Walcarius and E. Sibottier, *Electroanalysis*, 2005, **17**, 1716–

1726.
56 N. Vilà, E. André, R. Ciganda, J. Ruiz, D. Astruc and A. Walcarius, *Chem. Mater.*, 2016, **28**, 2511–2514.
57 J. Patel, L. Radhakrishnan, B. Zhao, B. Uppalapati, R. C. Daniels, K. R. Ward and M. M. Collinson, *Anal. Chem.*, 2013, **85**, 11610–11618.
58 P. Daggumati, Z. Matharu, L. Wang and E. Seker, *Anal. Chem.*, 2015, **87**, 8618–8622.
59 P. Daggumati, Z. Matharu and E. Seker, *Anal. Chem.*, 2015, **87**, 8149–8156.
60 H. Liu and G. Cao, *Sci. Rep.*, 2016, **6**, 23936.
61 J. Drelich, E. Chibowski, D. D. Meng and K. Terpilowski, *Soft Matter*, 2011, **7**, 9804.
62 V. A. Ganesh, a. S. Nair, H. K. Raut, T. M. Walsh and S. Ramakrishna, *RSC Adv.*, 2012, **2**, 2067.
63 D. Quéré, *Annu. Rev. Mater. Res.*, 2008, **38**, 71–99.
64 E. Martines, K. Seunarine, H. Morgan, N. Gadegaard, C. D. W. Wilkinson and M. O. Riehle, *Nano Lett.*, 2005, **5**, 2097–2103.
65 V. Pifferi, L. Rimoldi, D. Meroni, F. Segrado, G. Soliveri, S. Ardizzone and L. Falciola, *Electrochem. commun.*, 2017, **81**, 102–105.
66 D. Menshykau and R. G. Compton, *Langmuir*, 2009, **25**, 2519–2529.
67 S. Schwarz, K. Lunkwitz, B. Keßler, U. Spiegler, E. Killmann and W. Jaeger, *Colloids Surfaces A Physicochem. Eng. Asp.*, 2000, **163**, 17–27.
68 J. Sun, B. V. Velamakanni, W. W. Gerberich and L. F. Francis, *J. Colloid Interface Sci.*, 2004, **280**, 387–399.
69 R. G. Compton and C. E. Banks, *Understanding Voltammetry*, Imperial College Press, Oxford, 2nd edn., 2007.
70 F. G. Chevallier, L. Jiang, T. G. J. Jones and R. G. Compton, *J. Electroanal. Chem.*, 2006, **587**, 254–262.
71 M. E. Orazem and B. Tribollet, *Electrochemical Impedance Spectroscopy*, John Wiley & Sons, Inc., Hoboken, NJ, USA, 2008.
72 T. Doneux, A. de Ghellinck, E. Triffaux, N. Brouette, M. Sferrazza and C. Buess-Herman, *J. Phys. Chem. C*, 2016, **120**, 15915–15922.
73 G. Di Carlo, A. Trani, D. Zane, G. M. Ingo, M. Pasquali, A. Dell'Era

and A. Curulli, *Electroanalysis*, 2014, **26**, 1409–1418.
74 A. Fagan-Murphy, F. Watt, K. A. Morgan and B. A. Patel, *J. Electroanal. Chem.*, 2012, **684**, 1–5.
75 H. T. H. Chan, E. Kätelhön and R. G. Compton, *J. Electroanal. Chem.*, 2017, **801**, 135–140.

This Chapter has been adapted with permission from Rimoldi *et al*., *Electrochim. Acta*, 2018, **291**, 73–83. Copyright 2018 Elsevier.

Chapter 10

Alkylsilane-SiO_2 Hybrids. A Concerted Picture of Temperature Effects in Vapor Phase Functionalization

Organosilanes have attracted much attention due to their ability to functionalize oxide surfaces, such as SiO_2, TiO_2, and indium tin oxide. The resulting films control important physical properties of the oxide surface, such as friction, wettability,[1] work function and capacitance[2]. Promising applications of this class of molecules are described in several different fields, such as in microfluidics[3], nanolubrication[4], as coupling agents for adhesion improvement, self-cleaning coatings[5], lithographic methods[6], photovoltaics[7] and molecular sensing[8,9].

Organosilane derivatives in the presence of water tend to undergo condensation reaction with hydroxyl groups at the oxide surface and/or with other organosilane molecules.[1] The most commonly studied molecules, trifunctional alkylsilanes ($RSiX_3$ where X can be –Cl, –OEt or –OMet), can give rise to a number of possible surface structures: along with covalent attachment to the surface, 2D (self-assembly) and 3D surface-induced polycondensation are possible.[10] The obtained layer structure crucially depends on the deposition conditions.

Two approaches are commonly employed for depositing alkylsilane films: liquid-phase and vapor-phase methods. Although the liquid-phase approach has been the most extensively studied, it is neither environmentally friendly nor industrially viable because it generates significant amounts of solvent waste.[11] Compared to the liquid-phase approach, there have been relatively few reports of vapor-phase deposition methods for alkylsilane deposition, although the vapor-phase approach has

been reported to yield alkylsilane films with better quality in terms of water repellency and surface roughness.[12,13] Recent studies have focused on the role played by the water content[14] and surface hydration of the oxide substrate[15] on the final layer quality.

In this Chapter, a simple procedure of chemical vapor deposition adopted to functionalize silica substrates with two different trifunctional alkylsilanes is reported. Triethoxysilanes with different alkyl chains were employed, comparing fluorinated and unfluorinated molecules. The effect of the functionalization temperature (70–150 °C) was investigated in detail. An original combination of characterization techniques was used to provide a complete picture of the alkylsilane layer structure. Along with contact angle determinations and FTIR, less commonly employed techniques are reported. Electrochemical characterizations (cyclic voltammetry and impedance spectroscopy) proved to be a powerful tool to assess the defectiveness of the alkylsilane layers, while solid state nuclear magnetic resonance (NMR) provided a molecular insight into the grafting mode of the alkylsilane molecules on the surface. In this respect, the chosen substrates were silica-based materials (native oxide on Si wafers, glass, SiO_2 powders) owing to their application potential and versatility, which allowed us to carry out a wide range of characterizations.

10.1 Results and discussion

10.1.2 Surface free energy

Contact angle measurement is one of the most commonly employed techniques to assess the quality of alkylsilane layers. After pretreatment, the water contact angle (θ_w) of the bare silicon wafer surface, which is covered by a native layer of SiO_2, is close to 0°. The superhydrophilicity of the clean Si surface is related to its surface hydroxylation. After functionalization with Octyl(H), the interface turns hydrophobic (Fig. 10.1a), indicating that the alkyl chains completely control the wetting features and water interacts with the methyl and methylene groups of the alkyl chains. Literature has widely reported the correlation between θ_w and the formation of alkylsilane olygomers and monolayers,[10] showing that self-assembled ordered monolayers have higher contact angles because

water interacts with only methyl groups. Sugimura *et al.*[16] reported $\theta_w \approx$ 105–107° as the optimum for this family of alkylsilanes.

Figure 10.1a shows the θ_w of the functionalized surfaces with Octyl(H) at different temperatures. The bell-shaped curve has a maximum at 100 °C. The maximum contact angle ($\theta_w \approx 107°$) is in full agreement with literature results about complete monolayers. The contact angle varies sharply by changing the deposition conditions: at the highest tested deposition temperature, a water contact angle much lower than 90° was determined. Comparable results were obtained using a glass slide as a substrate (data not shown).

The implications of the wetting features of the functionalized surface on its structure are more clearly appreciable when the surface free energy (SFE) is considered. Several strategies can be adopted to determine the SFE of a solid. The most widely accepted approach correlates the SFE with contact angle measurements by different solvents. Among all literature models[17–19], the Owens-Wendt-Rabel-Kaelble (OWRK) method[20] was considered the most accurate one for the aim of the present work. This model considers the SFE as due to the sum of two components, a polar one which is related to polar surface interactions (*e.g.*, hydrogen bonds) and a disperse one influenced by the London dispersion forces. The total SFE for the functionalized surfaces and its components were obtained from the linearized OWRK equation:

$$\frac{\gamma_l(1+cos\theta)}{2\sqrt{\gamma_l^d}} = \sqrt{\gamma_s^p}\sqrt{\frac{\gamma_l^p}{\gamma_l^d}} + \sqrt{\gamma_s^d} \qquad (10.1)$$

where θ is the contact angle of the probe liquid on the functionalized surface, while γ_l^p and γ_l^d are the polar and disperse components of the probe liquid surface tension, γ_l.

The γ_s^p and γ_s obtained for the surfaces functionalized with Octyl(H) at different temperatures are reported in Figure 10.1a. While the γ_s^d values show a limited variation with respect to the functionalization temperature, the γ_s^p changes dramatically as a function of deposition conditions. It is noteworthy that $\gamma_s^p \approx 0$ at 100 °C, *i.e.*, no polar groups are present at the surface. On the grounds of considerations about the physical meaning of γ_s^p, the formation at 100 °C of a complete monolayer can thus be suggested.

Such hypothesis is supported also by AFM images (Fig. 10.1b) showing the occurrence of a smooth and homogeneous surface. At higher deposition temperatures, polar groups are appreciable at the interface ($\gamma_s^p \neq 0$), which implies the occurrence of either an incomplete coverage of the silica surface or the presence of disordered and multilayer structures.

A completely different picture emerges from the contact angle measurements of surfaces modified with the fluorinated analogue (Fig. 10.1c). The substrates, functionalized at temperature ranging from 70 °C to 150 °C, showed θ_w values comparable within the experimental error. The observed water contact angles were for all samples close to 117°, irrespectively of the functionalization temperature. The increased hydrophobicity of Octyl(F) samples with respect to the unfluorinated analogues has been related to the greater diameter of the perfluorinated chains, which gives rise to a larger energy penalty for hydration[26]. The obtained values are comparable or even larger than literature reports of similar compounds[13,15,21–23]. The SFE components reflect the increased hydrophobicity and oleophobicity of the fluorinated chain: the polar component is almost null and the disperse component is significantly reduced with respect to the unfluorinated analogue. Interestingly, the functionalization temperature seems to play a negligible role on the wetting features of Octyl(F) films. Considering the macroscopic scale of the technique, other characterization techniques were used to probe the layer quality at the molecular scale.

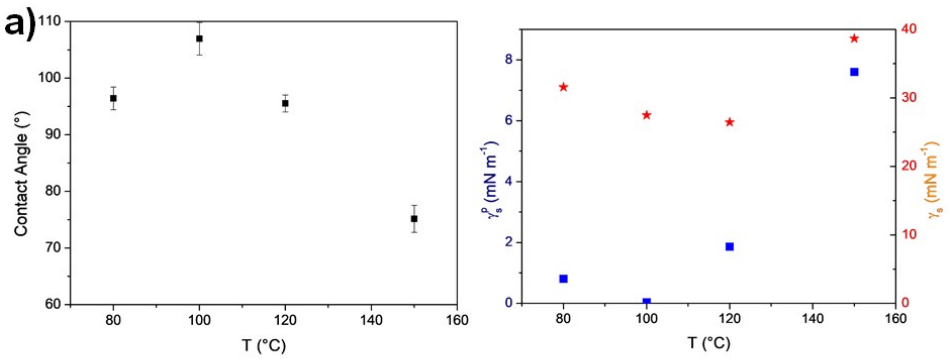

a) Effect of functionalization temperature on the wetting features of Octyl(H) layers on Si: water contact angle (left); surface free energy γ_s (red stars) and relative polar component γ_s^P (blue squares) (right).

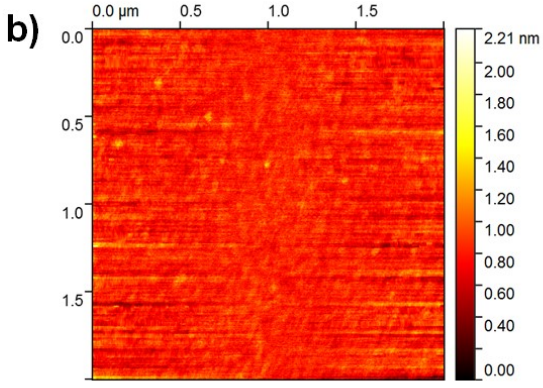

b) AFM tapping mode topographical image of H_100.

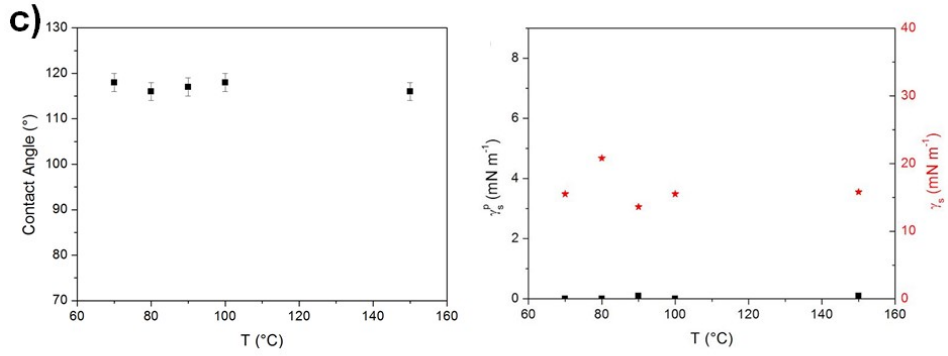

c) Effect of functionalization temperature on the wetting features of Octyl(F) layers on Si: water contact angle (left); surface free energy γ_s (red stars) and relative polar component γ_s^P (black squares) (right).

Figure 10.1 – Surface characterization results.

10.1.2 Electrochemical measurements

Alkyl chain layers are dielectric in nature due to the very large gap between the highest occupied molecular orbital (HOMO) and the lowest occupied molecular orbital (LUMO).[2] As a result, they behave as electronic insulators, they can serve as an ionic barrier, and depending on the nature of the terminal group, might behave as an ideal capacitor.[23] Electrochemical techniques have been utilized to study the insulating properties of alkylsilane monolayers at oxide surfaces, such as indium tin oxide[14,24,25] and SiO_2/Si[26,27]. The electrochemical properties have been correlated to the eventual presence of pinholes and structural defects within the monolayer. In the present study, electrochemical techniques were used to evaluate the barrier properties of the chemical vapor deposited alkylsilane layers, studying the effect of the deposition temperature and of the fluorination of the alkyl chain. To the authors' best knowledge, no previous studies on the characterization of triethoxy(octyl)silane and *1H,1H,2H,2H*-perfluoroctyltriethoxysilane on Si/SiO_2 surfaces have been reported.

Cyclic voltammetry (CV) was employed to obtain the capacitance of the organic layer present on the electrode surface, considered as a capacitor[14, 33] (Tab. 10.1). Actually, the measured capacitance is a combination of the support and film capacitances. The former can be assumed to be invariant with varying the film features.

In the case of Octyl(H), the highest capacitance was obtained for H_100, followed by H_80, while H_150 shows a capacitance one order of magnitude lower (Tab. 10.1). These results closely mirror the bell-shaped curve obtained by contact angle measurements. In the case of fluorinated precursor, the highest capacitance was obtained for F_90, followed by F_80. F_100 and F_70 present similar capacitances, while F_150 has the lowest value.

Electrochemical impedance spectroscopy (EIS) was adopted to further study the insulating and barrier properties of the alkylsilane layer by investigating the ionic permeation of an inert electrolyte in a wide frequency range (0.1–65000 Hz). EIS data were fitted using an electrical equivalent circuit (Fig. 10.2b) very often employed for these organic layers[25,26]; it is composed by a parallel combination of a double layer

capacitance, C_{dl}, and a charge transfer resistance to ionic permeation, R_{ct}, in series with the solution resistance, R_{Ω}, and with a constant phase element, denominated CPE_{pol}, corresponding to the film polarization capacitance. The R_{ct} parameter provides the resistance offered by the film toward the electron transfer across the electrode-electrolyte interface. The higher R_{ct}, the more inhibited is the electron transfer due to the presence of the alkylsilane layer.[27] The constant phase element CPE_{pol} allowed us to evaluate the dielectric behavior of the alkylsilane layer and, indirectly, the homogeneity of the layer: a CPE frequency exponent α equal to 1 corresponds to a pure capacitor (*i.e.*, defect-free layer), whereas an α value of 0.5 corresponds to a diffusion element (*i.e.*, a defective layer).[25]

Complex plane plots show for all the tested samples the typical trend correlated to this equivalent circuit (Fig. 10.2a,c): a semicircle at high frequencies followed by a straight line with different slopes at low frequencies. The parameters obtained by the equivalent circuit fitting procedure of EIS data are reported in Table 10.1.

Film capacitance values (Tab. 10.1) are in accordance with those obtained from cyclic voltammetry (Tab. 10.1), following also the same trend, and are coherent with values previously reported in the case of unfluorinated and fluorinated silanes[14,26].

Sample	C (μF cm^{-2})	R_{ct} (kΩ cm^2)	CPE_{pol} (μF cm^{-2} s$^{α-1}$)	α
H_80	1.19	34.36	1.36	0.87
H_100	1.25	147.39	1.64	0.91
H_150	0.32	29.45	0.60	0.60
F_70	0.43	129.04	1.06	0.84
F_80	0.75	108.19	1.52	0.86
F_90	0.79	145.08	2.17	0.92
F_100	0.41	54.33	0.66	0.72
F_150	0.33	31.53	0.73	0.70

Table 10.1 – Cyclic voltammetry and impedance data.

In the case of Octyl(H) (Fig. 10.2a), H_100 shows the highest charge transfer resistance, measured from the semicircle diameter, which is

indicative of a low ionic permeability of the electrolyte in the organic structure. The R_{ct} values strongly decrease for H_80 and H_150, indicating a more disordered and non-uniform layer, where the electrolyte can permeate. Moreover, while the semicircle is complete for H_100 and H_80, it is not for H_150, reflecting a lower homogeneity of the layer for the latter. These results were confirmed by Bode plots (Fig. 10.2a), which show a deviation at medium frequencies in the case of H_150, ascribable to a diffusion component due to ionic permeation. Consistently, an α value closer to unity was obtained for H_100, indicating a pure capacitive-like behavior for this system, typical of a very flat and homogeneous film.

In the case of Octyl(F) (Fig. 10.2c), the highest charge transfer resistance and α value were found for F_90, in agreement with capacitance results. The system behaves as a pure capacitor to the point that only the beginning of the semicircle is visible. This behavior can be observed exclusively for F_90, while the other samples show a consistent decrease in charge transfer resistances and α values (Tab. 10.1). F_70 and F_80 show similar α and R_{ct} values. However, with respect to F_70, F_80 presents a higher capacitance, a complete semicircle and a Bode plot without the diffusion component. The highest temperatures (100 °C and 150 °C) result in the lowest charge transfer resistances, capacitances and α values, as well as incomplete semicircles and diffusion components in Bode plots.

It is noteworthy that electrochemical measurements proved to be more sensitive to changes in the alkylsilane layers than water contact angle measurements, in agreements with previous reports[14]. Indeed, contact angle measurements use macroscopic probes (*i.e.*, microliter droplets) to investigate the alkylsilane layer, while electrochemical methods, such as ionic permeation studies by EIS, use much smaller probes (in this case Na^+ and ClO_4^- ions) to evaluate the barrier properties of the alkylsilane layer.

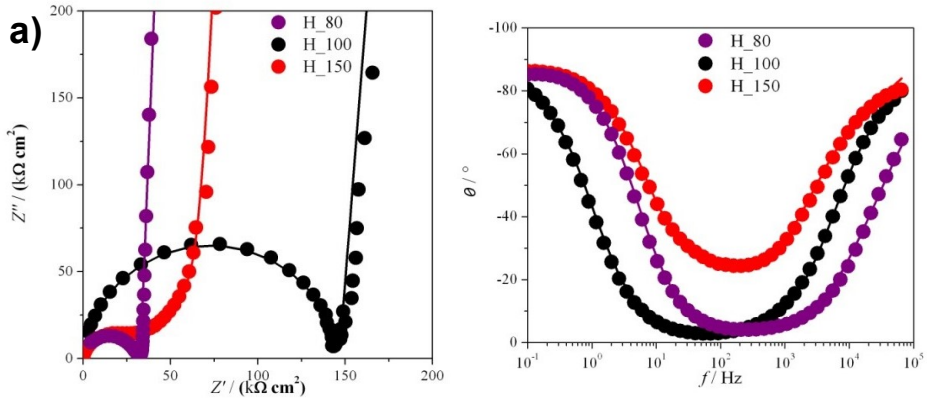

a) Complex plane (left) and Bode (right) plots with fitted data for Octyl(H) samples at different deposition temperatures; (c) equivalent circuit used to fit impedance spectra.

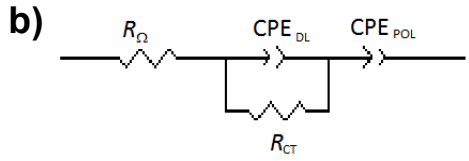

(b) Equivalent circuit used to fit impedance spectra.

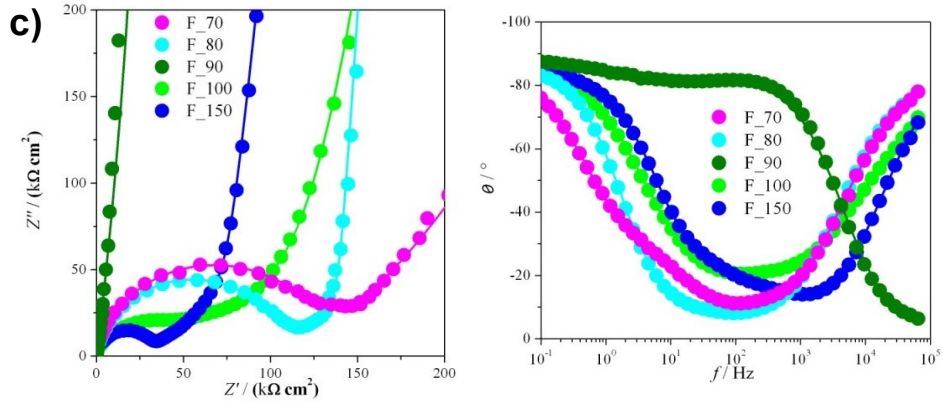

c) Complex plane (left) and Bode (right) plots with fitted data for Octyl(F) samples at different deposition temperatures.

Figure 10.2 – Electrochemical characterization results.

10.1.3 FTIR spectroscopy

Spectroscopic characterizations were resorted to study the functionalization process at the molecular level. FTIR spectroscopy

provided information about the extent of the functionalization and about the surface hydroxylation before and after the functionalization.

Figure 10.3a reports the FTIR spectrum of the starting material. The following spectral features can be appreciated:

- OH-stretching vibration of free surface hydroxyl groups in the 3700–3750 cm^{-1} spectral range;
- A broad band in the 3700–3000 cm^{-1} spectral range due to OH-stretching vibration of hydroxyl groups mutually interacting by hydrogen bonding;
- A typical component located at ~ 1630 cm^{-1} characteristic of the in-plane HOH bending mode of undissociated water molecules, which is normally indicated as spectroscopic partner of the broad envelope; quoted in point (ii);
- Three broad bands, located in the 2100–1750 cm^{-1} spectral region, attributed to Si–O–Si overtones typical of the silica matrix.

The differential FTIR spectra relative to the samples functionalized with Octyl(H) are reported in Figure 10.3b.

After the functionalization process with Octyl(H), the following spectral features are clearly detectable:

- In the 3000–2850 cm^{-1} spectral region a clear envelope, made up of three sharp components, ascribable to the CH stretching bands of all $–CH_n$ containing species;
- Their bending counterparts being normally located in the 1500–1350 cm^{-1} spectral region;
- A specific component located at ~ 1680 cm^{-1} ascribable to the –CO– group present in the Octyl(H) agent[28], which might be indicative of an incomplete substitution of the ethoxy groups.
- Negative peaks for both the –OH stretching vibration interacting by hydrogen bonding and HOH of undissociated molecular water occurs. The loss of silanol groups upon functionalization with organofunctional alkoxysilanes has been reported previously[12] and may be partly related to the formation of Si–O–Si bonds between the surface and alkylsilane molecules, as supported by NMR results.

The temperature of the functionalization treatment has mainly an effect on the peak intensity. The bands ascribable to –CH functionalities decrease at functionalization temperatures higher than 100°C. Moreover, in the

temperature range from 80 to 120°C, the peaks associated with silanols interacting by hydrogen bonding and undissociated molecular water become less intense. These aspects closely mirror solid state NMR results and will be discussed in detail therein.

Figure 10.3c reports the FTIR differential spectra relative to samples functionalized with Octyl(F).

After functionalization with Octyl(F) the following spectral features are clearly detectable, apart from those already described for the pristine silica system and described above:

- –CH stretching bands in the 3000–2850 cm^{-1} spectral region, due to the $–CH_n$ groups present in the functionalizing agent, with their spectroscopic bending counterpart located in the 1500–1350 cm^{-1} spectral region;
- A specific component located at ~ 1680 cm^{-1} ascribable to the –CO– group present in the Octyl(F) agent.
- Negative peaks are observed for both the –OH stretching vibration interacting by hydrogen bonding and HOH of undissociated molecular water. However, in this case a much lower dependence of the peak intensity on the deposition temperature is appreciable.

Unfortunately, we were not able to inspect in detail the region located at $\nu < 1200$ cm^{-1} to highlight the various C–F modes which characterize the functionalizing agent[29], due to the presence of the cut-off typical of all silica-based systems.

Similarly to the case of the Octyl(H), the functionalization temperature strongly affects the intensity of the peaks related to the alkylsilane layer, as clearly seen in Figure 10.3c for the ν_{CH}. However, in this case the maximum intensity of the ν_{CH} peaks is reached at 90°C.

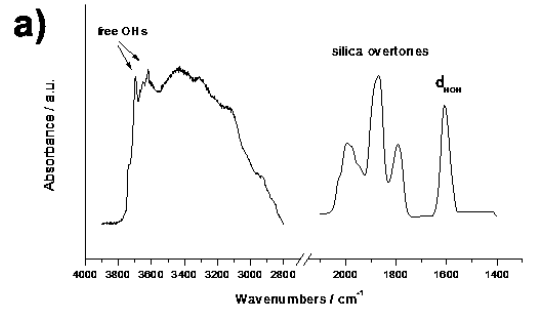

a) FTIR spectrum of the unfunctionalized silica.

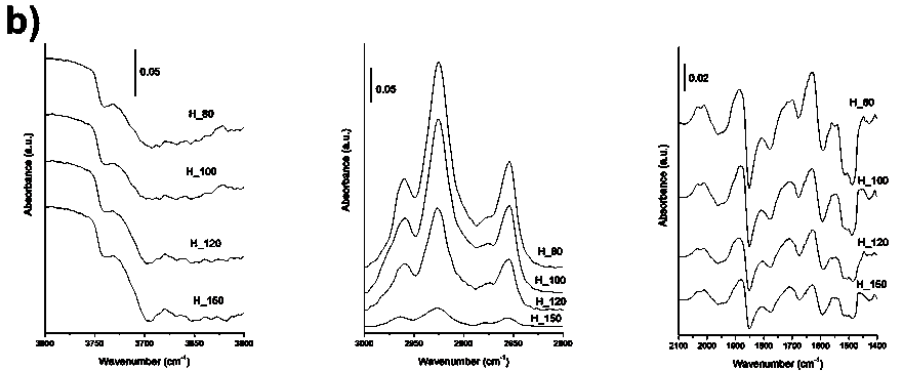

b) Differential absorbance FTIR spectra obtained by subtracting the curve of the pristine samples from those of samples functionalized with Octyl(H): 3800–3600 cm^{-1} spectral range (left); 3000–2800 cm^{-1} spectral range (middle); 2100–1400 cm^{-1} spectral range (right).

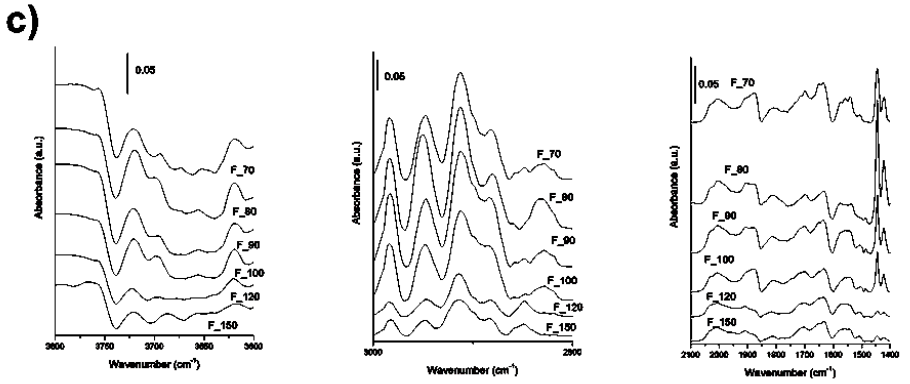

c) Differential absorbance FTIR spectra obtained by subtracting the curve of the pristine samples from those of samples functionalized with Octyl(F): 3800–3600 cm^{-1} spectral range (left); 3000–2800 cm^{-1} spectral range (middle); 2100–1400 cm^{-1} spectral range (right).

Figure 10.3 – FTIR spectroscopy results.

10.1.4 Solid state NMR

^{29}Si and ^{13}C solid state MAS NMR can provide relevant information about the changes taking place at the silica surface upon functionalization and about the different alkylsilane structures present at the surface[30–32]. However, to the authors' best knowledge, studies adopting this technique to characterize alkylsilane layers deposited by chemical vapor deposition have been scarce[12].

Figure 10.4a reports the ^{29}Si spectra of H_80, H_100 and H_150 samples, compared to the spectra of unfunctionalized silica.

The signal of the starting compound (-28 ppm) is not appreciable from the spectra, confirming the absence of unbound Octyl(H) molecules. All ^{29}Si NMR spectra show two sets of signals, the first between -85 and -110 ppm (Q^n signals) and the second one between -50 and -70 ppm (T^n signals). The former can be related to the unsubstituted silica surface, while the latter can be assigned to the Si atoms covalently bound to the alkylsilane molecules. The ratio between the two signals depends on the functionalization temperature: the T : Q ratio of H_80 and H_100 is very similar (1:3.0 and 1:2.8, respectively), while it decreases up to 1:4 for the H_150 samples. This behavior is indicative of a different functionalization degree of the samples.

The Q^n and T^n signals of H_150 are composite peaks, made of three different resolved resonances. This suggests the co-presence of several Si species with different chemical structures. The same species are present in all other spectra. The peak resolution is not high because the shift between the peaks is small and the width is large. However, we were able to determine the different components by a deconvolution program. On the basis of literature studies[12,33,34], we can assign the three high-field resonances (at –93/94, –101 and –108/110 ppm) to geminal silanols Q^2 [(≡SiO)$_2$ **Si**(OH)$_2$], single silanols Q^3 [(≡SiO)$_3$**Si**OH)] and alkoxysilane groups Q^4 [(≡SiO)$_4$**Si**)], respectively. Instead, the low-field resonances (at -51, -59 and -69 ppm) can be related to silicon atoms in position [(SiO)**Si**R(OH/Et)$_2$] (denominated as T^1), [(≡SiO)$_2$**Si**(OH/Et)R] (T^2) and [(≡SiO)$_3$**Si**R] (T^3), respectively.

A fitting analysis was performed using Lorentzian and Gaussian curves to deconvolute the components and determine the relative ratio of the

coexisting structures. Table 10.2 reports the peak position and content of the different structures for unfunctionalized silica and H_80, H_100 and H_150 samples.

The deconvolution analysis reveals that the relative content of the Q components varies as a function of the functionalization temperature. While the Q^4 component remains essentially unchanged, the Q^2 resonance, assigned to single silanols, tends to decrease at increasing functionalization temperatures, whereas the Q^3, relative to germinal silanols, shows an opposite trend. The disappearance of single silanols as a result of the functionalization with Octyl(H) is supported by FTIR results.

The T^1, T^2 and T^3 signals, relative to substituted alkylsilane derivatives, correspond to structures containing respectively one, two and three Si–O–Si bonds with either the silica surface or neighboring alkylsilane molecules. Although we cannot distinguish between the last two situations, an alkylsilane molecule cannot form three Si–O–Si bonds with the surface due to steric reasons. Previous results from our group in the case of nanometric TiO_2 functionalized with different trifunctional alkylsilanes via wet procedures, showed that the degree of lateral polymerization (*i.e.*, an increase in the T^3 content) increases at increasing alkylsilane content[30] and is crucially influenced by the lateral interactions taking place between the chains of neighboring alkylsilane molecules[31,32]. In the present study, we found that the functionalization temperature significantly impacts the relative amount of each species.

	SiO_2		**H_80**		**H_100**		**H_150**	
	x / ppm	%	x / ppm	%	x / ppm	%	x / ppm	%
Q^2	-93.3	33	-94.0	34	-93.3	21	-93.4	11
Q^3	-101.0	51	-101.3	46	-101.6	59	-101.7	68
Q^4	-109.4	16	-108.4	20	-109.9	20	-110.0	21
T^1	-	-	-49.6	16	-50.9	32	-	-
T^2	-	-	-59.0	62	-59.6	54	-62.7	54
T^3	-	-	-69.7	22	-69.0	15	-68.0	46

Table 10.2 – ^{29}Si CP/MAS NMR chemical shifts and relative percentages for the proposed Si structures of the unfunctionalized and Octyl(H) functionalized samples.

The H_80 and H_100 samples present all three T^n resonances, whereas H_150 shows only T^2 and T^3 signals. High temperatures seem thus to favor lateral polymerization.

^{13}C MAS NMR spectra of H_80 (a), H_100 (b) and H_150 (c) (Fig. 10.4b), performed in the same experimental conditions, show a decrease of the signal to noise ratio (S/N) passing from a) (S/N 27/1) to b) (S/N 10/1) and c) (S/N 7/1) spectrum. These results, along with T : Q ratios determined by ^{29}Si spectra, support a higher functionalization degree at 80–100 °C with respect to 150 °C. Such findings are in agreement with FTIR data showing a decrease of the alkyl chain content at increasing functionalization temperature.

^{13}C spectra present well defined peaks, which can be readily assigned for comparison with the Octyl(H) spectrum obtained in homogeneous solution: 12.6 ppm ($\underline{CH_3}$ and $\underline{CH_2}Si$), 22.6 ppm ($\underline{CH_2}CH_3$ and $\underline{CH_2}CH_2Si$), 29.9 ppm ($\underline{CH_2}CH_2CH_2CH_3$ and $\underline{CH_2}CH_2$ CH_2Si) and 32.3 ppm ($\underline{CH_2}CH_2CH_3$ and $\underline{CH_2}CH_2CH_2CH_2Si$). The low intensity or complete absence of the ethoxy group signal (58.0 and 16.0 ppm) supports a high substitution degree of the ethoxy group during the functionalization process for all samples. The presence of unhydrolyzed alkoxy groups on the alkylsilanes could sterically hinder dense monolayer formation[14].

The samples functionalized with the Octyl(F) show ^{29}Si spectra similar to corresponding compounds functionalized with the unfluorinated analogue. In the same way, ^{29}Si NMR spectra of Octyl(F) derivatives (Fig. 10.4a) are characterized by the presence of T^n and Q^n species, which are as well strongly affected by the functionalization temperature. Indeed, the T : Q ratio reaches a maximum for the sample F_90 (1 : 1.5) and decreases at higher temperatures (1 : 3.0 and 1 : 7.3 for F_100 and F_150, respectively).

Such observation is in agreement with the trend observed in the S/N ratio of ^{13}C NMR spectra, performed in the same experimental conditions. The S/N increases raising the functionalization temperature up to 90°C, while at higher values the S/N ratio decreases. Figure 10.4c shows the trend of ^{13}C NMR spectra, from 70 up to 150°C. Moreover, in the case of Octyl(F), the temperature effect appears to be more critical with respect to the unfluorinated analogue. Indeed, the optimal functionalization temperature seems a narrow range centered at 90°C: above and below this value the ^{13}C NMR spectra show a relevant S/N decrease.

^{13}C spectra show the following resonances: 1.9 ppm ($\underline{CH_2}Si$), 24.2 ppm ($\underline{CH_2}CH_2Si$), 11.9 and 118.0 ppm ($\underline{CF_2}$ and CF_3). The peaks at 58.0 and 16.0 ppm can be attributed to a 10–20% residual ethoxy group, in agreement with FTIR findings.

A deconvolution analysis was carried out on T^n and Q^n signals of ^{29}Si NMR spectra, in order to estimate the amount of the different species (Tab. 10.3). As for the unfluorinated analogue, the ^{29}Si NMR spectra show that the alkylsilane polymerization degree increases with the functionalization temperature, leading to higher T^3 and lower T^1 contents. On the contrary, the functionalization temperature does not significantly modify the ratio among the Q components. Such evidence suggests a lower degree of covalent bonding with the silica surface in the case of fluorinated alkylsilane.

	SiO_2		**F_70**		**F_80**		**F_90**		**F_100**		**F_150**	
	x / ppm	%	x / ppm	%	x / ppm	%	x / ppm	%	x / ppm	%	x / ppm	%
Q^2	-93.3	33	-93.5	34	-93.0	36	-93.5	30	-93.0	28	-93.6	36
Q^3	-101.0	51	-101.5	49	-101.2	44	-101.7	48	-101.6	50	-101.3	44
Q^4	-109.4	16	-109.6	17	-109.6	20	-109.7	22	-108.0	22	-108.6	20
T^1	-	-	-53.0	29	-54.0	11	-51.5	13	-	-	-	-
T^2	-	-	-59.9	71	-61.0	58	-59.8	62	-58.0	68	-59.0	85
T^3	-	-	-	0	-69.0	31	-69.6	25	-70.0	32	-70.0	15

Table 10.3 – ^{29}Si CP/MAS NMR chemical shifts and relative percentages for the proposed Si structures of the different bare and Octyl(F) functionalized samples.

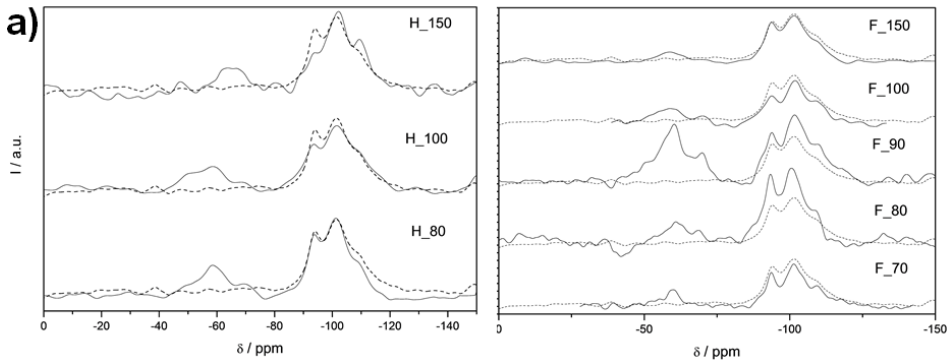

a) ^{29}Si CP/MAS NMR spectra of the Octyl(H) (left) and Octyl(F) (right) samples. The spectrum of unfunctionalized SiO_2 is reported as a reference (dashed line)

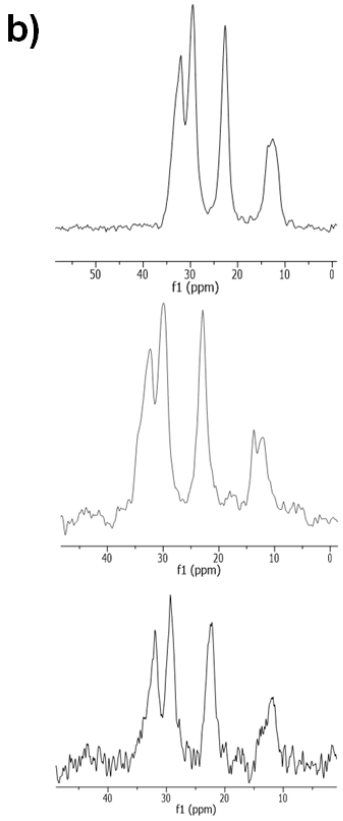

b) ^{13}C CP/MAS NMR spectra of H_80 (top), H_100 (middle) and H_150 (bottom).

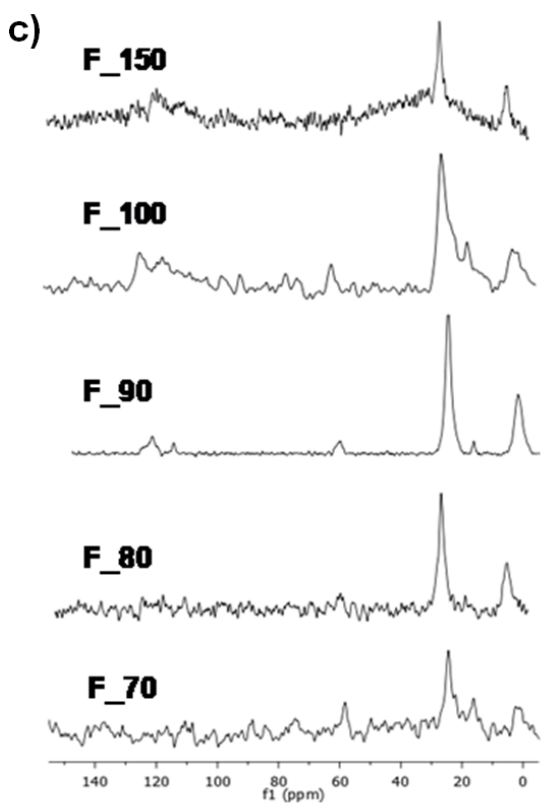

c) ^{13}C CP/MAS NMR spectra of Octyl(F) derivatives in the temperature range 70−150 °C.

Figure 10.4 – NMR spectroscopy results.

10.2 Conclusions

The chemical vapor deposition of triethoxy(octyl)silane and its fluorinated analogue on silica substrates was studied by a combination of surface, electrochemical and spectroscopic characterization techniques. The influence of the functionalization temperature was studied in the range from 70 to 150 °C.

An original combination of characterization techniques was adopted to probe the layer structure at different length scales. Notwithstanding the diverse nature of the utilized substrates (either SiO_2 particles, glass or native oxide layer on Si wafers), the different techniques provided a coherent picture of the alkylsilane layer structure as a function of the deposition conditions.

In the case of Octyl(H), both the wetting and ion permeability properties displayed a bell-shaped curve as a function of the functionalization temperature. FTIR and solid state NMR showed a similar trend in the functionalization degree of silica particles. The spectroscopic techniques suggested that the functionalization gives rise to oligomers/polymers covalently attached to the surface, as apparent from the loss of surface silanol groups. Furthermore, ^{29}Si NMR spectra proved that higher functionalization temperatures increase the lateral polymerization across the alkylsilane layer. Undesired self-polymerization of the alkylsilane molecules before vaporization might concur to reduce the functionalization degree at high temperatures[11,14], along with effects on the surface hydration[15]. Indeed, trialkoxy alkylsilanes are generally believed to first react with water adsorbed at the silica surface to form silanol intermediates, which then undergo condensation reactions with neighboring intermediates and hydroxyl groups on the silica surface. Increasing temperatures might thus initially play a beneficial role by increasing the vaporization of the alkylsilane molecules and promoting lateral polymerization in the layer. However, increasing the functionalization temperature above 100 °C leads to lower functionalization degrees and lower layer quality.

Conversely, the fluorinated analogue showed a much lower dependence of the wetting properties on the CVD temperature. However, the electrochemical barrier properties, as well as FTIR and NMR results, showed a marked dependence on the functionalization conditions. Indeed,

electrochemical capacitance measurements have already been reported to be more sensitive to changes in the density of the alkylsilane monolayers than water contact angle measurements[14]. Spectroscopic and electrochemical characterizations suggested an even higher sensitivity of the quality of the fluorinated alkylsilane layer on the functionalization temperature with respect to the unfluorinated analogue, which might be related to a higher thermal reactivity of Octyl(F)[35]. Further, the very high contact angles observed for Octyl(F) samples might be related to the occurrence of oligomerization. In this respect, the diffusion components in the Bode plots and the lower degree of covalent bonding with the surface (as apparent by the constant silanol consumption) seem to support the occurrence of vertical polymerization or disordered structures.

Optimal deposition conditions in terms of wettability and ionic permeability were thus identified for both alkylsilanes as a function of the deposition temperature (100°C for Octyl(H) and 90°C for Octyl(F)). Furthermore, the characterization approach here presented represents a powerful tool to investigate the structure and properties of alkylsilane layers at different length scales.

10.3 Specific procedures

Samples preparation. All of the chemicals were of reagent grade purity and were used without further purification; doubly distilled water passed through a Milli-Q apparatus was utilized.

Two different kinds of trifunctional alkylsilanes were investigated: Triethoxy(octyl)silane (named Octyl(H) in the Chapter) and 1H,1H,2H,2H-perfluorooctyltriethoxysilane (named Octyl(F) in the Chapter), both purchased from Sigma Aldrich. The substrate was n-type Si(100) (3–6 Ω cm, Ultrasil Corporation), having a native oxide layer *ca.* 1.5 nm thick. Due to experimental limits, solid state magic angle spinning nuclear magnetic resonance (MAS NMR) and Fourier transform infrared (FTIR) spectroscopies were carried out on SiO_2 powders (Sigma-Aldrich).

The substrates were functionalized using a chemical vapor deposition procedure adapted from Sugimura *et al.*[16]. The Si substrate was cleaned with water and acetone sonication, then treated in hot piranha solution for one hour at 80 °C until a complete water spreading was observed. The

substrate was rinsed with water, then dried under N_2 flux and placed in a glass container filled with N_2 gas together with a Teflon cup containing 80 mg of the chosen alkylsilane. The container was then placed in an oven at a fixed temperature for 3 h. Different functionalization temperatures in the range 70–150 °C were tested. Finally, the substrate was sonicated in toluene to remove the excess/unreacted alkylsilane. SiO_2 powders were functionalized using a comparable experimental procedure, in which the pretreatment in hot piranha solution was replaced by a prolonged UV light irradiation and the amount of alkylsilane was increased to compensate for the larger oxide surface area.

The samples are referred to using a letter indicative of the adopted alkylsilane (H or F for the unfluorinated and fluorinated molecules, respectively) followed by the temperature of the functionalization step.

Hazards. Piranha solution (a 3:1 v/v mixture of H_2SO_4 98% and H_2O_2 30%) reacts violently with organic matter.

Further details about the preparation and characterization methods can be found in Appendix A.

References

1 S. Onclin, B. J. Ravoo and D. N. Reinhoudt, *Angew. Chemie Int. Ed.*, 2005, **44**, 6282–6304.

2 S. A. DiBenedetto, A. Facchetti, M. A. Ratner and T. J. Marks, *Adv. Mater.*, 2009, **21**, 1407–1433.

3 N. G. Batz, J. S. Mellors, J. P. Alarie and J. M. Ramsey, *Anal. Chem.*, 2014, **86**, 3493–3500.

4 B. Bhushan, T. Kasai, G. Kulik, L. Barbieri and P. Hoffmann, *Ultramicroscopy*, 2005, **105**, 176–188.

5 Y. Lu, S. Sathasivam, J. Song, C. R. Crick, C. J. Carmalt and I. P. Parkin, *Science (80-.).*, 2015, **347**, 1132–1135.

6 D. Meroni, S. Ardizzone, U. S. Schubert and S. Hoeppener, *Adv. Funct. Mater.*, 2012, **22**, 4376–4382.

7 L. Liu, A. Mei, T. Liu, P. Jiang, Y. Sheng, L. Zhang and H. Han, *J. Am. Chem. Soc.*, 2015, **137**, 1790–1793.

8 G. Soliveri, V. Pifferi, G. Panzarasa, S. Ardizzone, G. Cappelletti, D. Meroni, K. Sparnacci and L. Falciola, *Analyst*, 2015, **140**.

9 S. K. Arya, P. R. Solanki, M. Datta and B. D. Malhotra, *Biosens. Bioelectron.*, 2009, **24**, 2810–2817.

10 A. Y. Fadeev and T. J. McCarthy, *Langmuir*, 2000, **16**, 7268–7274.

11 F. Zhang, K. Sautter, A. M. Larsen, D. A. Findley, R. C. Davis, H. Samha and M. R. Linford, *Langmuir*, 2010, **26**, 14648–14654.

12 G. Soliveri, D. Meroni, G. Cappelletti, R. Annunziata, V. Aina, G. Cerrato and S. Ardizzone, *J. Mater. Sci.*, 2014, **49**, 2734–2744.

13 A. Hozumi, K. Ushiyama, H. Sugimura and O. Takai, *Langmuir*, 1999, **15**, 7600–7604.

14 R. D. Lowe, M. A. Pellow, T. D. P. Stack and C. E. D. Chidsey, *Langmuir*, 2011, **27**, 9928–9935.

15 K. Wu, T. C. Bailey, C. G. Willson and J. G. Ekerdt, *Langmuir*, 2005, **21**, 11795–11801.

16 H. Sugimura, A. Hozumi, T. Kameyama and O. Takai, *Surf. Interface Anal.*, 2002, **34**, 550–554.

17 H. . Fox and W. . Zisman, *J. Colloid Sci.*, 1952, **7**, 428–442.

18 S. Wu, *J. Adhes.*, 1973, **5**, 39–55.

19 D. Li and A. . Neumann, *J. Colloid Interface Sci.*, 1992, **148**, 190–

200.
20 D. K. Owens and R. C. Wendt, *J. Appl. Polym. Sci.*, 1969, **13**, 1741–1747.
21 S. Kobayashi, T. Nishikawa, T. Takenobu, S. Mori, T. Shimoda, T. Mitani, H. Shimotani, N. Yoshimoto, S. Ogawa and Y. Iwasa, *Nat. Mater.*, 2004, **3**, 317–322.
22 G.-Y. Jung, Z. Li, W. Wu, Y. Chen, D. L. Olynick, S.-Y. Wang, W. M. Tong and R. S. Williams, *Langmuir*, 2005, **21**, 1158–1161.
23 O. Zenasni, A. C. Jamison and T. R. Lee, *Soft Matter*, 2013, **9**, 6356.
24 A. Muthurasu and V. Ganesh, *J. Colloid Interface Sci.*, 2012, **374**, 241–249.
25 H. Hillebrandt and M. Tanaka, *J. Phys. Chem. B*, 2001, **105**, 4270–4276.
26 H. Einati, A. Mottel, A. Inberg and Y. Shacham-Diamand, *Electrochim. Acta*, 2009, **54**, 6063–6069.
27 S. A. Kulkarni and K. P. Vijayamohanan, *Surf. Sci.*, 2007, **601**, 2983–2993.
28 N. B. Colthup, L. H. Daly and S. E. Wiberley, in *Introduction to Infrared and Raman Spectroscopy*, Elsevier, 1990, pp. 1–73.
29 M. Mohammad Raei Nayini, S. Bastani and Z. Ranjbar, *Prog. Org. Coatings*, 2014, **77**, 1007–1014.
30 F. Milanesi, G. Cappelletti, R. Annunziata, C. L. Bianchi, D. Meroni and S. Ardizzone, *J. Phys. Chem. C*, 2010, **114**, 8287–8293.
31 D. Meroni, S. Ardizzone, G. Cappelletti, M. Ceotto, M. Ratti, R. Annunziata, M. Benaglia and L. Raimondi, *J. Phys. Chem. C*, 2011, **115**, 18649–18658.
32 G. Soliveri, R. Annunziata, S. Ardizzone, G. Cappelletti and D. Meroni, *J. Phys. Chem. C*, 2012, **116**, 26405–26413.
33 S. Huh, H.-T. Chen, J. W. Wiench, M. Pruski and V. S.-Y. Lin, *Angew. Chemie Int. Ed.*, 2005, **44**, 1826–1830.
34 D. Kovaček, Z. B. Maksić, S. Elbel and J. Kudnig, *J. Mol. Struct. THEOCHEM*, 1994, **304**, 247–254.
35 D. Barriet, *Curr. Opin. Colloid Interface Sci.*, 2003, **8**, 236–242.

This Chapter has been adapted with permission from Soliveri *et al.*, *J. Phys. Chem. C.*, 2015, **119**, 15390−15400.

L.R. contribution: part of the experimental work.

Chapter 11

Wetting modification by photocatalysis: A hands-on activity to demonstrate photoactivated reactions at semiconductor surfaces

Apart from the typical applications of TiO_2 photocatalysis already discussed in depth in the first part of this Thesis, *e.g.* fuels production, pollutant remediation and energy conversion[1,2], more recently, researchers have started to explore photocatalysis for the modification of surface properties, such as wetting phenomena[3]. This exciting research field has led to the development of materials with enticing surface properties, both superhydrophobic and superhydrophilic, which have found widespread application such as antifogging mirrors, self-cleaning ceramics, anti-stain fabrics, anti-corrosion coatings[4], liquid transportation and separation devices[4], but also new lithographic techniques for application in offset printing[5]. These materials have widespread potential application in everyday life and are based on clearly appreciable and immediate phenomena.

Interestingly, the application of photocatalysis to the tailoring of wetting phenomena is well suited to provide engaging activities for students of all levels, which can introduce the general concepts of photocatalysis in a more tangible and immediate/compelling way than conventional experiments such as pollutant degradation[6–9]. Moreover, very few works have proposed teaching laboratory activities on the modification of wetting properties of oxide materials by chemical[10–12] or physical[13] means. Physical chemistry courses for both Bachelor's and Master's students rarely deal with these concepts and few practical experiences that can provide basic knowledge by adopting easy experimental procedures are reported.

In this Chapter, a hands-on activity focusing on the modification of the TiO_2 surface properties by photocatalysis is reported. On one hand, the effect of light irradiation on the wetting properties of pristine TiO_2 surfaces is investigated for antifogging applications. On the other hand, the photocatalyst surface properties are modified by grafting with alkylsilanes and then patterned films with wetting contrast are prepared by photocatalytic lithography to obtain the site-selective adsorption of dye molecules.

This activity was tested by 33 students of the first year of the Master's degrees in Chemical Sciences and Industrial Chemistry during a teaching laboratory of the course 'Physical Chemistry of Disperse Systems and Interfaces' and can be adopted as a laboratory activity for both Master's courses in photochemistry and physical chemistry of colloids and interfaces. The activity was performed at mid-semester after an introductory lecture. Thanks to the procedure simplicity, inexpensive instrumentation and tangible results, this experience could be easily adapted to be suited for undergraduates or high-school students, as well as to demonstrations for science festivals.

11.1 Experimental Overview

The TiO_2 surface is hydrophilic since it exposes polar moieties such as hydroxyl groups, which can form strong interactions with water. By UV irradiation, the hydrophilicity of TiO_2 surfaces can be enhanced, leading to complete water spreading (*superhydrophilicity*). The origin of this phenomenon has been highly debated in the literature: among the possible explanations that have been proposed there are the photo-activated degradation of adsorbed contaminants, the light activated promotion of surface hydroxylation driven by the formation of surface Ti^{3+} centers[3] and the decrease of the surface tension of H_2O clusters followed by H_2O desorption from TiO_2 surfaces during UV irradiation; the latter was found to play a major role as the driving force behind the photo-driven phenomenon[14].

The surface hydroxylation of TiO_2 can be exploited to graft alkylsilane derivatives via the formation of Si–O–Ti bonds (Fig. 11.1), conferring hydrophobicity to the oxide surface[15]. By this approach, water contact

angles higher than 150° (*superhydrophobicity*) can be achieved when films made of TiO_2 micro/nanoparticles are functionalized with long-chain or perfluorinated alkylsilanes. The resulting superhydrophobic behavior is due to the combination of inherently hydrophobic alkyl/perfluorinated chains and of the surface roughness imparted by the TiO_2 micro/nanoparticles, according to the Cassie-Baxter model[16].

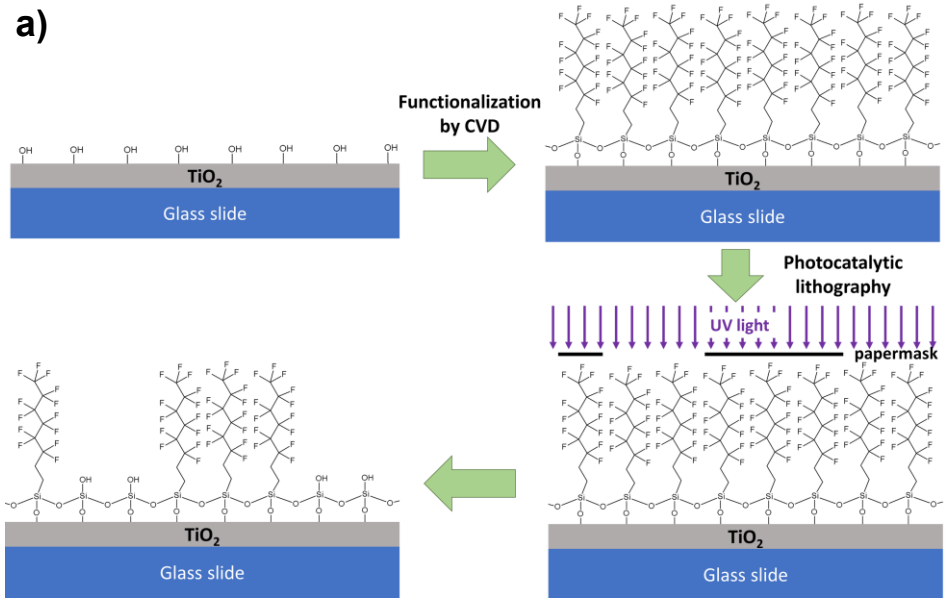

a) Schematic of the TiO_2 film functionalization and photocatalytic lithography.

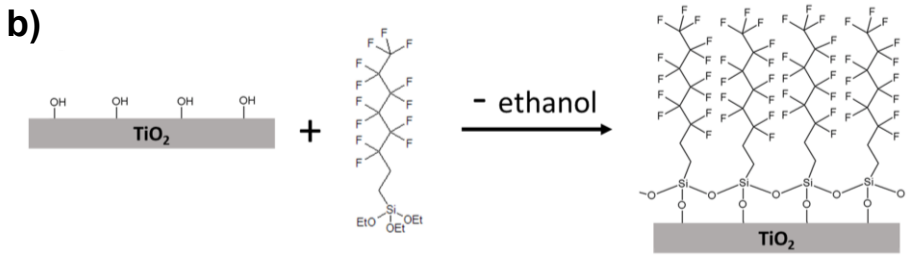

b) Reaction of TiO_2 films with PFOS.

Figure 11.1 – Functionalization and photocatalytic lithography processes.

Photocatalysis offers a tool to prepare patterned surfaces with superhydrophobic/superhydrophilic contrast[17–19]. By irradiating through a photomask a TiO_2 film functionalized with alkylsilanes (Fig. 11.1), the

alkyl chains can be degraded in the light-exposed areas, leading to superhydrophilic patches[20]. The film parts covered by the photomask are instead unaffected, retaining the superhydrophobic behavior. The resulting wetting contrast can then be revealed by pouring an aqueous solution onto the patterned surface.

11.2 Results and discussion

11.2.1 Students experience

The activity was performed in small groups and required 4 hours. The participants first deposited the TiO_2 films and functionalized two of them via chemical vapour deposition (CVD). During the time required by the CVD, students became familiar with contact angle measurements, performed antifogging tests on the pristine TiO_2 films, prepared the dye solution and designed their own photomasks. The activity showed excellent reproducibility among all the students' groups, who documented their results using photos and videos later implemented in a laboratory report.

11.2.2 Antifogging properties

Water contact angles were measured using a digital contact angle goniometer equipped with a software-controlled microsyringe. In case an instrument for contact angle measurements is not available, students can dispense the water droplets using micropipettes, then they can acquire the droplets images using a smartphone or a camera with a magnifying lens and determine the water contact angle between the surface and the tangent to the droplet profile, using a free goniometer software or app, such as BeforeOffice Snap.

Water contact angles of glass slides were 18°±2°, while those on pristine TiO_2 films before and after irradiation were 12°±2° and <5° (complete spreading), respectively (Fig. 11.2a, insets). Antifogging properties mirrored the observed differences in water contact angle. The bare glass surface got immediately covered in droplets upon steam exposure (Fig. 11.2a), impairing the glass transparency. In the case of non-irradiated TiO_2 films, fogging effects were still appreciable. Care must be taken to avoid accidental exposure of the TiO_2 films to direct sunlight or powerful lamps before the experiment to avoid inducing superhydrophilicity also in the

non-UV irradiated film. After irradiation under UV lamp, TiO_2 films showed instead excellent antifogging behavior (Fig. 11.2a): irradiated films retained their visual clarity upon steam exposure, as condensed water droplets immediately spread onto the TiO_2 surface creating a continuous water film.

11.2.3 Surface functionalization and photocatalytic lithography

TiO_2 films were functionalized by CVD using a perfluorinated alkylsilane, PFOS. The grafting mechanism involves the formation of silanol moieties from the reaction of PFOS with trace amount of water adsorbed onto the film surface; then silanols undergo condensation reaction with surface hydroxyls and with neighboring silanol molecules, giving rise to a grafted organic layer that imparts hydrophobic properties to the TiO_2 film. The observed contact angles were 160°±2°, characteristic of superhydrophobic materials and indicative of the formation of a Cassie-Baxter state. The measurement of such high contact angles can be complex, as water droplets tend to roll away before any measurements can be performed. In these cases, instead of dispensing a water droplet onto the solid surface using the syringe, the substrate should be lifted till it contacts the water droplet hanging from the syringe tip.

PFOS can be replaced by the less expensive non-fluorinated octyltriethoxysilane, although in this case the resulting contact angles might be lower[21].

The functionalized superhydrophobic films were patterned using the photocatalytic lithography technique. Several materials can be used for the photomask preparation (*e.g.*, paper, metals, …) if they are effective in shielding UV light. Students really enjoyed the creation of photomask from their own design (Fig. 11.2b). The wetting contrast can be revealed dripping water or a dye aqueous solution onto the film.

The lateral resolution of the technique can be investigated by using photomask grids with controlled spacing and revealing the wetting contrast using the steam condensation on the film surface and an optical microscope.

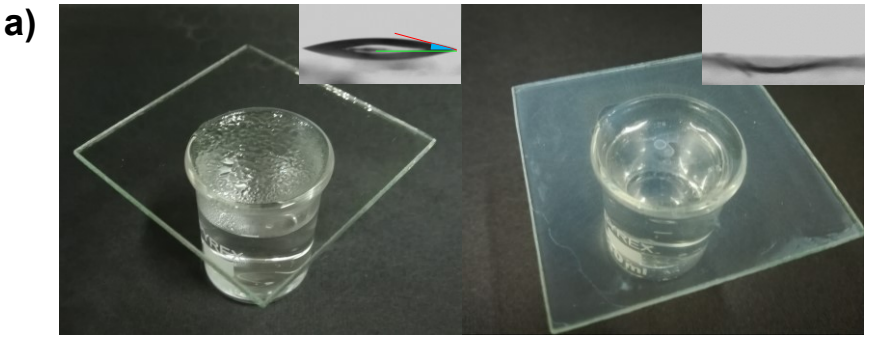

a) Fogging of a glass slide placed over a hot water beaker (left). Antifogging properties of a UV irradiated TiO_2 film (right). Insets: corresponding water contact angles; in the case of the irradiated TiO_2 film, no droplet profile can be appreciated due to the complete spreading of water.

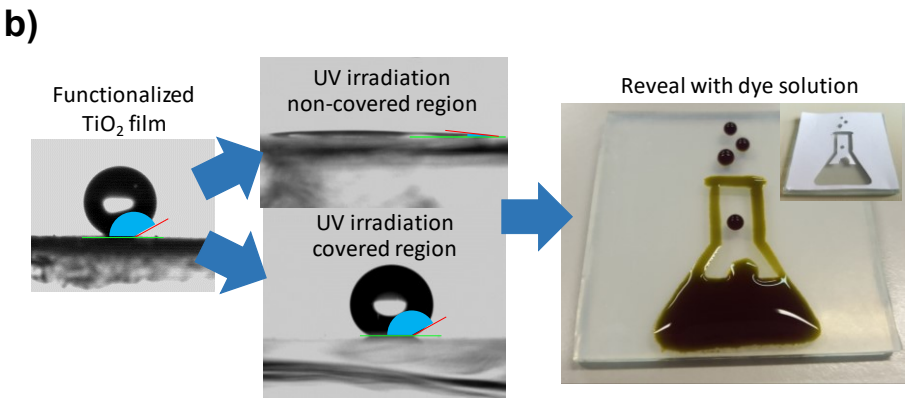

b) Water contact angles of the functionalized TiO_2 film before irradiation; difference between covered and non-covered regions of the film after irradiation using a photomask; a picture of the resulting patterned surface after revealing with a bromophenol blue solution (inset: photomask design).

Figure 11.2 – Antifogging and patterning properties.

11.2.4 Follow up assessment

At the end of the laboratory activity, students were asked to write a report, aimed at evaluating their learning level. Moreover, since the experience was part of a Master's degree course, the final exam included some questions pertaining the laboratory experience. Additionally, a survey was held to gather students' impressions: the overall reception was positive, scoring an average of 8.6/10, and all students were keen on recommending this activity to others. Generally, students were satisfied with the provided

theoretical explanations and the overall organization. In particular, some of them underlined that time schedules were respected and no hurdles were encountered; this may suggest the experience can be easily adapted for undergraduates as well. However, few students found the functionalization time too long: the dead times could be put to use by further explaining to the students the theory and applications of photocatalysis and superhydrophilic/superhydrophobic materials.

11.3 Conclusions

This hands-on activity displays photocatalysis potential to modify the wetting properties of TiO_2 films. Functionalization with alkylsilanes and UV irradiation were exploited to obtain superhydrophobic and superhydrophilic TiO_2-based films, respectively. The combination of the two treatments was also adopted to create patterned surfaces via photocatalytic lithography. The aim of the experience was to introduce students to photocatalysis basics and give them a grasp on surface science, mainly related to wetting phenomena. An engaging atmosphere was achieved by relating theoretical aspects and experimental work to everyday applications, thus improving the learning process, as demonstrated by the students' positive response.

11.4 Specific procedures

Samples preparation. Five glass slides (5 x 5 cm^2) are cleaned by sequentially sonicating in acetone, 2-propanol and water, then dried on a hot plate. A TiO_2 suspension in 2-propanol (0.5 g in 10 mL) is prepared by sonication. TiO_2 films are deposited by dispensing 2 mL of the TiO_2 suspension drop-wise on the glass slides, then spin coating adopting the following parameters: rotation time 20 s, rotation rate 3000 rpm and rotation acceleration/deceleration 500 rpm/s. After the deposition, the films are dried in an oven at 80°C for 5 min to remove any solvent residual. Alternatively, the TiO_2 films can be deposited by drop casting using a less concentrated TiO_2 slurry, although in that case a higher PFOS amount might be necessary for the functionalization.

Functionalization of TiO_2 films with perfluoroalkylsilane. The functionalization of TiO_2 films is carried out by CVD, according to a previously reported procedure[21]. Two of the TiO_2 films are placed on a Petri dish base together with a Teflon cup containing 250 μL of pure PFOS. The Petri dish is then covered with its lid to create a closed chamber, which is placed in an oven at 100°C for 2 h. The films are then removed from the oven and allowed to cool at room temperature before measuring their water contact angle.

Antifogging properties. One of the bare TiO_2 films is irradiated for 30 min under UV light, while the other is kept in the dark. The water contact angle of the two films is measured (using 5–10 μL droplets) and compared with that of the glass slides. Then, the antifogging properties of the irradiated and non-irradiated films are tested. The film fogging is promoted by placing the TiO_2 layers over a beaker filled with hot water.

Photocatalytic lithography. One of the functionalized TiO_2 films is covered with a photomask, prepared by cutting the desired pattern in a paper sheet. Then, the covered film is irradiated under UV light for 45 min. At the end of the irradiation step, the wetting contrast between the mask-covered areas (remained superhydrophobic) and the exposed regions (become superhydrophilic) is highlighted by depositing a dye aqueous solution (10 mg in 100 mL).

Further details about the preparation and characterization methods can be found in Appendix A.

References

1 X. Chen and S. S. Mao, *Chem. Rev.*, 2007, **107**, 2891–2959.

2 L. Rimoldi, D. Meroni, E. Falletta, A. M. Ferretti, A. Gervasini, G. Cappelletti and S. Ardizzone, *Appl. Surf. Sci.*, 2017, **424**, 198–205.

3 K. Liu, M. Cao, A. Fujishima and L. Jiang, *Chem. Rev.*, 2014, **114**, 10044–10094.

4 J. Drelich and A. Marmur, *Surf. Innov.*, 2014, **2**, 211–227.

5 K. Nakata and A. Fujishima, *J. Photochem. Photobiol. C Photochem. Rev.*, 2012, **13**, 169–189.

6 B. I. Stefanov, D. Lebrun, A. Mattsson, C. G. Granqvist and L. Österlund, *J. Chem. Educ.*, 2015, **92**, 678–682.

7 M. W. Pitcher, S. M. Emin and M. Valant, *J. Chem. Educ.*, 2012, **89**, 1439–1441.

8 S. Gravelle and B. Langham, *J. Chem. Educ.*, 2003, **80**, 911–913.

9 K. D. Giglio, D. B. Green and B. Hutchinson, *J. Chem. Educ.*, 1995, **72**, 352.

10 S. P. Flynn, M. McKenna, R. Monaghan, S. M. Kelleher, S. Daniels and A. MacCormac, *J. Chem. Educ.*, 2017, **94**, 221–225.

11 J. X. H. Wong and H.-Z. Yu, *J. Chem. Educ.*, 2013, **90**, 1203–1206.

12 C. L. Leverette, C. Wills, M. A. Perkins and S. A. Jacobs, *J. Chem. Educ.*, 2009, **86**, 719.

13 P. Kim, J. Alvarenga, J. Aizenberg and R. S. Sleeper, *J. Chem. Educ.*, 2013, **90**, 625–628.

14 M. Takeuchi, K. Sakamoto, G. Martra, S. Coluccia and M. Anpo, *J. Phys. Chem. B*, 2005, **109**, 15422–15428.

15 D. Meroni, L. Lo Presti, G. Di Liberto, M. Ceotto, R. G. Acres, K. C. Prince, R. Bellani, G. Soliveri and S. Ardizzone, *J. Phys. Chem. C*, 2017, **121**, 430–440.

16 A. B. D. Cassie and S. Baxter, *Trans. Faraday Soc.*, 1944, **40**, 546.

17 A. Fujishima, X. Zhang and D. Tryk, *Surf. Sci. Rep.*, 2008, **63**, 515–582.

18 Y. Paz, *Beilstein J. Nanotechnol.*, 2011, **2**, 845–61.

19 Y. Paz, *Comptes Rendus Chim.*, 2006, **9**, 774–787.

20 G. Soliveri, R. Annunziata, S. Ardizzone, G. Cappelletti and D. Meroni, *J. Phys. Chem. C*, 2012, **116**, 26405–26413.

21 G. Soliveri, V. Pifferi, R. Annunziata, L. Rimoldi, V. Aina, G. Cerrato, L. Falciola, G. Cappelletti and D. Meroni, *J. Phys. Chem. C*, 2015, **119**, 15390–15400.

This Chapter has been adapted with permission from Rimoldi *et al.*, *J. Chem. Educ.*, 2018, **95**, 2216–2221. Copyright 2018 American Chemical Society.

Part III
Oxide-based materials for energy conversion application

Part III – Introduction

The progressive depletion of the more adopted and conventional energy sources drives the mankind, and especially researchers, towards the search of new, viable and efficient energy sources[1]. Renewable energy sources may have a great impact to face the global climate change, not only by reducing the spreading of large amounts of CO_2 and other gases, but also by exploiting clean and inexhaustible energy sources and natural waste[1].

In this regard, two of the most massive renewable energy sources are biomass and solar light.

The word *biomass* is usually referred to the biodegradable fraction of product, waste and residues with biological origin coming from agricultural and connected activities and from urban and industrial waste. In the last years, it has been exploited as a source to produce fuels, properly referred as *biofuels*[2–4]. Nonetheless, biomass and even more lignocellulosic biomass, *i.e.* the most abundant raw material on Earth with vegetal origin, are mostly natural polymeric complex matrices which need to be not only converted but also successively upgraded for their usability as fuels.

Solar light, instead, is useful for different purposes connected with energetic applications, from hydrogen production to photovoltaics and thermal energy[5–8]. In this sense, materials and devices are being studied for increase the light harvesting and the capability to convert solar energy[9,10].

In this respect, nanostructured oxides are largely adopted either as substrates or catalytically active species for developing efficient catalysts. In this context, as most of the typical heterogeneous catalysis reaction, SiO_2, Al_2O_3 and ZrO_2 are widely used[11,12]. However, the optimization of the catalyst characteristics is still a challenging research topic for scientists involved in heterogeneous catalysis, also in the case of lignocellulosic biomass conversion and bio-oil (the main conversion product of lignocellulose) upgrading[13,14].

In the case, instead, of the solar light conversion for energetic applications, in the last few years small band gap semiconductors have

attracted much attention not only as photocatalysts, but also as photoelectrocatalysts[15–18]. Small band gap semiconductors are often ternary metal oxides, which can be adopted as photoanodes, in electrocatalytic devices. However, the difficulty of obtaining ternary oxides with high purity by simple preparation techniques, as well as the variety of structural forms usually characteristics of these materials and the need to enhance the processes efficiency, push the researchers towards new synthetic approaches and materials.

In this part of the Thesis, firstly nanostructured oxides were employed as substrates for developing Ni-based catalysts for guaiacol (a model molecule for lignin, one of the fraction of lignocellulosic biomass) hydrodeoxygenation and for developing heterostructures with application as photoanodes. The former work takes place in the context of the need of upgrading bio-oils for bio-fuels production[3,19,20], while in the latter a recently discovered material[9,21,22], copper vanadate, a small band gap ternary oxide, was employed for photoelectrochemical application together with tungsten oxide to obtain heterostructures with superior activity.

References

1 N. L. Panwar, S. C. Kaushik and S. Kothari, *Renew. Sustain. Energy Rev.*, 2011, **15**, 1513–1524.

2 A. Corma, S. Iborra and A. Velty, *Chem. Rev.*, 2007, **107**, 2411–2502.

3 M. V. Bykova, D. Y. Ermakov, V. V. Kaichev, O. A. Bulavchenko, A. A. Saraev, M. Y. Lebedev and V. A. Yakovlev, *Appl. Catal. B Environ.*, 2012, **113**–**114**, 296–307.

4 A. Demirbas, *Prog. Energy Combust. Sci.*, 2007, **33**, 1–18.

5 Q. Yan, J. Yu, S. K. Suram, L. Zhou, A. Shinde, P. F. Newhouse, W. Chen, G. Li, K. A. Persson, J. M. Gregoire and J. B. Neaton, *Proc. Natl. Acad. Sci.*, 2017, **114**, 3040–3043.

6 X. Shi, I. Y. Choi, K. Zhang, J. Kwon, D. Y. Kim, J. K. Lee, S. H. Oh, J. K. Kim and J. H. Park, *Nat. Commun.*, 2014, **5**, 4775.

7 K. Wojciechowski, S. D. Stranks, A. Abate, G. Sadoughi, A. Sadhanala, N. Kopidakis, G. Rumbles, C. Z. Li, R. H. Friend, A. K. Y. Jen and H. J. Snaith, *ACS Nano*, 2014, **8**, 12701–12709.

8 D. Kraemer, B. Poudel, H. P. Feng, J. C. Caylor, B. Yu, X. Yan, Y. Ma, X. Wang, D. Wang, A. Muto, K. McEnaney, M. Chiesa, Z. Ren and G. Chen, *Nat. Mater.*, 2011, **10**, 532–538.

9 C. Gadiyar, M. Strach, P. Schouwink, A. Loiudice and R. Buonsanti, *Chem. Sci.*, 2018, **9**, 5658–5665.

10 A. Loiudice, J. Ma, W. S. Drisdell, T. M. Mattox, J. K. Cooper, T. Thao, C. Giannini, J. Yano, L. W. Wang, I. D. Sharp and R. Buonsanti, *Adv. Mater.*, 2015, **27**, 6733–6740.

11 P. M. Mortensen, J.-D. Grunwaldt, P. A. Jensen and A. D. Jensen, *ACS Catal.*, 2013, **3**, 1774–1785.

12 S.-K. Wu, P.-C. Lai, Y.-C. Lin, H.-P. Wan, H.-T. Lee and Y.-H. Chang, *ACS Sustain. Chem. Eng.*, 2013, **1**, 349–358.

13 A. M. Robinson, J. E. Hensley and J. W. Medlin, *ACS Catal.*, 2016, **6**, 5026–5043.

14 C. Larabi, A. Garron, P. Rouge, K. C. Szeto, S. Norsic, A. De Mallmann, N. Merle and M. Taoufik, *ChemCatChem*, 2017, **9**, 2160–2166.

15 A. Murphy, P. Barnes, L. Randeniya, I. Plumb, I. Grey, M. Horne

and J. Glasscock, *Int. J. Hydrogen Energy*, 2006, **31**, 1999–2017.

16 J. Su, L. Guo, N. Bao and C. A. Grimes, *Nano Lett.*, 2011, **11**, 1928–1933.

17 C.-M. Jiang, M. Farmand, C. H. Wu, Y.-S. Liu, J. Guo, W. S. Drisdell, J. K. Cooper and I. D. Sharp, *Chem. Mater.*, 2017, **29**, 3334–3345.

18 N. Serpone and A. V. Emeline, *J. Phys. Chem. Lett.*, 2012, **3**, 673–677.

19 Y. Yang, C. Ochoa-Hernández, V. A. de la Peña O'Shea, P. Pizarro, J. M. Coronado and D. P. Serrano, *Appl. Catal. B Environ.*, 2014, **145**, 91–100.

20 N. Arun, R. V. Sharma and A. K. Dalai, *Renew. Sustain. Energy Rev.*, 2015, **48**, 240–255.

21 M. Ghiyasiyan-Arani, M. Masjedi-Arani and M. Salavati-Niasari, *J. Mater. Sci. Mater. Electron.*, 2016, **27**, 4871–4878.

22 P. F. Newhouse, D. A. Boyd, A. Shinde, D. Guevarra, L. Zhou, E. Soedarmadji, G. Li, J. B. Neaton and J. M. Gregoire, *J. Mater. Chem. A*, 2016, **4**, 7483–7494.

Chapter 12

Guaiacol hydrodeoxygenation as a model for lignin upgrading. Role of the support surface features on Ni-based alumina-silica catalysts

In the last decades, the progressive depletion of fossil fuels, together with environmental concerns related to global warming, have prompted the search for sustainable and renewable energy sources, such as biomass[1–3]. Lignocellulosic biomass is the most abundant and renewable biomass on our planet and it represents an excellent feedstock for conversion to fuels, also because its use does not compete with food sources being mainly the result of agricultural wastes[4–6]. Lignocellulosic biomass is composed by hemicellulose, cellulose and lignin and it can be adopted to produce compounds of great interest in the field of renewable energy: bio-oils. Bio-oils are directly produced from biomass by fast pyrolysis transformation, but they are unfortunately characterized by a large amount of oxygen-containing compounds which are responsible for their high viscosity, instability and tendency to polymerization[7]. Therefore, sustainable processes to obtain liquid fuels from biomass require the transformation of compounds with high oxygen content into hydrocarbons[8]. Two main treatments may be carried out for bio-oils upgrading: cracking or hydrodeoxygenation (HDO) reactions[9,10]. Since cracking processes usually produce high amounts of undesired coke[9,10], in the last few years HDO reactions have attracted much attention as more efficient and sustainable processes offering a suitable means to convert oxygen-rich bio-oils to hydrocarbons and other compounds of interest[7,11–13].

With respect to the widely-investigated cellulose-derived components of bio-oils, the lignin-derived components have received less attention. In

this respect, lignin, a three-dimensional amorphous and highly cross-linked polymer which constitutes around 30% of lignocellulosic biomass, is more attractive than the carbohydrates fraction due to its lower oxygen to carbon ratio. In order to mimic the catalytic behaviour of lignin, guaiacol is generally adopted as a model molecule, thanks to the presence of both phenol and methoxy groups, typical lignin chemical bonds[5,14,15].

In recent years, the attention of researchers has been focused on the development of efficient catalysts for the hydrodeoxygenation of guaiacol and other model compounds[15–18]. The need to avoid sulphide-based catalysts suffering from rapid deactivation, the adoption of cheaper reaction promoters with respect to noble metals, the use of bimetallic catalysts and the research of the best catalytic supports stand nowadays as tools of primary importance in the field of HDO reactions[5,16,19]. While nickel is now widely recognized as an efficient and low cost active element in the HDO of guaiacol and similar compounds, the role played by the catalyst support on the HDO activity has been less studied. However, the physicochemical features of the catalytic support are crucial for obtaining high guaiacol conversion and suitable selectivity.

In this regard, a wide range of materials has been reported as catalyst supports for HDO reactions, including γ-Al_2O_3, mesoporous SiO_2, ZrO_2, zeolites, TiO_2 and activated carbons. Several works compared the performance of catalysts prepared by adopting substrates of different chemical nature[20–23]. As a general trend, moderate acidic materials seem to be more efficient supports in the case of HDO reactions on lignin model compounds[16,24,25]. However, owing to the high variability of the substrate features (*e.g.* crystal structure, composition, morphology, surface features, …), it is often difficult to distinguish the influence provided by each physicochemical parameter on the final performance. Very recently, the work by Sankaranarayanan *et al.* in which the increase of the total acidity of zeolites is reported to promote the HDO reaction during bio-oils upgrading[26]. Further, Yang *et al.* recommended the study of catalyst surface features in terms isoelectric point as a crucial parameter in this kind of reactions[20]. However, works reporting this kind of analysis are scarce.

In the work presented in this Chapter, Al_2O_3-SiO_2 supports adopted for the preparation of Ni-promoted and copromoted catalysts for guaiacol

HDO were studied. The effect of the support morphology and surface features was investigated by tuning the support composition (silica content) in a wide range of metal loadings. The role of a thermal pretreatment of the oxide support was also investigated on the best performing substrates. The synthesized materials were characterized for their bulk and surface properties and their efficiency, selectivity and regeneration for guaiacol HDO were compared. To the best of our knowledge, for the first time the influence of the support isoelectric point and of the SiO_2/Al_2O_3 support composition ratio was studied for HDO reactions.

12.1 Results and discussion

12.1.1 Catalytic supports

Commercial alumina-silica powders were used as support for the active metal catalysts as they allowed us to easily tune both the morphology and surface acidity of the substrate, as previously reported in the case of the dimerization of isobutene[27].

The physicochemical features of the bare substrates, after thermal pretreatment, were firstly investigated. Structurally, the phase composition of the samples could be identified as θ-Al_2O_3[28,29], which become less crystalline by the progressive increase of the silica amorphous component. In the case of the thermally untreated support (AlSi40*), the phase composition is that of an alumina oxohydroxide (AlOOH, bohemite) promoted with 40% amorphous silica.

N_2 adsorption-desorption isotherms collected under subcritical conditions (Fig. 12.1) exhibit profiles typical of mesoporous materials for all substrates[30]. The samples exhibited different surface areas as showed by the position of the isotherm knee. In this respect, increasing the SiO_2 content leads to a progressive increase in the specific surface area (Fig. 12.1a,b), from 103 $m^2\ g^{-1}$ for pure alumina to 511 $m^2\ g^{-1}$ for the sample with 40% silica. Fig. 1a shows a H2 hysteresis loop, according to the IUPAC classification, for the AlSi0 sample, suggesting the presence of bottleneck-shaped pores. Differently, the hysteresis loop of the other substrates may be classified as H1 or H3 type, usually referred to as cylindrical or slit-shaped pores. The total pore volume shows a progressive

increase with the silica content (Fig. 12.1a), a decrease of the average pore size and broader pore size distributions.

The effect of the thermal pretreatment at 550°C on the morphological features was investigated on the AlSi40 sample, showing negligible modifications. In this respect, the isotherm and the pore size distribution of the un-pretreated support (AlSi40*), show features fully comparable to those of the corresponding calcined support, with a slightly larger surface area.

The studied alumina-silica systems were submitted to microelectrophoretic determinations in order to study their electrification features and determine the isoelectric point (iep), *i.e.* the pH value at which the ζ-potential is zero (Fig. 12.1c). Both the effect of the SiO_2 content and of the thermal pretreatment were investigated. The pure alumina substrate exhibited the most basic isoelectric point (iep = 8.6), in agreement with the reported values for different alumina oxides[31,32]. A marked effect is introduced by the SiO_2 presence: in the case of the 5% and 10% SiO_2 supports a lowering of the iep of about one pH unit (iep = 7.3 – 7.5) was recorded, with no significant differences between the two samples. By increasing the SiO_2 amount to 40%, the iep sharply shifted in the acidic direction up to pH 4.8, as expected on the grounds of the strongly acidic iep values of amorphous silica[31,32]. The un-pretreated AlSi40* sample was also analysed, revealing an even more acidic iep (about 4.3). The latter two curves show also, beside a lower iep, less steep ζ-potential curves that reflect a lower density of dissociated sites or an internal charge imbalance between the two oxides.

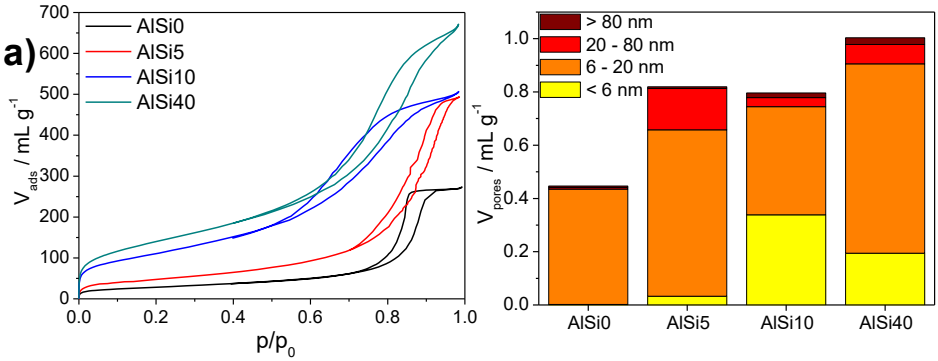

a) N_2 adsorption-desorption isotherms (left) and pore size distributions (right) of the studied catalytic supports.

b)

support	specific surface area (m^2 g^{-1})				
	Ni0	**Ni5**	**Ni15**	**Ni30**	**Ni45**
AlSi0	103	103	96		
AlSi5	169	191	172		
AlSi10	400	361	297		
AlSi40	511		350	342	225
AlSi40*	532			349	205
support	**total pore volume (mL g^{-1})**				
	Ni0	**Ni5**	**Ni15**	**Ni30**	**Ni45**
AlSi0	0.447	0.419	0.338		
AlSi5	0.820	0.760	0.621		
AlSi10	0.796	0.706	0.534		
AlSi40	1.003		0.764	0.657	0.384
AlSi40*	0.959			0.614	0.395

b) Specific surface area and total pore volume of the bare and Ni-modified alumina-silica systems.

c)

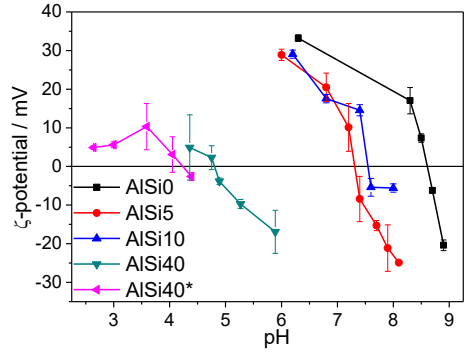

c) ζ-potential curves as a function of pH for the determination of the iep of the different supports.

d)

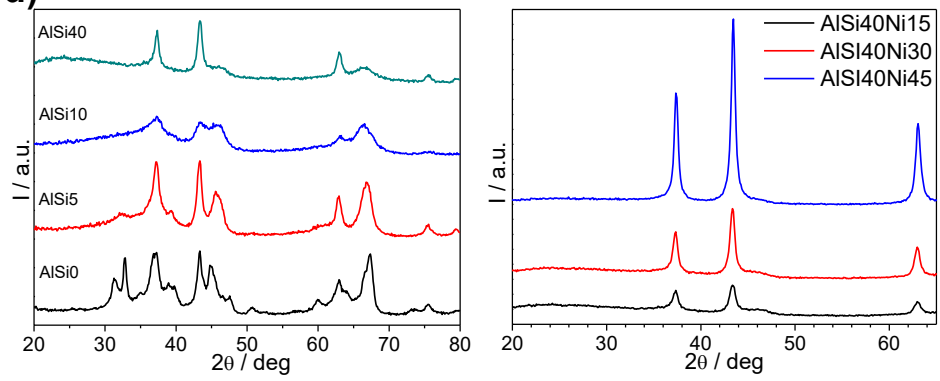

d) XRPD patterns of the different supports modified with 15% Ni (left) and of AlSi40 support loaded with different Ni amounts (right).

Figure 12.1 – Morphological, surface and structural characterization results.

12.1.2 Physicochemical characterization of the catalysts

The alumina-silica supports were then loaded with variable amounts of Ni species, upon impregnation and subsequent thermal treatment in oxidizing conditions.

ICP measurements revealed Ni contents comparable to the nominal amounts adopted in the impregnation treatment. Ni loading generally leads to a progressive decrease of both the specific surface area and the total pore volume with respect to bare supports (Fig. 12.1b), which might suggest the partial filling of the substrate pores by Ni species.

Figure 12.1d compares the XRPD patterns of catalysts loaded with 15% Ni. Peaks at 37°, 43°, 63°, and 76° can be identified as NiO-bunsenite (cubic crystalline lattice; space group: *Fm3m*) diffraction peaks. The different supports exhibited variable degrees of crystallinity. The typical XRPD pattern of θ-Al_2O_3 (monoclinic crystalline lattice; space group: *C2/m*) can be recognized in the case of AlSi0Ni15, which showed high crystallinity. The amorphous character of the support progressively increased by increasing the SiO_2 content. Nonetheless, no diffraction peaks besides those typical of θ-Al_2O_3 and bunsenite were detected, thus excluding phase transitions or the presence of other alumina polymorphs. AlSi40Ni15 exhibits almost totally amorphous structure, as a result of the high SiO_2 content. At higher Ni content, the peaks corresponding to bunsenite become both sharper and more intense (Fig. 12.1d). This suggests not only a higher Ni content but also that NiO crystallites become bigger when the Ni loading is increased. The Scherrer equation was applied to the (200) peak of NiO at 43° (which does not fully overlap with the θ-Al_2O_3 peaks) in order to calculate the crystallite average dimension as a function of the Ni content: the AlSi40Ni15 sample has an average NiO crystallite size of 10 nm, while the diameter increases to 18 nm for the 30% Ni loading and further to 22 nm in the case of AlSi40Ni45 (Fig. 12.1d).

SEM images (Fig. 12.2a) show that nickel species form nanometric domains at the surface of the micrometric supports. At variance with samples at lower Ni contents, in the case of samples with 45% Ni a homogeneous catalyst coating is appreciable at the surface of the oxide particles. Interestingly, a marked effect of the thermal pretreatment on the size distribution of the support particles is apparent: with respect to the

pretreated sample, AlSi40Ni45* shows a much broader particle size distribution.

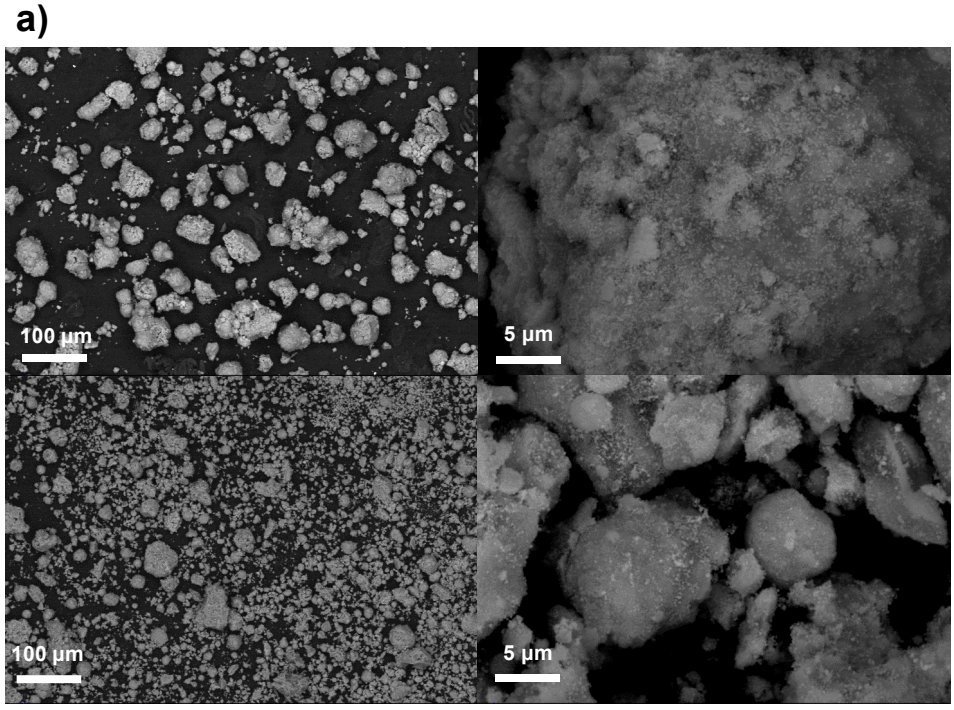

a) SEM images of SiAl40Ni45 (top) and SiAl40Ni45* (bottom) samples at different magnifications.

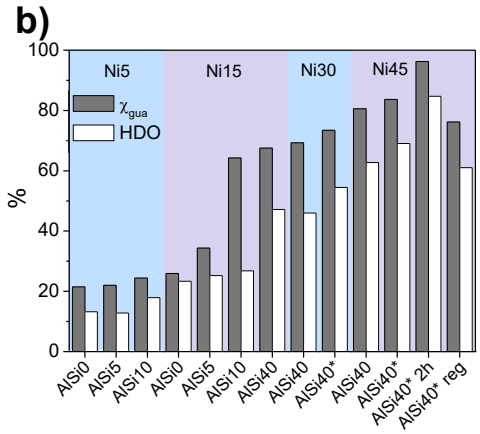

b) Guaiacol conversion and HDO degree of the tested samples.

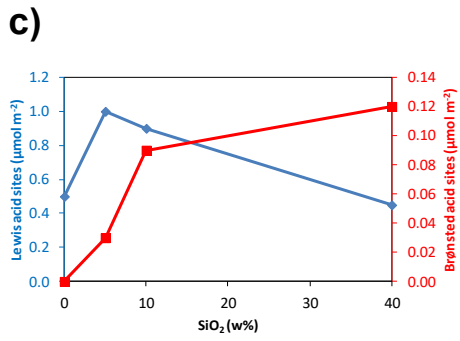

c) Brønsted and Lewis acid site content, obtained from pyridine adsorption/desorption experiments, in silica/alumina samples of the PURALOX/SIRALOX family (redrawn from Sasol technical sheet).

Figure 12.2 – SEM images, catalytic results and acidic features of the supports.

12.1.3 Catalytic activity

The synthesized catalysts were activated in H_2 at the reaction conditions (300°C, 50 bar), right before the catalytic reaction.

Figure 12.2b reports the guaiacol conversion and the hydrodeoxygenation degree (HDO) at one hour reaction time (unless for the case of sample AlSi40Ni45* 2h) for samples with 5% Ni content or higher. Bare supports gave rise to less than 8% guaiacol conversion and 7% HDO.

Figure 12.2b shows a marked role played by the nickel amount on the catalysts performance. The larger the Ni amount, the larger is the conversion and also the HDO degree. Accordingly, the increasing Ni amount leads to an increasingly homogeneous coverage of the oxide support. A beneficial role played by nickel on the guaiacol hydrodeoxygenation is widely recognized in the literature[7,10,14,33]. Less reported instead is the role played by the catalyst support features. By comparing the activity of the 15% Ni catalysts, the conversion follows the sequence: AlSi0Ni15 < AlSi5Ni15 < AlSi10Ni15 < AlSi40Ni15. The amount of silica in the support appears to definitely promote the reaction. This effect can be related to the progressive increase in surface area of the catalysts, but also to the variation in the acid properties of the support, which also benefits the HDO. The latter phenomenon can be best appreciated by comparing the activities of AlSi10Ni15 and AlSi40Ni15. In this case, the conversion is comparable (64 and 68%) since the surface areas (297 and 350 m^2g^{-1}) are similar and both samples have the same Ni content; the HDO instead is much larger in the case of AlSi40Ni15 (almost twice than that of AlSi10Ni15), due to the higher acidity of AlSi40.

Increasing the silica content in alumina-silica samples by Sasol gives rise to a progressive increase of the Brønsted acidity and a parallel loss of Lewis sites (Fig. 12.2c), as also reported in a previous literature study concerning a different catalytic reaction[27]. The present HDO reaction appears therefore to be promoted by the Brønsted acidity of the catalytic support.

The same phenomenon can explain the differences observed between the two samples with 30% and 45% Ni content respectively obtained with calcined and uncalcined supports. In both cases, the un-calcined samples

present a better performance with respect to the analogous calcined sample, from both the guaiacol conversion and the HDO degree point of view. In the case of 30% Ni samples, the guaiacol conversion slightly increases from 69 to 73% passing from the calcined to the uncalcined more acidic support. Similarly, an increase by 8% (from 46 to 54%) was measured for the HDO degree, suggesting an even more beneficial effect on the hydrodeoxygenation process. In the case of 45% Ni samples, the guaiacol conversion and above all the HDO are higher for the uncalcined support, achieving 84% conversion and 69% HDO for AlSi40Ni45*. It is well known that by thermal treatment a promotion of the Lewis surface sites occurs with a parallel loss of Brønsted sites[34]. Consistently, ζ-potential measurements show a further shift of the iep in the acid direction for the uncalcined support (AlSi40*).

Concerning the composition in liquid by-products of the reaction, in all cases naphtenics (cyclohexane), aromatics (benzene, xylene, anisol), phenols (phenol, cresols) and methyl-guaiacol were detected by gas chromatography analyses. Only trace amounts of aliphatic alcohols (cyclohexanol) were detected only in the case of AlSi0Ni15 and AlSi40Ni45*. Guaiacol HDO reaction may proceed through two different mechanisms, the former involving the cleavage of $C_{aromatic}$–O bonds (hydrogenolysis route) and the latter the hydrogenation of aromatic bonds (hydrogenation route)[10,24]. In our case, the adopted catalysts produced most of all aromatics compounds with a lower oxygenation degree with respect to guaiacol (Fig. 12.3a). The aromaticity conservation upon guaiacol HDO is often regarded as an important aspect to produce high-value fuels[20,35]. Samples with 30% or less Ni amount exhibited a relevant fraction of methyl-guaiacol (Fig. 12.3a). At low Ni content, the nature of the main intermediates suggests a low reaction kinetics, since methyl-guaiacol production from guaiacol is an early stage of the reaction due to transmethylation reactions, *i.e.* the direct attack of a $CH_3^{\bullet}$ radical in a non-substituted position of the target molecule (guaiacol) aromatic ring[36]. Moreover, for all samples loaded with 15 or 30% Ni, phenols, which are a result of the loss of the metoxy group from guaiacol, are the second more abundant class of intermediates. On the other hand, phenols are the main class of compounds for the samples with the highest Ni amount, which also show a dramatic decrease of the methyl-guaiacol content (Fig. 12.3a).

Several studies have reported phenol to be either the main product or one of the more common intermediate in the case of guaiacol hydrodeoxygenation[37–40]. These results, together with the appreciable increase of the aromatics and naphtenics fractions for these catalysts with respect to the lesser loaded ones, are at the basis of the increased performance in terms of HDO for these samples.

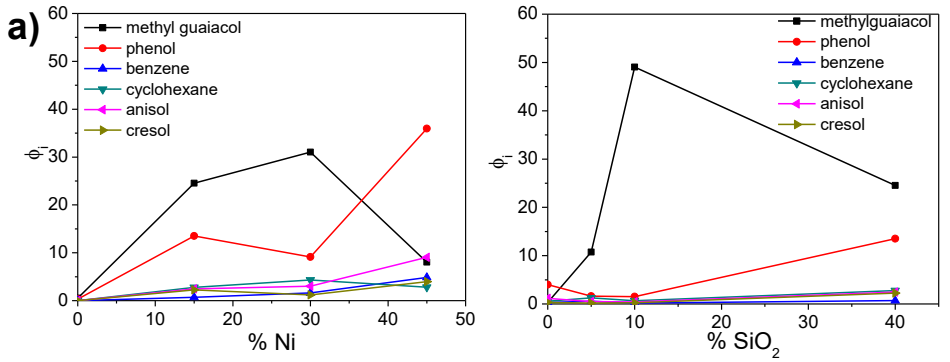

a) Main liquid products at 1 h reaction time for AlSi40 samples as a function of Ni content (left) and for samples with 15% Ni as a function of the SiO_2 content (right).

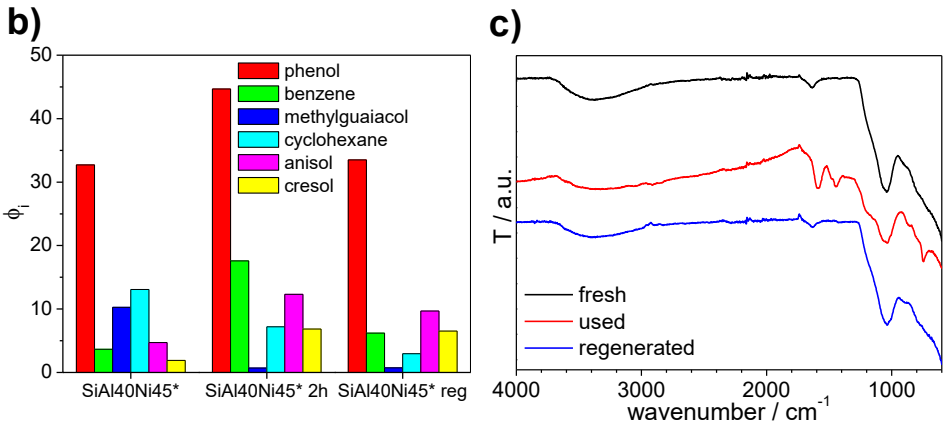

b) Product distribution for sample AlSi40Ni45*: pristine, 1 h reaction time; pristine, 2 h reaction time; regenerated, 1 h reaction time.

c) FTIR spectra of the fresh, used and regenerated AlSi40Ni45 catalyst.

Figure 12.3 – Further catalytic and spectroscopic results.

The most performing sample (AlSi40Ni45*) was tested in prolonged reaction time (2h) conditions. This test permitted to get information about the reaction proceeding and the results are presented in Fig. 12.2b. Both the conversion and the HDO degree significantly increased with respect to the

test conducted for 1 h, reaching 96% and 85%, respectively. The proceeding of the reaction is also testified by the much lower amount of methylguaiacol (the earliest stage by-product) detected at the end of the 2 h test (Fig. 12.3b). Conversely, all the other aromatic compounds increase, especially benzene (totally deoxygenated compound with conserved aromacity) at the expense most of all of cyclohexane.

12.1.4 Regeneration tests

With the aim to assess the reusability of the catalysts, a possible route to restore the initial surface properties of the used catalyst was investigated. Selected sample were withdrawn from the reactor by filtration at the end of the catalytic process and the powder was submitted to a thermal treatment at 400°C for 2 h under oxygen stream in order to regenerate it. Figure 12.3c reports, as a representative example, the FTIR spectra of the AlSi40Ni45 as prepared (fresh), at the end of the catalytic reaction (used) and after regeneration (regenerated). The comparison of the FTIR spectra before and after the regeneration procedure shows that the thermal treatment fully restores the pristine surface state of the catalyst. In all spectra, a broad peak centered at 3400 cm^{-1} was detected, referring to the presence of –OH groups at the surface of alumina and silica. The similar intensity of those peaks among the samples suggest no variations in the amount of –OH groups upon the catalytic reaction and the regeneration treatment. The fresh and regenerated sample revealed the presence of a peak at 1635 cm^{-1} identified as bending modes of H_2O adsorbed onto the oxide surface[41]. In the case of the used catalyst, this peak is partially covered, appearing as a shoulder of the peak at 1590 cm^{-1}, attributable to the stretching of C=C aromatic bonds[42]. Other peaks related to organic compounds can be appreciated, such as the band at 1448 cm^{-1}, present only in the used catalyst spectrum, which may be related to bending modes of C=C or $–CH_2–$ groups. These characteristic bands can be referred to the presence of phenol, anisol, methyl-guaiacol and guaiacol itself adsorbed onto the catalyst surface. The broad band covering the 1000 – 1300 cm^{-1} region in all spectra refers to Si–O–Si bonds of the support[41]. In the case of the used catalysts, this band is characterized by the presence of a shoulder at about 1205 cm^{-1}, which was attributed to C–O phenolic bonds[42]. The peak at 747 cm^{-1} in the spectrum of the used catalyst is due to –CH– sp^2 moieties,

typical of phenols. The disappearance of peaks referring to organic moieties in the spectrum of the regenerated sample stands for a complete removal of the reaction products from the catalyst surface upon combustion by thermal treatment at 400°C under O_2 flux. CHNS measurements allowed the amount of carbon to be measured for the fresh, used and restored catalyst. The used catalysts had a carbon amount of about 30% while both the fresh and the restored catalysts were characterized by a presence of carbon lower than 0.5%.

Figure 12.2b reports the results in terms of conversion and product distribution of the regenerated AlSi40Ni45* sample. Both the conversion and the HDO degree are slightly lower than the parent fresh oxide. It is noteworthy that both parameters of the regenerated sample are comparable within experimental error to the case of AlSi40Ni45. Moreover, also for the regenerated sample phenol is the most abundant product in Figure 12.3b. The catalytic performance of the regenerated catalyst can be traced back to the morphological modifications apparent from SEM images (Fig. 12.4). As appreciable from Figure 12.4, Ni species in both the used and regenerated catalysts appear to be less homogeneously distributed at the surface of the support than for the fresh catalyst (Fig. 12.2a). It is noteworthy that the total Ni amount was not affected by the reaction conditions (Ni/Al molar ratio from ICP analyses: 3.69 and 3.64 for the fresh and regenerated samples, respectively). Furthermore, Figure 12.4 shows the predominance of larger aggregates with respect to the fresh sample (Fig. 12.2a), much more similar to the case of the pretreated sample (AlSi40Ni45). These effects can be related to the drastic reaction conditions (300°C, 50 bar) as well as to the loss of finer particles as a result of the procedure of the sample recovery from at the end of the reaction.

12.1.5 Catalyst copromotion

The possible further promotion of these samples by the addition of a second metal species was tested by preparing a representative Ni,W modified sample. The development of catalysts promoted by two different metallic species, often referred as *promoter* and *co-promoter*, holds great promise for HDO reactions[24,43]. Numerous transition metals have been reported as co-promoters together with Ni for bio-oils upgrading catalysts. Apart from cobalt and molybdenum, which were studied in depth, other elements can

play an important role. Among these, tungsten has been proposed both as a good catalyst in its oxide or carbide forms[44] and as a promising co-promoter of Ni-based catalysts[24]. However, Ni-W copromoted materials have attracted less attention to date, more so for guaiacol HDO.

An explorative test was conducted on the most promising substrate (AlSi40*) for the co-modification by Ni and W. In order not to modify the substantial reaction route, the amount of Ni was kept constant to the maximum loading amount and 1.5% W was added in the impregnating solution. The effect of the co-loading of W and Ni onto the support is favorable: despite the slightly lower specific surface area (191 m^2 g^{-1}), the conversion increases from 84% (AlSi40Ni45*) to 91% (AlSi40Ni45W1.5*), while the HDO degree remains almost invariant (69 to 71%). Regarding liquid product distribution, again the picture with respect to the sole Ni-loaded catalysts is comparable, with the Ni,W-loaded sample showing a slightly lower amount of methyl-guaiacol and of naphtenics. The co-promotion of alumina-silica supports with Ni and a lower amount of W seems thus a promising strategy for the development of guaiacol HDO catalysts.

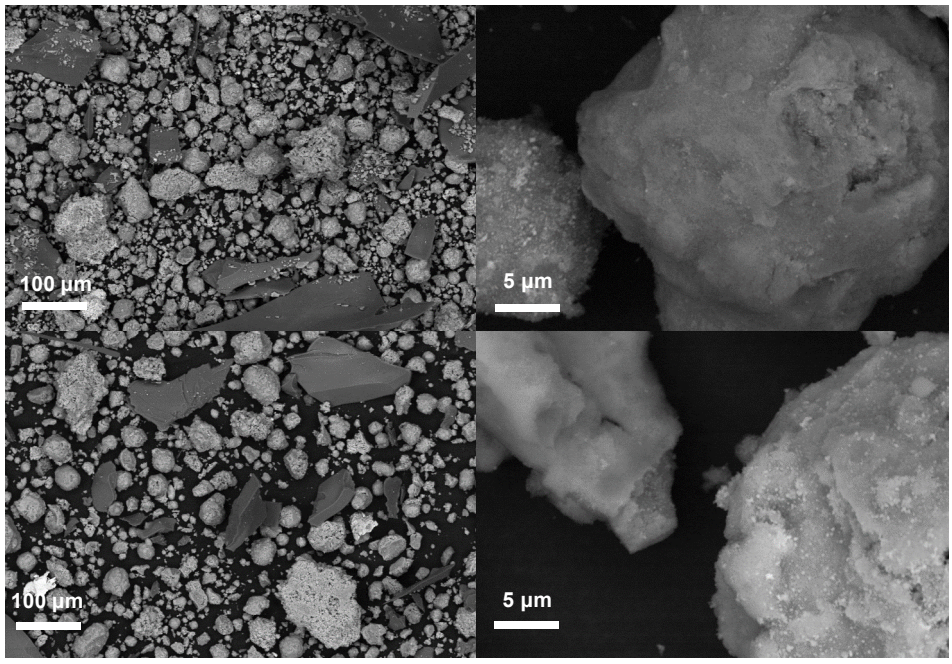

Figure 12.4 – SEM images of the spent (top) and the regenerated (bottom) AlSi40Ni45* sample. Broken glass species are appreciable in the low magnification images, due to the procedure adopted for the reaction.

12.2 Conclusions

In this study, the hydrodeoxygenation of guaiacol was investigated as a model reaction for the upgrading of the lignin component of bio-oils. A wide range of catalysts was prepared by varying Ni contents and modulating the properties of alumina-silica supports. High conversion values were achieved (up to 84%) in a very short time scale (1 h). The sample showing the highest conversion also displays the largest fraction of deoxygenated compounds. A further increase in conversion and HDO degree was obtained by addition of minor contents of tungsten, leading to more than 90% conversion and over 70% of HDO.

By increasing the Ni content, both conversion and HDO degree increase reaching no plateau even for the largest Ni amount. Considering the homogeneous coating apparent from SEM images of the samples at the highest Ni content, an open texture fully accessible to the reactants can be suggested. The increase of the silica amount in the support leads to progressively larger conversion and HDO. If AlSi10Ni15 and AlSi40Ni15 are compared, the effect on the composition of the liquid fraction is striking: for the former sample, methyl-guaiacol is almost the only product, whereas for the latter, HDO degree is doubled and naphtenics, aromatics and phenols markedly increase.

The promotion introduced by the increasing silica amounts can be traced back to two different effects: the progressive increase in surface area of the support, which might lead to a better distribution of the metal centers, and its acid-base features. In this respect, the measured isoelectric point of the bare supports appeared to be predictive of the final performance of the relative Ni-based catalyst: the more acidic the iep, the better the overall performance of the catalyst. This is particularly true in the case of the twin samples obtained using calcined and uncalcined supports: despite the identical composition and similar morphological properties, the small shift of the iep (about 0.5 pH units) leads to an overall improved activity. This

trend is in agreement with the Lewis/Brønsted sites ratio, as apparent from data in Figure 12.2c.

An excellent response of the spent catalyst upon a thermal regeneration treatment was obtained, both in terms of surface features and catalytic performance.

A copromoted catalyst prepared by loading both Ni and W revealed a better performance with respect to the relative Ni promoted sample, mainly under the guaiacol conversion point of view. Thus, the use of small amounts of W as a copromoter for HDO reactions adopting alumina-silica catalytic supports could be favorable, needing future investigations.

12.3 Specific procedures

Samples preparation. Ni-based catalyst were prepared by impregnation method on commercial alumina supports with a variable silica content. The effect of the metal content and the addition of a copromoter were also investigated.

Commercial oxide supports of the PURALOX, SIRAL, and SIRALOX family by SASOL were used, characterized by different amounts of SiO_2 (0, 5, 10 or 40%). Unless stated otherwise, oxohydroxo supports were thermally pretreated at 550°C before impregnation in order to obtain the relative oxide. The catalysts were then dipped in a $Ni(NO_3)_2$ (Sigma-Aldrich) aqueous solution: different concentrations were tested to achieve a final Ni/support mass ratio of 5, 15, 30 or 45%. For the preparation of the bimetallic catalyst, K_2WO_4 (W/support mass ratio = 1.5%) was also introduced in the $Ni(NO_3)_2$ aqueous solution. The impregnating suspensions were stirred for 1 h at room temperature, then dried in an oven at 80°C overnight and calcined at 570 °C for 6 h under oxygen flux (9 NL h^{-1}). Catalysts were activated for 4 h at 50 bar and 300°C in H_2 just before conducting the catalytic test.

Pristine and metal-promoted samples were labelled as AlSix and AlSixNiyWz, where *x*, *y* and *z* are the percentage of SiO_2 in the catalytic support, the nominal amount of loaded Ni and the nominal amount of loaded W, respectively. The symbol * was used where non-precalcined supports were adopted.

Catalytic tests. All the prepared catalysts were tested in the catalytic hydrodeoxygenation of guaiacol at 300°C under H_2 (50 bar). The reaction was performed in a stainless-steel autoclave (A1120HC6, Parr instrument Co., Moline, IL, USA) with a volume of 100 mL. 2 g of guaiacol and 100 mg of catalyst were selected as initial amounts. Unless differently stated, the reaction was performed for 1 h while stirring. The amounts of reagent and products were quantified at the end of the reaction by gas chromatography (GC) analyses. GC-FID (Clarus 600, Perkin Elmer) measurements (adopting eugenol as internal reference) were performed to quantify the liquid products, as well as the non-reacted amount of guaiacol, while GC-TCD (6890A/N, Agilent) was used for the analysis of the gas products. The reaction progress was evaluated by calculating the percentage of guaiacol conversion (χ_{gua}), the hydrodeoxygenation degree (HDO), and the percentage product distribution, according to the following equations:

$$\chi_{gua} = \frac{n^i_{gua} - n^f_{gua}}{n^i_{gua}} \times 100 \quad (12.1)$$

$$HDO = \left(1 - \frac{n_{O,l}}{n^i_O}\right) \times 100 \quad (12.2)$$

$$\Phi_i = \left(\frac{n_i}{\sum_i n_i}\right) \times 100 \quad (12.3)$$

where n^i_{gua} and n^f_{gua} are respectively the initial and final moles of guaiacol, n_i are the moles of the identified liquid products (taking into account unreacted guaiacol), while $n_{O,l}$ and n^i_O are the moles of oxygen of liquid compounds and the initial moles of oxygen, respectively. The estimated standard deviation for these parameters is around 2%.

Reactivation tests. At the end of the catalytic reaction, selected catalysts were recovered by washing the reactor by acetone and filtering over a Millipore filter (0.45 μm). The reactivation was tested by thermally treating a fraction of the used material at 400°C for 2 h under O_2 flux. The reactivated catalyst (added with a fraction of fresh catalyst in order to reach the desired amount) was then tested in the same reaction conditions of the fresh catalyst.

Further details about the preparation and characterization methods can be found in Appendix A.

References

1 G. W. Huber, S. Iborra and A. Corma, *Chem. Rev.*, 2006, **106**, 4044–4098.

2 N. L. Panwar, S. C. Kaushik and S. Kothari, *Renew. Sustain. Energy Rev.*, 2011, **15**, 1513–1524.

3 A. Demirbas, *Prog. Energy Combust. Sci.*, 2007, **33**, 1–18.

4 A. Corma, S. Iborra and A. Velty, *Chem. Rev.*, 2007, **107**, 2411–2502.

5 M. Saidi, F. Samimi, D. Karimipourfard, T. Nimmanwudipong, B. C. Gates and M. R. Rahimpour, *Energy Environ. Sci.*, 2014, **7**, 103–129.

6 J. Park, A. Riaz, R. Insyani and J. Kim, *Fuel*, 2018, **217**, 202–210.

7 M. V. Bykova, D. Y. Ermakov, V. V. Kaichev, O. A. Bulavchenko, A. A. Saraev, M. Y. Lebedev and V. A. Yakovlev, *Appl. Catal. B Environ.*, 2012, **113**–**114**, 296–307.

8 A. T. W. M. Hendriks and G. Zeeman, *Bioresour. Technol.*, 2009, **100**, 10–18.

9 M. Grilc, G. Veryasov, B. Likozar, A. Jesih and J. Levec, *Appl. Catal. B Environ.*, 2015, **163**, 467–477.

10 J.-S. Moon, E.-G. Kim and Y.-K. Lee, *J. Catal.*, 2014, **311**, 144–152.

11 T. Szarvas, Z. Eller, T. Kasza, T. Ollár, P. Tétényi and J. Hancsók, *Appl. Catal. B Environ.*, 2015, **165**, 245–252.

12 N. Arun, J. Maley, N. Chen, R. Sammynaiken, Y. Hu and A. K. Dalai, *Catal. Today*, 2017, **291**, 153–159.

13 P. M. Mortensen, J.-D. Grunwaldt, P. A. Jensen and A. D. Jensen, *ACS Catal.*, 2013, **3**, 1774–1785.

14 E. J. Roberts, S. E. Habas, L. Wang, D. A. Ruddy, E. A. White, F. G. Baddour, M. B. Griffin, J. A. Schaidle, N. Malmstadt and R. L. Brutchey, *ACS Sustain. Chem. Eng.*, 2017, **5**, 632–639.

15 T.-S. Nguyen, D. Laurenti, P. Afanasiev, Z. Konuspayeva and L. Piccolo, *J. Catal.*, 2016, **344**, 136–140.

16 N. Arun, R. V. Sharma and A. K. Dalai, *Renew. Sustain. Energy Rev.*, 2015, **48**, 240–255.

17 A. M. Robinson, J. E. Hensley and J. W. Medlin, *ACS Catal.*, 2016,

6, 5026–5043.
18 W. Wang, S. Tan, K. Wu, G. Zhu, Y. Liu, L. Tan, Y. Huang and Y. Yang, *Fuel*, 2018, **214**, 480–488.
19 H. Shafaghat, P. S. Rezaei and W. M. Ashri Wan Daud, *RSC Adv.*, 2015, **5**, 103999–104042.
20 Y. Yang, C. Ochoa-Hernández, V. A. de la Peña O'Shea, P. Pizarro, J. M. Coronado and D. P. Serrano, *Appl. Catal. B Environ.*, 2014, **145**, 91–100.
21 S.-K. Wu, P.-C. Lai, Y.-C. Lin, H.-P. Wan, H.-T. Lee and Y.-H. Chang, *ACS Sustain. Chem. Eng.*, 2013, **1**, 349–358.
22 X. Xu and E. Jiang, *Energy & Fuels*, 2017, **31**, 2855–2864.
23 O. U. Valdés-Martínez, V. A. Suárez-Toriello, J. A. de los Reyes, B. Pawelec and J. L. G. Fierro, *Catal. Today*, 2017, **296**, 219–227.
24 S. Echeandia, P. L. Arias, V. L. Barrio, B. Pawelec and J. L. G. Fierro, *Appl. Catal. B Environ.*, 2010, **101**, 1–12.
25 A. Centeno, E. Laurent and B. Delmon, *J. Catal.*, 1995, **154**, 288–298.
26 T. M. Sankaranarayanan, M. Kreider, A. Berenguer, S. Gutiérrez-Rubio, I. Moreno, P. Pizarro, J. M. Coronado and D. P. Serrano, *Fuel*, 2018, **214**, 187–195.
27 C. Larabi, A. Garron, P. Rouge, K. C. Szeto, S. Norsic, A. De Mallmann, N. Merle and M. Taoufik, *ChemCatChem*, 2017, **9**, 2160–2166.
28 L. Kovarik, M. Bowden, D. Shi, N. M. Washton, A. Andersen, J. Z. Hu, J. Lee, J. Szanyi, J. H. Kwak and C. H. F. Peden, *Chem. Mater.*, 2015, **27**, 7042–7049.
29 R. -S Zhou and R. L. Snyder, *Acta Crystallogr. Sect. B Struct. Sci.*, 1991, **47**, 617–630.
30 D. Meroni, V. Pifferi, B. Sironi, G. Cappelletti, L. Falciola, G. Cerrato and S. Ardizzone, *J. Nanoparticle Res.*, 2012, **14**, 1086.
31 M. Kosmulski, *Adv. Colloid Interface Sci.*, 2016, **238**, 1–61.
32 M. Kosmulski, *J. Colloid Interface Sci.*, 2014, **426**, 209–212.
33 A. B. Dongil, L. Pastor-Pérez, A. Sepúlveda-Escribano, R. García and N. Escalona, *Fuel*, 2016, **172**, 65–69.
34 C. Morterra, G. Cerrato, S. Ardizzone, C. L. Bianchi, M. Signoretto and F. Pinna, *Phys. Chem. Chem. Phys.*, 2002, **4**, 3136–3145.

35 R. N. Olcese, M. Bettahar, D. Petitjean, B. Malaman, F. Giovanella and A. Dufour, *Appl. Catal. B Environ.*, 2012, **115**–**116**, 63–73.
36 S. Pichaikaran and P. Arumugam, *Green Chem.*, 2016, **18**, 2888–2899.
37 J. Mao, J. Zhou, Z. Xia, Z. Wang, Z. Xu, W. Xu, P. Yan, K. Liu, X. Guo and Z. C. Zhang, *ACS Catal.*, 2017, **7**, 695–705.
38 Q. Lai, C. Zhang and J. H. Holles, *Appl. Catal. A Gen.*, 2016, **528**, 1–13.
39 R. Olcese, M. M. Bettahar, B. Malaman, J. Ghanbaja, L. Tibavizco, D. Petitjean and A. Dufour, *Appl. Catal. B Environ.*, 2013, **129**, 528–538.
40 H. Y. Zhao, D. Li, P. Bui and S. T. Oyama, *Appl. Catal. A Gen.*, 2011, **391**, 305–310.
41 G. Soliveri, V. Pifferi, R. Annunziata, L. Rimoldi, V. Aina, G. Cerrato, L. Falciola, G. Cappelletti and D. Meroni, *J. Phys. Chem. C*, 2015, **119**, 15390–15400.
42 J. W. Ledbetter, *J. Phys. Chem.*, 1977, **81**, 54–59.
43 Y. Elkasabi, Q. Liu, Y. S. Choi, G. Strahan, A. A. Boateng and J. R. Regalbuto, *Fuel*, 2017, **207**, 510–521.
44 R. W. Gosselink, D. R. Stellwagen and J. H. Bitter, *Angew. Chemie Int. Ed.*, 2013, **52**, 5089–5092.

Chapter 13

Assembly of β-$Cu_2V_2O_7$/WO_3 heterostructured nanocomposites and the impact of their composition-dependent structure on the photoelectrochemical properties

Heterostructured nanocomposites are attractive material platforms where the interface between the components plays a key role in conferring improved functionalities compared to those of the isolated counterparts. In solar energy conversion, organic bulk-heterojunction solar cells exemplify the importance of interfaces for enhanced photoconversion efficiencies as the donor/acceptor blend overcomes the charge transport limitations of light absorbing polymers[1–6]. The impact of the morphology in the organic blends on charge carrier separation and dynamics has been widely investigated, and has been shown to be crucial for performance optimization[1–6]. Photoelectrochemical cells (PEC) are a promising technology to convert sunlight into renewable chemicals (hydrogen from water or hydrocarbons from CO_2)[7]. At the present, these devices suffer from the lack of optimal n-type inorganic semiconductors to carry the water oxidation reaction, referred to as photoanodes. Metal oxides (MOs) are typically chosen because of their higher stability in alkaline aqueous electrolyte compared to silicon, III-V and II-VI semiconductors. So far the most studied photoanodes are α-Fe_2O_3 and $BiVO_4$[8–10]. One of the common limitations for MOs is the incompatibility between light absorption capabilities and carrier transport length[8–10]. The combination of smaller band gap and larger band gap MO semiconductors has been demonstrated to enhance charge separation and thus water oxidation photocurrents

(*e.g.* $BiVO_4/WO_3$[11–14], $BiVO_4/TiO_2$[15–18], α-Fe_2O_3/WO_3 [19], α-Fe_2O_3/TiO_2[20,21]). Yet, the detailed mechanisms of charge separation at the semiconductor/semiconductor interface are not often fully elucidated and the understanding of how the structure/composition of the MO nanocomposites correlate with their photoelectrochemical properties is at its infancy when compared to organic heterojunctions[1-6]. In the case of $BiVO_4$, the combination of doping, nanostructuring and heterostructuring has allowed to achieve performance very close to the theoretical limit[22,23]. Nevertheless, the band gap of $BiVO_4$ of around 2.5 eV is still too wide for optimal solar harvesting. Recently, copper vanadates with their band gaps around 2 eV have emerged as a novel class of photoanode materials[24,25,34,26–33]. The two major limitations of copper vanadates for solar water oxidation are the position of their conduction band minimum (which is a few hundreds of millivolts more positive than the water reduction potential) and their short carrier-diffusion lengths (around 20–40 nm)[25,32]. We have recently demonstrated that some photocurrent increase can be achieved by nanostructuring of β-$Cu_2V_2O_7$ or by creating the β-$Cu_2V_2O_7/CuV_2O_6$ heterojunction, which supposedly favors charge separation.[31]

In the work reported in this Chapter, first tailored β-$Cu_2V_2O_7/WO_3$ (CVO/WO_3) heterostructured nanocomposites in a wide compositional range were prepared by exploiting our recently developed nanocrystal-seeded method for nanocrystalline β-$Cu_2V_2O_7$[31]. While it is difficult to make conclusive remarks solely based on the band alignment of bulk and the actual interfacial energetics need to be carefully probed, we preferred WO_3 to TiO_2 as a starting wide band gap MO based on its more favorable energetic alignment for charge transfer from β-$Cu_2V_2O_7$ compared to TiO_2 and on the knowledge gained through our previous studies[11,14]. After assembling the CVO/WO_3 nanocomposites, the impact of the different compositions on the photoelectrochemical performance of the nanocomposites through photocurrent measurements was studied and compared to the behaviour of the pure counterparts. Finally, the investigation of the charge carrier dynamics of the best performing nanocomposite by means of transient absorption spectroscopy enables us to suggest the possible mechanism behind the observed behavior.

13.1 Results and discussion

For the assembly of the CVO/WO_3 heterostructured nanocomposites, a solution containing 6 nm surface oxidized Cu nanocrystals (NCs), $VO(acac)_2$ and 4 nm x 15 nm $WO_{2.7}$ nanorods (NRs) in dimethylformamide was drop-casted on a substrate and annealed at 350°C for 8h. These synthesis parameters were chosen based on our previous results for pure nanocrystalline CVO.[31] Nanocomposites with three different mass ratios of the two components CVO:WO_3 = 1:0.25, 1:0.5 and 1:1 were prepared by adding different amounts of $WO_{2.7}$ NRs in the precursor solution. Figure 13.1a show the transmission electron microscopy (TEM) images of the Cu NCs and $WO_{2.72}$ NRs used as building blocks for the assembly of the nanocomposites. A representative top-view scanning electron microscopy (SEM) image and the corresponding compositional mapping by energy dispersive X-ray (EDX) spectroscopy of one of the CVO/WO_3 nanocomposites (mass ratio 1:0.25) are reported in Figure 13.1b. SEM reveals a continuous film composed of a network of nanograins. The limited resolution does not allow to distinguish between the copper vanadate and the WO_3, yet the EDX mapping evidences a spatially homogeneous distribution of Cu, V, and W both in plane (Fig. 13.1b) and in cross-section (Fig. 13.1c). Similar results were obtained for the nanocomposites with different compositions and elemental analysis confirmed the CVO:WO_3 nominal ratio.

To get more insights into the CVO/WO_3 interface for the synthesized nanocomposite transmission electron microscopy (TEM) was employed (Fig. 13.2a). Figure 13.2a shows the high-angle annular dark-field scanning transmission electron microscopy (HAADF-STEM) image of one of the nanocomposites. The stark difference in contrast and in morphology between β-$Cu_2V_2O_7$ (irregular shaped areas) and WO_3 (rod shaped areas) clearly identify the two different domains in the nanocomposite. EDX-TEM analysis in Figure 13.2b provides evidence of the uniform coverage of WO_3 nanorods by β-$Cu_2V_2O_7$. The interface between the two materials in the nanocomposite was further investigated by high resolution TEM (HR-TEM). Figure 13.2a also evidences a continuous interface between the two domains, which might suggest a hetero-epitaxial growth of β-$Cu_2V_2O_7$ on WO_3 along the *a* crystallographic direction (lattice spacing 7.687Å) of

the monoclinic β-$Cu_2V_2O_7$ structure and one of the monoclinic WO_3 directions.

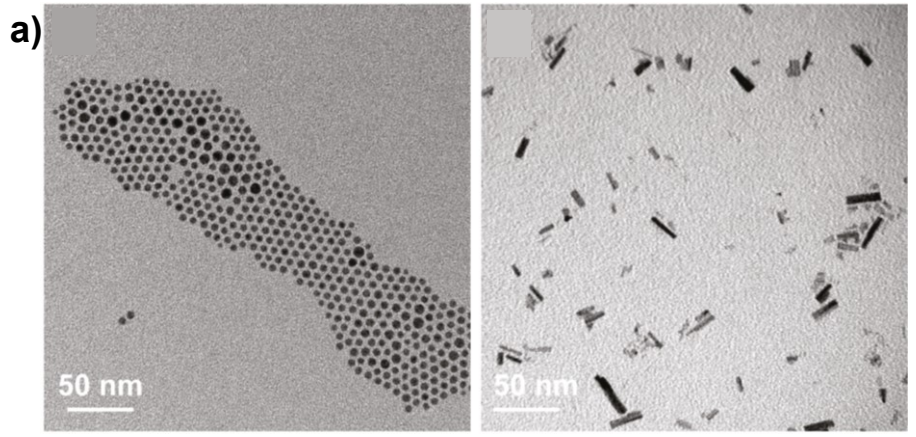

a) TEM images of the 6 nm Cu NC seeds (left) and of the 4 nm x 15 nm $WO_{2.72}$ NRs, (right).

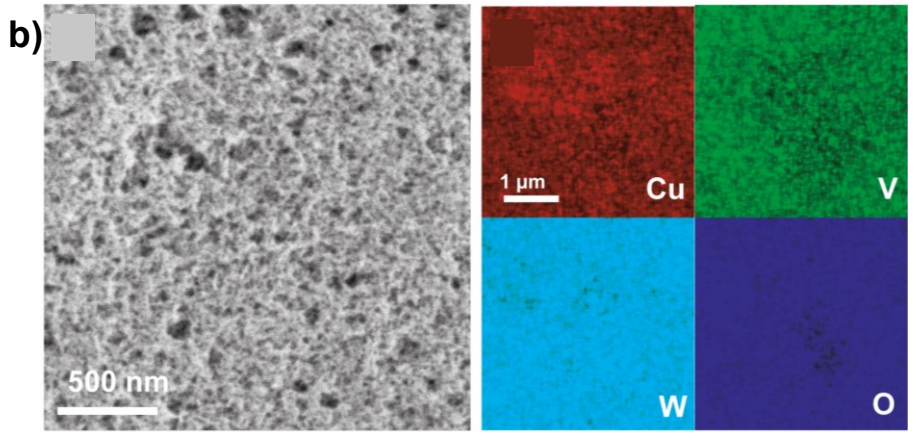

b) SEM image (left) and EDX mapping (right) of a typical CVO /WO_3 nanocomposite film with mass ratio 1: 0.25.

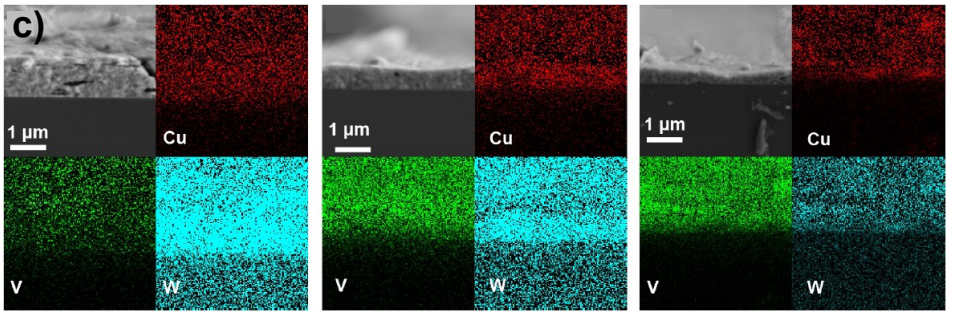

c) Cross-sectional SEM images and elemental EDX mapping of CVO/WO_3 = 1:1 (left), CVO/WO_3 = 1:0.5 (middle) and CVO/WO_3 = 1:0.25 (right) nanocomposite films.

Figure 13.1 – Morphological and elemental characterization results.

The structural and compositional characterization of the nanocomposites was completed by X-ray diffraction (XRD) (Fig. 13.2c) and Raman spectroscopy (Fig. 13.3a). The XRD data were acquired in grazing-incident mode using synchrotron radiation. Figure 13.2c reports the XRD data of the nanocomposites along with the pure components for comparison. The broadening of the peaks in all patterns is consistent with the formation of nano-sized crystalline domains and the patterns are in agreement with the previously reported data for the WO_3 NR thin film and for the nanocrystalline CVO[11,31,35]. The main reflections of the WO_3 phase are observed in all composite samples with the intensity increasing proportionally to the amount of WO_3. The preservation of the peak width and relative peak ratio for WO_3 in the nanocomposites indicates that the NR size and shape is maintained upon annealing at 350°C for 8 hours, consistently with the TEM data. This observation is not surprising, considering no morphological changes were observed even in a previous work when the same NRs were annealed at much higher temperature[11]. The CVO peaks are distinguishable in the 1:0.25 and 1:0.5 samples, instead in the 1:1 nanocomposite they are completely covered by the more strongly scattering WO_3. XRD patterns were also acquired while heating the deposited precursor solution in order to get deeper insights into the formation of the nanocomposites (Fig. 13.2c). The data relative to the CVO/WO_3 sample with mass ratio 1:0.25 are reported as one representative example, taking into account that all the nanocomposites behaved similarly to each other. In the initial scans at room temperature, the most intense peaks of the $WO_{2.72}$ phase together with the vanadium molecular precursor are detected. Cu reflections are not observed due to peak broadness and low intensity associated with the small size of the NCs (6 nm). During the heating, the sharp reflections of $VO(acac)_2$ disappear at around 150°C, which corresponds to the melting temperature of the salt. Thermal dilatation of the $WO_{2.72}$ lattice is detected until about 230°C, when the main (010) peak at 10.4° starts shifting at a higher angles, which is indicative of a $WO_{2.72}$ → δ-WO_3 (Triclinic P-1) phase transition[36]. At 270°C the CVO reflections become evident, as the Cu NCs and the VO_x species start reacting. At this temperature γ-WO_3 (Monoclinic P2(1)/n) is expected to be the stable polymorph, but the quality of the data does not allow to discern this phase transition. The reflections grow in intensity until the temperature

reaches 350°C, indicating improved crystallinity, and remain then constant over time. The same behavior was observed in the binary mixture of surface oxidized Cu NCs and $VO(acac)_2$, indicating that the presence of the NRs does not impact significantly the kinetics of the chemical transformations leading to the formation of CVO. The reactivity of the binary mixtures $WO_{2.72}$ NRs + $VO(acac)_2$ and $WO_{2.72}$ NRs + surface oxidized Cu NCs was also investigated by in-situ experiments. Significant structural and compositional changes were observed only above 400°C, thus confirming that in the synthesis conditions chosen for the nanocomposites bulk doping or alloying of WO_3 by Cu- or V- and of CVO by W- can be most likely excluded.

Regarding Raman spectroscopy data (Fig. 13.3a), the broad peaks at 800 cm^{-1}, 680 cm^{-1} and 270 cm^{-1} correspond to the nanosized WO_3[37]. The peaks at 903 cm^{-1}, 910 cm^{-1}, 860 cm^{-1}, 786 cm^{-1} and 389 cm^{-1} can be assigned, instead, to β-$Cu_2V_2O_7$, which is clearly seen in the CVO sample[38]. All the nanocomposites have the peak at 800 cm^{-1} which can be assigned to WO_3 and the peak at 903 cm^{-1} which can be assigned to β-$Cu_2V_2O_7$. An increase in the intensity of the WO_3 peak (800 cm^{-1}) with respect to the β-$Cu_2V_2O_7$ peak (903 cm^{-1}) with the increase in mass loading of WO_3 in the nanocomposites can be observed.

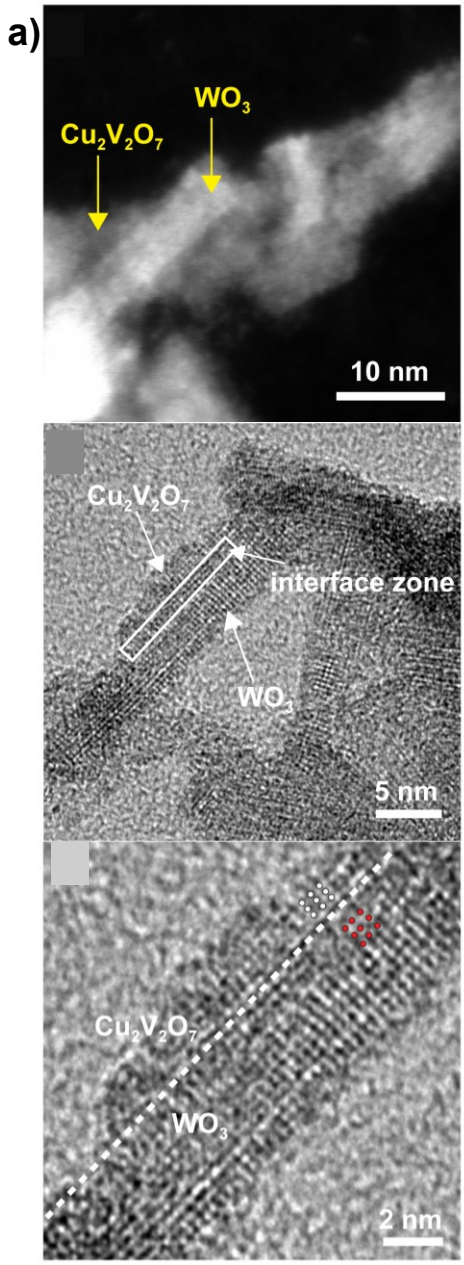

a) HAADF-STEM image of the 1:0.25 CVO/WO_3 nanocomposite film, indicating with the yellow arrows β-$Cu_2V_2O_7$ and WO_3 domains (top); HR-TEM image of the same nanocomposite evidencing the interface zone (middle); zoom image showing a continuous interface between β-$C_2V_2O_7$ and the WO_3 nanorod (bottom).

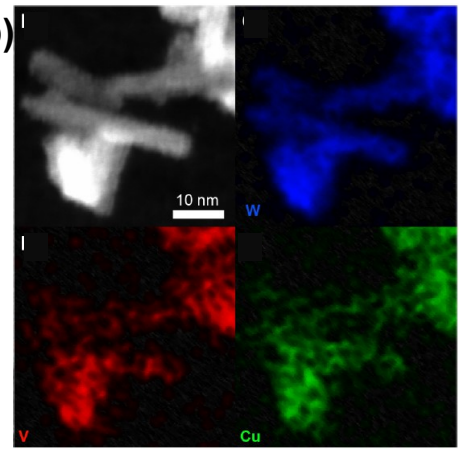

b) HAADF-STEM and corresponding EDX images of W, V and Cu respectively.

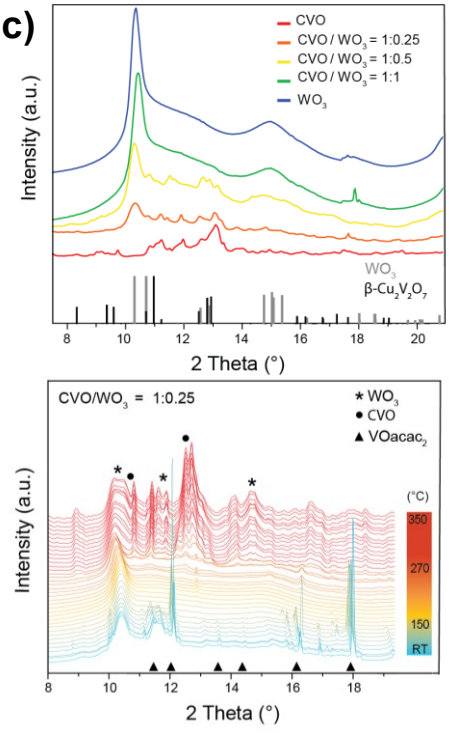

c) XRD patterns of the CVO/WO_3 nanocomposites, along with the patterns of pure WO_3 and CVO films (top); in-situ XRD measurements during the formation of the 1:0.25 CVO/WO_3 nanocomposites (bottom).

Figure 13.2 – Structural characterization results.

The photoelectrochemical (PEC) performance of the nanocomposites were evaluated by measuring the photocurrent density (J) of the films versus the applied potential (E) in a buffer borate electrolyte (pH=8.2) with Na_2SO_3 as a hole scavenger (Fig. 13.3b). The factors contributing to the photocurrent density are light absorption, charge transport within the photoelectrode and the charge transfer at the semiconductor/electrolyte interface. The slow water oxidation kinetics on the CVO as well as on WO_3 electrodes lead to accumulation of holes at the semiconductor/electrolyte interface[25,28,39]. Hence, in order to mitigate this issue, a hole scavenger is utilized to accelerate the charge transfer at the semiconductor/electrolyte interface and thus independently study the charge generation and charge transport properties in the nanocomposites. The large dark currents for sulfite oxidation have already been observed in various reports on copper vanadates and it might be an indication of the electrochemical activity of these materials towards the sulfite oxidation[25,28,31–34]. The dark currents decrease as the amount of WO_3 increases, thus confirming that they originate from the CVO component. A new nanocomposite CVO/WO_3=1:0.1 was prepared with lower WO_3 mass ratio in order to follow the trends of photocurrent over a broader range of compositions. The onset potential of all the nanocomposites cathodically shifts as the amount of WO_3 decreases (Fig. 13.3c). Such a cathodic shift has been previously observed in $BiVO_4/WO_3$ nanocomposites and attributed to reduced charge recombination in comparison to the individual metal oxides[12]. To facilitate the comparison between the different samples, the net photocurrent density, obtained by subtracting the dark current from the total photocurrent, is reported in Figure 13.3b. The potential of 1.23 V versus the reversible hydrogen electrode (RHE) is used as a reference to ease the comparison with the literature. The highest photocurrent value of 0.45 mA cm^{-2} at 1.23 V *vs*. RHE is observed for the nanocomposite with a CVO:WO_3 mass ratio of 1:0.1 which corresponds to a 10 fold increase compared to the bare CVO counterpart (0.05 mA cm^{-2}). The increased photocurrent does not correspond to increased light absorption (Fig. 13.3d), which suggests that charge separation and transport drive the performance of the nanocomposites.

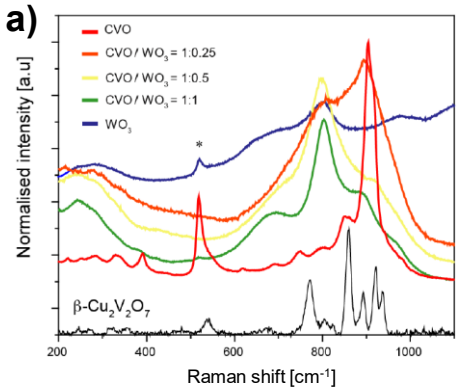

b) Raman spectra of WO_3, CVO and CVO/WO_3 films. The signal corresponding to the Si substrate is indicated as *.

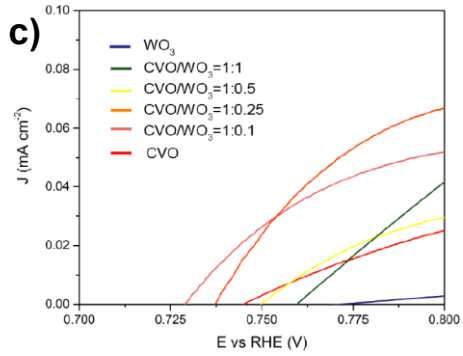

c) The onset potential of the nanocomposites in in a 0.1M sodium borate buffer (pH 8.2) containing 0.1M Na_2SO_3 as the hole scavenger.

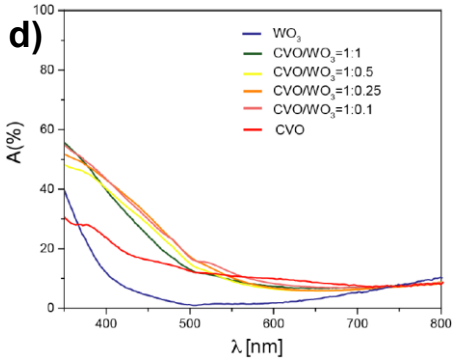

d) Optical absorption spectra of the pure WO_3, the pure CVO and the CVO/WO_3 nanocomposites for different mass ratios. The films were prepared on FTO for the PEC measurements. FTO background was not subtracted.

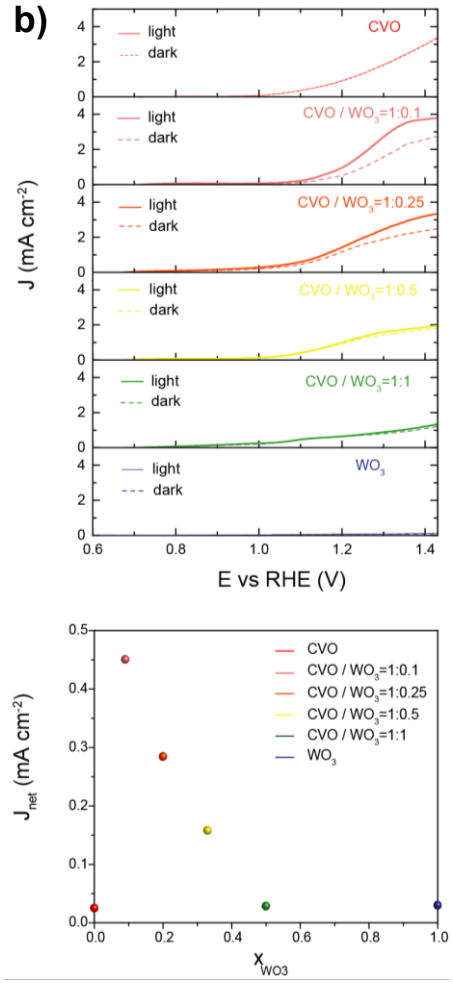

b) J-E curves under dark and illuminated conditions for WO_3, CVO/WO_3 nanocomposites with different mass ratios and CVO measured in a 0.1M sodium borate buffer (pH 8.2) containing 0.1M Na_2SO_3 as the hole scavenger; the dark currents are shown as dashed lines and the photocurrents are shown as solid lines (top); net photocurrent density ($J_{net} = J_{light} - J_{dark}$) at 1.23V *vs.* RHE plotted against the mass fraction of WO_3 (x_{WO_3}) in the nanocomposites, given by the formula $x_{WO_3} = \frac{Mass\ of\ WO_3}{(Mass\ of\ WO_3 + Mass\ of\ \beta - Cu_2V_2O_7)}$.

Figure 13.3 – Spectroscopic and photoelectrochemical results.

Optical spectroscopies were utilized to get insights into the PEC results. Steady-state absorption spectra of pure WO_3, pure CVO and CVO/WO_3

nanocomposites are reported in Figure 13.4a. The WO_3 has an absorption band edge at 420–430 nm, typical of nanostructured samples[40], and presents also a characteristic tail which starts to rise at 600 nm and extends in the near IR-range. The literature has attributed this tail to the absorption from oxygen vacancies and defects, which here persist even upon annealing[41,42]. As for the pure nanocrystalline CVO, we observe a very specific feature of copper vanadates, which is the symmetric shoulder peaking between 800–1000 nm very similar to the one reported by Sharp *et al.*, which the authors attributed to the ligand field effect of Cu^{2+} cations[25,32.] In the nanocomposites, the absorption edge blue-shifts as the amount of WO_3 increases similarly to what observed by Lee *et al.* for $BiVO_4/WO_3$ heterojunctions with different amounts of WO_3[12].

Photoluminescence (PL) spectroscopy is one simple yet powerful tool to investigate the efficiency of charge carrier generation which accompanies the suppression of the electron-hole pairs in the heterojunctions[15,16,43]. Usually, metal oxides do not have strong emission at room temperature and its origin can be attributed to the radiative recombination from surface trapped-excitons or from intra-band defects, such as oxygen vacancies[15]. Figure 13.4b shows the PL spectra of pure WO_3, pure CVO and CVO/WO_3 nanocomposites with different mass ratios. To avoid misinterpretation, the emission spectra have been normalized and compared with respect to the shape, thus we will not discuss the changes in amplitude which can only provide meaningful information for very similar samples. The spectra have been recorded upon excitation at 457 nm (2.7 eV) at room temperature. In the pure WO_3, one major peak at 492 nm is observed. Since the excitation wavelength does not allow to reach the conduction band of WO_3, this emission peak must come from intra-band defects such as oxygen vacancies[42,44]. The pure CVO presents a pronounced emission peak at 496 nm. The fact that the emission at room temperature is observed is an indication that the electron-hole pairs might be very strongly bound. In the nanocomposites samples with mass ratio of 1:1 and 1:0.5, the emission peaks of both WO_3 and CVO are evident, instead the nanocomposite with mass ratio 1:0.25 exhibits a much broader PL emission peak indicating that the emission from the WO_3 and from the CVO are strongly suppressed. This finding is consistent with the interpretation that in the blended nanocomposite with a 1:0.25 proportion

of the two domains, the electron-hole pairs are more efficiently separated. To further elucidate the role of the bulk heterojunction in the charge separation efficiency and to monitor the charge recombination time scale of the generated species to the ground state, transient absorption (TA) in the μs time scale was performed and the results comparing the pure CVO and one of the nanocomposites are reported in Figure 13.4c. In these measurements, the excitation energy is higher than the band gaps of both WO_3 and β-$Cu_2V_2O_7$ in order to better simulate the solar illumination conditions wherein both components of the heterojunction are excited. The charge carrier dynamics are faster in the pure CVO compared to the CVO/WO_3 nanocomposite with a time constant $\tau_{50\%}$ (which represents the time to reach half of the initial absorption[45]) equal to 250 ns and to 730 ns, respectively. The longer time decay for the nanocomposite is the signature that the recombination of electrons and holes has been suppressed. If we assume that the transient absorption signal originates from photo-excited holes as in the case of $BiVO_4$, then this observation suggests the occurrence of electron transfer from the CVO to WO_3, which results in longer lived holes, indicating that this novel heterojunction behaves consistently with a Type II band alignment, similarly to previously reported systems (*e.g.* $BiVO_4/TiO_2$ and $BiVO_4/WO_3$)[11,15]. While estimating the band gap alignment of the CVO/WO_3 junction from the values of the onset potential and of the optical band gap supports this hypothesis, further proofs are needed to confirm a type II band alignment in the CVO/WO_3 nanocomposites as shown for $BiVO_4/TiO_2$[15].

Considering the position of the onset potentials at 0.76 V and 0.74 V (Fig. 13.3c) and the band gaps of 2.9 eV and 2 eV for WO_3 and β-$Cu_2V_2O_7$, respectively, the CBM of the WO_3 results 20 mV downshifted with respect to the CBM of the CVO. Here, the assumption that the onset potential corresponds to the flat band potential of the electrodes is made taking into account that the presence of the hole scavenger should reduce the kinetic limitation of charge transfer at the semiconductor/electrolyte interface. While this still remains an approximation, the experimental approach has already been followed and validated by Jae Sung Lee *et al.*[46]. In addition, the photocurrent measurement for the best performing sample β-$Cu_2V_2O_7/WO_3$ = 1:0.1 presents a well-defined plateau (Fig. 13.3b), generally associated with enhanced charge generation efficiency[47]. Hence,

we can conclude the formation of a type II junction is the most suitable of the two possibilities for explaining our findings.

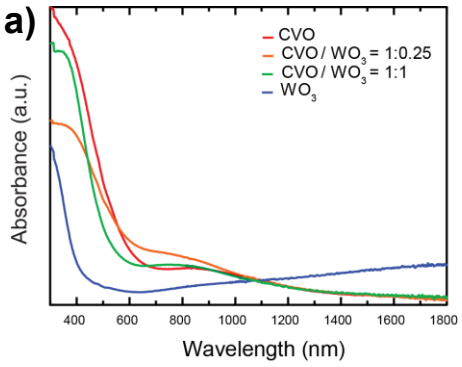

a) Steady-state absorption spectra of the CVO/WO_3 nanocomposites along with pure WO_3 and CVO for the sake of comparison.

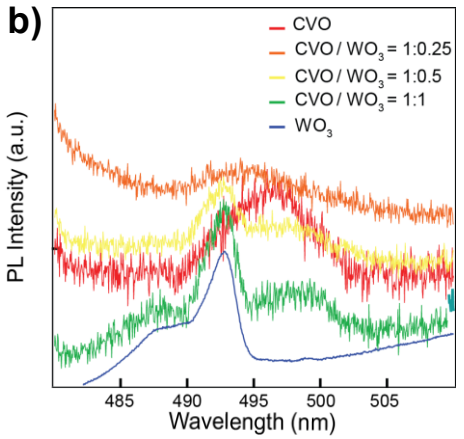

b) Normalized room-temperature PL emission spectra of of pure WO_3, CVO, CVO/WO_3 films deposited on quartz substrate upon excitation of 457 nm.

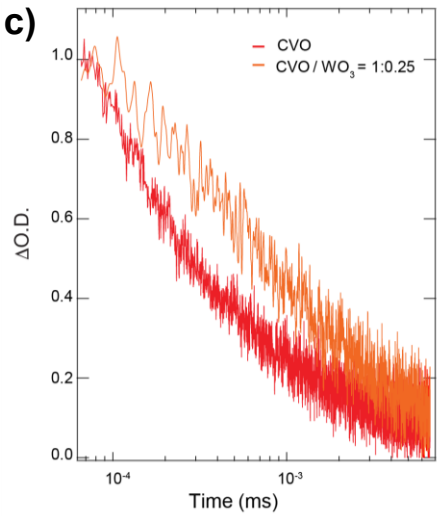

c) Normalized transient absorption decay response in the ms timescale for the pure CVO and the 1:0.25 CVO/WO_3 nanocomposite. The pump wavelength was 355 nm, the transient signal was probed at 700 nm and the fluence was 3.5 mJ cm^{-2} to avoid sample damage.

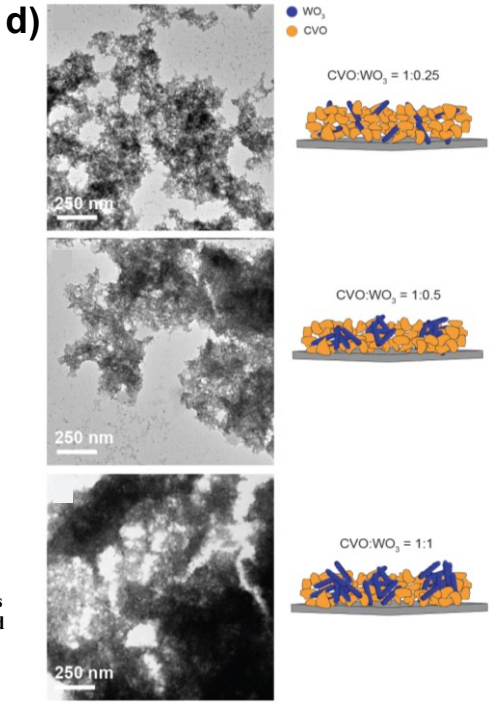

d) TEM images of the precursor solution for CVO/WO_3 with different mass ratios, containing the Cu NCs and $WO_{2.7}$ NRs in dimethylformamide, along with the corresponding schematics of the composition-dependent structure in the resulting CVO/WO_3 nanocomposites.

Figure 13.4 – Further spectroscopic and morphological results.

Finally, it is interesting to comment the finding that a lower loading of WO_3 is associated with higher PEC performance in the CVO/WO_3 nanocomposites. To explain this behavior, NC assembly must be discussed. Periodic 2D and 3D binary NC solids are obtained only when two species of highly monodisperse NCs with a properly chosen relative size self-assemble upon drying of the solvent in controlled conditions[48–50]. Being far from these ideal conditions, the Cu NCs and $WO_{2.7}$ NRs used as building blocks in this work tend to phase segregate, as commonly observed also in other systems[51]. Figure 13.4d shows TEM images of the precursor solutions utilized for the synthesis of the CVO/WO_3 nanocomposites. Upon the removal of the native ligands, which enable the dispersion of the NRs and NCs in polar solvents, the $WO_{2.7}$ NRs tend to aggregate and segregate in domains which are a few hundreds of nanometers in size on the TEM grid. Low resolution SEM and optical microscopy suggest that such phase segregation at the nanoscale is accompanied by the formation of mesoscale features with a branched morphology in the order of 100 μm in size (Fig. 13.5a,b). As the amount of the $WO_{2.7}$ NRs in the precursor solution increases, the domains become bigger (Fig. 13.4d). Bigger domains imply a less extended interfacial area between CVO and WO_3 in the resulting nanocomposite, thus less efficient charge injection and worse PEC performance[11]. In fact, while in the case of the 1:0.25 and 1:0.5 CVO/WO_3 nanocomposites needle-shaped domains about 100 μm long can be identified, with the higher WO_3 loading in CVO/WO_3 = 1:1 nanocomposites, these needles turn into a continuous, hierarchical branching pattern on the surface of the films. Since this patterning is also present before the annealing, we propose that it might be due to ordered aggregation of the NRs during film deposition and solvent evaporation. While this ordered aggregation is detrimental in our case, it represents an interesting example of how nanoscale assembly impacts mesoscale structure in inorganic blends.

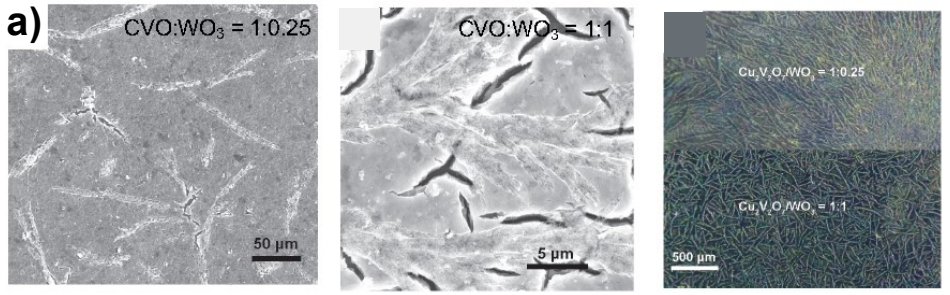

a) Low magnification SEM (left and middle) and optical microscopy (right) images of the 1:1 and 1:0.25 CVO/WO_3 nanocomposites.

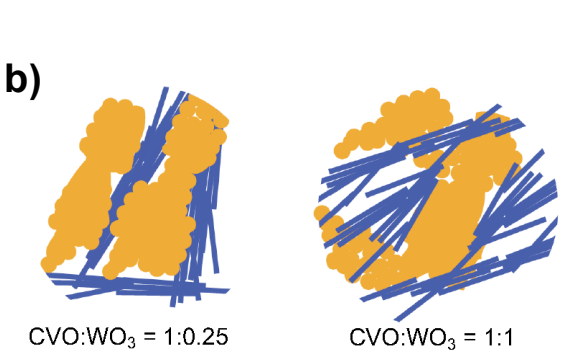

b) Illustration of the composition-dependent mesoscale structure induced by the nanoscale assembly of the Cu NCs and $WO_{2.7}$ NRs.

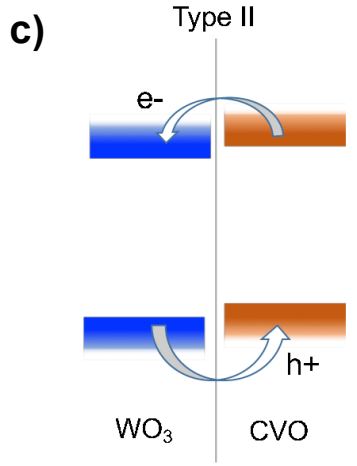

c) Proposed bands alignment for the CVO/WO_3 heterostructure.

Figure 13.5 – SEM images and schematics of the prepared heterostructures.

13.2 Conclusions

CVO/WO_3 heterostructured nanocomposites with tunable composition were assembled through a novel solution-based approach from a precursor ink containing Cu NCs, $WO_{2.7}$ NRs, and $VO(acac)_2$. The WO_3 loading was found to be the key parameter controlling the PEC performance of the nanocomposites, with the highest photocurrent density towards sulfite oxidation measured for the CVO/WO_3 with a 1:0.1 mass ratio, which corresponds to the lowest loading of WO_3. Optical spectroscopies provided insights into the charge injection mechanism across the interface and a type-II heterojunction is finally suggested. The better performance of the nanocomposites with lower WO_3 content is attributed to the more extended

contact area between the two components, which is beneficial for charge injection. While the segregation between CVO and WO_3 is detrimental in our case, this study reveals an interesting correlation between the nanoscale assembly and the mesoscale structure in inorganic nanocomposites (Figs. 13.4d and 13.5a,b,c), in a similar manner in which the molecular interaction in organic bulk heterojunctions impacts the macroscale morphology of the polymeric blends[1-6]. Together with a few others[11,18], this work strengthens the importance to aim at a superior structural tunability and control of the intrinsic inhomogeneity in inorganic bulk heterojunctions, and motivates researchers to explore ordered NC binary superlattices wherein the number of contact point between the individual NCs can be increased and finely tuned with superior control[49,50,52].

13.3 Specific procedures

Samples preparation. 6nm Cu NCs were synthesized by modifying the procedure from Hung *et al.*[53] 10 mL of trioctlyamine was introduced into a three-necked flask and kept under vacuum for 30 min. This step was followed by heating under nitrogen flow at 130°C for 30 minutes. Following the cooling of trioctylamine to room temperature, 1 mmol of copper(I) acetate and 0.5 mmol of tetradecylphosphonic acid were added to the flask under vigorous stirring. The solution was then heated to 180°C and maintained at this temperature for 30 min followed by one final heating step to 300°C for 30 min. The solution was naturally cooled to 60°C and transferred to a vial under N_2 flow. Anhydrous ethanol was added for washing and the solution centrifuged at 6000 rpm for 20 min. The precipitate was dispersed in hexane and kept under N_2 in glovebox.

WO_3 nanorod synthesis was conducted by following a procedure previously reported by Loiudice *et al.*[11,35] Briefly, 5.3 mL of oleic acid were added to a three-necked flask together with 1.8 mL of oleylamine and 100 mg of WCl_4. The mixture was heated under the nitrogen flow to 300°C. The mixture was maintained at 300°C for 2 h while stirring and then cooled to room temperature. Successively, the obtained colloidal solution was washed in acetone several times by centrifugation/resuspension cycles (15 min each, 3800 rpm) adopting 0.5 mL toluene for resuspension. The solution was finally dispersed in hexane.

In order to make a homogeneous solution in dimethylformamide of Cu NCs, WO_3 NRs and $VO(acac)_2$ the native ligands of the Cu NCs and WO_3 NRs need to be removed. The ligand stripping was performed following a previously reported procedure[54]. Firstly, the concentration of the nanocrystal solutions was determined by ICP-OES. Then, 1 mL of a solution 0.05 M of the as-synthesized Cu NCs (or WO_3 NRs) in hexane was added to a solution of 50 mg of trimethyloxonium tetrafluoroborate (Me_3OBF_4) in 1 mL of acetonitrile and vigorously stirred for 3 min. 1 mL of toluene was added to the solution followed by centrifugation at 6000 rpm for 15 min. The precipitate was dispersed in 250 µL of dimethylformamide. The above procedure was performed in a glove box for Cu NCs and in air for WO_3 NRs.

The preparation of nanocrystalline CVO was performed according to a recent work[31]. 3 µmol from a 0.05 M solution of ligand-stripped Cu NCs in dimethylfrmamide were surface-oxidized in a vial by flowing oxygen for 15 min to form Cu@Cu_2O core@shell NCs. After this step, 3 µmol from a 0.05 M stock solution of $VO(acac)_2$ in dimethylfrmamide were mixed with surface oxidized Cu NCs. The precursor solution (around 120 µL) was drop casted on 1.5 cm x 1.5 cm substrates on a hot plate at 60°C in glove box. Annealing was carried out in air in a tube furnace at 350°C for 8 h, preceded by 8°C min^{-1} heating ramp and followed by natural cooling.

For the nanocomposites, a precursor solution containing 3 µmol of Cu, 3 µmol of $VO(acac)_2$ and a varied amount of WO_3 in 210 µL dimethylfrmamide is prepared. To determine the amount of WO_3 to be added, it is assumed that all the Cu is converted to β-$Cu_2V_2O_7$ and thus, the film must contain 1.5 µmol of β-$Cu_2V_2O_7$. This corresponds to $5.11 \cdot 10^{-4}$ g of β-$Cu_2V_2O_7$ and this mass is used to calculate the mass of WO_3 to be added in the precursor solution to obtain CVO/WO_3 with mass ratios of 1, 0.5 and 0.25. Thus, 2.2 µmol, 1.1 µmol and 0.55 µmol of WO_3 are added to form CVO/WO_3 with mass ratio of 1, 0.5 and 0.25, respectively. The precursor solution is then drop-casted on 1.5 cm x 1.5 cm substrates on a hot plate kept at 60°C. Annealing is performed in air in a tube furnace at 350°C for 8 h, preceded by 8°C min^{-1} heating ramp and followed by natural cooling.

Photoelectrochemical (PEC) characterization. For the PEC characterization, 105 µL of precursor solution is deposited on 1.5 cm x 1.5

cm FTO substrates. The film thickness varies from around 350 nm for the pure CVO up to around 600 nm for the 1:1 CVO/WO_3 nanocomposite. J-E curves were acquired in a typical three-electrode configuration using a SP-200 (BioLogic) potentiostat/galvanostat. The light source was an AM 1.5 solar simulator with the illumination intensity adjusted to 100 mW cm^{-2}. All the illuminated areas were approximately 0.8 cm^2. The electrolyte was a sodium borate buffer solution (pH 8.2) with 0.1 M sodium sulfite (Na_2SO_3) as a hole scavenger. Photocurrents were monitored while sweeping the potential to the positive direction at a scan rate of 10 mV s^{-1}. The data reported in this study are obtained in back-illumination, yet front illumination leads to very similar curves considering the electrodes are porous and thin. A set of 3 photoelectrodes was tested for each studied photoanode and the average values are reported.

Further details about the preparation and characterization methods can be found in Appendix A.

References

1 J. J. M. Halls, K. Pichler, R. H. Friend, S. C. Moratti and A. B. Holmes, *Appl. Phys. Lett.*, 1996, **68**, 3120–3122.

2 A. C. Morteani, P. Sreearunothai, L. M. Herz, R. H. Friend and C. Silva, *Phys. Rev. Lett.*, 2004, **92**, 247402.

3 W. Zhang, M. Saliba, D. T. Moore, S. K. Pathak, M. T. Hörantner, T. Stergiopoulos, S. D. Stranks, G. E. Eperon, J. A. Alexander-Webber, A. Abate, A. Sadhanala, S. Yao, Y. Chen, R. H. Friend, L. A. Estroff, U. Wiesner and H. J. Snaith, *Nat. Commun.*, 2015, **6**, 6142.

4 R. H. Friend, R. W. Gymer, A. B. Holmes, J. H. Burroughes, R. N. Marks, C. Taliani, D. D. C. Bradley, D. A. Dos Santos, J. L. Brédas, M. Lögdlund and W. R. Salaneck, *Nature*, 1999, **397**, 121–128.

5 K. Wojciechowski, S. D. Stranks, A. Abate, G. Sadoughi, A. Sadhanala, N. Kopidakis, G. Rumbles, C. Z. Li, R. H. Friend, A. K. Y. Jen and H. J. Snaith, *ACS Nano*, 2014, **8**, 12701–12709.

6 Y. S. Huang, S. Westenhoff, I. Avilov, P. Sreearunothai, J. M. Hodgkiss, C. Deleener, R. H. Friend and D. Beljonne, *Nat. Mater.*, 2008, **7**, 483–489.

7 Y. Tachibana, L. Vayssieres and J. R. Durrant, *Nat. Photonics*, 2012, **6**, 511–518.

8 A. Loiudice, J. Ma, W. S. Drisdell, T. M. Mattox, J. K. Cooper, T. Thao, C. Giannini, J. Yano, L. W. Wang, I. D. Sharp and R. Buonsanti, *Adv. Mater.*, 2015, **27**, 6733–6740.

9 I. D. Sharp, J. K. Cooper, F. M. Toma and R. Buonsanti, *ACS Energy Lett.*, 2017, **2**, 139–150.

10 K. Sivula, F. Le Formal and M. Grätzel, *ChemSusChem*, 2011, **4**, 432–449.

11 A. Loiudice, J. K. Cooper, L. H. Hess, T. M. Mattox, I. D. Sharp and R. Buonsanti, *Nano Lett.*, 2015, **15**, 7347–7354.

12 S. J. Hong, S. Lee, J. S. Jang and J. S. Lee, *Energy Environ. Sci.*, 2011, **4**, 1781.

13 I. Grigioni, K. G. Stamplecoskie, D. H. Jara, M. V. Dozzi, A. Oriana, G. Cerullo, P. V. Kamat and E. Selli, *ACS Energy Lett.*, 2017, **2**, 1362–1367.

14 J. Su, L. Guo, N. Bao and C. A. Grimes, *Nano Lett.*, 2011, **11**, 1928–1933.
15 L. H. Hess, J. K. Cooper, A. Loiudice, C. M. Jiang, R. Buonsanti and I. D. Sharp, *Nano Energy*, 2017, **34**, 375–384.
16 S. Ho-Kimura, S. J. A. Moniz, A. D. Handoko and J. Tang, *J. Mater. Chem. A*, 2014, **2**, 3948.
17 J. Resasco, H. Zhang, N. Kornienko, N. Becknell, H. Lee, J. Guo, A. L. Briseno and P. Yang, *ACS Cent. Sci.*, 2016, **2**, 80–88.
18 M. Xie, X. Fu, L. Jing, P. Luan, Y. Feng and H. Fu, *Adv. Energy Mater.*, 2014, **4**, 1300995.
19 K. Sivula, F. Le Formal and M. Grätzel, *Chem. Mater.*, 2009, **21**, 2862–2867.
20 M. Bartsch, M. Sarnowska, O. Krysiak, C. Willa, C. Huber, L. Pillatsch, S. Reinhard and M. Niederberger, *ACS Omega*, 2017, **2**, 4531–4539.
21 D. Barreca, G. Carraro, A. Gasparotto, C. Maccato, M. E. A. Warwick, K. Kaunisto, C. Sada, S. Turner, Y. Gönüllü, T. P. Ruoko, L. Borgese, E. Bontempi, G. Van Tendeloo, H. Lemmetyinen and S. Mathur, *Adv. Mater. Interfaces*, 2015, **2**, 1500313.
22 Y. Qiu, W. Liu, W. Chen, G. Zhou, P. C. Hsu, R. Zhang, Z. Liang, S. Fan, Y. Zhang and Y. Cui, *Sci. Adv.*, 2016, **2**, e1501764.
23 X. Shi, I. Y. Choi, K. Zhang, J. Kwon, D. Y. Kim, J. K. Lee, S. H. Oh, J. K. Kim and J. H. Park, *Nat. Commun.*, 2014, **5**, 4775.
24 Q. Yan, J. Yu, S. K. Suram, L. Zhou, A. Shinde, P. F. Newhouse, W. Chen, G. Li, K. A. Persson, J. M. Gregoire and J. B. Neaton, *Proc. Natl. Acad. Sci.*, 2017, **114**, 3040–3043.
25 C. M. Jiang, G. Segev, L. H. Hess, G. Liu, G. Zaborski, F. M. Toma, J. K. Cooper and I. D. Sharp, *ACS Appl. Mater. Interfaces*, 2018, **10**, 10627–10633.
26 P. F. Newhouse, D. A. Boyd, A. Shinde, D. Guevarra, L. Zhou, E. Soedarmadji, G. Li, J. B. Neaton and J. M. Gregoire, *J. Mater. Chem. A*, 2016, **4**, 7483–7494.
27 D. Cardenas-Morcoso, A. Peiro-Franch, I. Herraiz-Cardona and S. Gimenez, *Catal. Today*, 2017, **290**, 65–72.
28 W. Guo, W. D. Chemelewski, O. Mabayoje, P. Xiao, Y. Zhang and C. B. Mullins, *J. Phys. Chem. C*, 2015, **119**, 27220–27227.

29 L. Zhou, Q. Yan, A. Shinde, D. Guevarra, P. F. Newhouse, N. Becerra-Stasiewicz, S. M. Chatman, J. A. Haber, J. B. Neaton and J. M. Gregoire, *Adv. Energy Mater.*, 2015, **5**, 1500968.
30 L. Zhou, Q. Yan, J. Yu, R. J. R. Jones, N. Becerra-Stasiewicz, S. K. Suram, A. Shinde, D. Guevarra, J. B. Neaton, K. A. Persson and J. M. Gregoire, *Phys. Chem. Chem. Phys.*, 2016, **18**, 9349–9352.
31 C. Gadiyar, M. Strach, P. Schouwink, A. Loiudice and R. Buonsanti, *Chem. Sci.*, 2018, **9**, 5658–5665.
32 C.-M. Jiang, M. Farmand, C. H. Wu, Y.-S. Liu, J. Guo, W. S. Drisdell, J. K. Cooper and I. D. Sharp, *Chem. Mater.*, 2017, **29**, 3334–3345.
33 J. A. Seabold and N. R. Neale, *Chem. Mater.*, 2015, **27**, 1005–1013.
34 M. A. Lumley and K. S. Choi, *Chem. Mater.*, 2017, **29**, 9472–9479.
35 T. M. Mattox, A. Bergerud, A. Agrawal and D. J. Milliron, *Chem. Mater.*, 2014, **26**, 1779–1784.
36 P. M. Woodward, A. W. Sleight and T. Vogt, *J. Solid State Chem.*, 1997, **131**, 9–17.
37 M. Boulova and G. Lucazeau, *J. Solid State Chem.*, 2002, **167**, 425–434.
38 D. de Waal and C. Hutter, *Mater. Res. Bull.*, 1994, **29**, 843–849.
39 J. A. Seabold and K. S. Choi, *Chem. Mater.*, 2011, **23**, 1105–1112.
40 H. Zheng, J. Z. Ou, M. S. Strano, R. B. Kaner, A. Mitchell and K. Kalantar-Zadeh, *Adv. Funct. Mater.*, 2011, **21**, 2175–2196.
41 Z. Xu, X. Li, J. Li, L. Wu, Q. Zeng and Z. Zhou, *Appl. Surf. Sci.*, 2013, **284**, 285–290.
42 F. Zheng, M. Guo and M. Zhang, *CrystEngComm*, 2013, **15**, 277–284.
43 H. Li, H. Yu, X. Quan, S. Chen and H. Zhao, *Adv. Funct. Mater.*, 2015, **25**, 3074–3080.
44 M. Ghiyasiyan-Arani, M. Masjedi-Arani and M. Salavati-Niasari, *J. Mater. Sci. Mater. Electron.*, 2016, **27**, 4871–4878.
45 A. Kafizas, X. Wang, S. R. Pendlebury, P. Barnes, M. Ling, C. Sotelo-Vazquez, R. Quesada-Cabrera, C. Li, I. P. Parkin and J. R. Durrant, *J. Phys. Chem. A*, 2016, **120**, 715–723.
46 S. J. Hong, S. Lee, J. S. Jang and J. S. Lee, *Energy Environ. Sci.*, 2011, **4**, 1781.

47 A. J. Cowan and J. R. Durrant, *Chem. Soc. Rev.*, 2013, **42**, 2281–2293.
48 Z. Chen, J. Moore, G. Radtke, H. Sirringhaus and S. O'Brien, *J. Am. Chem. Soc.*, 2007, **129**, 15702–15709.
49 X. Ye, J. A. Millan, M. Engel, J. Chen, B. T. Diroll, S. C. Glotzer and C. B. Murray, *Nano Lett.*, 2013, **13**, 4980–4988.
50 Y. Kang, X. Ye, J. Chen, L. Qi, R. E. Diaz, V. Doan-Nguyen, G. Xing, C. R. Kagan, J. Li, R. J. Gorte, E. A. Stach and C. B. Murray, *J. Am. Chem. Soc.*, 2013, **135**, 1499–1505.
51 A. Brumberg, B. T. Diroll, G. Nedelcu, M. E. Sykes, Y. Liu, S. M. Harvey, M. R. Wasielewski, M. V Kovalenko and R. D. Schaller, *Nano Lett.*, 2018, **18**, 4771–4776.
52 A. Dong, J. Chen, P. M. Vora, J. M. Kikkawa and C. B. Murray, *Nature*, 2010, **466**, 474–477.
53 L.-I. Hung, C.-K. Tsung, W. Huang and P. Yang, *Adv. Mater.*, 2010, **22**, 1910–1914.
54 E. L. Rosen, R. Buonsanti, A. Llordes, A. M. Sawvel, D. J. Milliron and B. A. Helms, *Angew. Chemie Int. Ed.*, 2012, **51**, 684–689.

This Chapter has been adapted with permission from Scarongella *et al.*, *J. Mater. Chem. C*, 2018, **6**, 12062–12069. Copyright 2018 Royal Society of Chemistry.

L.R. contribution: synthesis of Cu NPs and WO_3 NRs, films preparation, part of the photoelectrochemical measurements.

Conclusions and Outlooks

This Thesis can be read as a brief overview about the versatility of nanostructured oxides, in the scenario of the main challenges of our century.

My PhD work wants to highlight the potential of innovative techniques and applications (photocatalysis, surface modification, sensing and energy conversion) in which nanostructured oxides can be an efficient tool, but also to underline the role played on the overall oxide behaviour by often disregarded properties as *e.g.* surface electrification, wettability and competition effects. The main highlights concerned the understanding of the structure-activity relation of TiO_2-based photocatalysts for both air and water pollutant degradation reactions, the engineering of a floating photocatalytic device based on a novel tailored ter-polymer and of a novel electrochemical sensor with anti-biofouling based on templated mesoporous silica films.

The studies relative to oxides wettability and surface functionalization have also led to the publication of a paper appeared on the *Journal of Chemical Education*, aimed at developing tools to show in teaching laboratory experiments these less common aspects of physical chemistry.

Some of the investigations presented here paved the way for further new studies by myself and my group which are in progress at the present time. For example, new investigations about visible light active N-doped and Sn-modified TiO_2 materials and the role of the synthetic route, also for the preparation of SnO_2/TiO_2 composites, are under study. A project on this type of materials deserved beamtime in different synchrotron facilities, where my group and myself had the possibility to better understand the role of the electronic and structural features by means of advanced techniques.

Moreover, natural silica/alumina-based minerals are being surface modified for the preparation of hybrid materials, which are being employed even for drug-delivery applications, in an early stage project. Here again, my group and I have had the possibility to investigate the surface and the

spectroscopic properties by means of synchrotron techniques, for better understanding the chemical properties of the modified interface. Composite inorganic/organic compounds, obtained by a novel and green synthetic route combining polyaniline and TiO_2 are being exploited for environmental applications as pollutants absorbers.

Appendix A

Materials and methods

In this Appendix, typical synthesis the characterization procedures frequently adopted during this Thesis are described. Moreover, the molecular structures of frequently used organic molecules are reported.

All reagents adopted in this Thesis were purchased from Sigma-Aldrich and used without any further purification. Doubly-distilled water passing through a Milli-Q apparatus was adopted to prepare solutions and suspensions.

A.1 Synthetic procedures

A.1.1 TiO_2 sol-gel synthesis

For the synthesis of the nanostructured TiO_2 powders reported throughout this Thesis, two different sol-gel synthetic routes were basically employed. In general, these procedures gave rise to nanostructured materials which mainly differ from the phase composition. In fact, while through the first one biphasic anatase / brookite samples (ratio *ca.* 60:40) are obtained, the second route allow pure (or almost pure, especially if the classic procedure is amended) anatase samples to be synthesized, thanks to the use of acetic acid (acting as a sort of chelating agent favouring the growth of the anatase crystal structure).

The first TiO_2 procedure reported in the following was used, with possible specific modifications, for Chapters 3, 4, 5 and 6, while the second one was employed for Chapters 1, 2 and 4.

In the first case, in a classical synthesis, 18.38 g of titanium(IV) isopropoxide (97%) and 18.81 g of 2-propanol are mixed in a three-necked flask for 10 min. Then, 113 mL of a mild acidic HCl aqueous solution (pH 3) are added dropwise in 30 min, while stirring (300 rpm). The reaction is left under stirring for other 90 min to complete the hydrolysis. Successively, the suspension is dried at 80°C in an oven overnight and

finally calcined in oxygen flux (9 NL h^{-1}) for 6 h at 400°C. In the different Chapters of this Thesis, the classical procedure was sometimes modified in terms of reactant amounts, doping routes, pH of the hydrolysing solution, washing and purification procedures, reaction and calcination temperatures.

For the synthesis of the pure anatase, the reaction is performed at 0°C in a water-ice bath. In a classical procedure, 18.38 g of titanium(IV) isopropoxide (97%) and 3.78 g of acetic acid are mixed in a three-necked flask. Then, 220 mL of water are added dropwise in 30 min, while stirring (300 rpm). The reaction is left under stirring for other 90 min to complete the hydrolysis. The reaction is left under stirring for other 90 min to complete the hydrolysis. Successively, the suspension is stored in the dark overnight for ageing and then put in an oven at 70°C for 3 h and then at 100°C overnight until complete drying. Finally, the xerogel is calcined in oxygen flux (9 NL h^{-1}) for 6 h at 400°C. In the different Chapters of this Thesis, the classical procedure was sometimes modified in terms of reactant amounts, doping routes, washing and purification procedures and calcination temperatures. Modifications of the classical procedure can affect the phase composition of the final material.

A.1.2 TiO_2 and SiO_2 sol preparations

For the preparation of titania and silica films, stable and transparent colloidal solutions were prepared.

The titania sol was prepared was prepared according to a previously reported procedure[1]. Typically, 31.7 g of titanium(IV) isopropoxide (97%) is mixed with 113 mL of absolute ethanol in a flask. Then, 1 mL of HCl (37%) is added. Successively, a solution of 0.52 g of Lutensol ON 70® (BASF) in 113 mL of ethanol was prepared and added. Eventually, the resulting solution is stirred for 1 h.

The silica sol was prepared by modifying a previously reported procedure[2]. Firstly, 10 g of TEOS is added to a solution of 4.5 g of 0.1 M HCl and 25 g of ethanol. The mixture is stirred at room temperature for 120 min and then refluxed at 60°C for 60 min. After cooling down, a solution prepared by dissolving 2 g of Lutensol ON 70® (BASF) in 25 g of ethanol, was added to the reaction mixture and stirred for 1 h.

A.1.3 Functionalization procedures by Chemical Vapour Deposition (CVD)

In Chapters 10 and 11, chemical vapor deposition procedures adapted from Sugimura *et al.*[3] were adopted to prepare functionalized SiO_2 and TiO_2 films, respectively. In the former case, the Si substrate was cleaned with water and acetone sonication and then treated in hot piranha solution for 1 h at 80 °C until a complete water spreading was observed. The substrate was rinsed with water and then dried under N_2 flux and placed in a Petri dish filled with N_2 gas together with a Teflon cup containing 80 mg of the chosen alkylsilane. The container was then placed in an oven at the chosen temperature for 3 h. In the latter case, instead, four titania films spin-coated on glass substrates were put in a Petri dish together with two Teflon cups containing 250 μL each of perfluorooctyl triethoxysilane. The container was then placed in an oven at 100°C for 2 h.

A.2 Characterization procedures

A.2.1 X-ray Powder Diffraction (XRPD)

X-ray powder diffraction analyses were performed by using a Philips PW 3710 Bragg-Brentano goniometer equipped with a scintillation counter and 1° divergence slit, 0.2 mm receiving slit, and 0.04° Soller slit systems. Graphite-monochromated Cu Kα radiation at 40 kV × 40 mA nominal X-ray power was adopted. Different acquisition ranges were selected throughout the different Chapters, in accordance with the needs.

The Quanto software, based on the Rietveld refinement, was usually adopted to get information about the materials phase composition. The average crystallite size was estimated by applying the Scherrer's equation on the most intense peak of each phase.

In Chapter 3, Rietveld refinement was performed by the GSAS software[4,5] to investigate the microstructure and the crystallographic structure of the TiO_2 powders. A pseudo-Voigt function[6] was employed to model the experimental profile, together with a power series in $Q^{2n}/n!$ and $n!/Q^{2n}$ for describing the background. Surface roughness[7], surface shift and 2θ zero terms were explicitly accounted for in the model. Preferred orientation of crystallites was also modelled by refining suitable spherical

harmonic terms[8]. During the last cycles of the refinement, scale coefficient(s), cell parameters, positional coordinates of anatase, and thermal factors were all allowed to vary as well as background and profile coefficients. The integral breadths of individual h0l reflections up to $\sin\theta/\lambda = 0.30$ Å^{-1} were computed from the refined profile coefficients and then employed to estimate the average volume-weighted crystallite dimensions, by means of the Williamson-Hall method.

In Chapter 13, X-ray diffraction data were acquired on a Bruker D8 Discover diffractometer with a non-monochromated Cu Kα source equipped with a Lynxeye 1-D detector. Grazing incidence X-ray diffraction experiments were instead performed at The European Synchrotron Research Facility BM01 SNBL using a custom heating stage. All measurements were carried out with an incident wavelength of 0.6897 Å, and patterns were acquired with a PILATUS2M detector. The incident angle was set usually between 1.5 and 2.5 degrees. The spot size was fixed at 0.5x0.5 mm^2. After the alignment, data was acquired for 10 s for the in-situ experiments, and 30 s for ex-situ experiments.

A.2.2 Surface area and porosity determinations

A Coulter SA3100 apparatus was used to record adsorption-desorption isotherm of N_2 in subcritical conditions (-196 °C) and determine specific surface areas by applying the Brunauer-Emmett-Teller (BET) method. Before the measurement the samples were outgassed at 150 °C for 2 h under vacuum. Pore size distributions were determined from the desorption isotherms by the Barrett-Joyner-Halenda (BJH) method.

A.2.3 UV-Vis spectroscopy

Diffuse reflectance spectra of solid samples, as well as transmittance spectra of films and absorption spectra of solutions and suspensions measurements were carried out on a Shimadzu UV-2600 UV-vis spectrophotometer, collecting data in different wavelength ranges, in accordance to needs.

The spectrophotometer was equipped with an integrating sphere for diffuse reflectance and transmittance analyses. $BaSO_4$ was used as a

reference. Band gap determinations were performed applying the Kubelka-Munk equation.

Just for data reported in Chapter 13, the transmission and reflectance measurements were recorded on a Perkin Elmer-Lambda 1050 UV/Vis/NIR spectrophotometer equipped with an integrating sphere and a D2(Deuterium) lamp for ultraviolet and a WI(halogen) lamp for the visible and infrared range. The absorption coefficient used for the Tauc plot calculation has been calculated with the following formula: $\alpha=-\ln(T/100+R/100)/d$, where d is the film thickness. All the samples for these measurements were deposited on quartz substrate.

The absorption UV-Vis spectroscopy was exploited to quantify the degradation of the target molecules during photocatalytic tests, by recording absorbance values at 357, 277, 246, and 224 nm for tetracycline, caffeine, paracetamol and atenolol, respectively.

In the case of photocatalysts suspension stability tests, the powder samples were suspended in water (about 7 g L^{-1}) and sonicated for 15 min, before recording absorbance values at 500 nm as a function of time.

A.2.4 X-ray Photoelectron Spectroscopy (XPS)

X-ray Photoelectron Spectroscopy spectra were obtained using an M-probe apparatus (Surface Science Instruments). The source was monochromatic Al Kα radiation (1.486 keV). A spot size of 200 μm x 750 μm and pass energy of 25 eV were used. 1s level hydrocarbon-contaminant carbon was taken as the internal reference at 284.6 eV. Atomic ratios were obtained by elaboration of Survey spectra.

A.2.5 Fourier-Transform Infrared spectroscopy (FT-IR)

FTIR measurements reported in Chapter 10 were carried out with a Bruker IFS 28 spectrometer equipped with both MCT and DTGS detectors. Spectra were collected in the 4000–400 cm^{-1} spectral range (4 cm^{-1} resolution and 128 scans). Before the FTIR analyses, all samples were pressed into self-supporting pellets (≈ 10 mg cm^{-2}), placed in a quartz cell equipped with KBr windows and activated in-vacuo at room temperature by connecting the quartz cell to a conventional high-vacuum glass line

(residual pressure ~ 10^{-4} Torr) in order to remove the species physisorbed at the surface.

FTIR spectra reported in Chapters 1, 6, 7 and 12 were acquired in the 400-4000 cm^{-1} range on a PerkinElmer Spectrum 100 FT-IR (ATR) spectrometer.

A.2.6 Raman spectroscopy

Micro-Raman spectra presented in Chapter 6 were recorded on a Horiba Jobin Yvon HR800 spectrometer, equipped with a laser (532 nm) and an Olympus BX microscope.

Raman spectra reported in Chapter 13 were recorded using a confocal Raman microscope (Renishaw inVia Raman microscope) with a 532 nm laser source of maximum power of 45W. The measurements were performed with a 100x objective in the Raman microscope with 5% of laser power. The photoluminescence measurements were performed on the same instrument equipped with a 450 nm laser.

A.2.7 Nanosecond Transient Absorption Spectroscopy (TAS)

The ns-TAS measurements reported in Chapter 13 were recorded with a custom set-up (LP980, Edinburgh Instruments Ldt., UK) able to record dynamics in the μs time range. The samples were pumped with 355 nm excitation pulse (third harmonic of a Nd:YAG laser; Ekspla NT 342, 5 ns pulse duration, 10 Hz repetition rate). A shutter before the sample regulates the pump frequency on the sample at 5 Hz. The intensity of the pump beam was regulated with neutral density filter. The pulsed probe beam was generated with a Xenon arc lamp 150 W, ozone free. The probe beam transmitted through the sample and filtered through a monochromator placed after the sample (300 mm focal length, Czerny-Turner with Triple Grating Turret). The signal was detected with a photomultiplier detector PMT (Hamamatsu R928) equipped with 5 stage dynode chain for high current linearity and collected with an oscilloscope (Tektronik MDO 3022). A cut-off filter was used in the entrance of the monochromator to cut the scattered light. Each trace has been averaged on 300 shots for almost 1 h. All the TAS measurements have been corrected from the fluorescence background and the probe background.

A.2.8 Electron Paramagnetic Resonance (EPR)

Electron paramagnetic resonance spectra were measured at room temperature and at 77 K using an X-band EPR spectrometer (Bruker Elexsys) at the working frequency of 9.4 GHz. The Bruker SimFonia program was used to perform the spectral simulations.

A.2.9 Nuclear Magnetic Resonance (NMR)

^{1}H NMR spectra reported in Chapter 7 were collected at 25°C by using a Bruker 400 MHz spectrometer. The samples for the analyses were prepared dissolving 10–15 mg of POMA/ter-polymer in 1 mL of $CDCl_3$.

Solid state NMR analyses reported in Chapter 10 were carried out using a Bruker Advance 500 spectrometer equipped with a 4-mm MAS broadband probe. ^{13}C and ^{29}Si MAS NMR spectra were recorded at 125.62 and at 99.36 MHz, respectively, packing approximately 0.15 g of solid sample into a 4-mm MAS rotor spinning at 10 kHz and at 300 K. No resolution improvement was found at higher spinning rate and/or temperature. ^{13}C and ^{29}Si nuclei were observed using direct polarization (DP) or cross polarization (CP) methods, adopting a previously reported procedure[9]. All chemical shifts were externally referenced to tetramethylsilane.

A.2.10 Elemental composition analyses

In Chapter 12, induced coupled plasma (ICP) analyses were performed by using a Perkin Elmer Optima 3000 instrument upon mineralization of the sample (*ca.* 20 mg) by nitric acid. CHNS measurements (elemental combustion system, Costech instruments) were performed to characterize the sample composition before and after the regeneration treatment.

In Chapter 13, ICP analyses were performed on Agilent 5100 model to determine the metals concentration. For the solutions, upon evaporation of hexane, 285 µL of 70% HNO_3 was added to 20 µL of the as-synthesized Cu or WO_3 colloidal solutions until complete digestion of the samples. Then, 9.715 mL of ultrapure water was added to the solution to reach the 2% acid content needed for the analysis. The nanocomposite films were digested in 500 µl of 70% HNO_3 and the solution left overnight for

complete dissolution of the film. The solution was further diluted to 2% HNO_3 for analysis using ICP to determine the metals concentration.

A.2.11 Differential Scanning Calorimetry (DSC)

In Chapter 7, the polymer glass transition temperature (T_g) was measured by DSC analyses on a Mettler Toledo DSC1, using a 10°C/min heating rate and under nitrogen atmosphere. Before measurement, samples were heated at 90°C to eliminate residual internal stresses from the synthesis.

A.2.12 Film adhesion test

Adhesion tests were performed by using a TQC model CC3000 apparatus, according to the ISO 2409 standard.

A.2.13 Permeability test

The permeability test reported in Chapter 7 was conducted in oxygen atmosphere, at 23 °C and with a relative humidity of 40%, in accordance to the ASTM D3985 standard test method for oxygen gas transmission rate through plastic films and sheeting using a colorimetric sensor.

A.2.14 Mechanical properties evaluation

In Chapter 7, the determination of the elastic modulus, the tensile strength and the elongation at break was performed in agreement with the ISO 527-1/2 standard method using a Kistler 9273 dynamometer.

A.2.15 UV stability test

In Chapter 7, in order to evaluate the stability under UV radiation of the prepared polymer foils an accelerated aging test was conducted according to the UNI10925:2001 standard method. The test was conducted for 100 h (T = 25°C and p = 1 atm), with a Jelosil HG500 lamp.

A.2.16 Scanning Electron Microscopy (SEM)

Typical scanning electron microscopy images (and Energy Dispersive X-ray Analyses) were acquired by using a Leo 1430 Zeiss or a Hitachi TM1000 instruments.

Top and cross-sectional SEM images reported in Chapters 8, 9 and 12 were acquired by using a Zeiss EVO50 instrument.

FE-SEM images reported in Chapters 8 and 9 were obtained on pristine films on a Zeiss Supra 40 working in high vacuum and equipped with a GEMINI column, with a high efficiency In-lens detector. Electron energy: 200 V–30 kV. Max resolution: 1 nm @ 20kV (detector In-lens).

SEM images reported in Chapter 13 were acquired on a FEI Teneo 200 FEG Analytical Scanning Electron Microscope using a beam energy of 5 keV.

A.2.17 Transmission Electron Microscopy (TEM)

The transmission electron microscopy images reported in Chapter 4 were acquired by using a Zeiss Libra FE 200 keV instrument, equipped with in column second generation Omega filter for energy selected spectroscopy. The TEM samples were prepared following this procedure: first the nanostructured powders were finely smashed in a mortar, then suspended in isopropanol and finally sonicated 15 minutes. Immediately after sonication process the suspensions were dropped onto a holey carbon coated copper TEM grid. All specimens were dried at room temperature for 24 h. The micrograph analyses were performed using the iTEM TEM Imaging Platform software (Olympus). The equivalent diameter was estimated calculating the median of the distribution.

High resolution transmission electron microscopy images reported in Chapters 5 and 6 were acquired using a 300 kV JEOL JEM 3010UHR microscope equipped with a LaB_6 single crystal filament and an energy dispersive X-ray (EDX) detector (Oxford INCA Energy TEM 200). Sample powders were dry deposited on 200 mesh Cu “holey” carbon grids.

TEM images reported in Chapter 13 were acquired on a FEI Tecnai Spirit using a beam energy of 200 kV, equipped with a Gatan camera. STEM-HAADF imaging, HRTEM and energy dispersive X-ray analysis (EDX) were performed on a FEI Tecnai Osiris transmission electron microscope at an accelerating voltage of 200 kV. EDX maps of 512x512 pixels were acquired using a beam current of 630 pA and with a dwell time of 50 msec per pixel.

A.2.18 Atomic Force Microscopy (AFM)

Atomic force microscopy analyses reported in Chapters 8 and 9 were performed on a FastScan (Bruker) microscope working in tapping mode. Root mean squared roughness (RMS) values were obtained on 1 × 1 μm^2 areas.

Measurements reported in Chapter 10 were performed in tapping mode using a Solver LS AFM (NT-MDT) equipped with NSC35 tips (μMash).

A.2.19 Contact angle determinations

Contact angle measurements were carried out on a Krüss EasyDrop instrument adopting 5 μL drops. The contact angle determinations with water and diiodomethane were used to determine the surface free energies, according to a procedure reported by Lee *et al.*[10].

A.2.20 Electrospray ionization mass spectroscopy (ESI-MS)

A Thermo Finnigan (MA, USA) LCQ Advantage system MS spectrometer with an electrospray ionisation source and an 'Ion Trap' mass analyser was adopted to perform ESI-MS analyses, in order to analyse photocatalytic reactions intermediates. The samples were solubilized in methanol, while formic acid was added in order to enhance the sample volatility. The MS spectra were obtained by direct infusion of the sample solutions under positive electrospray ionisation by application of +3.0 kV at the entrance of the capillary with the drying gas heated to 350 °C. Full-scan mass spectra were recorded in the mass/charge (m/z) range of 50–1000.

A.2.21 Gas chromatography mass spectroscopy (GC-MS)

GC-MS measurements were performed by using an ISQ™ QD Single Quadrupole GC-MS (Thermo Fisher). The injection temperature was fixed at 250 °C with a flow of 1.2 mL min^{-1} and a ZB-1MS 60 m (0.25 μm I.D.; 0.25 μm thickness) column, fixing at 260 °C the transfer line temperature and at 250 °C the ion source temperature.

A.2.22 Size Exclusion Chromatography (SEC)

In Chapter 7, the polymer molecular weight before and after accelerated ageing was investigated by SEC using a Waters 1515 Isocratic HPLC pump and a four Phenomenex Phenogel (5×10^{-3}Å-5×10^{-4}Å-5×10^{-5}Å-5×500Å) column set with a RI detector (Waters 2487) using a flow rate of 1 mL/min and 40 μL as injection volume. Samples were prepared dissolving 40 mg of polymer in 1 mL of anhydrous THF; before the analysis, the solution was filtered with 0.45 μm filters. Molecular weight data were expressed in polystyrene (PS) equivalents. The calibration was built using monodispersed PS standards having the following nominal peak molecular weight (Mp) and molecular weight distribution (D): Mp = 1600000 Da (D≤1.13), Mp = 1150000 Da (D≤1.09), Mp = 900000 Da (D≤1.06), Mp = 400000 Da (D≤1.06), Mp = 200000 Da (D≤1.05), Mp =90000 Da (D≤1.04), Mp =50400 Da (D=1.03), Mp= 30000 Da (D=1.06), Mp = 17800 Da (D=1.03), Mp = 9730 Da (D=1.03), Mp = 5460 Da (D=1.03), Mp = 2032 Da (D=1.06), Mp = 1241 Da (D=1.07), Mp = 906 Da (D=1.12), Mp = 478 Da (D=1.22); Ethyl benzene (molecular weight = 106 g/mol). For all analyses, 1,2-dichlorobenzene was used as internal reference. The molecular weights of the samples obtained after the UV exposure test were also determined.

A.2.23 Total Organic Carbon (TOC) measurements

The mineralization degree of the pollutants during photocatalytic degradation tests was determined by TOC measurements by using a Shimadzu TOC-V CPN Analyzer.

A.2.24 Electrophoretic measurements

ζ-potential measurements were performed on 0.5 or 1 mg mL^{-1} sample suspensions in 10^{-2} M KNO_3 aqueous solutions using a Malvern Zetasizer Nano instrument. The isoelectric point of the powder materials was determined by recording ζ-potential values, as a function of pH, by using HNO_3 and KOH solutions.

A.2.25 Dynamic Light Scattering (DLS) analyses

DLS measurements were performed by using a Malvern Zetasizer Nano ZS instrument.

A.2.26 Electrochemical measurements

Electrochemical characterizations were carried out using a PGStat30 potentiostat/galvanostat equipped with FRA module (Metrohm, Autolab, The Netherlands).

In Chapter 10, measurements were recorded in a standard three electrodes cell, using a saturated calomel, a Pt wire and a functionalized Si wafer electrode as reference, counter and working electrodes, respectively. Cyclic voltammetry (CV) was performed in 0.1 M $NaClO_4$ aqueous solution, scanning the potential in the range – 0.1 V/ + 0.4 V. Electrochemical impedance spectroscopy was performed at three different potentials, – 0.1 V, + 0.1 V and + 0.25 V, in the same conditions of CV, in the frequency range 0.1-65000 Hz with amplitude 0.01 V.

In Chapter 8 and 9, KCl 0.1 M was used as supporting electrolyte and 3 mM $[Fe(CN)_6]^{4-}/[Fe(CN)_6]^{3-}$ or $[Ru(NH_3)_6]^{3+}/[Ru(NH_3)_6]^{2+}$ as redox probes. CV analyses were performed scanning the potential in the – 0.3/+ 0.7 V (SCE) and in the + 0.2/– 0.5 V (SCE) voltammetric windows in the case of $[Fe(CN)_6]^{4-}/[Fe(CN)_6]^{3-}$ and $[Ru(NH_3)_6]^{3+}/[Ru(NH_3)_6]^{2+}$, respectively. CV parameters were the following: step potential 0.005 V, scan rate range 0.01–0.75 V s^{-1}. Electrochemical impedance spectroscopy (EIS) measurements were carried out at – 0.1, + 0.1 and + 0.25 V (SCE) for $[Fe(CN)_6]^{4-}/[Fe(CN)_6]^{3-}$ and at + 0.1, – 0.15 and – 0.25 V for $[Ru(NH_3)_6]^{3+}/[Ru(NH_3)_6]^{2+}$. EIS parameters were the following: frequency range 0.1–65000 Hz, amplitude 0.01 V.

Impedance data were elaborated by Z-view 3.1 software.

A.3 Instrumentation

A.3.1 Lamps for photocatalytic tests

Photocatalytic tests in the gas phase under UV irradiation were performed by adopting a Jelosil HG500 iron halogenide lamp, with an effective power density of 17 mW cm^{-2} in the 280–400 nm, measured using a Thorlabs

S314C radiometer. The same lamp, in a different experimental setup, was adopted for the photocatalytic tests in the liquid phase. In this case the effective power density was equal to 30 mW cm^{-2}.

Photocatalytic tests and simulated solar light (both in the gas and the liquid phase) were performed by using a Lot Oriel halogen lamp, with an effective power density 1 mW cm^{-2} in the range 280–400 nm and 14 mW cm^{-2} in the range 400–800 nm. A filter with wavelength cut-off under 400 nm was adopted for photocatalytic tests under visible light (effective power density: 14 mW cm^{-2} in the range 400–800 nm).

Only in the case of the photocatalytic tests under simulated solar light reported in Chapter 7, a UltraVitalux lamp with an effective power density of 4.5 mW cm^{-2} in the 280–400 nm range and of 14 mW cm^{-2} in the 400–800 nm range was adopted.

An ORIEL LCS-100 Series AM 1.5 Solar Simulator with an illumination intensity adjusted to 100 mW cm^{-2} was used for the photoelectrochemical measurements reported in Chapter 13.

The light emission spectra of the two most adopted lamps are reported in Figure A.1.

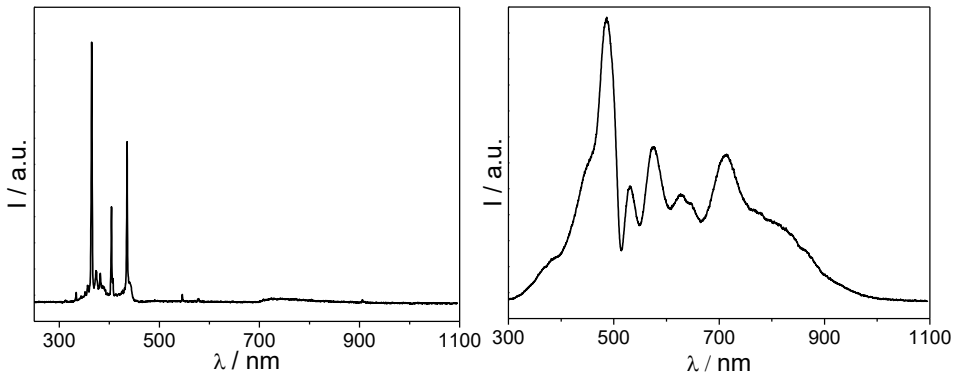

Figure A.1 – Light emission spectra of the Jelosil UV (left) and the Lot Oriel solar (right) lamps.

A.3.2 Experimental setup for gas phase photocatalytic tests

The photocatalytic reactions in the gas phase were performed in a 9.7 L Pyrex glass cylindrical batch reactor, thermostated at 40°C and filled with an 80:20 N_2:O_2 dry atmosphere. After the pollutant injection by means of

a microsyringe, the system was held in the dark for an equilibration time of 20 min. Both the disappearance of the pollutant molecule and the formation of intermediates and products were followed during photocatalytic tests, by adopting an Agilent 7890 gas-chromatographic system equipped with DB-VAX and Porapak columns, two FID detectors and a methanator.

A.4 Molecular structures

Molecule	Chemical structure
Tetracycline	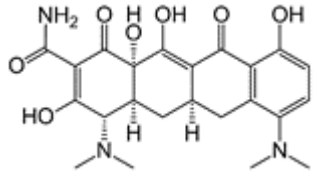
Caffeine	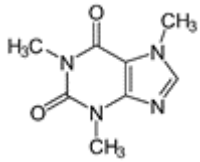
Paracetamol	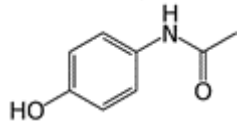
Atenolol	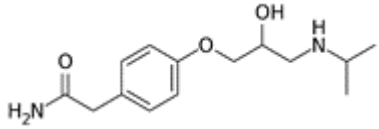
Octyl triethoxysilane	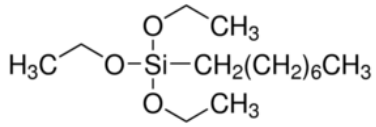
Perfluorooctyl trehoxysilane	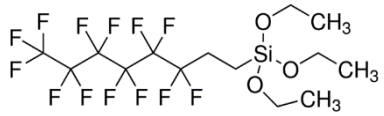
Dopamine	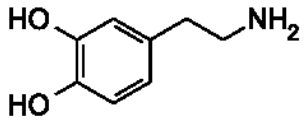

References

1 G. Maino, D. Meroni, V. Pifferi, L. Falciola, G. Soliveri, G. Cappelletti and S. Ardizzone, *J. Nanoparticle Res.*, 2013, **15**, 2087.

2 G. Soliveri, V. Pifferi, G. Panzarasa, S. Ardizzone, G. Cappelletti, D. Meroni, K. Sparnacci and L. Falciola, *Analyst*, 2015, **140**.

3 A. Hozumi, K. Ushiyama, H. Sugimura and O. Takai, *Langmuir*, 1999, **15**, 7600–7604.

4 B. H. Toby, *J. Appl. Crystallogr.*, 2001, **34**, 210–221.

5 A. C. Larson and R. B. Von Dreele, *General Structural Analysis System (GSAS)*, 2004.

6 P. Thompson, D. E. Cox and J. B. Hastings, *J. Appl. Crystallogr.*, 1987, **20**, 79–83.

7 W. Pitschke, H. Hermann and N. Mattern, *Powder Diffr.*, 1993, **8**, 74–83.

8 H. J. Bunge, *Texture Analysis in Materials Science*, Butterworth-Heinemann: Oxford, 1993.

9 F. Milanesi, G. Cappelletti, R. Annunziata, C. L. Bianchi, D. Meroni and S. Ardizzone, *J. Phys. Chem. C*, 2010, **114**, 8287–8293.

10 J. P. Lee, Y. J. Jang and M. M. Sung, *Adv. Funct. Mater.*, 2003, **13**, 873–876.

Appendix B

List of publications

- L. Rimoldi*, A. Giordana, G. Cerrato, E. Falletta, D. Meroni*, Insights on the photocatalytic degradation processes supported by TiO_2/WO_3 systems. The case of ethanol and tetracycline., *Catal. Today*, DOI: 10.1016/j.cattod.2018.11.035, in press.
- V. Sabatini*, L. Rimoldi*, L. Tripaldi, D. Meroni*, H. Farina, M. A. Ortenzi, S. Ardizzone, TiO_2-SiO_2-PMMA terpolymer floating device for the photocatalytic remediation of water and gas phase pollutants, *Catalysts*, 2018, **8**, 568.
- F. Broglia, L. Rimoldi*, D. Meroni*, S. De Vecchi, M. Morbidelli, S. Ardizzone, Guaiacol hydrodeoxygenation as a model for lignin upgrading. Role of the support surface features on Ni-based alumina-silica catalysts., *Fuel*, submitted.
- L. Rimoldi*, V. Pifferi*, D. Meroni*, G. Soliveri, S. Ardizzone, L. Falciola, Three-dimensional mesoporous silica networks with improved diffusion and interference-abating properties for electrochemical sensing, *Electrochim. Acta*, 2018, **291**, 73–83.
- M. Scarongella, C. Gadiyar, M. Strach, L. Rimoldi, A. Loiudice, R. Buonsanti*, Assembly of β–$Cu_2V_2O_7/WO_3$ heterostructured nanocomposites and the impact of their composition-dependent structure on the photoelectrochemical properties., *J. Mater. Chem. C*, 2018, **6**, 12062−12069.
- L. Rimoldi*, T. Taroni, D. Meroni*, Wetting modification by photocatalysis: A hands-on activity to demonstrate photoactivated reactions at semiconductor surfaces, *J. Chem. Educ.,* 2018, **95**, 2216–2221.
- L. Rimoldi*, E. Pargoletti*, D. Meroni*, E. Falletta, G. Cerrato, F. Turco, G. Cappelletti, Concurrent role of metal (Sn, Zn) and N species in

enhancing the photocatalytic activity of TiO_2 under solar light, *Catal. Today*, 2018, **313**, 40−46.

- V. Pifferi*, L. Rimoldi*, D. Meroni*, F. Segrado, G. Soliveri, S. Ardizzone, L. Falciola, Electrochemical characterization of insulating silica-modified electrodes: transport properties and physicochemical features, *Electrochem. Commun.*, 2017, **81**, 102−105.
- L. Rimoldi*, D. Meroni*, E. Falletta, V. Pifferi, L. Falciola, G. Cappelletti, S. Ardizzone, Emerging pollutant mixture mineralization by TiO_2 photocatalysts. The role of the water medium, *Photochem. Photobiol. Sci.*, 2017, **16**, 60−66.
- L. Rimoldi*, D. Meroni*, E. Falletta, A.M. Ferretti, A. Gervasini, G. Cappelletti, S. Ardizzone, The role played by different TiO_2 features on the photocatalytic degradation of paracetamol, *Appl. Surf. Sci.*, 2017, **424**, 198−205.
- L. Rimoldi, D. Meroni, G. Cappelletti, S. Ardizzone*, Green and low cost tetracycline degradation processes by nanometric and immobilized TiO_2 systems, *Catal. Today*, 2017, **281**, 38−44.
- L. Rimoldi, C. Ambrosi, G. Di Liberto, L. Lo Presti*, M. Ceotto, C. Oliva, D. Meroni, S. Cappelli, G. Cappelletti, G. Soliveri, S. Ardizzone, Impregnation vs. bulk synthesis: how the synthetic route affects the photocatalytic efficiency of Nb/Ta:N codoped TiO_2 nanomaterials, *J. Phys. Chem. C*, 2015, **19**, 24104−24115.
- G. Soliveri, V. Pifferi, R. Annunziata, L. Rimoldi, V. Aina, G. Cerrato, L. Falciola, G. Cappelletti, D. Meroni*, Alkylsilane−SiO_2 Hybrids. A Concerted Picture of Temperature Effects in Vapor Phase Functionalization, *J. Phys. Chem. C*, 2015, **119**, 15390−15400.